

Tesis Doctoral

Thermo-mechanical modelling to evaluate solar receiver damage

Autora:

Marta Laporte Azcué

Tesis depositada en cumplimiento parcial de los requisitos para el
grado de Doctor en Ingeniería Mecánica y de Organización
Industrial

Universidad Carlos III de Madrid

Director:

Domingo Santana Santana

Co-directora:

María de los Reyes Rodríguez Sánchez

Leganés (Madrid), Julio 2021

Esta tesis se distribuye bajo licencia "Creative Commons **Reconocimiento - No Comercial - Sin Obra Derivada**"



A mis padres

*Where must we go, we who wander this wasteland,
in search for our better selves?*

Mad Max: Fury Road (2015)

Agradecimientos

Al término de esta etapa, debo empezar por agradecerle a Domingo la confianza que depositó en mí al darme la oportunidad de embarcarme en ella. Me gustaría darles las gracias tanto a él como a Reyes, directores de esta tesis, por su implicación constante, su guía, su apoyo y su paciencia durante estos años. También quiero agradecer a Pedro su inmensa ayuda, sin la cual el desarrollo de esta investigación hubiese sido muy diferente.

A los miembros del departamento de Ingeniería Térmica y Fluidos, que siempre me han brindado la máxima cercanía y apoyo, gracias por hacerme formar parte de este equipo. A María Venegas, Dani Serrano, Antonio Soria, Alberto Sánchez y Sergio, responsables de las asignaturas de las que he coordinado prácticas, por todas las facilidades, recomendaciones y ayuda que me han proporcionado. A Rafa, por amenizarme los días en el despacho con tus ocurrencias, y a Vanesa, por todas esas charlas y confidencias compartidas. A Álex y Carol, por todas las risas y tarde-noches épicas *Coca-Cola* en mano. A Mariano, por tus ganas de escuchar, tus ánimos y tus buenos consejos. A Luismi, Antonio Acosta, por su amabilidad y predisposición para ayudar. También a María, Andrés, Alejandro Millán, Wil, Patri, Fer, Alberto, Kike, Jesús, Espe, Alen, por los grandes ratos en la universidad y, sobre todo, fuera de ella. A Dani, gracias por tus consejos, tu apoyo y, sobre todo, por compartir conmigo ese sentido del humor que te caracteriza; gracias por los incontables buenos momentos.

A los compañeros del departamento de Ingeniería Mecánica, Andrés, Álvaro y José, por su ayuda y colaboración.

Gracias a Marta, Lu, Ana, Marián y Dani por seguir acompañándome en la distancia igual que siempre, gracias por vuestros ánimos y cariño. A Sara, Yudith y Sandra, por seguir contagiando la misma energía que el primer día de carrera. A Mike, por abrirme las puertas del *pisuco* y ser un compañero excepcional durante tres años.

Finalmente, quiero agradecer a mi familia todo el apoyo, comprensión y cariño incondicional. A mi abuela, mis primas y mis tíos. A mis padres, Alfredo y Marta, por vuestro sacrificio y por animarme siempre a dar lo mejor de mí.

Published and submitted content

As a result of the work of this dissertation, the following papers have been published or submitted for publication:

- M. Laporte-Azcué; P.A. González-Gómez; M.R. Rodríguez-Sánchez; D. Santana. Exergy analysis of solar central receivers. *Solar Energy* 2020;207: 957-73. DOI: 10.1016/j.solener.2020.07.033. This publication is partially included in **Chapter 2** but is not indicated as a reference in the main text.
- M. Laporte-Azcué; P.A. González-Gómez; M.R. Rodríguez-Sánchez; D. Santana. Deflection and stresses in solar central receivers. *Solar Energy* 2020;195: 355-68. DOI: 10.1016/j.solener.2019.11.066. This publication is partially included in **Chapter 3** but is not indicated as a reference in the main text.
- M. Laporte-Azcué; P.A. González-Gómez; M.R. Rodríguez-Sánchez; D. Santana. Material selection for solar central receiver tubes. *Submitted for publication in Solar Energy Materials Solar Cells*. This publication is partially included in **Chapter 4** but is not indicated as a reference in the main text.
- M. Laporte-Azcué; M.R. Rodríguez-Sánchez; P.A. González-Gómez; D. Santana. Assessment of time resolution for the central-solar-receiver lifetime estimation. *Submitted for publication in Applied Energy*. This publication is partially included in **Chapter 5** but is not indicated as a reference in the main text.
- M. Laporte-Azcué; P.A. González-Gómez; M.R. Rodríguez-Sánchez; D. Santana. A procedure to predict solar receiver damage during transient conditions. *Submitted for publication in Renewable and Sustainable Energy Reviews*. This publication is partially included in **Chapter 6** but is not indicated as a reference in the main text.

The following conference presentations are also an outcome of the thesis:

- M. Laporte-Azcué; J. Gómez-Hernández; M.R. Rodríguez-Sánchez; D. Santana. Solar Power Tower Plants Receiver Design Studying the Entropy

of the Receiver's Tubes. In *XI National and II International Engineering Thermodynamics Congress*. Albacete, Spain. Oral presentation.

- M. Laporte-Azcué; P.A. González-Gómez; M.R. Rodríguez-Sánchez; D. Santana. Lifecycle Estimation for Different Solar Central Receiver Configurations. In *26th SolarPACES Conference*. Online event. Poster presentation.
- M. Laporte-Azcué; P.A. González-Gómez; M.R. Rodríguez-Sánchez; D. Santana. Creep and fatigue damage assessment for molten-salt central receivers. In *ISES Solar World Congress 2021*. Online event.

Other research merits

Apart from this work, further related papers have also been published in international journals:

- P.A. González-Gómez; M.R. Rodríguez-Sánchez; M. Laporte-Azcué; D. Santana. Calculating molten-salt central-receiver lifetime under creep-fatigue damage. *Solar Energy* 2021;213:180-97. DOI: 10.1016/j.solener.2020.11.033.

The following works have also been presented in conferences:

- M. Laporte-Azcué; M.R. Rodríguez-Sánchez; D. Santana. Análisis de la eficiencia del receptor con nuevos tubos de geometría elíptica en centrales termosolares tipo torre. In *XVI Congreso Ibérico y XIII Congreso Iberoamericano de Energía Solar*. Madrid, Spain. Poster presentation. Published as *Libro de Actas XVI Congreso Ibérico y XIII Congreso Iberoamericano de Energía Solar*, 427-434. ISBN: 978-84-86913-14-4.
- M. Laporte-Azcué; M.R. Rodríguez-Sánchez; D. Santana. Elliptical tubes receivers efficiency analysis in solar power towers. In *24th SolarPACES Conference*. Casablanca, Morocco. Poster presentation. Accepted for publication as *AIP Conference Proceedings*.
- M.R. Rodríguez-Sánchez; M. Laporte-Azcué; J.A. Artero-Guerrero; D. Santana. Asymmetric tubes to increase the lifetime of solar receivers. In *26th SolarPACES Conference*. Online event. Poster presentation.
- J. Pastor-Peña; P.A. González-Gómez; M. Laporte-Azcué; D. Santana. A novel storage system to recover energy during fast startups of combined cycle power plants. In *15th International Conference on Heat Transfer, Fluid Mechanics and Thermodynamics (HEFAT2021)*. Online event.

And a patent has been granted:

- D. Santana; M.R. Rodríguez-Sánchez; M. Laporte-Azcué; J. López-Puente; A. Acosta-Iborra. Receptor solar de torre exterior. P201830587, ES Patent. 2018. University Carlos III of Madrid.

Abstract

Seeking for greener alternatives to decrease the dependence on fossil fuels, one of the main challenges faced is their variability due to the ambient conditions. Among the renewable options, some concentrating solar power technologies can integrate thermal storage systems; this increases their cost but results in firm and flexible plants, able to dispatch energy even during solar resource interruptions. In this regard, solar power tower plants working with molten salt allow a direct integration of such thermal storage, coupled to a conventional subcritical Rankine cycle. However, the solar tower receiver is one of the most critical subsystems, working under extremely demanding conditions: high uneven heat fluxes and cyclic operation due to diurnal cycles and cloud passages. These can jeopardize its reliability, being necessary to improve their design and operation to diminish such risk and thus make the whole plant more economically appealing. The first step in that path is to determine the temperature on the receiver tubes, which can result in a task with a high computational cost since it varies with the sun position and the DNI. Then, the elastic stresses and strains distribution on the receiver tubes can be obtained. Finally, the receiver lifetime estimation can be performed, considering the creep and fatigue damages. With that in mind, this thesis comprehends:

The development of a low computational cost model to obtain the temperature distribution on the receiver tubes, discretized in circumferential and axial divisions, taking into account the multiple reflections and emissions happening on the receiver surfaces. This thermal model integrates an exergy one, allowing to explore opportunities to enhance the receiver performance.

Then, a low computational cost model is proposed to calculate the elastic stresses and strains on the receiver, based on the thermal forces and moments on the tubes. It considers the temperature dependence of the tubes material properties and allows to study different mechanical boundary conditions such as the tube free bending, the inclusion of intermediate supports, and even an infinite number of them (generalized plane strain scenario).

Lastly, the creep and fatigue damages on the receiver, and the subsequent lifetime results, are investigated. For that end, the receiver thermal and mechanical restrictions are watched, ensuring not surpassing the film temperature limit, to avoid accelerated corrosion, and the stress reset limit, that would pre-

vent the desirable global stress relaxation. The damage analysis allows us to determine the most suitable alloy alternative for the receiver tubes manufacturing, considering their lifetime prospects and power production potential to perform an economic study. Then, the most adequate time discretization for the damage analysis is examined during a clear-sky day, regarding the accuracy of the results and the computational cost and taking into account the receiver hours of operation required for the thermal energy storage system filling. Moreover, the results obtained when selecting several days throughout the year instead of just a representative one are also investigated. Subsequently, the influence of the cloud passages and hazy days is determined, showing that fatigue damage has a less relevant role than the creep one in the resulting receiver lifetime. Fatigue is mainly affected by multiple start-ups during the day, being the effects of small cloud transients negligible. In high energy days, which are the most common ones at the location studied—as should be for any suitable location for concentrating solar technologies—, the long operating of the receiver favors high creep levels.

Resumen

Uno de los principales retos en la búsqueda de alternativas renovables con el fin de reducir la dependencia de los combustibles fósiles es la variabilidad de las fuentes de energía renovables. Entre las opciones renovables, algunas tecnologías de concentración solar pueden integrar sistemas de almacenamiento térmico; estos incrementan su coste, pero dan lugar a plantas firmes y flexibles, capaces de proporcionar energía incluso en períodos de interrupción del recurso solar. En este sentido, las plantas termosolares tipo torre trabajando con sales fundidas permiten la integración directa del sistema de almacenamiento, acoplado a un ciclo de Rankine subcrítico convencional. Sin embargo, el receptor de torre es uno de los subsistemas más críticos, trabajando en condiciones extremadamente exigentes: altos flujos de calor no uniformes y una operación cíclica causada por la alternancia de periodos diurnos y nocturnos así como por los pasos de nubes. Estos pueden hacer peligrar su fiabilidad, siendo necesario mejorar su diseño y operación para reducir tal riesgo y hacer que el conjunto de la planta sea económicamente más atractivo. El primer paso hacia esa meta consiste en determinar la temperatura en los tubos que integran el receptor, lo que puede ser una tarea computacionalmente costosa ya que depende de la radiación directa y la posición del sol. Tras ello, la distribución de tensiones y deformaciones elásticas en los tubos puede obtenerse. Finalmente, esto permite llevar a cabo una estimación del tiempo de vida del receptor, teniendo en cuenta los daños por fluencia lenta y fatiga. Con todo esto, la presente tesis doctoral comprende:

El desarrollo de un modelo de bajo coste computacional para obtener la distribución de temperaturas en los tubos del receptor, discretizados en divisiones circunferenciales y axiales, y teniendo en cuenta los múltiples intercambios radiativos que ocurren en las superficies del receptor. Tal modelo térmico integra un análisis exergético, permitiendo explorar las posibles oportunidades de mejora de la eficiencia del receptor.

A continuación, se propone un modelo, también de bajo coste computacional, para calcular las tensiones y deformaciones elásticas causadas por las fuerzas y momentos térmicos presentes en los tubos. El modelo tiene en cuenta la dependencia de la temperatura de las propiedades del material de los tubos y permite estudiar distintas alternativas para las condiciones de contorno mecánico.

cas, como la flexión libre del tubo, la inclusión de apoyos intermedios e incluso un número infinito de ellos (condición de deformación plana generalizada).

Para concluir, se investigan los daños por fluencia lenta y fatiga en el receptor, así como el tiempo de vida resultante. Para ello, se tienen en cuenta las restricciones térmicas y mecánicas del receptor, garantizando temperaturas de película por debajo de la admisible (para evitar una corrosión acelerada) y tensiones por debajo del límite de restablecimiento de tensiones, que impedirían la relajación de tensiones, deseable ante tan altas tensiones y temperaturas en los tubos. El análisis de daños nos permite determinar la aleación más adecuada para la fabricación de los tubos del receptor, teniendo en cuenta su vida útil esperada, sus costes y la potencia térmica que permiten otorgar al receptor para realizar un estudio económico. Tras esto, se estudia cuál es la discretización temporal óptima para el análisis de daños, considerando la precisión en los resultados y el coste computacional, así como el impacto de utilizar varios días a lo largo del año en lugar de un único representativo. Finalmente, se investiga la influencia del paso de nubes y de los días brumosos en el daño del receptor, mostrando que el daño por fatiga tiene un menor peso que el daño por fluencia lenta. El daño por fatiga está afectado en su mayor parte por los arranques diarios, siendo despreciables los efectos de los pequeños pasos de nubes. Durante los días de alto nivel de energía, los más frecuentes en la localización estudiada, como cabría esperar de cualquier localización adecuada para este tipo de tecnologías, las largas horas de operación favorecen altos niveles de daño por fluencia lenta.

Contents

Agradecimientos	i
Published and submitted content	iii
Other research merits	v
Abstract	vii
Resumen	ix
List of figures	xx
List of tables	xxii
1 General introduction	1
1.1 Motivation	1
1.2 Concentrating solar power	3
1.3 Solar power tower plants	4
1.3.1 Subsystems	6
1.3.2 Solar power tower receiver operation limits and issues	8
1.3.3 Costs, efficiencies, and improvement potential	17
1.4 Scope of the thesis	19
1.5 Outline of the thesis	20
References	22
2 Thermal and exergy analysis of solar central receivers	27
2.1 Introduction	28
2.2 Proposed modelling	31
2.2.1 Discretization of the receiver	31
2.2.2 Thermal model of the receiver (ECGM)	34
2.2.3 Exergy calculation (XCGM)	40
2.3 Case of study	44
2.3.1 Ambient conditions	44
	xi

2.3.2 Heliostat field	44
2.3.3 Receiver configuration	45
2.4 Results	49
2.4.1 Optical properties influence	50
2.4.2 Aiming strategy and DNI influence	53
2.4.3 Ambient temperature influence	58
2.5 Conclusions	61
References	65
3 Calculation of the elastic stresses and deflections in solar central receiver tubes	69
3.1 Introduction	70
3.2 Elastic stress calculation in cylindrical tubes	74
3.2.1 Yield criterion	75
3.2.2 Radial and hoop thermal stress	76
3.2.3 Axial stresses	78
3.3 Central receiver with a non-symmetrical temperature distribution	82
3.4 Results and discussion	84
3.4.1 Initial verification: Analytical vs numerical model	85
3.4.2 Guided tube	90
3.5 Conclusions	95
References	97
4 Material selection for solar central receiver tubes	101
4.1 Introduction	102
4.2 Methodology	106
4.2.1 Heliostat field and thermal model	106
4.2.2 Elastic stresses and strains model	107
4.2.3 Lifetime model	108
4.2.4 Levelized cost of alloy (LCOA)	113
4.3 Case of study	114
4.3.1 Receiver characteristics	114
4.3.2 Alloys characteristics	115
4.3.3 Design day and field aiming	123
4.4 Results and discussion	124
4.4.1 Maximum aiming factor allowable	124
4.4.2 Creep-fatigue results: lifetime analysis	129
4.4.3 Receiver costs	142

4.5 Conclusions	145
References	149
5 Assessment of time resolution for the receiver lifetime estimation	159
5.1 Introduction	160
5.2 Methodology	163
5.2.1 Models employed	163
5.2.2 Calculation procedure	167
5.3 Characteristics studied	168
5.3.1 Heliostat field and receiver description	168
5.3.2 Cases of study	170
5.4 Results and discussion	172
5.4.1 Time resolution analysis	172
5.4.2 Design day analysis	182
5.5 Conclusions	187
References	190
6 Creep-fatigue damage calculation during transient conditions	195
6.1 Introduction	196
6.2 Receiver models employed	198
6.2.1 Optical model, aiming strategy and thermal model	198
6.2.2 Elastic stresses and strains model and lifetime model	200
6.3 Configurations analysed	202
6.3.1 Reference design days, and heliostat field and receiver configuration	202
6.3.2 Receiver control modes during transient conditions	203
6.3.3 DNI cases of study	207
6.4 Methodology proposed to calculate the transient operation	208
6.4.1 Clean design day and cloudy day levels characterization	208
6.4.2 Calculating the creep and fatigue damages	210
6.5 Results and discussion	210
6.5.1 DNI database clustering	211
6.5.2 Creep and fatigue damage results for clustered days	215
6.5.3 Damage analysis using the 2018 DNI database	222
6.6 Conclusions	224
References	227
7 General conclusions	233

A Appendix A: Fourier series coefficients	237
B Appendix B: Stresses calculation for homogeneous properties	239
C Appendix C: Time resolution analysis extended results	243
D Appendix D: Set of days lifetime analysis extended results	245
Alphabetical list of references	249

List of Figures

1.1	CSP technologies (Solar Concentra, 2013). (a) Linear Fresnel, (b) Parabolic trough, (c) Parabolic dish and (d) Central receiver.	4
1.2	Solar power tower plant schematic representation.	6
1.3	Solar power tower technology issues. Adapted from (Mehos <i>et al.</i> , 2020).	9
1.4	Creep curve showing the different creep stages.	10
1.5	Creep and fatigue interaction and failure modes.	11
1.6	(a) Strain transference from elastic to inelastic during creep. (b) Global stress relaxation during cyclic operation (solid line) and stress relaxation interrupted by stress reset (dashed line).	12
1.7	Solar One receiver bending and warpage (Radosevich & Skin- rood, 1989).	14
1.8	Tubes material, environment and operation conditions interacta- tion leading to stress corrosion cracking.	15
1.9	Shouhang Dunhuang operation during clouds period.	16
2.1	Models involved in the receiver exergy analysis.	32
2.2	(a) Discretization of the geometries interacting in an external receiver (b) Plant view of one axial division.	33
2.3	Iterative process of the thermal model.	35
2.4	Exergies schematic representation.	41
2.5	Discretized heat flux distribution on the receiver surface with the flat aiming strategy.	45
2.6	Schematic of the elements considered for the pressure drop cal- culation in one panel. Only one tube has been depicted.	47
2.7	Sankey diagram for the exergy analysis of the receiver.	50
2.8	(a) Evolution with the optical properties degradation of the a) exergy efficiency and (b) thermal efficiency.	51
2.9	Breakdown of the percentage exergies evolution with the optical properties degradation.	52

2.10	Discretized heat flux distribution on the receiver surface with the peak aiming strategy.	54
2.11	(a) Axial evolution of the tube wall temperature at $\theta=0^\circ$ and (b) circumferential evolution of the tube wall temperature at $h=10$	55
2.12	Evolution, for flat and peak aiming strategies and different DNI levels, of the (a) exergy efficiency and the (b) thermal efficiency.	55
2.13	Breakdown of the percentage exergies evolution with the DNI for flat and peak aiming strategies.	56
2.14	Exergy efficiency of the SPT receiver for flat and peak aiming strategies under different DNI.	58
2.15	Exergy efficiency evolution with the DNI for different ambient temperatures.	59
2.16	Breakdown of the percentage exergies evolution with the DNI for different ambient temperatures.	61
3.1	Graphical abstract.	70
3.2	Support arrangement and boundary conditions.	74
3.3	(a) Grid of calculation in the cross section and coordinates origins in the centroid (x, y, z) and in the neutral axis (x^*, y^*, z). (b) Deflection of a tube axial division.	75
3.4	Schematic of the receiver studied.	83
3.5	Schematic temperature profile evolution of the HTF. The HTF is heated as it flows through the panels tubes, from panel a to panel b.	84
3.6	Axial division of the receiver tube under free bending conditions.	86
3.7	Average temperature difference between the right and left halves of the tube cross section along the tube length, representing the asymmetry (blue solid line). Maximum temperature gradient in the cross section along the tube length (orange solid line).	86
3.8	Cross sectional temperature distribution.	87
3.9	σ_r stress for variable properties (left panel) and constant properties (right panel).	88
3.10	σ_θ stress for variable properties (left panel) and constant properties (right panel).	88
3.11	$\sigma_{z,MA}$ stress for variable properties (left panel) and constant properties (right panel).	88
3.12	$\sigma_{VM,MA}$ stress for variable properties (left panel) and constant properties (right panel).	89

3.13 (a) Temperature difference between the right and left halves of the first axial division cross section and (b) Temperature difference between the right and left halves of the tube outer wall.	90
3.14 (a) Tube bending in the y axis.	91
3.14 (b) Tube bending in the x axis (cont.).	92
3.15 Maximum Von Mises stress for the tube with clips, considering variable and constant properties. Maximum von Mises stress in the case of GPS and MA.	93
3.16 $\sigma_{VM,clips}$ stress for variable properties (left panel) and constant properties (right panel).	93
3.17 Maximum Tresca stress for the tube with clips, considering variable and constant properties. Maximum Tresca stress in the case of GPS and MA.	94
4.1 Creep-fatigue interaction diagram.	109
4.2 Logarithmic half strain range versus number of allowable cycles plot for Inconel 625 at 815 °C, showing the plastic and elastic regions.	123
4.3 Maximum film temperature for every alloy, depicted hourly.	127
4.4 Equivalent elastic stress at the tube crown at 12:00 h for the different alloys under the aiming strategies of Table 4.8 and $2S_y$ limit (dashed lines) for alloys Haynes 230, 316H and 800H.	128
4.5 Hourly depiction of (a) Pressure drop in the Eastern path and (b) Receiver thermal efficiency.	128
4.6 Equivalent elastic stress at the tube crown at 12:00 h and the corresponding stress reset limit for each alloy.	130
4.7 Equivalent elastic strain at the tube crown for the different alloys at 12:00 h.	130
4.8 (a) Creep stress achieved after full relaxation for Haynes 230, Inconel 625 and Inconel 740H, working under the shakedown to elastic cyclic regime. (b) Creep stress after relaxation for Incoloy 800H, working in stress reset regime, for two consecutive operating days.	132
4.9 Effect of stress relaxation in terms of the creep stress as function of the temperature and elastic-plastic equivalent stress solicitation.	133
4.10 Elastic stress, elastic-plastic equivalent stress and creep stress for the alloys studied at the tube crown, at 12:00 h and at 17:00 h. .	135

4.10	Elastic stress, elastic-plastic equivalent stress and creep stress for the alloys studied at the tube crown, at 12:00 h and at 17:00 h (cont.)	136
4.11	Rupture time as function of the creep stress and the temperature.	137
4.12	EODs for the alloys studied, Eastern path.	138
4.13	(a) Minimum EODs for a receiver panel. (b) Number of total panels substitutions in the different receivers to achieve an operation of 25, 30 and 35 years.	140
4.14	Stress regimes diagram with the most critical regimes found for each alloy.	141
5.1	Calculation procedure, including the different models used and the operation limits considered.	168
5.2	Plan view of the receiver schematic representation and the two flow paths.	169
5.3	DNI for the days analyzed.	171
5.4	Heat flux map on the receiver surface, with its maximum and average value for (a) $k = 3$ at 7:00h, (b) $k = 2.6$ at 7:00h, (c) $k = 2.6$ at 10:00h, (d) $k = 2.3$ at 12:00h.	173
5.5	(a) Maximum heat flux on the Eastern half and (b) DNI for the different time step cases.	174
5.6	Tubes outer temperatures, creep stresses and creep damages for the representative tubes of the 5-min time step at solar noon.	176
5.7	Lifetime results for the receiver panels using the 1, 5, 15 and 60-min time steps. (a) Eastern and (b) Western flow paths.	176
5.8	Minute by minute creep damage of the 60 and 1-minute time step at the 12 th axial division of the first Eastern panel.	179
5.9	Temperature, stress and creep damage minute-by-minute ratio of the 60-minute time resolution over the 1-minute one during (a) 12:00 to 12:59 h, (b) 7:00 to 7:59 h and (c) 8:00 to 8:59 h.	180
5.10	Stress relaxation at each axial division (a) in the Eastern path and (b) detail on its first panel.	181
5.11	Maximum heat flux in the Eastern half for the set of representative days.	183
5.12	Lifetime results of the first two panels from (a) the Eastern and (b) Western halves, for each representative day individually.	185
5.13	Final lifetime results for the set of representative days: (a) Eastern and (b) Western flow paths.	185

5.14 Lifetime results of the first two panels from (a) the Eastern and (b) Western halves, considering a salts tank of half the original capacity, for each representative day individually.	186
5.15 Lifetime percentage difference of the spring equinox results with respect the set of days.	187
6.1 DNI to guarantee a minimum heat flux on the receiver equal to 40 kW/m ² , opposite to the reference DNI.	205
6.2 (a) Receiver operation control diagram for a given day, with in- stances of the possible situations represented in (b).	206
6.3 Minimum heat flux on the receiver surface for the DNI layers during the spring equinox day (81). The limiting 40 kW/m ² appears in dashed lines.	209
6.4 Day-types cluster classification according to their DNI features. .	212
6.5 Arrangement of the 2018 year into the cluster groups.	213
6.6 (a) Distribution of the high and medium energy day-type through the year and (b) number of days of each type during each season.	214
6.7 Transient DNI for the day-type analyzed, with their clear-sky reference DNI and their operation windows.	216
6.8 Creep (c) and fatigue (f) damages for the cases of study. Both re- ceiver halves have been included (E and W), as well as the results for clear-sky DNI (C) during the receiver operation, opposite to the transient actual DNI (TR).	219
6.9 Creep and fatigue damages for the TR, C and P DNI and mass- flow rate control cases.	220
6.10 HTF outlet temperature during the transient operation and total HTF mass flow rate through the receiver.	221
6.11 (a) Hours of operation and (b) number of start-ups of the high and medium energy days of 2018. Average results in dashed lines.	222
6.12 (a) Lifetime estimation considering the high and medium energy days of 2018 and (b) annual creep damage percentage under the transient DNI and the clear-sky one.	223
6.13 Annual creep and fatigue damages for the Eastern and Western panels of the receiver under the transient DNI and the clear-sky one.	224

D.1 Lifetime of the receiver panels during the set of representative days, in order to achieve the tank filling. (a) Eastern and (b) western flow paths.	246
D.2 Lifetime of the receiver panels during the set of representative days, in order to achieve half the tank filling. (a) Eastern and (b) western flow paths.	248

List of Tables

2.1	Optical properties.	48
4.1	Chemical composition (weight %) of the alloys selected.	118
4.2	Maximum allowable film temperature for the alloys studied.	119
4.3	Alloys prices.	119
4.4	Coefficients of the stress-strain monotonic and cyclic curves.	120
4.5	Coefficients of the Norton-Bailey model.	121
4.6	Coefficients of the M-R-M parametrization.	122
4.7	Fatigue coefficients.	122
4.8	Hourly maximum aiming strategy factor and heliostat field maximum availability.	126
4.9	Receiver thermal power for the design day.	129
4.10	Receiver costs.	143
4.11	LCOA of the receiver alternatives.	145
5.1	Days selected for the design day analysis and their maximum solar height.	171
5.2	HOP for the tank filling considering different time resolutions. . .	175
5.3	Molten salts (T_n) collected for a fixed HOP equal to the one required for tank filling with 1-min time step	178
5.4	Comparison of the percentage lifetime difference with respect the 1-min results for the 5-min time resolution results and its interpolation to 1-min time intervals.	182
5.5	Hours of operation and tons of molten salt in the tank.	184
6.1	Fatigue coefficients at different experimental temperatures. . . .	201
6.2	Receiver main parameters.	203
6.3	Number of each day-type during the year 2018.	214
C.1	Lifetime results for the different time steps with receiver operating until the tank filling.	243

C.2	Percentage lifetime variation with respect the 1-minute time step, with the receiver operating until the tank filling.	244
C.3	Percentage lifetime variation with respect the 1-minute time step. The receiver operates a fixed HOP corresponding to the 1-minute time step tank filling.	244
D.1	Lifetime of the receiver panels for the set of representative days and average results.	245
D.2	Lifetime for the receiver panels during the filling operation of a tank with half the salts capacity.	247

General introduction

Contents

1.1	Motivation	1
1.2	Concentrating solar power	3
1.3	Solar power tower plants	4
1.3.1	Subsystems	6
1.3.2	Solar power tower receiver operation limits and issues	8
1.3.3	Costs, efficiencies, and improvement potential	17
1.4	Scope of the thesis	19
1.5	Outline of the thesis	20
	References	22

1.1 Motivation

The industrial revolution put fossil fuels in the energy sources spotlight, being one of the main factors that helped drive it. In the form of coal in the first industrial revolution and as petroleum and natural gas in the second, they are responsible for the immense progress we still enjoy at the present day, from industries to the reshape of transportation. However, attempts to reduce our dependence on them sparked during the 70s fueled by economical aspects, when the oil crisis skyrocketed petroleum prices. In addition, the last decades have been key to raise awareness of environmental issues such as global warming and have been an eye-opener regarding the negative impact these fossil fuels entail (IPCC, 2018). With that new mindset, and also looking at their potential exhaustion, the room for fossil fuels becomes less and less, and the need of developing and improving alternative and renewable energy sources grows stronger. Thus, the rising tendency in the last years involving greener alternatives use for electricity production comes as no surprise: the renewable energy

2 *General introduction*

share in power generation has increased from the 20% in 2010 to the 25% in 2017/2018 (IRENA, 2019).

In the renewable energy landscape, concentrating solar power (CSP) technologies are gaining relevance, circling the 100 plants-mark worldwide by year 2020 (Mehos *et al.*, 2020) and having increased their capacity over a 396% worldwide in the last decade (IRENA, 2020a). This ranks them third, just behind the growth experienced by solar photovoltaic (PV) and offshore wind. Moreover, from 2010 to 2018, the GWh of electricity production due to the concentrated solar technologies have increased a 630% (IRENA, 2020a). In the CSP plants, the direct normal irradiance (DNI) is reflected by an array of mirrors into the surface of a receiver device. Such solar radiation is transferred to the heat transfer fluid (HTF) through its interior in form of thermal energy. Then, said energy is converted into electricity in the power block. Some of these technologies allow thermal energy storage (TES) which, depending on the HTF through the receiver, can be either direct, by means of the heated HTF in the receiver itself, or indirect, exchanging the heat transferred to the HTF in the receiver to a different fluid more suitable for the storage; the TES enables continued electricity production once the daily operation has ceased and provides these facilities a greater degree of flexibility on electricity dispatch, despite their inherent variability due to the climate conditions dependence. Such is the case of solar power tower (SPT) plants using molten salt as HTF, being able to substitute the current combined-cycle plants in the load-following scenario. Moreover, the TES contributes to the SPT economic viability since it enables them to take part in ancillary grid services, opening the door to an additional source of incomes (Madaeni *et al.*, 2012). With respect to other renewable technologies, such as wind or PV, molten-salt storage is still far way more competitive than the large batteries these alternatives integrate to face the climate conditions variability (Zurita *et al.*, 2018; Mehos *et al.*, 2017). Then, in comparison to other CSP technologies, SPTs using molten salt as HTF benefit from the higher working temperatures they can reach (IRENA, 2012), which entail greater steam cycle efficiencies, a greater capacity factor and lower TES costs.

Despite these advantages, the SPT installations still demand a great capital investment, opposite to other renewable technologies. Moreover, this is aggravated by the critical working conditions some of their elements must endure since they could cause major unexpected issues that could jeopardize the project economical viability. This consideration is specially relevant for the receiver, with high uneven heat fluxes and a cyclic operation that favour the appearance

of the creep and fatigue failure mechanisms. Given these extreme working conditions, the placement of sensors to obtain accurate measurements regarding the receiver operation is not feasible; consequently, high-resolution numerical and analytical models are required in order to provide a better understanding of the receiver behaviour, essential at the design and operation stages of the project. The present dissertation is focused on the study of creep and fatigue damages during the receiver operation following an analytical methodology. The thermal and mechanical characterization of the receiver, required upstream the damage study, is also approached from an analytical point of view.

1.2 Concentrating solar power

The basic principle of any CSP technology is the exploitation of the beam radiation by reflecting it into the receiver surface, where is converted into thermal energy. Thus, the CSP systems are commonly arranged taking into account how that beam radiation is reflected. According to that criteria, four technologies can be distinguished (Figure 1.1):

- **Linear Fresnel:** it is a line focusing technology in which a series flat or slightly curved mirrors reflect the direct normal irradiance into a linear receiver mounted in an independent structure. These mirrors are arranged in long rows parallel to the receiver, being each row provided with sun-tracking devices.
- **Parabolic trough:** it is also a line focusing technology with a linear receiver mounted on the supporting frame that also holds the mirrors and the sun-tracking device. The mirrors are arranged one after the other forming a long trough and present a parabolic profile.
- **Parabolic dish:** a point focusing system constituted by a paraboloidal mirror that concentrates the beam radiation onto a receiver placed at the mirror focal point.
- **Central receiver or solar power tower:** a point focusing technology where a field of mirrors aim towards the receiver placed at the top of a tower.

Line focusing systems (Linear Fresnel and Parabolic trough) can be oriented North to South or East to West; thus, they require less sun-tracking effort since

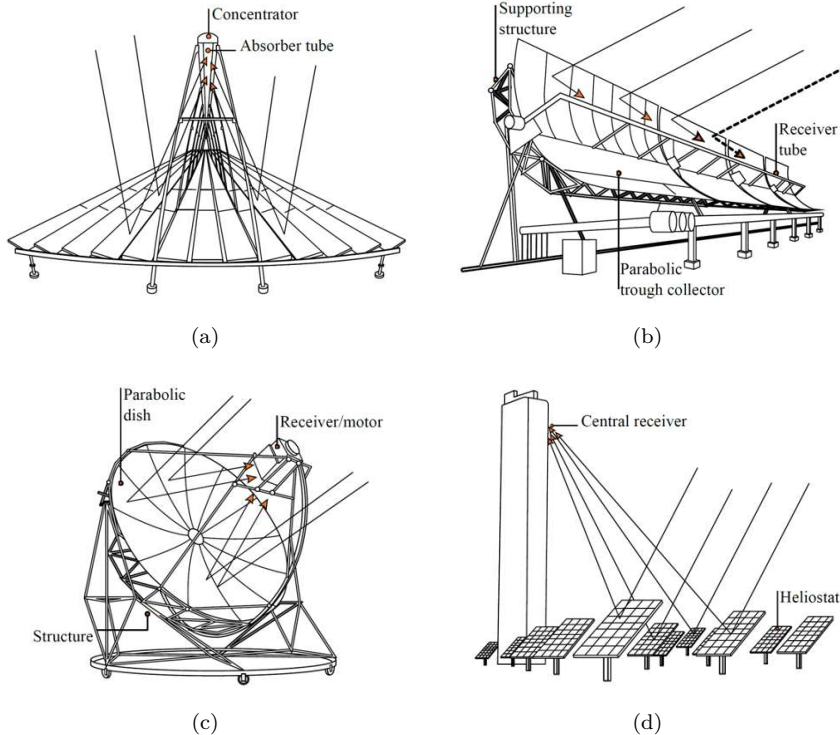


Figure 1.1: CSP technologies (Solar Concentra, 2013). (a) Linear Fresnel, (b) Parabolic trough, (c) Parabolic dish and (d) Central receiver.

they only have one rotation axis, reducing their cost. On the contrary, they can reach lower HTF temperatures in comparison to the point focusing devices (Parabolic dish and Central receiver): linear focusing technologies present maximum temperatures from 400 to 500°C, whereas the point focusing ones can reach temperatures from 600 to 1000°C (Richter *et al.*, 2009). This PhD thesis deals with solar power tower technology aspects and thus it is described more in depth in the following section.

1.3 Solar power tower plants

The first central receiver of cylindrical design placed on top of a tower was proposed by Hildebrandt *et al.* (1972). On the other hand, the first demonstration tower plants to use molten salt as HTF were Thémis (France, 1983) and MSEE (Molten salt electric experiment, US, 1984), both with cavity-type

receivers (Lovegrove & Stein, 2012). An important step forward towards the improvement of the SPT technology designs as well as for understanding the main challenges it faces were the demonstration projects Solar One (1982-1984. CA, US), which mounted an external steam receiver, and its subsequent adaptation to the molten-salt technology, Solar Two (1996-1999. CA, US). The latter was coupled to a 10 MWe steam generator and was provided with a TES system of 1,380 tonnes, which translated in 3 thermal storage hours (Pacheco, 2002). Nevertheless, the plant was shutdown prior any commercial operation due to multiple failures in the piping, steam generator and receiver.

This technology then experienced an hiatus that lasted until 2005 and served to improve its components in order to reduce their cost and while increasing their efficiency (Lovegrove & Stein, 2012). From there, several institutions and organizations, such as Abengoa Solar, eSolar and Brightsource, showed interest in developing commercial scale facilities. In 2010, the efforts culminated in the construction of the first commercial SPT, Gemasolar (Solar Tres), located in Spain and built by Torresol Energy. It produces 19 MWe and its TES tank provides it an additional 15-hour autonomy (Torresol, 2021). Led by the Gemasolar successful example, a number of commercial SPT plants with molten salt have been built up to this day, such as NOOR III (2018, Morocco, with 7 h of TES and a turbine net capacity of 134 MWe), Atacama-1 (2018, Chile, 17.5 h of TES and 110 MWe) or Shouhang Dunhuang Phase II (2018, China, 11 h of TES and 100 MWe) (National Renewable Energy Laboratory (NREL), 2020). Additionally, the Dewa CSP Tower project (15 h of TES and 100 MWe) is already under construction, with its start of operation forecasted by 2021, and more projects are already being developed, Copiapó (Chile) or Redstone (South Africa), showing the existing confidence in this technology.

Amid these promising instances, the other side of the story is told by the once-cutting-edge Crescent Dunes SPT facility (NV, US), victim of a series of severe technical and management problems. The 10 h of TES and 110 MWe plant, that went operational in 2015, was temporarily shutdown for almost a year (October 2016 - July 2017) due to a tank leak. Additionally, issues regarding much lower energy production than expected had already arisen by that time (Feldman *et al.*, 2019). The USD 1 billion project was eventually found unprofitable, leading to its exploitation contract (power purchase agreement, PPA) being terminated in 2019 and with the US Department of Energy (DOE) taking over the facility (Feldman *et al.*, 2020), yet showing an uncertain future. Although a rare instance, it serves as a reminder of the early stage at

which this technology finds itself—compared to other CSP alternatives—and the need to continue looking for its improvement in order for it to keep expanding successfully.

1.3.1 Subsystems

The main subsystems of a SPT plant, depicted in Figure 1.2, are the heliostat field, the receiver and the power block. Additionally, these facilities can also incorporate a TES system. The aforementioned subsystems are detailed below.

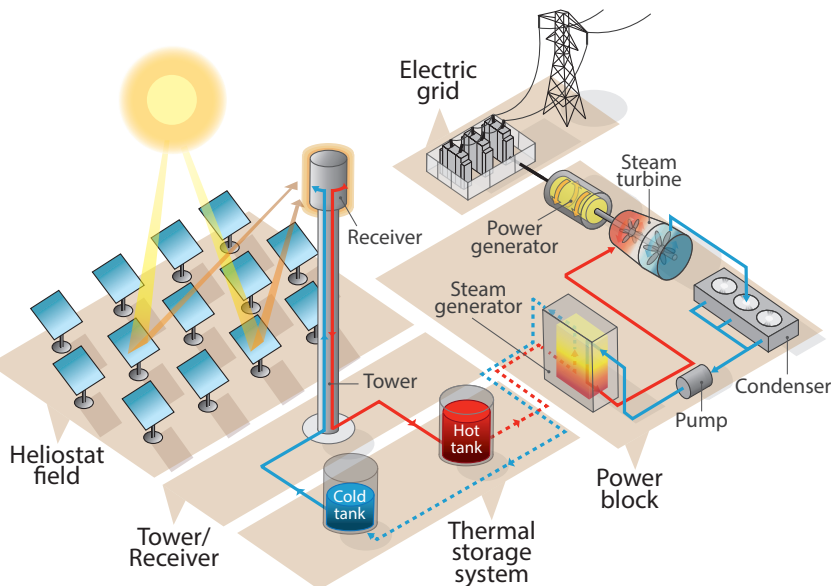


Figure 1.2: Solar power tower plant schematic representation.

Heliostat field

The heliostat field is an array of mirrors that concentrate the beam radiation into the receiver surface. Each heliostat is constituted by a group of mirrors, disposed either flat or with a slight curvature, and is provided with a two axis sun-tracking system in order to follow the sun position with the maximum precision.

In SPT systems, the heliostat field can present two different configurations, depending on the receiver design. For an external cylindrical receiver, like the

one studied in this dissertation, it is placed surrounding the whole receiver; on the other hand, for cavity-type receivers and external billboard receivers, the field is placed facing the receiver North side for a plant located at the Northern Hemisphere.

Receiver

The receiver is a heat exchanger placed at the top of a tower in order to intercept the direct normal irradiance reflected by the heliostat field. In the case of cylindrical external receivers, these are constituted by a series of panels held by a cylindrical frame. These panels comprise a series of vertically disposed thin-walled tubes, with the HTF flowing in parallel through them. The path described by the HTF varies depending on the configuration chosen, with the HTF being able to go through just one path or through two parallel and symmetrical paths that may even present a cross-over between them. In any case, the HTF alternates its flowing direction, upwards and downwards, from panel to panel.

The goal of the receiver is to transform the solar radiation received into thermal energy in the HTF. The latter can be selected from a handful of alternatives: air/gas, water/steam, thermal oils, organics, molten salt and liquid metals (Benoit *et al.*, 2016). Some aspects to regard in the HTF selection are the possibility to use it as thermal energy storage, its admissible temperature range, its thermal properties, environmental impact or its cost. The use of molten salt is widely extended in commercial plants, with instances like Gemasolar (Spain), Crescent Dunes (Nevada, US) or Atacama (Chile). Its main asset is their suitability for thermal energy storage. Moreover, molten salt present good thermal properties at high temperatures and are cheaper than other alternatives; their main drawback is their high freezing point. These salts are distinguished by their composition, being solar salt (60% NaNO₃ - 40% KNO₃) one of the most popular options for CSP applications.

Thermal energy storage system (TES)

The thermal energy storage system in nitrate molten salt SPTs is constituted by two storage tanks, a cold and a hot one. The cold tank, at a minimum temperature of 290°C, contains the salt coming from the power block that will be pumped through the receiver, while the hot one holds the salt that have left the receiver, at a maximum temperature of 565°C. Whenever the power generated in the receiver is sufficient to satisfy the power block demands, the

salt is accumulated in the hot tank; however, if that is not the case, the power block uses the storage molten salts to meet the demand.

The TES system in a SPT plant using molten salt is an almost mandatory feature due to the salt excellent thermal storage properties—unlike other HTFs like water/steam—, its chemical stability in presence of air or water—a critical issue for the liquid metals alternatives—, and the benefits that the TES provides to the whole facility. The thermal energy storage not only allows to mitigate the effect of transient interruptions, for instance due to cloud passages, during the receiver regular operation on the electricity production but also provides extra hours of operation after the daily shut-down. In Gemasolar, for instance, the TES installed allows to extend the plant operation up to 15 more hours, while Atacama-1 benefits from 17.5 additional hours (National Renewable Energy Laboratory (NREL), 2020).

Steam generator and power block

In order to convert the thermal energy of the HTF in electricity, SPT plants operating with molten salt equip a steam generator consisting of an economizer, an evaporator a superheater and a reheater. That way, the steam obtained through these four heat exchangers presents the required conditions to use it in the power block, which is a Rankine cycle. The steam turbine of the cycle is coupled to an alternator, producing electricity.

1.3.2 Solar power tower receiver operation limits and issues

From the testing facilities to fully operational SPT commercial plants, they all have served to gather valuable information through the years about the principal problems this technology faces during operation. The report conducted by Mehos *et al.* (2020) compiles firsthand information about these aspects through the testimonies of individuals involved in currently-operating SPT plants, who claim that the main issues faced have to do with systems involving salt, which is the receiver case. A compilation of the SPT problematic is shown in Figure 1.3, with the multiple sources of failure involving the receiver underlined, highlighting the wide variety of issues it can encounter; among these issues, the ones addressed throughout this dissertation appear underlined in green. According to the cited report, receiver-associated problems account for the 42% of the total of this technology issues, with salt-piping being the most brought

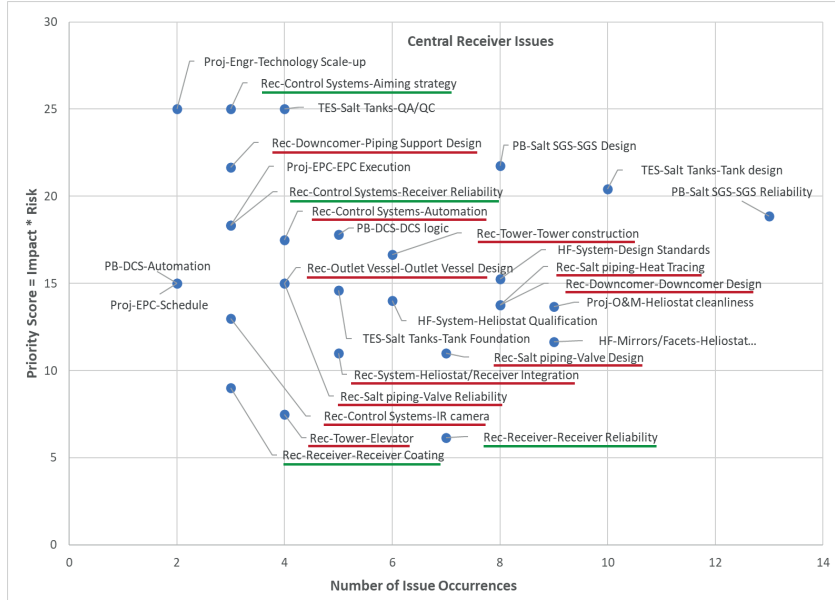


Figure 1.3: Solar power tower technology issues. Adapted from (Mehos *et al.*, 2020).

up system for the receiver by the interviewed stockholders and ranking third in the total facility.

Besides the actual impact of the problems the receiver encounters in SPT plants, careful consideration should also be put in the fact that this subsystem is the source of the principal limitations of the facility operation, highly influencing its design as well.

Receiver reliability. Creep and fatigue damages.

Regular SPT external receivers operation conditions involve high non-uniform heat fluxes on its surface: the front side of the tubes face the radiation reflected from the heliostat field while the rear side is almost adiabatic (Marugán-Cruz *et al.*, 2016). This leads to great temperature gradients on its thin-walled tubes, at their axial, radial and circumferential directions, which are responsible for thermal stresses and deformations. The thermal gradients between the front and rear side of the tubes cause their bending in the receiver radial direction, while the thermal gradients among the halves of the tubes cross-section do the same in the normal direction to the receiver radial direction one. Thus, the final bending direction is a composition of both. In order to prevent the tubes

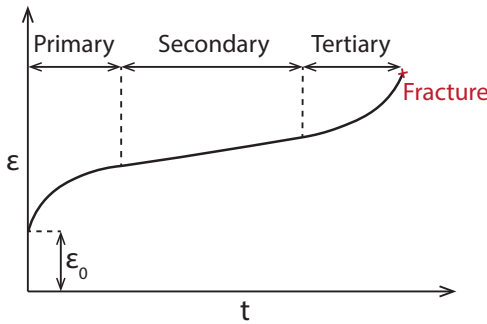


Figure 1.4: Creep curve showing the different creep stages.

excessive bending, which could even lead to adjacent tubes touching one another and, consequently, the apparition of hot spots, they are vertically guided by a series of supports, commonly called “clips”, resulting in additional mechanical stresses (Montoya *et al.*, 2018). Besides the high operation temperatures, it should also be considered that the SPT receiver operation is cyclic, not only due to the night periods but also because of daytime inactivity periods caused by the interference of clouds passing covering the heliostat field. In sight of the typical operation conditions of the receiver, two main damage factors are considered for the receiver tubes: creep and fatigue.

Creep occurs during dwell periods at high temperatures—around 0.3 times the material melting temperature for metals (Ashby, 1983)—and stresses and is defined as the slow accumulation of inelastic deformations over time, with the material flowing slowly as if it were viscous, causing its mechanical degradation. Now strain is not only dependent on the stress, but also the temperature and time; hence, creep is characterized by a strain vs. time curve, in which three differentiated stages can be described, Figure 1.4: primary creep, secondary creep and tertiary creep. During primary creep the creep rate decreases progressively. Then, during secondary creep, the rate remains constant, and it is regarded as the steady-state creep. Lastly, during tertiary creep, the creep rate is accelerated and eventually leads to fracture, although creep damage defects can initiate at early stages, prior the tertiary creep. Given the short duration of primary creep and the danger that lies in the accelerated third stage, the steady-state stage is the most commonly regarded in the design phase (Jones & Ashby, 2019a), with the primary creep that occurs before it being assimilated to a simple elastic deflection. Creep failure manifests by the formation of creep voids or cavities (also called vacancies) on interior grain boundaries (see

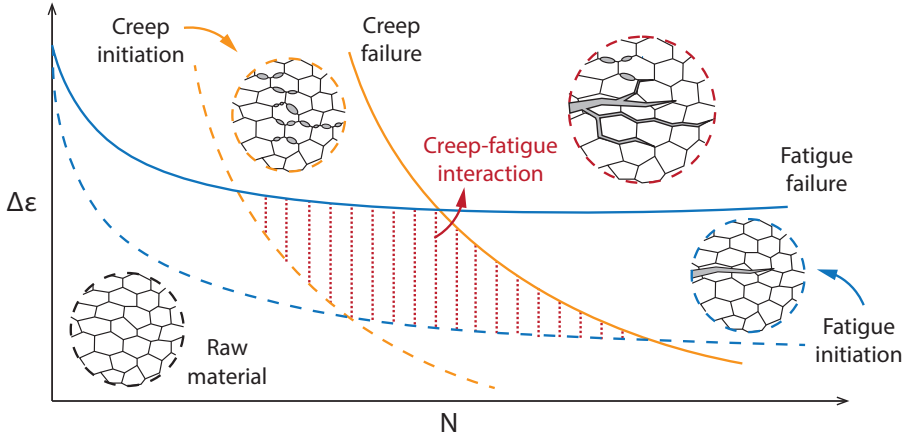
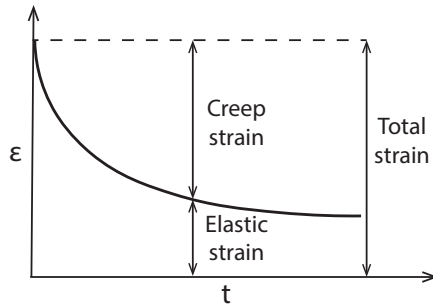


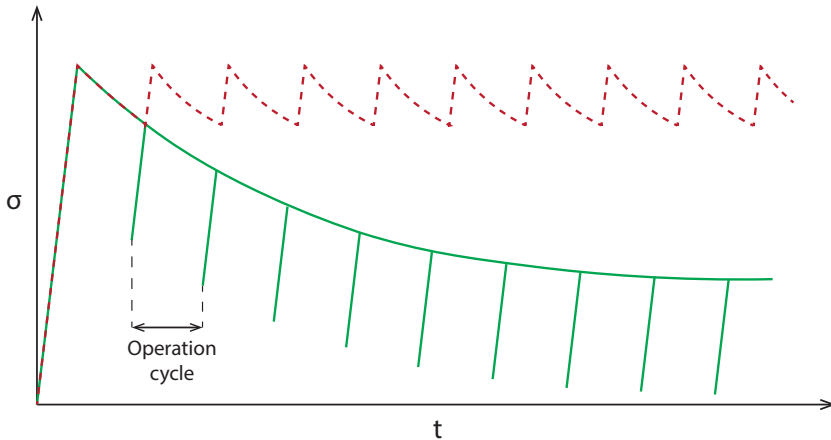
Figure 1.5: Creep and fatigue interaction and failure modes.

Figure 1.5) and two different creep mechanisms can occur in metals, depending on the temperature, stress and grain size in some cases: *i*) diffusion creep, at high temperatures and low stresses, *ii*) and power-law (or dislocation) creep, at high temperatures and stresses, both following Arrhenius law. Then, two different diffusion creep mechanisms are observed (Meyers & Chawla, 2008): *i.a*) bulk diffusion (Nabarro and Herring creep) and *i.b*) grain boundary diffusion (Coble creep). The former occurs if the vacancy diffusivity dominates over the grain boundary diffusion coefficient, and Coble creep occurs for the opposite situation. Essentially, they imply the displacement of the vacancies from grain regions normal to the tensile direction (or as normal as possible) towards grain boundaries in the tensile direction, stretching the grain in that same direction (Ashby, 1983; Jones & Ashby, 2019b); the difference between them strives in the fact that the mass transport happens through the crystal in *i.a*), while for *i.b*) the diffusion takes place through grain boundaries. Dislocation creep can be either *ii.a*) climb-controlled or *ii.b*) glide-controlled, and they imply the movement of dislocations besides the vacancies one. The main parameter to measure creep resistance of alloys is the rupture time, temperature and stress dependent.

A moderate creep, however, could be a reasonable design option since it leads to stress relaxation of the material at elastic regime and constant strain. Its basic principle is that the plastic strain caused by creep implies a reduction of the elastic one, decreasing the stress on the component, Figure 1.6(a). The same mechanisms involved during creep occur during stress relaxation. Nev-



(a)



(b)

Figure 1.6: (a) Strain transference from elastic to inelastic during creep. (b) Global stress relaxation during cyclic operation (solid line) and stress relaxation interrupted by stress reset (dashed line).

ertheless, with cyclic operation, such as the one occurring in a SPT receiver, the stress relaxation accumulation over time, known as global stress relaxation, is subject to not surpassing the stress reset limit (Becht IV, 2011); otherwise, shakedown to elastic cyclic does not occur and the high stresses are reset once the diurnal operation (cycle) starts again, with a new relaxation cycle happening and starting from the stress that has been reset, Figure 1.6(b).

Fatigue consists in the degradation of the mechanical properties of a material during cyclic loading. Fatigue failure is characterized by the initiation and propagation of cracks, Figure 1.5. Prior the crack appearance, the material experiences microstructural changes, mainly driven by dislocation movements

causing slip along the crystallographic planes (Ellyin, 1996). Eventually, the agglomeration of dislocations serves as a strain accumulator and leads to the formation of persistent slip bands (PSBs). The following deformations will mostly concentrate on these PSBs, favouring the crack appearance. Then, in absence of previous flaws, the crack initiation occurs at the surface and it is observable at a macroscopic level. From there, the propagation occurs in the normal direction of the solicitation and results in beach markings (macroscopic), that originate during hold periods, and striations (microscopic), that advance with the cycling. The failure occurs when eventually the remaining section of non-fractured material cannot endure the load at which is subjected to. Fatigue can be either high-cycle, with failure occurring between 10^4 and 10^8 cycles, or low-cycle fatigue, below 10^4 cycles. In solar central receivers, the thermal cycling favours the appearance of the low-cycle type (Fahrmann & Srivastava, 2014), which can be predicted with the Coffin-Manson law. The fatigue phenomenon on SPT receivers has been a concern from this technology early days (Kistler, 1987; Babcock & Wilcox Company, 1984; Narayanan *et al.*, 1985).

Both creep and fatigue are relevant aspects to address in the receiver design phase since, besides the failure that they can lead to on their own, the working conditions of SPT receivers favour the appearance of both, resulting in their interaction and jeopardizing the receiver integrity even more. Fatigue appears in the absence of hold times (or when these are short) and/or the strain ranges are significant; on the other hand, creep is associated with great hold times and lower strain ranges. In an intermediate situation, see Figure 1.5, the fatigue cracks interact with the creep voids, accelerating the cracking process and, thus, the failure of the specimen in question.

Early days testing facilities were already a testimony of the demanding conditions at which the receiver is subjected. Radosevich & Skinrood (1989) reported that in Solar One, just one year after its production phase began, cracks in the receiver tubes were found, which caused leaks and altered the schedule of the plant. The bending and warpage suffered by the receiver tubes in Solar One during its 3-year operation are shown in Figure 1.7. According to their investigation, these cracks were the result of the thermal stresses due to the temperature gradients on the tubes and clips, the mechanical stresses motivated by the clips itself, and the weldings in the tubes. They concluded that the weldings needed to be minimized and the supports redesigned in order to decrease the solicitations in the tubes.

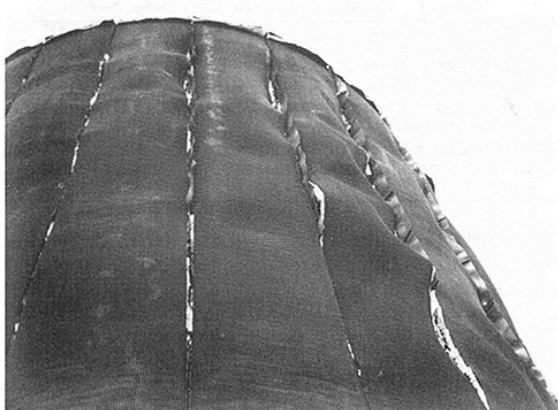


Figure 1.7: Solar One receiver bending and warpage (Radosevich & Skinrood, 1989).

Moreover, in molten-salt receivers, special consideration should be put into the interaction between the HTF and the tubes material since the latter is subjected to the corrosive effects of the salt, which are particularly aggressive at the elevated receiver operation temperatures (Patel *et al.*, 2017). The combination of the environment characteristics–HTF mixture, temperatures, etc.–, the selection of a tubes material susceptible to corrosion, and the receiver operation, cyclic and under high stresses, can lead to the appearance of stress corrosion cracking (SCC) on the receiver if its design and operation are not adequate, accelerating the failure of this component. Figure 1.8 shows the main factors leading to SCC, as discussed by Bauer *et al.* (2013). Regarding the HTF, the presence of chloride impurities is one of the most hazardous aspects since it favours the spalling of the oxide layer in-between the HTF and the tubes, exposing the tube material directly to the corrosive medium. The chemical stability of the HTF is also important in order to keep the corrosion levels controlled, being required to prevent the HTF decomposition by limiting its temperature. As for the tube material, the admissible film temperature—the tube temperature in contact with the HTF—is a key parameter to watch. The materials with a greater tolerance in this regard when working with molten nitrite salts are the nickel alloys, typically being able to endure up to 650 °C, followed by stainless Cr-Ni steel, 570 °C, (Bauer *et al.*, 2013).

In Solar Two, chloride stress corrosion cracking (SCC) appeared in the receiver tubes, suggesting the need substituting their current material, the stainless-steel alloy 316, for an advanced one that could endure it (Litwin,

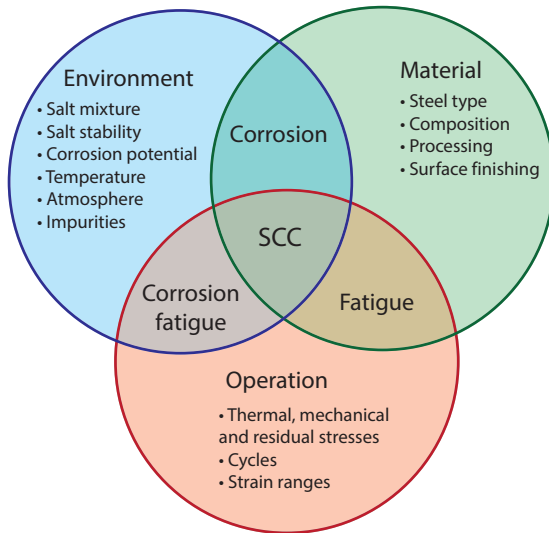


Figure 1.8: Tubes material, environment and operation conditions interaction leading to stress corrosion cracking.

2002). As a result, two years after such testing facility became operational, one of the panels was replaced by one constituted by tubes in an advanced high-nickel alloy instead (Litwin, 2002). The panel location was specifically selected to test its performance under one of the highest heat fluxes on the whole receiver surface so meaningful results could be obtained. After a 15-month use with such new panel mounted, the receiver was dismantled and the panel inspection showed no leaks or deflection. Consequently, the SPT receiver tubes material selection must take the salt corrosive effects into consideration, and the film temperature must be kept under the safe limits during operation to avoid accelerated corrosion rates. The latter is achieved with the heliostat field aiming strategy control.

Solar resource assessment

Solar radiation is available every day on the Earth surface and it becomes especially interesting for electricity production applications in locations benefiting from a high DNI (Qiu & Li, 2019). The most favourable regions in such sense are located in the commonly named “Sun Belt”, with a great amount of solar radiation available, a vast quantity of sunshine hours and few cloudy periods. However, despite these highly desirable conditions, an accurate solar resource evaluation through all the stages of the project, from the site selection and plant



Figure 1.9: Shouhang Dunhuang operation during clouds period.

design to its operation, is key to ensure its success. Its overestimation can lead to a higher damage on the tubes, while its underestimation could result in the underperformance of the plant, yielding lower thermal powers than expected, as occurred in Crescent Dunes (Feldman *et al.*, 2019).

Short-term cloud passages usually occur in a matter of a few minutes and are characterized by a variety of features such as their velocity, direction, transmissivity or size (Augsburger & Favrat, 2013). These cloud transients are responsible for descends in the expected clear-sky DNI, which lead to the transient operation of the plant and may even cause its temporal shut-down. Two issues are specially relevant regarding the DNI assessment: the time resolution and the spatial resolution.

Approaching the plant design or making performance forecasts based on DNI data provided with coarse time resolution measurements is not the most suitable strategy to capture the transient operation of the plant over the day. Consequently, the typical meteorological year (TMY) methodology, based on previous DNI data acquired on an hourly basis for the location studied, is inaccurate, being advisable to use time resolutions from 15 to 5 minutes (Mehos *et al.*, 2020). Ideally, the 1-minute time resolution would be used. Additional aspects to take into account are the wind velocity, the atmospheric attenuation and the mirrors soiling rates and mirror cleanliness. Related to the direction and size of the clouds passing, the combination of both factors can result in cloud transients that may not affect evenly the whole heliostat field during the

duration of the transient. However, it should be noted that the usual DNI data from a location comes from either a single point measurement or it is averaged with the measures of multiple points within a certain area. Such low spatial-resolution DNI measures cannot capture the partial coverage of the heliostat field. This drawback is successfully dodged in the Ashalim SPT plant (Israel), which is equipped with an heliostat field shaped especially unusually, by mounting a photovoltaic sensor on every heliostat (Minis *et al.*, 2019). Each PV unit, aimed to charge the battery that provides energy to their corresponding heliostat, is also understood as an insolation sensor, which can measure the DNI for that particular heliostat when combined with a few more fixed sensors through the field. Thus, following such approach, the heliostat field aiming strategy can be accurately selected and the heat flux on the receiver surface can be properly estimated. Yet, if a finer DNI spatial-resolution control is not feasible, it should be at least considered that, in a two-paths receiver, each half has its individual needs due to the different incident heat flux at every time instant due to the sun movement.

1.3.3 Costs, efficiencies, and improvement potential

A great drawback of SPT plants has been the initial capital investment they require. Despite its already listed benefits opposite to other CSP technologies, SPT penetration in the commercial scale market has been lesser when compared with parabolic trough, preventing it from benefiting from a more accelerated technology improvement and economies of scale appearance on its components manufacturing process (Lilliestam *et al.*, 2017). Nevertheless, the trend is currently changing thanks to the learning acquired through the pioneer molten-salt SPT projects and the greater scale it is developing (Murphy *et al.*, 2019). A study conducted by IRENA (2016) projected a descend on the installed cost of SPT of a 37% over a ten-year horizon, from 2015 to 2025; effectively so, SPT installed cost have remarkably fallen thus far, dropping from 7,650 USD/kW in 2015 to an average around 5,200 USD/kW (all costs adjusted to 2019 inflation), a descend of a 32.3% (IRENA, 2020b).

For SPT facilities, the total installed cost breakdown (IRENA, 2012) shows that the heliostat field is the most expensive subsystem ($\sim 38\%$, (Kolb *et al.*, 2011)), followed by the receiver ($\sim 17\%$, (Singer *et al.*, 2014)) and, then, the power block and TES. According to the DOE SunShot initiative goals set for 2030 (Murphy *et al.*, 2019), the current SPT improvement relies on its subsystems costs reduction while increasing their lifetime and efficiency, driven by

research and development (R&D) activities:

- The heliostat field cost, currently at value near to 100 \$/m² (above the SunShot initiative goal for 2020 (US Department of Energy, 2021)) is expected to drop below the 50 \$/m². Its optical errors are to be lower than 3 miliradians.
- As for the receiver, the costs goal for 2020 was below 150 \$/kWt (US Department of Energy, 2021), while for 2030 it has been lowered down to 120 \$/kWt. They are expected to endure over 10,000 cycles and provide an efficiency above the 90%. According to IRENA (2016), the focus should be put in the latter to reduce the plant levelized cost of electricity (LCOE).
- The TES costs are set to decline around a 33%, reaching a 15 \$/kWt.
- The power block gross efficiency target is established in 55% and its costs are expected to be around 900 \$/kWe.
- Operation and maintenance costs (O&M) aim to a 40 \$/kW-yr value, descending from the 2017 reference one, 66 \$/kW-yr.

For the 10-year horizon from 2015 to 2025, IRENA (2016) set the possible SPT LCOE descend by a 43%, from 2015 values ranging between 0.15 \$/kWh to 0.19 \$/kWh. Such decrement would be mainly due to the reduction of installed costs (up to a 61%). Overall, SPT plants yield improvement would lead to a higher electricity output, responsible for up to a 25% reduction of the LCOE. Moreover, despite the thermal storage was initially regarded as uneconomic from the capital investment point of view, it has turned to be a decisive factor for increasing the capacity factors and a descend on the LCOE, and so sparking additional interest besides the straight-forward benefits its intrinsic flexibility provides during operation. So much so that since 2015 only one SPT project has been installed with no TES; the majority of the projects present a TES of 4 hours or above, being the average TES installed of 7.7 h in the 2015 to 2019 period (IRENA, 2020b). This situation brings yet more to light the interest of the molten salt use. Currently, additional SPT projects under development invite to further optimism regarding the future of this technology. Such is the case of the fourth phase of Mohammed bin Rashid Al Maktoum Solar Park (Dubai) (Lilliestam & Pitz-paal, 2018). It presents an extraordinarily low PPA of USD 0.074/kWh, being its long projected lifecycle—35 years opposite to the usual 25—the second cause of such plummeting (IRENA, 2020b).

Hence, ensuring a long-enough lifetime for the SPT components turns out key for the economic viability of future projects, as well as its yield improvement.

1.4 Scope of the thesis

The challenges still faced today by SPT technologies motivate the main objectives of the present Ph.D thesis, summarized below:

- Development of a high-resolution analytical method to study the SPT tubular receivers from a thermal and exergy perspective. Aspects such as the influence of the tubes coating degradation, the aiming strategy selection and the ambient temperature of the location facility are investigated in order to find potential room for the receiver exergy yield improvement.
- Development of an analytical model to obtain the thermal elastic stresses and strains, as well as the mechanical ones resulting from the tubes boundary restrictions to prevent their excessive bending. The accuracy of the proposed methodology, which takes into account the properties temperature dependence, is numerically validated.
- Creep and fatigue damage analysis of the receiver tubes aiming to predict their lifetime.
- Global comparison of various alloys alternatives for the receiver tubes manufacturing, taking into account their operation limits, expected lifetime and the power supplied by the receiver in each case. For different lifespan horizons, determination of which alloy is the most economically beneficial. A costs metric, similar to the LCOE or the levelized cost of coating (LCOC), is proposed for the receiver alloys: the levelized cost of alloy (LCOA).
- Assessment of how the lifetime estimation results are influenced by the time resolution selected for the analysis during a clear-sky day. Investigation of the suitability of picking just one design day to perform the lifetime analysis, opposite to a representative set of days throughout the year.
- Shed light on which is the main damage mechanism under conventional operation conditions, either during clean days or with transient interruptions.
- Lifetime analysis of the receiver during transient conditions operation, considering different types of days, clustered according to their energy level, variability and distribution during the day.

1.5 Outline of the thesis

Seeking to tackle the cited objectives, the dissertation has been organized in 7 Chapters. Chapters from 2 to 6 have been written as independent articles, with their own abstract, introduction, notation and bibliography.

Chapter 2 presents an analytical thermal model of the receiver. It is complemented with a module to study the exergy in the receiver dissecting the various heat transfer processes involved, from the beam radiation reflection by the heliostat field to the heat conduction through the receiver tubes wall into the HTF. It is a high-resolution method that takes into account the multiple reflection and absorptions occurring among the receiver tubes, ambient and rear wall, with the tubes being discretized in axial and circumferential divisions. Since it provides information on the different process contribution to the irreversibility share, the model is used to study the influence in the system exergy of issues such as the tubes coating degradation, heliostat field aiming strategy or site selection.

As a starting point for the receiver tubes mechanical evaluation, an analytical method to obtain the thermal and mechanical elastic stresses and strains is introduced in Chapter 3. The main characteristic of the mentioned model is that it regards the tubes material properties dependence, with its accuracy being validated against a numerical method. The results show the importance of such properties temperature dependence consideration opposite to having them being constant.

Upon the calculation of the elastic stresses and strains in the receiver tubes, Chapter 4 follows an analytical creep-fatigue damage model to estimate the lifetime of the receiver panels, taking into account the elastic-plastic stresses and strains, the stress relaxation phenomenon and the thermal and mechanical limits of the receiver, which determine the allowable flux density (AFD) on the receiver surface. Various alloy alternatives for the tubes manufacturing are compared in terms of their expected lifetime during a clear-sky day, without disregarding their disparate thermal outcomes. For a fixed plant lifecycle horizon, the analysis is expanded to an economic dimension, considering the costs of each particular receiver—including the panels substitutions required by each alloy—and the thermal energy they provide. The leveled cost of alloy (LCOA) metric proposed constitutes a direct comparison indicator between material options.

Then, in Chapter 5, the damage and subsequent lifetime estimation of the receiver are investigated more in-depth by studying the impact of the time res-

olution selection for the analysis. Besides considering the AFD thermal and mechanical limits introduced in the previous Chapter, a TES tank that establishes the receiver hours of operation required to fill it is implemented in the study. On the other hand, the suitability of just choosing one design day as representative to perform the receiver lifetime forecast is put to test opposite to a series of equally-spaced in solar altitude days through the year. The impact of the TES tank capacity is also investigated in terms of its implications for the receiver lifetime.

Continuing with the creep and fatigue damage mechanisms, Chapter 6 explores which one is more relevant during the receiver transient operation. Thus, its operation is controlled by the fulfilling of favourable heat flux conditions on the receiver surface as well as guaranteeing a previous preheat before each start-up. The mass-flow rate and aiming strategy of the heliostat field are kept as the clear-sky scheduled ones. Considering the DNI data of a whole year database and arranging its days into clusters depending on the features of their DNI, the creep and fatigue damages are obtained for three representative days—around the spring equinox, the summer solstice and the winter solstice—of each kind in order to explore the different alternatives in the creep-fatigue damage outcome. The analysis of these cases is performed for both their actual transient DNI and their corresponding clear-sky one. Subsequently, the whole year analysis is carried out, resulting in the lifetime estimation of the receiver and providing a final result on the magnitudes of each type of damage in the total share.

Finally, the main conclusions of the thesis are summarized in Chapter 7.

Nomenclature

N	number of fatigue cycles
t	time

Greek letters

$\Delta\varepsilon$	strain range	σ	stress
ε	strain		
ε_0	initial elastic strain		

Abbreviations

AFD	Allowable flux density		laboratory
CSP	Concentrating solar power	O&M	Operation and maintenance costs
DNI	Direct normal irradiance	PPA	Power purchase agreement
DOE	US Department of Energy	PV	Solar photovoltaic
HTF	Heat transfer fluid	PSBs	Persistent slip bands
LCOA	Levelized cost of alloy	R&D	Research and development
LCOC	Levelized cost of coating	SCC	Stress corrosion cracking
LCOE	Levelized cost of electricity	SPT	Solar power tower
MSEE	Molten salt electric experiment	TES	Thermal energy storage
NREL	National renewable energy		

References

- ASHBY, M.F. 1983 Mechanisms of deformation and fracture. *Advances in Applied Mechanics*, vol. 23, pp. 117–177. Elsevier.
- AUGSBURGER, G. & FAVRAT, D. 2013 Modelling of the receiver transient flux distribution due to cloud passages on a solar tower thermal power plant. *Solar Energy* 87 (1), 42–52.
- BABCOCK & WILCOX COMPANY 1984 Molten Salt Receiver Subsystem Research Experiment Phase 1 -Final Report, Volume 1- Technical. *Tech. Rep. SAND82-8178*. Barberton, OH, United States.
- BAUER, T., PFLEGER, N., BREIDENBACH, N., ECK, M., LAING, D. & KAESCHE, S. 2013 Material aspects of Solar Salt for sensible heat storage. *Applied Energy* 111, 1114–1119.
- BECHT IV, C. 2011 Elevated temperature shakedown concepts. *Journal of Pressure Vessel Technology, Transactions of the ASME* 133 (5), 051203–1–5.
- BENOIT, H., SPREAFICO, L., GAUTHIER, D. & FLAMANT, G. 2016 Review of heat transfer fluids in tube-receivers used in concentrating solar thermal systems: Properties and heat transfer coefficients. *Renewable and Sustainable Energy Reviews* 55, 298–315.

- ELLYIN, F. 1996 *Fatigue Damage, Crack Growth and Life Prediction*, 1st edn. Dordrecht: Springer Netherlands.
- FAHRMANN, M.G. & SRIVASTAVA, S.K. 2014 Low cycle fatigue behaviour of HAYNES 230 alloy. *Materials at High Temperatures* 31 (3), 221–225.
- FELDMAN, D.J., O'SHAUGHNESSY, E. & MARGOLIS, R.M. 2020 Q3/Q4 2019 Solar Industry Update. *Tech. Rep.* NREL/PR-6A20-76158. National Renewable Energy Laboratory (NREL), Golden, CO, United States.
- FELDMAN, D.J., ZWERLING, M. & MARGOLIS, R.M. 2019 Q2/Q3 2019 Solar Industry Update. *Tech. Rep.* NREL/PR-6A20-75484. National Renewable Energy Laboratory (NREL), Golden, CO, United States.
- HILDEBRANDT, A.F., HAAS, G.M., JENKINS, W.R. & COLACO, J.P. 1972 Large-scale concentration and conversion of solar energy. *Eos, Transactions American Geophysical Union* 53 (7), 684–692.
- IPCC 2018 Global Warming of 1.5°C. An IPCC Special Report on the impacts of global warming of 1.5°C above pre-industrial levels and related global greenhouse gas emission pathways, in the context of strengthening the global response to the threat of climate change,. *Tech. Rep.* 1. Intergovernmental Panel on Climate Change, Geneva, Switzerland.
- IRENA 2012 Renewable Energy Cost Analysis: Concentrating Solar Power. *Tech. Rep.* June. International Renewable Energy Agency, Abu Dhabi.
- IRENA 2016 The Power to Change: Solar and Wind Cost Reduction Potential to 2025. *Tech. Rep.* June. Internation Renewable Energy Agency, Abu Dhabi.
- IRENA 2019 Global energy transformation: A roadmap to 2050 (2019 edition). *Tech. Rep.* April. International Renewable energy Agency, Abu Dhabi.
- IRENA 2020a Renewable Energy Statistics 2020. *Tech. Rep.* July. International Renewable Energy Agency, Abu Dhabi.
- IRENA 2020b Renewable Power Generation Costs in 2019. *Tech. Rep.* June. International Renewable Energy Agency, Abu Dhabi.
- JONES, D.R.H. & ASHBY, M.F. 2019a Creep and Creep Fracture. In *Engineering Materials 1*, chap. 21, pp. 351–366. Elsevier.

- JONES, D.R.H. & ASHBY, M.F. 2019b Mechanisms of Creep, and Creep-Resistant Materials. In *Engineering Materials 1*, chap. 23, pp. 381–394. Elsevier.
- KISTLER, B.L. 1987 Fatigue analysis of a solar central receiver design using measured weather data. *Tech. Rep.* SAND86-8017. Sandia National Laboratories, Albuquerque, NM, United States.
- KOLB, G.J., HO, C.K., MANCINI, T.R. & GARY, J.A. 2011 Power tower technology roadmap and cost reduction plan. *Tech. Rep.* SAND2011-2419. Sandia National Laboratories, Albuquerque, NM, United States.
- LILLIESTAM, J., LABORDENA, M., PATT, A. & PFENNINGER, S. 2017 Empirically observed learning rates for concentrating solar power and their responses to regime change. *Nat. Energy* 2, 17094.
- LILLIESTAM, J. & PITZ-PAAL, R. 2018 Concentrating solar power for less than USD 0.07 per kWh: finally the breakthrough? *Renewable Energy Focus* 26, 17–21.
- LITWIN, R.Z. 2002 Receiver System: Lessons Learned From Solar Two. *Tech. Rep.* SAND2002-0084. Sandia National Laboratories, Albuquerque, NM, and Livermore, CA, United States.
- LOVEGROVE, K. & STEIN, W. 2012 *Concentrating solar power technology: principles, developments and applications*, 1st edn. Cambridge (U.K.): Woodhead publishing.
- MADAENI, S.H., SIOSHANSI, R. & DENHOLM, P. 2012 How thermal energy storage enhances the economic viability of concentrating solar power. *Proceedings of the IEEE* 100 (2), 335–347.
- MARUGÁN-CRUZ, C., FLORES, O., SANTANA, D. & GARCÍA-VILLALBA, M. 2016 Heat transfer and thermal stresses in a circular tube with a non-uniform heat flux. *International Journal of Heat and Mass Transfer* 96, 256–266.
- MEHOS, M., PRICE, H., CABLE, R., KEARNEY, D., KELLY, B., KOLB, G. & MORSE, F. 2020 Concentrating Solar Power Best Practices Study. *Tech. Rep.* NREL/TP-5500-75763. National Renewable Energy Laboratory, Solar Dynamics LLC, Golden, CO, United States.

- MEHOS, M., TURCHI, C., VIDAL, J., WAGNER, M., MA, Z., HO, C., KOLB, W., ANDRAKA, C. & KRUIZENGA, A. 2017 Concentrating Solar Power Gen3 Demonstration Roadmap. *Tech. Rep.* NREL/TP-5500-67464. National Renewable Energy Laboratory, Sandia National Laboratories, Golden, CO, United States.
- MEYERS, M.A. & CHAWLA, K.K. 2008 *Mechanical behavior of materials*, 2nd edn. Cambridge university press.
- MINIS, N., ROSENBLUTH, E., HAYUT, R. & AM-SHALLEM, M. 2019 Spatial DNI measurement for accurate solar flux control in Megalim 121 MWe solar receiver power plant. *AIP Conference Proceedings* 2126 (July), 030037.
- MONTOYA, A., RODRÍGUEZ-SÁNCHEZ, M.R., LÓPEZ-PUENTE, J. & SANTANA, D. 2018 Numerical model of solar external receiver tubes: Influence of mechanical boundary conditions and temperature variation in thermoelastic stresses. *Solar Energy* 174, 912–922.
- MURPHY, C., SUN, Y., COLE, W., MACLAURIN, G., TURCHI, C. & MEHOS, M. 2019 The Potential Role of Concentrating Solar Power within the Context of DOE's 2030 Solar Cost Targets. *Tech. Rep.* NREL/TP-6A20-71912. National Renewable Energy Laboratory (NREL), Golden, CO, United States.
- NARAYANAN, T.V., RAO, M.S.M. & CARLI, G. 1985 Structural Design and Life Assessment of a Molten Salt Solar Receiver. *Journal of Solar Energy Engineering* 107 (3), 258–263.
- NATIONAL RENEWABLE ENERGY LABORATORY (NREL) 2020 Concentrating solar power projects: Power tower projects. <https://solarpaces.nrel.gov/by-technology/power-tower>, accessed: 07/06/2021.
- PACHECO, J.E 2002 Final Test and Evaluation Results from the Solar Two Project. *Tech. Rep.* SAND2002-0120. Sandia International Laboratories, Albuquerque, NM, United States.
- PATEL, N.S., PAVLÍK, V. & BOČA, M. 2017 High-Temperature Corrosion Behavior of Superalloys in Molten Salts-A Review. *Critical Reviews in Solid State and Materials Sciences* 42 (1), 83–97.
- QIU, Z. & LI, P. 2019 *Advanced Energy Efficiency Technologies for Solar Heating, Cooling and Power Generation*, 1st edn. Hull, UK: Springer International Publishing.

- RADOSEVICH, G. & SKINROOD, A.C. 1989 The Power Production Operation of Solar One, the 10 MWe Solar Thermal Central Receiver Pilot Plant 1. *Journal of solar Energy Engineering* 111, 144–151.
- RICHTER, C., TESKE, S. & SHORT, R. 2009 Concentrating Solar Power Global Outlook 09- Why renewable energy is hot. *Tech. Rep.* June. Greenpace international, SolarPACES, ESTELA.
- SINGER, C., GIULIANO, S. & BUCK, R. 2014 Assessment of improved molten salt solar tower plants. *Energy Procedia* 49, 1553–1562.
- SOLAR CONCENTRA 2013 Plataforma Tecnológica de la Energía Solar Térmica de Concentración. <https://www.solarconcentra.org>.
- TORRESOL 2021 Torresol Energy: Gemasolar. <https://torresolenergy.com/en/gemasolar/>, accessed: 16/03/2021.
- US DEPARTMENT OF ENERGY 2021 CSP Component Research and Development. <https://www.energy.gov/eere/solar/csp-component-research-and-development>, accessed: 17/03/2021.
- ZURITA, A., MATA-TORRES, C., VALENZUELA, C., CARDEMIL, J.M. & ESCOBAR, R. A. 2018 Techno-economic analysis of a hybrid CSP+PV plant integrated with TES and BESS in Northern Chile. *AIP Conference Proceedings* (November), 180013.

Thermal and exergy analysis of solar central receivers

Contents

2.1	Introduction	28
2.2	Proposed modelling	31
2.2.1	Discretization of the receiver	31
2.2.2	Thermal model of the receiver (ECGM)	34
2.2.3	Exergy calculation (XCGM)	40
2.3	Case of study	44
2.3.1	Ambient conditions	44
2.3.2	Heliostat field	44
2.3.3	Receiver configuration	45
2.4	Results	49
2.4.1	Optical properties influence	50
2.4.2	Aiming strategy and DNI influence	53
2.4.3	Ambient temperature influence	58
2.5	Conclusions	61
	References	65

Summary

A high-resolution method to analyse the exergy of the solar power tower (SPT) external tubular receivers is presented, examining the different heat transfer process involved individually. This sheds light on the role that each irreversibility source plays in the outcome, aiding in the receiver design and the facility location selection. The exergy efficiency is around 32% in the base configuration. Besides the exergy loss in the heliostat field, over 40%, it is found that the

biggest exergy destruction cause are the radiation emissions and absorptions in the tube outer surface, around 17%. From the remaining ones, the greatest are the exergy destructed in the heat transfer fluid (HTF) and the one escaping to the ambient (over 4% each). Then, the exergy balance for a variety of strategies and ambient conditions is performed: optical properties of the tubes coating, peak and flat aiming strategies, direct normal irradiation (DNI) and ambient temperature. The heliostat field exergy loss rate only varies when changing the aiming. However, the emission and absorption losses and the ones in the HTF suffer the greater modifications with all the parameters studied. The impact of the optical properties degradation, 1% descent in the efficiency per 5% degradation, would advise repainting works in order to avoid greater exergy destruction. The surroundings temperature modification impacts considerably the exergy efficiency, showing the suitability of locations with low ambient temperature and a moderate DNI: descends of over 0.35% occur every 5 °C increase of the temperature for a fixed DNI.

2.1 Introduction

The potential SPT plant cost reduction associated to its yield improvement motivates the efforts of trying to increase these facilities performances, especially focusing the attention on the most critical subsystems. It is worth stressing that for any energy source the most important aspect consists in determining what is the maximum quantity of energy that can be transformed in useful work. In order to achieve greater efficiencies, it should be concluded what that solar energy is capable of offering in the SPT plant: its real potential and the ways to maximize its exploitation. Hence, the different causes of losses and irreversibilities should be studied to obtain the actual profitability of the energy. For that purpose, the exergy efficiency analysis is key since it indicates the quality of the energy, considering the useless fraction of it due to irreversibility. More precisely, the work production potential of a certain substance can be studied analyzing its exergy, while for a certain process, the exergy conservation equation is the suitable procedure.

In the solar thermal energy field, and more specifically in the receiver subsystem, the main exergy to analyze is the exergy of radiation of the processes involved. The numerous emissions and absorptions that convert radiation energy into heat are irreversible processes, resulting in exergy losses. The exergy depends highly on the temperature of the absorbing surface, increasing when

the temperature grows. Hence, it is understandable the low exergy efficiency in solar driven processes and devices (Petela, 2005): the Sun temperature is around 6000 K and its exergy is degraded to a maximum temperature of 840 K in the HTF outlet, in the case of a solar salt receiver. The exergy efficiency also increases the lower the ambient temperature is, since a substance or process can produce work until it reaches the dead state, which is no other than the thermal equilibrium with the surroundings. Thus, in a SPT plant is not only important the DNI in the location selected, as stated above. There is also room for improvement in the way that solar irradiation is used for the electricity production.

Given its relevance and usefulness in process engineering, some authors have focused their research in understanding the exergy of radiation. Petela (1964) paved the way, introducing the equations for the calculation of such radiation exergy. He later further developed his previous studies (Petela, 2003), where he found that there is an optimum temperature for the absorbing surface. A reasonable outcome since a high temperature translates in a higher exergy but it also produces greater energy losses due to the emission of the surface. The results obtained by Petela regarding radiation exergy were reaffirmed by Candau (2003). In a more wider field, second law analysis gained popularity in the analysis of heat transfer processes, introducing the entropy minimization in the design process and highlighting the importance of the study of irreversibility in the thermodynamic performance of heat transfer devices (Bejan, 1982). The work by Flesch *et al.* (2020) remarks the relevance of the thermophysical properties of the HTF used in the heat transfer devices regarding the entropy generation minimization.

Different exergy analysis of concentrating solar power (CSP) receivers have been found in the literature. An experimental exergy analysis of a cylindrical-parabolic cooker was performed by Öztürk (2004), motivating its latter analytical study (Petela, 2005). The linear Fresnel receiver has also been studied from the exergy viewpoint (Cocco *et al.*, 2017), as well as the parabolic through receiver (Padilla *et al.*, 2014; Bellos & Tzivanidis, 2017, 2019). In (Bellos & Tzivanidis, 2017), the parabolic through receiver is analyzed operating not only with a liquid HTF, Therminol VP1, but also with air, both under various flow rates and inlet temperatures. Other aspects such as the wind velocity or the solar irradiation are examined by Padilla *et al.* (2014) for a silicone heat transfer fluid. An in-depth review of the literature available related to the exergy in parabolic collectors is presented in the work by Kumar *et al.* (2020). Regarding

ing the SPT technologies, Pye *et al.* (2014) tested different HTF alternatives performing an exergy analysis of the receiver, proving the great performance of molten salts; however, it did not take into account the circumferential variations of the tubes temperature nor the multiple reflections between surfaces. Not only the receiver subsystem has been studied but also the concentrators (Asselineau *et al.*, 2018) of all CSP technologies and the power block (Gómez-Hernández *et al.*, 2018), including supercritical cycles (Novales *et al.*, 2019; Hernández-Jiménez *et al.*, 2019). In the literature, there can be found several global analysis of SPT plants, which have shown that the receiver is among the elements suffering from greater exergy losses (Pye *et al.*, 2014; Gómez-Hernández *et al.*, 2018; Kouta *et al.*, 2016) given the high heat fluxes exchanged on that device. However, detailed analysis of the SPT receiver have not been yet conducted.

With everything presented above, the objective of this Chapter is to perform an exergy analysis of the receiver of a SPT plant, coupling its behavior to the heliostat field, since it is the main subject of the radiation heat in such facilities. The principal particularity of this study is that the thermal model that precedes the exergy efficiency calculation has been done for the tubes of the receiver discretized not only in axial divisions, but also in circumferential ones. Hence, the exergy model also considers the temperature gradient in the circumferential coordinate. In this study, the mentioned models are referred to, respectively, as energy coarse grid model (ECGM) and exergy coarse grid model (XCGM). The circumferential cells provide a more precise estimation of the tube wall temperature distribution at its outer surface (Rodríguez-Sánchez *et al.*, 2014). As previously discussed, the temperature of the absorbing surface is a highly relevant parameter in the exergy efficiency so this would lead to a more reliable exergetic analysis. Hence, as opposed to the works found in the literature, the tubes are not considered as a single exchange surface for a certain length of the receiver, but rather a series of them, each one at their corresponding temperature. Moreover, the receiver tubes design implemented in the ECGM is such that takes the minimum thickness that is able to endure the pressure and the corrosive effects present during the receiver expected lifespan, aiming to lower the entropy generation. In the present Chapter, Section 2.2 describes the discretization of the geometry of the receiver and shows the modelling selected, both for the thermal resolution of the receiver with the ECGM and the exergy balance and efficiency with the XCGM. In Section 2.3, the chosen design parameters of the SPT plant are indicated: the ambient conditions and the heliostat field and receiver configurations. The results obtained for the

case of study are shown in Section 2.4, as well as the comparison with the ones resulting from the modification of the optical properties of the tubes coating, the aiming strategy of the heliostat field, the DNI and the ambient temperature. The main conclusions reached with this analysis are summarized in Section 2.5.

2.2 Proposed modelling

In order to analyse the receiver, the discretization of its characteristic geometries needs to be described, which is done in Section 2.2.1. Also, although the present study is only focused on the receiver subsystem, the interaction with the upstream elements and their influence cannot be neglected if the purpose is to realistically analyse the behaviour of the receiver as a part of a SPT plant. Hence, the configuration and behaviour of the heliostat field is especially relevant for such study, since it dictates how the heat flux is distributed on the receiver surface. In this case, the software tool FluxSPT^[a] (Sánchez-González *et al.*, 2018) has been used for that end, serving as the optical model and providing the information needed to couple the heliostat field operation to the receiver. Using that knowledge and data, the thermal model of the receiver is separately developed, as presented in Section 2.2.2. With it, the receiver is fully characterized in terms of energy exchanged between surfaces and transferred to the HTF during its steady state operation. The temperatures of the diverse surfaces interfering are also obtained. Thereafter, the exergy analysis of the receiver can be fully undertaken following the procedure in Section 2.2.3. The interaction between the different models and modules used for the exergy analysis of the receiver is shown in Figure 2.1.

2.2.1 Discretization of the receiver

The system studied is an external tubular receiver, which is now introduced in a simplified way. Its particularities will be further detailed in Section 2.3, where the selected case of study is presented. The receiver has at its core a cylindrical shape that will be referred to as base cylinder or rear wall indistinctly. This base cylinder reflects greater amount of insolation and serves of frame to support a series of vertical panels that are constituted by the tubes conducting the HTF. The panels are also composed by an inlet and outlet collector that, respectively, distribute equally the HTF mass flow in all the tubes and regroup it.

^[a] <http://ise.uc3m.es/research/solar-energy/fluxspt/>

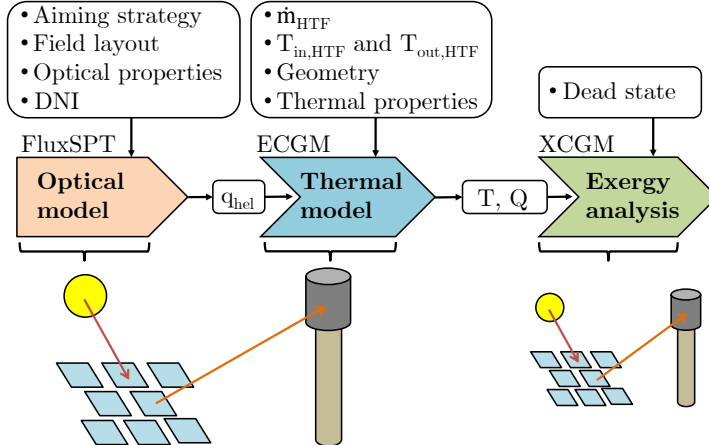


Figure 2.1: Models involved in the receiver exergy analysis.

To obtain the exergy generated in the receiver subsystem, the different agents interacting need to be properly delimited: the receiver tubes, the base cylinder and the ambient, as schematically depicted in Figure 2.2(a) for two consecutive tubes of a panel. The tubes, whose length is named as L_t (m), from all the panels are all equally divided in a series of axial and circumferential divisions. The axial divisions encountered by the HTF through its whole path, from the receiver inlet to the receiver outlet, are counted with the index h , that goes from 1 to m , being m the total number of axial divisions. These axial parcels present a height of Δz , which is selected long enough to allow the assumption of the hypothesis of a bidimensional radiative heat exchange. Thus, the interaction between axial divisions at different “levels” from one tube to the other does not occur. It does not mean that just a single set of axial division out of the whole receiver is studied, but that they must be analysed separately depending on their z position. Hence, the study focuses on the exchanges in one certain axial division level, h , at a time. This makes the circumferential cells of the tubes the relevant ones for the energy exchanges between surfaces at an axial position. The circumferential divisions in a specific axial level h of one tube are collectively referred to as t and go from 1 to n . The rear wall has been considered to be touching the rear side of the tubes, as represented in Figure 2.2(b). Hence, for the radiative exchange, adjacent tubes can be reduced to two tube halves facing, since they are confined between the rear wall and the imaginary surface representing the ambient. This is not the case in real life receivers, where there is a gap between the base cylinder and the tubes. Such

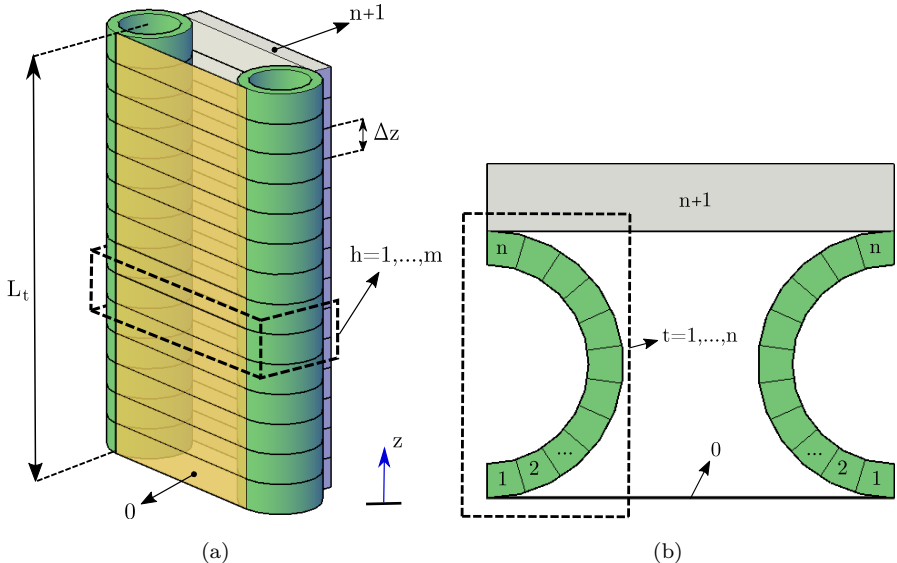


Figure 2.2: (a) Discretization of the geometries interacting in an external receiver
(b) Plant view of one axial division.

simplification has been adopted to ease the view factors calculation. It is a reasonable assumption justified by the small distances between adjacent tubes and between the tubes and the base cylinder. Thus, given the symmetry of the present scenario, n is the total number of parcels in half the cross section of a tube.

On the other hand, the rear wall is a portion of the base cylinder extending between the two tubes halves limits. It is designated with the $n+1$ subscript and it is also discretized in the same number of axial cells than the tubes. Therefore, each set of half tubes divisions has a corresponding h rear wall portion with a uniform temperature, T_{n+1} , along its surface but differing from one axial division to another.

The emission of the tubes and the rear wall at a h level can be written as

$$E_i = A_i \varepsilon_i \sigma T_i^4, \quad i = 1, 2, \dots, n + 1, \quad (2.1)$$

where A_i is the area of the different surfaces (m^2), ε_i is the emissivity, σ refers to the Stefan-Boltzmann constant ($5.67 \times 10^{-8} \text{ W}/(\text{m}^2\text{K})$) and T_i corresponds to the temperature of each cell (K).

Lastly, the surface 0 is an imaginary surface that represents the ambient around the receiver, which supplies in a diffuse way the direct insolation re-

flected by the heliostat field. The surroundings find themselves at the following temperature (Berger *et al.*, 1984) in all of the h divisions

$$T_0 = T_{\text{ref}} = \frac{[(\varepsilon_{\text{amb}} T_g)^4 + (\varepsilon_g T_{\text{amb}})^4]^{\frac{1}{4}}}{[\varepsilon_{\text{amb}} + \varepsilon_g]^{\frac{1}{4}}}. \quad (2.2)$$

Here ε_{amb} and ε_g represent the ambient and ground emissivity respectively. ε_{amb} depends on the ambient pressure, the temperature at the location of the receiver, T_{amb} , the relative humidity and the solar time. T_g is the ground temperature. This $T_0 = T_{\text{ref}}$ temperature is taken into account for the thermal analysis of the receiver and as the temperature of the dead state. However, the temperature at which surface 0 emits is regarded to be the temperature of the Sun surface, $T_0 = T_S$, 6000 K, as considered by Petela (2005). At an h level, the emission of the surroundings surface is

$$E_0 = A_0 q_{\text{hel}}, \quad (2.3)$$

where A_0 is the area of such surface and q_{hel} is the heat flux arriving from the heliostat field (W/m^2). It is not a uniform heat flux as a whole; just like the rear wall, it is divided in a series of h cells in which the heat flux is uniform, but different from one division to the other, as it will be depicted in Section 2.4.

2.2.2 Thermal model of the receiver (ECGM)

The radiative exchanges between neighbouring tubes are analysed for just two facing halves, as discussed in Section 2.2.1. Also, the present model contemplates not only axial divisions of the tubes but circumferential partitions as well, which lead to a more accurate calculation of the radiation losses, increasing the precision of the tube temperatures obtained (Rodríguez-Sánchez *et al.*, 2014).

The initial parameters are the geometrical characteristics of the receiver and the tubes, the inlet temperature of the HTF, $T_{\text{in,HTF}}$, and the desired outlet one, $T_{\text{out,HTF ref}}$, as well as the heat flux on the receiver surface arriving from the heliostat field at every h , q_{hel} . Although the thickness of the tubes, th , is assumed at the beginning alongside the rest of the geometrical parameters, the model is designed so it is recalculated. The objective of the recalculation is to finally set the thickness in the minimum value allowable to meet the safety requirements, aiming to decrease the entropy generation of the receiver. The temperature of the tube and rear wall surfaces, T_t and T_{n+1} , as well as the HTF mass flow, \dot{m}_{HTF} , are also initially presupposed, although they are recalculated, $T_{t,\text{rec}}$, $T_{n+1,\text{rec}}$ and $\dot{m}_{\text{HTF,rec}}$, until the HTF leaves at the desired outlet temperature.

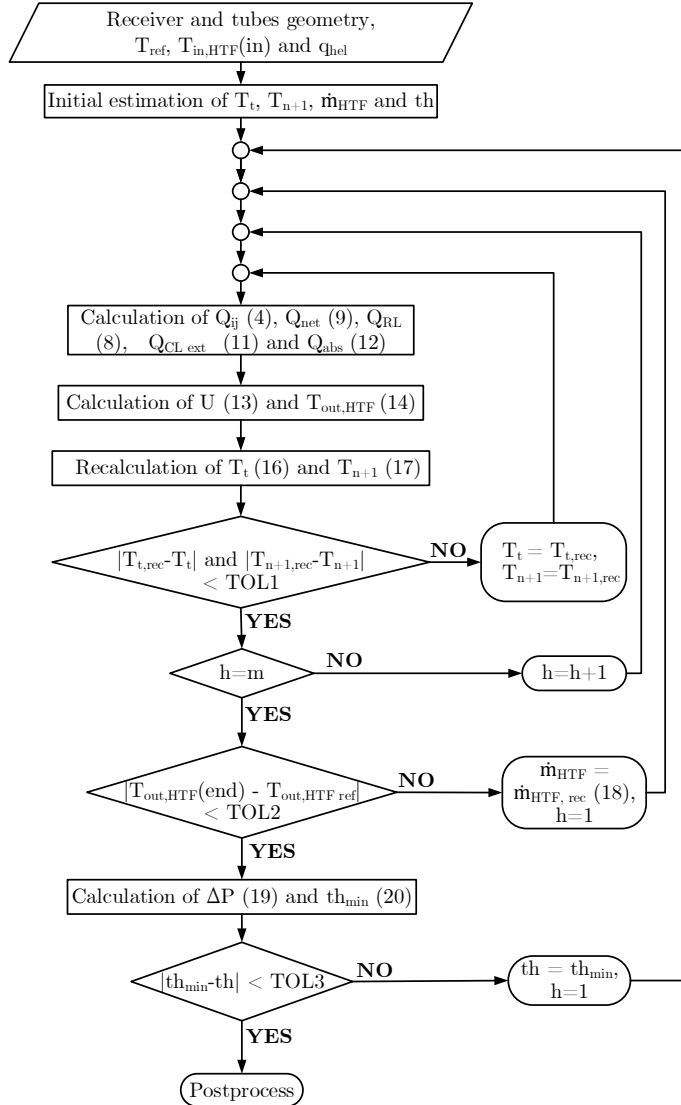


Figure 2.3: Iterative process of the thermal model.

The calculation process, illustrated in Figure 2.3, is performed as follows:

- In a certain axial division, h , the heat delivered to any surface j by any surface i , Q_{ij} , is obtained considering the emission of surface i , calculated with Eqs. 2.1 and 2.3. On the one hand, that heat is constituted by emission leaving from i , E_i , and being absorbed by j with no intermediate reflections. On the other hand, there is the emission arriving from i , E_i ,

to the absorbing surface j after a succession of reflections involving the rest of the surfaces (k, l, \dots) that are also included in the system. Such reflections occur in between the “departure” of the radiation from i and the “arrival” to j . Hence, the heat Q_{ij} is obtained as

$$Q_{ij} = E_i F_{ij} \alpha_j + E_i \sum_{k=0}^{n+1} F_{ik} \rho_k F_{kj} \alpha_j + E_i \sum_{k,l=0}^{n+1} F_{ik} \rho_k F_{kl} \rho_l F_{lj} \alpha_j + \dots, \quad (2.4)$$

where F_{ij} is the view factor between the surfaces involved in the radiative exchange, α_j is the absorptivity of the surface receiving the heat from i , and ρ is the reflectivity of the intermediate surfaces reflecting the emission leaving i . The summation terms regarding the multiple reflections are added in an iterative process until Q_{ij} converges. This set of equations for the delivered heat can be written in matrix form as

$$Q_{\text{deliv}} = \begin{pmatrix} Q_{00} & \cdots & Q_{0,n+1} \\ \vdots & \ddots & \vdots \\ Q_{n+1,0} & \cdots & Q_{n+1,n+1} \end{pmatrix} = E \Phi A + E \Phi R \Phi A + E \Phi R \Phi R \Phi A + \dots, \quad (2.5)$$

with E , R and A being diagonal matrices for the emission, reflectivity and absorptivity of the surfaces and Φ being the view factors matrix:

$$\begin{aligned} E &= \text{diag}(E_0, \dots, E_{n+1}), \\ R &= \text{diag}(\rho_0, \dots, \rho_{n+1}), \\ A &= \text{diag}(\alpha_0, \dots, \alpha_{n+1}), \\ \Phi &= (F_{ij}), \quad i, j = 0, 1, \dots, n+1. \end{aligned} \quad (2.6)$$

The optical properties for the heat leaving the ambient, $i = 0$, are all (surface i , surface j and intermediate surfaces $k, l \dots$) in the visible spectrum, while the properties for the heat leaving the rest of the surfaces $i = 1, 2, \dots, n+1$ are the ones in the infrared spectrum. Hence, the matrixes E , A and R presented above have two variants, one for the visible spectrum properties and one for the infrared spectrum properties. This means that the heat delivered matrix, Q_{deliv} , is also obtained for these two cases. The definitive Q_{deliv} is composed by the row corresponding to $i = 0$ in the visible spectrum Q_{deliv} matrix, and the rows from $i = 1$ to $i = n+1$ from the infrared spectrum one.

With all of the above, the total heat arriving to a tube division j and the rear wall can be expressed as

$$Q_{\text{deliv},j} = \sum_{i=0}^{n+1} Q_{ij}, \quad j = 1, 2, \dots, n+1, \quad (2.7)$$

while the radiation losses can be understood as the heat delivered to the ambient,

$$Q_{\text{RL}} = Q_{\text{deliv},0} = \sum_{i=0}^{n+1} Q_{i0}. \quad (2.8)$$

- Hence, the net heat intercepted by the j surface, prior the external convection losses, is the difference between the heat extracted from it and the heat delivered to it that it absorbs.

$$Q_{\text{net},j} = E_j - Q_{\text{deliv},j}. \quad (2.9)$$

A negative net heat means that the surface absorbs energy indeed, while a positive one indicates that it delivers heat to the system. The addition of all the net heats involved in the system must be zero,

$$\sum_{j=0}^{n+1} Q_{\text{net},j} = Q_{\text{net},0} + Q_{\text{net},t} + Q_{\text{net},n+1} = 0, \quad (2.10)$$

where $Q_{\text{net},t} = \sum_{j=1}^n Q_{\text{net},j}$. However, the heats will be treated in terms of their absolute value for the following calculations.

- The external convection losses, $Q_{\text{CL,ext}}$ are obtained as

$$Q_{\text{CL,ext},j} = h_{\text{ext},j} A_j (T_j - T_{\text{ref}}), \quad j = 1, 2, \dots, n, \quad (2.11)$$

where A_j is the area (m^2) of surface j and h_{ext} is the external convective coefficient ($\text{W}/(\text{m}^2\text{K})$), obtained for cylindrical external receivers as presented by Siebers & Kraabel (1984), taking into account both natural and forced convection.

- Once Q_{net} and $Q_{\text{CL,ext}}$ are known, the heat absorbed by the tubes can be calculated

$$Q_{\text{abs},j} = Q_{\text{net},j} - Q_{\text{CL,ext},j}, \quad j = 1, 2, \dots, n, \quad (2.12)$$

- It is considered the turbulent and fully developed regime flow of the HTF so the Petukov correlation is used to obtain the Darcy factor (Romeo *et al.*, 2002). That factor is used in the Gnielinski correlation (Gnielinski, 1976) to calculate the Nusselt number for the internal convective coefficient, h_{int} . Then, the global transfer coefficient is obtained as

$$U = \left(\frac{1}{h_{\text{int}} d_{\text{int}}} + \frac{d_{\text{ext}} \ln(d_{\text{ext}}/d_{\text{int}})}{2k_t} + R_{\text{foul}} \frac{d_{\text{ext}}}{d_{\text{int}}} \right)^{-1} \quad (2.13)$$

taking into account the convection inside the tube, the effect of the thermal conductivity of the tube wall with k_t (W/(mK)) and the fouling inside the duct with the resistance R_{foul} (m²K/W). The d_{ext} and d_{int} (m) are the external and internal diameters of the tube, respectively. Given that for the first axial division, the inlet temperature of the HTF, $T_{\text{in,HTF}}$, is known, the outlet temperature of the HTF is calculated as

$$T_{\text{out,HTF}} = \bar{T}_t - (\bar{T}_t - T_{\text{in,HTF}}) \exp \left(\frac{Up\Delta z}{\dot{m}_t C_p} \right), \quad (2.14)$$

where p is the tube perimeter (m), C_p is the specific heat at constant pressure of the HTF (J/(kgK)), \dot{m}_t is the HTF mass flow inside one tube (kg/s) and \bar{T}_t is the mean temperature in the tube surface (K):

$$\bar{T}_t = 2 \frac{\sum_{j=1}^n A_j T_j}{p\Delta z}. \quad (2.15)$$

- The temperature of the tube is recalculated, since it was estimated at the beginning of the process:

$$T_{j,\text{rec}} = \frac{Q_{\text{abs},j}}{A_j U} + \frac{T_{\text{out,HTF}} + T_{\text{in,HTF}}}{2}, \quad j = 1, 2, \dots, n. \quad (2.16)$$

Regarding the rear wall, it is considered to be reradiating, which means that it is an adiabatic surface where the heat absorbed is equal to the heat leaving from it. Thus, the net heat at surface $n+1$ must be zero. This allows us to recalculate the temperature at the rear wall as

$$T_{n+1,\text{rec}} = \left(\frac{Q_{\text{deliv},n+1}}{A_{n+1} \varepsilon_{n+1} \sigma} \right)^{\frac{1}{4}}. \quad (2.17)$$

- Since the temperatures of the tube and rear wall were initially estimated, the recalculated temperatures are checked with the previous ones. The steps above are repeated until the temperatures of the precedent iteration are within the selected tolerance range with respect to the recalculated ones.

- As for the following axial cell, its $T_{\text{in,HTF}}$ is the same that the $T_{\text{out,HTF}}$ of the previous division, and so on. The $T_{\text{out,HTF}}$ of the final cell of the last panel must match the desired outlet HTF temperature, $T_{\text{out,HTF ref}}$. Thus, the outlet temperature of the salts at the end of the receiver needs to be checked. If it is not the one expected, a new mass flow of the HTF is recalculated, and the previous procedure is performed again until the convergence is reached. The new mass flow is established to be

$$\dot{m}_{\text{HTF,rec}} = \dot{m}_{\text{HTF}} + \dot{m}_{\text{HTF}} [\bar{T}_{\text{out,HTF}}(\text{end}) - \bar{T}_{\text{out,HTF ref}}]. \quad (2.18)$$

- In the next step, the total pressure drop, ΔP (Pa) in the receiver is obtained. Not only the straight tube sections are taken into account, but also the elbows, straight connectors and manifolds need to be included as a relevant part of the pressure losses (Idel'chik, 1960),

$$\begin{aligned} \Delta P = & \sum_{\text{straight}} fr \frac{L_d \dot{m}^2}{2d_d \rho C^2} + \sum_{\text{exp/con}} K \frac{\dot{m}^2}{2\rho C^2} + \\ & + \sum_{\text{elbow}} \left[1.3 - 0.29 \ln \left(\frac{Re}{10^5} \right) \times 0.21 a_1 \left(\frac{R_0}{d_d} \right)^{-\frac{1}{4}} \right] \frac{\dot{m}^2}{2\rho C^2}, \quad (2.19) \end{aligned}$$

where fr is the Darcy friction factor, L_d is the length of the straight duct (m), d_d is its internal diameter (m), \dot{m} the HTF mass flow through that duct (kg/s) and ρ is the HTF density (kg/m^3). Re is the Reynolds number, C is the cross section area of the tubes (m^2), R_0 is the elbow curvature radius (m) of the pipe, a_1 is a coefficient depending on the angle covered by the elbow and K is the resistance coefficient for expansions and contractions happening at the inlet and outlet of the manifolds: $K_{\text{exp}} = (1 - C_1/C_2)^2$ and $K_{\text{con}} = 0.5(1 - C_2/C_1)$ (Idel'chik, 1960).

- Knowing the pressure drop, the minimum allowable thickness can be obtained. It must be such that the tubes are able to endure the working pressure at their inside as well as the corrosive effects of the HTF flowing through them during the whole operative life of the receiver. The term related to the corrosion, th_{corr} , is obtained as the corrosion ratio, cr , by the expected lifecycle of the plant, lc . As for the pressure term, th_{press} , the minimum thickness is calculated as presented in Section 8 of the ASME

code for Boiler and Pressure Vessel (ASME, 2013),

$$\begin{aligned} th_{\min} &= th_{\text{corr}} + th_{\text{press}} = cr \times lc + \frac{\Delta P d_{int}}{2(\sigma_{adm} E_1 - 0.6\Delta P)} = \\ &= cr \times lc \frac{\sigma_{adm} E_1 - 0.6\Delta P}{\sigma_{adm} E_1 + 0.4\Delta P} + \frac{\Delta P d_{ext}}{2(\sigma_{adm} E_1 + 0.4\Delta P)}. \end{aligned} \quad (2.20)$$

Here σ_{adm} (Pa) is the maximum admissible tensile, evaluated at the tube working temperature and E_1 is the joint efficiency factor coefficient, that takes the value 1 for seamless tubes. While the second part of the equation is originally presented in terms of the internal diameter, the global expression has been recalculated to write it related to the external one. This is so to avoid the modification of the external diameter with the new thickness when working with the internal diameter expression, which would lead to a possible number of tubes per panel alteration, complicating the iterative process. If that minimum thickness calculated does not correspond to the one initially selected, the whole process is done over from the beginning, taking this minimum thickness as the new value for the next iteration.

2.2.3 Exergy calculation (XCGM)

In a SPT central receiver, the energy conversion from solar irradiation to heat is a radiation driven process. Thus, relying on radiation heat, optical properties and geometry pay an important role. To study the exergy in such receiver, the different energy exchanges, from the Sun irradiating to the heat transfer to the HTF, need to be included in the analysis. With that in mind, the maximum efficiency ratio (Petela, 1964) must be obtained in the first place for each emitting surface at each axial division as

$$\psi_i = 1 + \frac{1}{3} \left(\frac{T_{\text{ref}}}{T_i} \right)^4 - \frac{4}{3} \frac{T_{\text{ref}}}{T_i}, \quad i = 0, 1, \dots, n+1, \quad (2.21)$$

where, as stated in Section 2.2.1, T_0 is the Sun temperature in the exergy analysis. Therefore, $\psi_0 = \psi_S$. This exergy efficiency ratio is a characteristic parameter involved in radiation processes and is obtained as the quotient between the maximum work that can be obtained from radiation energy and the energy of such radiation. Then, the processes involved in the SPT external receiver are analysed with the expression for the exergy conservation. For a single axial division the balance is written as

$$X_S = X_{\text{opt}} + X_0 + X_t + X_{n+1} + X_{\text{CL,ext}} + X_{\text{wall},t} + X_{D,\text{HTF}} + X_{\text{HTF}}. \quad (2.22)$$

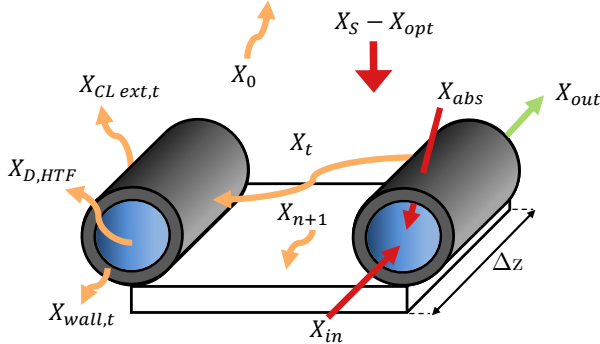


Figure 2.4: Exergies schematic representation.

On the one hand there is the solar exergy inlet of the system, that must be equal to the different radiating fluxes, the exergy losses and destructions due to irreversible processes in the receiver and the net exergy finally exiting the receiver in the HTF, which is the difference between the exergy outlet and inlet of the HTF, $X_{HTF} = X_{out} - X_{in}$. The exergies appearing in an axial discretization are depicted in Figure 2.4.

The different terms in the balance are:

- The exergy of the sunlight incident in the heliostat field,

$$X_{S,tot} = \psi_S A_m DNI. \quad (2.23)$$

Being the DNI the direct normal irradiation (W/m^2) and A_m the total mirrors area in the heliostat field. It represents the exergy initially entering the system. The subscript “tot” means that the exergy is referred to the whole receiver, not just one axial division.

Some of that sunlight exergy is lost in the reflection and concentration of the direct irradiation from the mirrors to the receiver surface. This is the exergy loss in the heliostat field,

$$X_{opt,tot} = \psi_S A_m DNI (1 - \eta_{field}), \quad (2.24)$$

where η_{field} is the average optical efficiency of the heliostat field. For an axial division, the difference between X_S and X_{opt} results in the exergy arriving to the receiver through surface 0 at a certain h . Hence, it is the emission E_0 of that surface multiplied by the exergy efficiency ratio at Sun temperature:

$$X_S - X_{opt} = \psi_S E_0 = \psi_S q_{hel} A_0. \quad (2.25)$$

- Part of the exergy escapes from the receiver system through surface 0 because of the reflections of the heat emitted by surfaces $0, 1, \dots, n+1$,

$$X_0 = \sum_{i=0}^{n+1} \psi_i Q_{i0}. \quad (2.26)$$

This irreversible exergy loss can be divided into the fraction that escapes the system which originally came from surface 0 and has not been absorbed by the tubes (just a reflection process), $X_{0,\text{refle}}$, and the fraction that comes from the emission of the tubes and the rear wall and reaches 0, $X_{0,\text{emi}}$.

- There are also exergy losses due to the multiple irreversible emissions and absorptions in the tubes. These losses exist because, although the heat is eventually absorbed by the tubes, the availability of such heat is dictated by its temperature, which can differ from the temperature of the emitting surface. Therefore, such exergy destruction in j is obtained as the difference between the exergy gains minus the exergy losses. Regarding the gains, these are the heats arriving from surfaces i at temperature T_i ($\psi_i Q_{ij}$) and the heat needed for emission of surface j ($(1 - T_{\text{ref}}/T_j) E_j$). On the other hand, the exergy outlets are the emission of surface j at T_j ($(1 - T_{\text{ref}}/T_j) Q_{ij}$) and the heat from surface i absorbed as heat by j at temperature T_j ($\psi_j E_j$):

$$\begin{aligned} X_t = \sum_{j=1}^n X_j &= \sum_{j=1}^n \left(1 - \frac{T_{\text{ref}}}{T_j} - \psi_j \right) E_j + \\ &+ \sum_{j=1}^n \sum_{i=0}^{n+1} \psi_i Q_{ij} + \sum_{j=1}^n \sum_{i=0}^{n+1} \left(1 - \frac{T_{\text{ref}}}{T_j} \right) Q_{ij}. \end{aligned} \quad (2.27)$$

- The same irreversible exergy losses are present at the rear wall. Thus, in this case, j is just surface $n+1$

$$X_{n+1} = \left(1 - \frac{T_{\text{ref}}}{T_{n+1}} - \psi_{n+1} \right) E_j + \sum_{i=0}^{n+1} \psi_i Q_{i,n+1} + \sum_{i=0}^{n+1} \left(1 - \frac{T_{\text{ref}}}{T_{n+1}} \right) Q_{i,n+1}. \quad (2.28)$$

- Exergy destruction due to irreversibility of the external heat convection in the j surfaces of the tube wall,

$$X_{\text{CL,ext},t} = \sum_{j=1}^n Q_{\text{CL,ext},j} \left(1 - \frac{T_{\text{ref}}}{T_j} \right). \quad (2.29)$$

- Exergy flow in the tube wall, which deals with the heat conduction through it,

$$\begin{aligned} X_{\text{wall},t} &= \sum_{j=1}^n Q_{\text{abs},j} \left(\frac{T_{\text{ref}}}{T_{\text{film}}} - \frac{T_{\text{ref}}}{T_j} \right) = T_{\text{ref}} \Delta S_{\text{th}} = \\ &= \int_{z=0}^{\Delta z} \int_0^{2\pi} \frac{k_t}{\ln \left(1 + \frac{t_h}{d_{\text{int}}/2} \right)} \frac{(T_j - T_{\text{film}})^2}{T_j T_{\text{film}}} d\theta dz, \end{aligned} \quad (2.30)$$

with T_{film} (K) being the salt temperature in contact with the tube internal wall at $j = 1, 2, \dots, n$.

- Exergy destruction occurring in the HTF, considering the fouling resistance and the internal convection when transferring the heat to the HTF from the inner tube wall and the friction of the HTF with the tube walls (Bejan, 1978)

$$\begin{aligned} X_{D,\text{HTF}} &= T_{\text{ref}} \Delta S_{\text{gen}} = T_{\text{ref}} (\Delta S_{\text{gen},\Delta T} + \Delta S_{\text{gen},\Delta P}) = \\ &= T_{\text{ref}} \left[\int_{z=0}^{\Delta z} \int_0^{2\pi} \frac{0.5 d_{\text{int}} (T_{\text{film}} - T_{\text{HTF}})^2}{\left(\frac{1}{h_{\text{int}}} \frac{d_{\text{ext}}}{d_{\text{int}}} + R_{\text{foul}} \frac{d_{\text{ext}}}{d_{\text{int}}} \right) T_{\text{HTF}} T_{\text{film}}} d\theta dz + \frac{\dot{m}_t \Delta P}{T_{\text{HTF}} \rho} \right]. \end{aligned} \quad (2.31)$$

- The last term in the balance is the net exergy gain in the HTF

$$X_{\text{HTF}} = X_{\text{out}} - X_{\text{in}} = \sum_{j=1}^n \left[Q_{\text{abs},j} \left(1 - \frac{T_{\text{ref}}}{T_{\text{film}}} \right) \right] - T_{\text{ref}} \Delta S_{\text{gen}}. \quad (2.32)$$

Finally, the exergy efficiency of that h axial division of the SPT receiver is calculated as the exergy of the process output, leaving the HTF, over the exergy of the input from the Sun:

$$\eta_X = 100 \frac{X_{\text{HTF}}}{X_S}. \quad (2.33)$$

The percentages of the exergy destruction and losses involved in the balance ($\xi_{X_{\text{opt}}}, \xi_{X_0}, \xi_{X_t}, \xi_{X_{n+1}}, \xi_{X_{\text{CL,ext}}}, \xi_{X_{\text{wall},t}}, \xi_{X_{D,\text{HTF}}}$) can be obtained in the same way in order to analyse how much they contribute in the exergy destruction in the system. They can also serve to determine where there is still room for improvement in the receiver design, coupled with the heliostat field performance. Thus, Eq. 2.22 can be rewritten in terms of the exergy efficiency and losses as:

$$100 = \xi_{X_{\text{opt}}} + \xi_{X_0} + \xi_{X_t} + \xi_{X_{n+1}} + \xi_{X_{\text{CL,ext}}} + \xi_{X_{\text{wall},t}} + \xi_{X_{D,\text{HTF}}} + \eta_X. \quad (2.34)$$

On the other hand, the thermal efficiency of the receiver and heliostat field can be obtained as:

$$\eta_{\text{thermal}} = 100 \frac{Q_{\text{abs}}}{Q_{\text{hel}}} \eta_{\text{field}}. \quad (2.35)$$

2.3 Case of study

In the previous sections, the procedure to analyse the exergy of a tubular external receiver has been introduced. It has been done trying to include the least possible particularities, aiming to provide a generalized method for the study of this specific subsystem. Now, the parameters of the selected receiver configuration are presented.

2.3.1 Ambient conditions

Regarding the conditions of the surroundings of the SPT plant, the ones selected are an ambient pressure of 1 atm, an ambient temperature, T_{amb} , of 25 °C and a relative humidity of 60%. With such conditions, ε_{amb} results in 0.8506. The ground emissivity is 0.955 and its temperature is obtained as $T_{\text{amb}}\varepsilon_S^{1/4}$ (Berger *et al.*, 1984). The wind velocity is null so the external convection is due only to the natural convection effect. The latitude of the location is 37.56°.

The ambient conditions are relevant in the exergy analysis since the maximum work depends on them, given that the ambient temperature defines the dead state.

2.3.2 Heliostat field

The heliostat field chosen in the software tool FluxSPT is a Gemasolar-like one, with 2,650 heliostats of 115.7 m² of mirror each. This makes a total mirror surface, A_m , of 306,605 m².

The design point is the solar-noon spring equinox, when the DNI incident on the mirrors is 930 W/m², and the aiming strategy is a flat one, making the heat flux incident on the receiver as axially homogeneous as possible on its surface, minimizing the peak fluxes which are harmful to the receiver (Sánchez-González *et al.*, 2018). Selecting that aiming strategy, the mean optical efficiency of the field, η_{field} , obtained is 58.59%.

The chosen aiming strategy and the mirrors field characteristics result in the heat flux on the receiver surface shown in Figure 2.5. Such heat flux has been

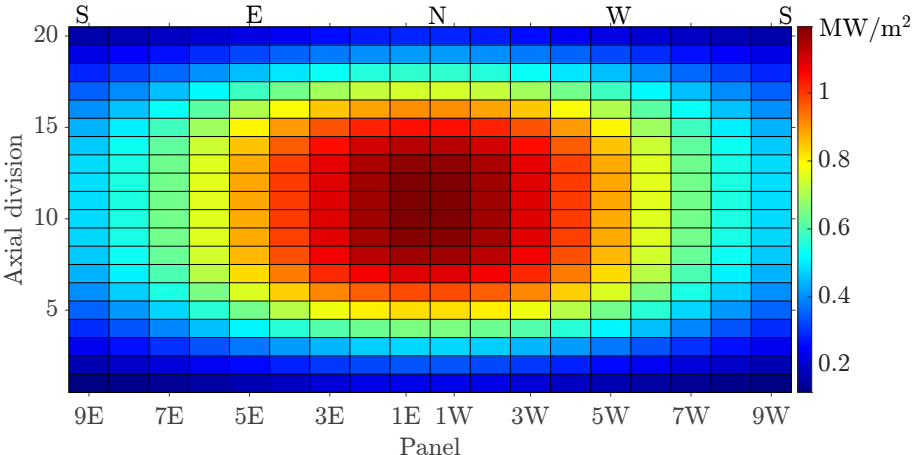


Figure 2.5: Discretized heat flux distribution on the receiver surface with the flat aiming strategy.

discretized in a series of vertical and horizontal divisions. Since the radiation received by all the tubes of a panel is considered to be the same, these divisions have been done in such way that the number of vertical discretizations is equal to the number of axial divisions of one tube, while the horizontal ones correspond to the number of panels. For each individual cell, the heat flux is considered homogeneous.

2.3.3 Receiver configuration

The receiver is an external tubular receiver placed at the top of a 130 m high tower. The base cylinder of the receiver has a diameter, D , of 8.4 m and serves of supporting frame for 18 equal panels, N_p , that hold the tubes vertically disposed. The external tube diameter has been set to 4.22 cm. The separation between the tubes of a panel is 4.1 mm. That diameter and tube gap result in 32 tubes per panel. The initial thickness of the tube wall has been set in 1.65 mm. However, as stated in Section 2.2.2, it is later recalculated so the entropy generation due to the heat conduction through the wall is minimized. The length of the tubes, L_t , is 10 m.

Solar salt (60% NaNO_3 , 40% KNO_3) is selected as the HTF in this receiver, as in the case of the commercial SPT plants (Tian & Zhao, 2013; Conroy *et al.*, 2019). The inlet temperature, $T_{\text{in,HTF}}$, is 290 °C to avoid its freezing, while the outlet temperature, $T_{\text{out,HTF}}$, is limited at 565 °C, preventing its decomposition (Zavoico, 2001). The salt mass flow after the iterative process of the thermal

model results in 358.76 kg/s, with the receiver being able to produce 150 MWt due to the thinner tube-wall resulting from Eq. 2.20. The salt properties can be obtained in (Zavoico, 2001). A two path flows configuration, symmetrical in the N-S direction, has been selected (Rodríguez-Sánchez *et al.*, 2015). The inlet of the salt is at the bottom of the two Northern panels while the outlet is at the top of the most Southern ones. Since the crossover between patterns has been shown irrelevant at the solar noon (Rodríguez-Sánchez *et al.*, 2015), no crossover has been implemented. The total HTF mass flow is equally divided into all the tubes of a panel, and hence the HTF mass flow through one tube results in

$$\dot{m}_t = \frac{\dot{m}_{\text{HTF}}}{N_{\text{fp}} N_t}, \quad (2.36)$$

being N_{fp} the number of flow paths for the HTF through the receiver and N_t the number of tubes per panel.

The material selected for the tubes manufacturing is Inconel 625, a highly available material which has been widely studied in the present field. Its properties are available in (ASME, 2013). The tubes are guided through the panel by a series of equally spaced supports along its length, called clips. These prevent the tubes from bowing excessively, both in the radial direction of the receiver and towards the adjacent tubes of the panel. Three smoothly bended pipes connect the tubes to their respective inlet and outlet collectors, with two elbows of 120° and one of 60°. This results in a_1 coefficients (Eq. 2.19) of 1.16 and 0.78 respectively. The curvature radius of the elbows, R_0 , is 0.13 m. Also, the HTF inside the collectors is considered to experience a trajectory similar to the circulation inside two 90° elbows, with an a_1 coefficient of 1. There are two 90° elbows in the section connecting two consecutive panels as well. For the pressure drop calculation in the receiver, only the elements in series, not in parallel, are considered; this means that only one flow path is studied, as well as just one tube per panel in that flow path. In Eq. 2.19, the length of the straight ducts, L_d , the internal diameter of such ducts, d_d , and the mass flow of HTF through them, \dot{m} , are:

- For the receiver tubes, L_t , d_{int} , and \dot{m}_t .
- For the straight sections after the elbows connecting the tubes to the collectors, lengths of 0.7 m, 1.7 m and 0.2 m per tube, d_{int} , and \dot{m}_t .
- For the manifolds, the width of the panel or the length of the collector,

1.4811 m, the internal diameter of the collector 162.76 mm, and the total mass flow through one flow path, $\dot{m}_{\text{HTF}}/N_{\text{fp}}$.

- For the ducts connecting the inlet and outlet manifolds from different panels, lengths of 0.2544 m and 0.599 m (half the length of the whole pipe), 170 mm of d_d , and $\dot{m}_{\text{HTF}}/N_{\text{fp}}$.

The mentioned connecting sections are presented in Figure 2.6. The only ones that are insulated are the receiver tubes, being the remaining three different kind of components at a constant temperature. The considered fouling resistance inside the tubes is $8.8 \times 10^{-5} \text{ m}^2\text{K}/\text{W}$. The corrosion ratio of the Inconel 625, with solar salt flowing through and at a film temperature of 600 °C, is $16.8 \times 10^{-6} \text{ m/year}$ (McConohy & Kruizenga, 2014), while the expected lifecycle of the plant has been set to 30 years.

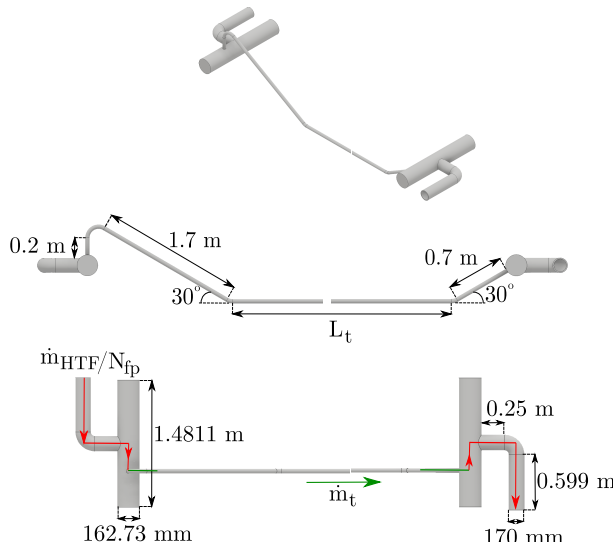


Figure 2.6: Schematic of the elements considered for the pressure drop calculation in one panel. Only one tube has been depicted.

All tubes are covered with a black Pyromark coating in order to increase their absorptivity. On the other hand, the base cylinder (surface $n+1$) is covered with a white Pyromark ceramic painting of high reflectivity. The optical properties of both coatings when applied on Inconel 625 are presented in Table 2.1 for both the visible and infrared spectrum. The properties considered for surface 0 have also been included. The imaginary ambient surface in reality presents a transmissivity of 1, since all the radiation that it receives passes

Table 2.1: Optical properties.

Coating	Surface	Visible spectrum		Infrared spectrum			ε
		α	ρ	α	ρ		
-	Ambient (0)	1	0	1	0		1
Black Pyromark	Tube (1, ..., n)	0.93 [b]	0.07	0.95 [c]	0.05	$f(T)$ [d] 0.81@588 K to 0.94@1366 K	
White Pyromark	Rear wall (n+1)	0.2	0.8 [b]	0.215	0.785 [e]		0.84 [b]

through it without increasing its temperature, making the absorptivity and reflectivity 0. However, for the ECGM and XCGM, this imaginary surface has been modelled like an opaque surface with an absorptivity of 1 (thus reflectivity and transmissivity are 0) and leaving its temperature fixed as T_{ref} , resulting in the same outcome.

Regarding the thermal model, it is used to study the whole receiver by analysing just one representative tube per panel. This simplification is feasible since the heat flux reaching the tubes surface is considered to be the same in all of them, leading them to have the identical temperature distribution. However, the radiative influence of the adjacent tubes of the panel is indeed taken into account. The insulated straight zone of the tubes is discretized in a series of 74 circumferential cells ($n=37$) and the axial divisions are 0.5 m long (Δz), giving a total of 20 of them per tube. Therefore, following one flow path (9 panels) and studying just one tube per panel, the number of axial divisions faced is $m = 180$,

$$m = \frac{L_t N_p}{\Delta z N_{\text{fp}}}. \quad (2.37)$$

The tolerance values selected for the iterative process are: 10^{-3} (K) for TOL1, 10^{-3} (K) for TOL2 and 10^{-6} (m) for TOL3, see Figure 2.3. TOL1 is the condition for the convergence of the tube and rear wall temperature, TOL2

[b] (Zavoico, 2001)

[c] (Ho *et al.*, 2012)

[d] (Wade & Slemp, 1962)

[e] (Scannapieco, 1968)

is the one for the convergence of $T_{\text{out,HTF}}$ and TOL3 the one for the convergence of the thickness of the tubes.

2.4 Results

The exergy analysis of a molten-salt central-receiver has been performed for the case of study introduced in Section 2.3. To do so, the different exergies conforming the balance in Eq. 2.22 have been obtained. It has been done for all of the axial levels of the panels corresponding to one of the two flow paths in which the receiver has been discretized. Given the symmetry of the heat flux on the receiver surface at solar noon, the exergy results are the same for the remaining flow path. Hence, the total amount of the different exergies is obtained as the sum of the exergies of the 180 axial divisions of one flow path and multiplying that sum by the number of tubes per panel and flow paths. The Sankey diagram for the case of study is presented in Figure 2.7.

The exergy efficiency of the configuration chosen is a 32.05%. The results show that the maximum exergy loss occurs in the heliostat field, X_{opt} , being almost half of the exergy that arrives from the sun ($\xi_{X_{\text{opt}}}$), an 41.41%. As can be sensed with Eqs. 2.23 and 2.24, such percentage of exergy loss solely depends on the optical efficiency of the mirrors, η_{field} , related to the aiming strategy selected. Since this study is undertaken for a fixed heliostat field layout, this exergy loss can only be affected by the aiming strategy of the field. The second greater exergy destruction is found in the radiative heat exchange in the tubes, X_t , involving the multiple emissions, reflections and absorptions (ξ_{X_t} of 16.84%). Given its relevance in the balance, different operation conditions will be analysed with the intent to decrease its value. The exergy destruction in the HTF, $X_{D,\text{HTF}}$, accounts for the third greater exergy losses (4.35%) and it is affected by the internal convective coefficient, the fouling resistance and the friction of the HTF with the tube wall. Almost on a par with $X_{D,\text{HTF}}$ is the exergy loss escaping through the ambient, X_0 , that depends on the heat emitted by the receiver, Q_{i0} , and the temperatures of the surfaces emitting that heat through the value of ψ_i , (Eq. 2.26). The percentage of exergy loss due to the external convection losses, $X_{\text{CL,ext}}$ is found to be negligible (0.69%) in comparison to the other exergy loss sources appearing. With such low value, it seems that the wind velocity modification is not a highly relevant aspect to study the exergy improvement. The exergy destruction in the absorptions and emissions in the rear wall, X_{n+1} , is just a 0.21% and the exergy loss in the tube

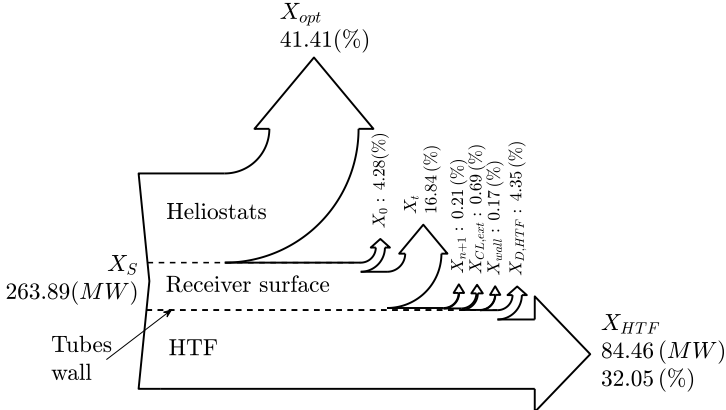


Figure 2.7: Sankey diagram for the exergy analysis of the receiver.

wall, $X_{wall,t}$, is the lower of them all, a 0.17%. This last exergy loss has been minimized in the design phase by selecting the smallest admissible thickness for the tube, according to Eq. 2.20. Having performed the exergy balance of the base case of study, it is then compared with scenarios of other operating conditions.

2.4.1 Optical properties influence

The importance of the optical properties of the coating of the tubes cannot be disregarded since they intervene in a handful of heat exchanges happening in the receiver surface. The higher the absorptivity, the lesser the radiative exergy losses will be since most of the heat received is absorbed, increasing the temperature of the surface as well, which is desirable to obtain higher exergies. Alternatively, a high emissivity and a high surface temperature result in greater radiative losses, counteracting the benefits from the high absorptivity (Petela, 2003). Nevertheless, it must be considered that these properties degrade with time (Ho & Pacheco, 2014), given the demanding conditions at which the receiver is exposed. Thus, the exergy analysis has been performed for the cases of a degradation of a 5%, 10%, 15% and 20% of the absorptivity and emissivity of the tube coating, where the nominal values (0% degradation) can be found in Table 2.1. The evolution of the exergy efficiency has been obtained when both the absorptivity and emissivity degrade in the same amount as well as separately (one fixed in the nominal value and the other one degrading), Figure 2.8(a). The same has been done for the thermal efficiency, Figure 2.8(b).

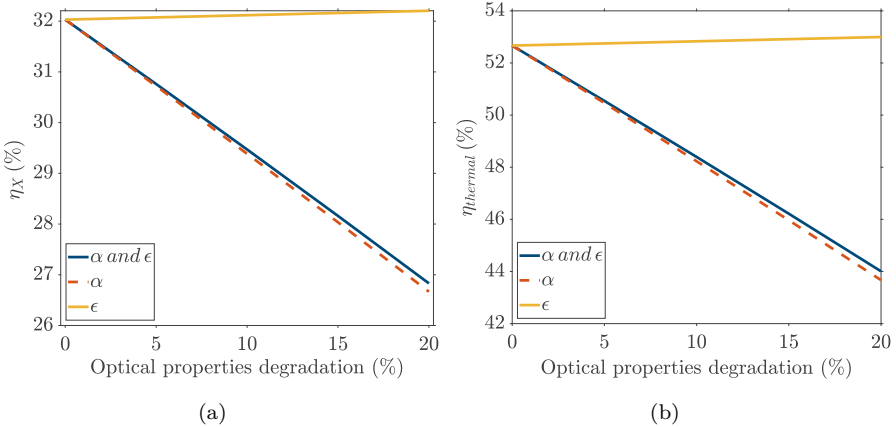


Figure 2.8: (a) Evolution with the optical properties degradation of the a) exergy efficiency and (b) thermal efficiency.

As expected, lower values of absorptivity lead to a slightly lesser exergy efficiency since the losses increase considerably, with a rate of over a 1% decline of the exergy efficiency every 5% of degradation of the optical properties. This highlights the need of the repainting maintenance tasks considering that, as stated by (Ho & Pacheco, 2014), the degradation rate for the Pyromark 2500 coating is in between a 0.25%/year and a 0.75%/year. It would be desirable a coating with the most stable optical behaviour as possible, as well as the higher feasible absorptivity. On the other hand, a lower emissivity results in a greater exergy efficiency, but the improvement is found to be negligible. The thermal efficiency follows the same tendency than the exergy one, although it is higher since it does not consider the temperature of the source. With the inclusion of that temperature, the exergy study constitutes an in-depth analysis that allows to observe the real possibilities for the solar energy exploitation in the receiver subsystem, analysing its different sources. Hence, it is understandable the high quantitative separation between the energy and exergy efficiencies.

The breakdown of the different percentage exergy and losses in the Eq. 34 balance is shown in Figure 2.9. The goal is to provide a better understanding of the evolution of the exergy efficiency, η_X , with the optical properties of the tubes coating. The case of the non-degraded properties (0%) is compared with the results obtained for a combined degradation of the absorptivity and emissivity of 10% and 20%. The alternatives of isolated degradation of the absorptivity and isolated degradation of emissivity have been omitted since,

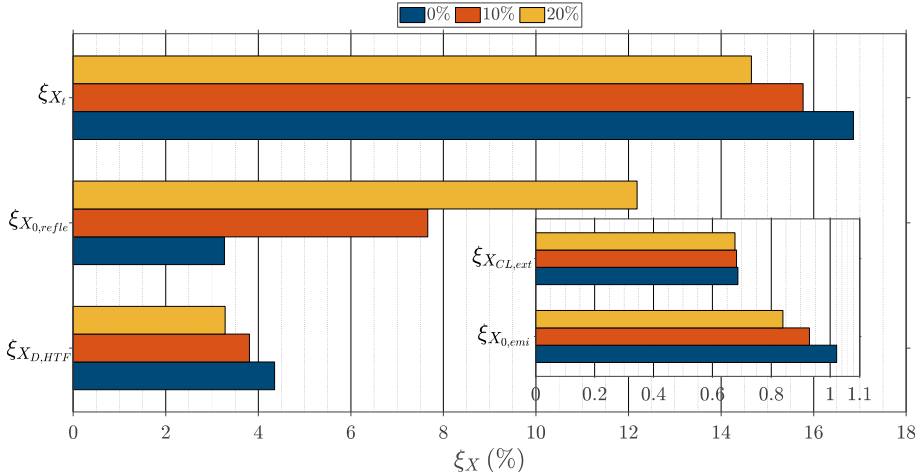


Figure 2.9: Breakdown of the percentage exergies evolution with the optical properties degradation.

as seen in Figure 2.8, the variation of the emissivity on its own has barely any effect respect to the initial scenario. Consequently, the degradation of just the absorptivity results almost identical to the combined situation. Also, the intermediate scenarios of 5% and 15% of degradation are not shown since they follow the linear tendency observed between the cases of 0% degradation, 10% and 20%. The exergy loss in the heliostat field, $\xi_{X_{opt}}$, is not presented either since it occurs upstream of the optical properties of the tubes coating modification. Also, the exergy loss in the rear wall, $\xi_{X_{n+1}}$, and in the tube wall, ξ_{X_t} , have not been included since they are almost negligible (Figure 2.7) and are barely modified in the different alternatives studied in this Section. The exergy escaping the receiver through surface 0 (the ambient), ξ_{X_0} , is presented divided into the components mentioned in Section 2.2.3, $\xi_{X_{0,refle}}$ and $\xi_{X_{0,emi}}$, to get a better sense of the influence that the optical properties have on them.

This representation of the different percentage exergies shows that the exergy destruction due to the radiation heat absorbed by the tubes, ξ_{X_t} , decreases with the absorptivity degradation of their coating over a 2%. Such lesser absorptivity is translated in a lower heat absorbed by the tubes, decreasing the wall temperature as it “retains” less heat. It means then that the heats exchanged between surfaces (Eq. 2.4) are lesser since lower temperature values of the surfaces mean less emission (Eq. 2.1). Looking at the X_t exergy loss term (Eq. 2.27), the lower temperatures as well as emission and heat exchanged

between surfaces, although not being extreme cases, result in a notable descend of this exergy loss. On the other hand, the exergy loss of radiation heat to the ambient, ξ_{X_0} , increases. In that ξ_{X_0} , the most relevant increment (of over a 9%) takes place for the exergy destruction due to the radiation heat escaping through the ambient that initially entered the receiver system through the ambient as well, $\xi_{X_{0,\text{refle}}}$. Thus, it is radiation heat that has only been reflected by the tubes and/or rear wall but not absorbed by them. Again, its increment is motivated by the degradation of the absorptivity (which implies a greater reflectivity), affecting the temperatures distribution on the tubes and the heats exchanged, modifying the result of the product $\psi_i Q_{ij}$ (Eq. 2.26). On the other hand, the exergy escaping also through the ambient, but originated from the emissions of the tubes and rear wall, $\xi_{X_{0,\text{emi}}}$, is smaller than the former one, being that difference even more notable with the optical properties degradation, since the emissivity decreases. Hence, most of the exergy leaving to the ambient has its origin in the ambient itself. Summing up, the temperature of the tube wall decreases since the radiation losses are greater, being closer to the HTF temperature. Thus, the exergy losses due to convection and due to the heat conduction in the tube wall both decrease as well. Moreover, the temperature in the tube inner wall, T_{film} , is more similar to the HTF temperature, which also explains the descend of $\xi_{X_{D,\text{HTF}}}$. The exergy efficiency decreases considerably the greater the optical properties degradation is, even though the entropy generation is also lower, which means that the heat reaching the fluid is also lesser. As seen in the breakdown, that descend in the heat transferred to the HTF is due to the greater $X_{0,\text{refle}}$.

2.4.2 Aiming strategy and DNI influence

The effect of the DNI level modification, from 550 W/m^2 to 1000 W/m^2 , in the exergy efficiency has been studied for the base case. It would be equivalent to a change in location or the variation in the number of mirrors in the heliostat field and it results in a modification of the HTF velocity (and therefore its mass flow). The base configuration has been tested under a peak aiming of the heliostat field as well. An instance of the peak distribution at a DNI of 930 W/m^2 (the same one that was initially considered for the base case with flat aiming) is depicted in Figure 2.10. This peak aiming provides a maximum heat flux of 1.5 MW/m^2 , opposite to the maximum of 1.2 MW/m^2 found in the flat aiming strategy (Figure 2.5), as well as a much narrow area of maximum values of such incident heat flux on the receiver.

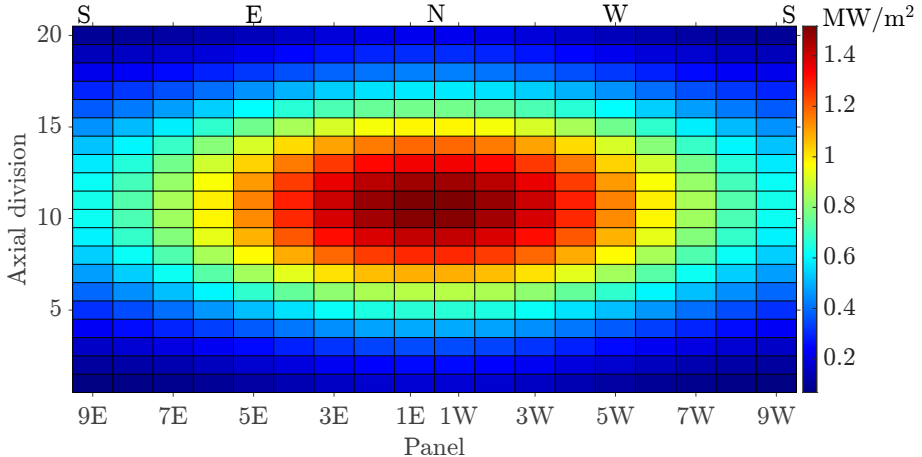


Figure 2.10: Discretized heat flux distribution on the receiver surface with the peak aiming strategy.

The temperature distribution in the outer tube wall presents the same tendency than the corresponding heat flux in each strategy. Figure 2.11 gives a better sense of the differences in the temperature distribution on the outer tube wall resulting from both strategies. The temperature evolution through the axial divisions for a fixed circumferential position ($\theta=0^\circ$), is depicted in Figure 2.11(a). As it can be observed, the peak aiming reaches higher temperatures at the middle of each panel ($h=10, 30\dots$) as well as a lesser homogeneous temperature in z : the temperature gradient between the middle of the panels, i.e. $h=10$, and its ends, i.e. $h=20$, is greater than in the flat aiming. The peak aiming strategy gives a maximum temperature of $752.8\text{ }^\circ\text{C}$ while the flat one results in $678.1\text{ }^\circ\text{C}$. On the other hand, Figure 2.11(b) provides the temperature evolution in θ for the tenth axial division, showing that the rear half of the tubes is at almost the same temperature with both aiming strategies. However, the front side of them is at greater temperatures in the peak configuration. Thus, the circumferential gradient for the peak case is around $433\text{ }^\circ\text{C}$, opposite to the $347\text{ }^\circ\text{C}$ of the flat one. The understanding of how both tube outer temperature distributions diverge, while the HTF temperature remains the same in the two cases, will ease the comprehension of the different exergy losses.

It can be seen in Figure 2.12 that the exergy efficiency grows when the DNI level increases. This tendency is observed for the peak and flat cases, showing also a reduction of the efficiency growth rate (gradient) when the DNI moves to greater levels. Between the two aiming strategies, the peak one provides

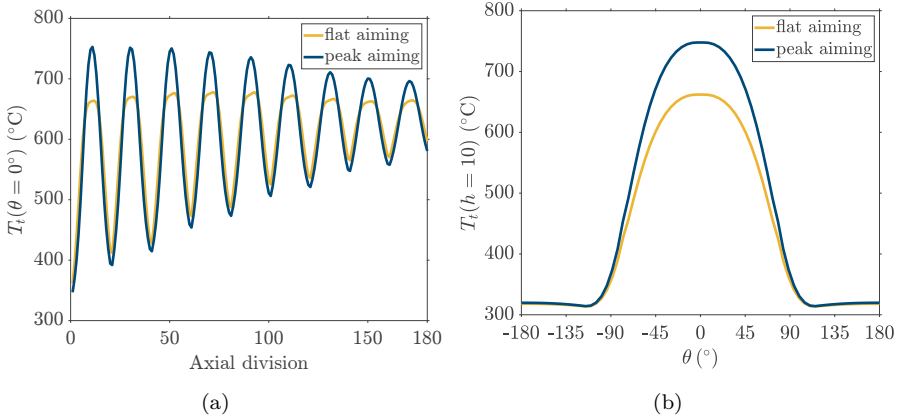


Figure 2.11: (a) Axial evolution of the tube wall temperature at $\theta=0^\circ$ and (b) circumferential evolution of the tube wall temperature at $h=10$.

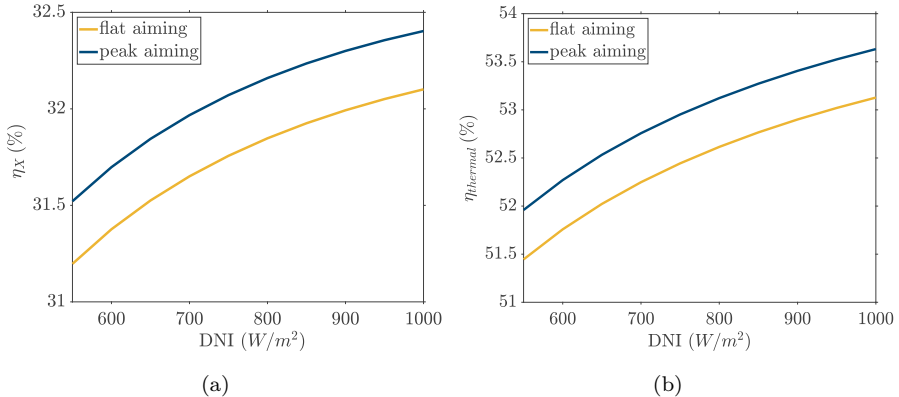


Figure 2.12: Evolution, for flat and peak aiming strategies and different DNI levels, of the (a) exergy efficiency and the (b) thermal efficiency.

the greater exergy efficiency. However, it should be considered that the non-homogenization of the incident flux on the receiver obtained with the peak aiming strategy leads to excessively high temperatures at some spots of the tubes as well as circumferential gradients, resulting in greater thermal and mechanical stresses. Hence, the structural limits of the receiver need to be watched to ensure the correct operation of the receiver during the lifetime projected for the SPT plant. On the other hand, just as happened in Section 2.4.1, the thermal efficiency is greater than the exergy one.

The breakdown for the percentage of the exergy losses of Eq. 2.34 is also

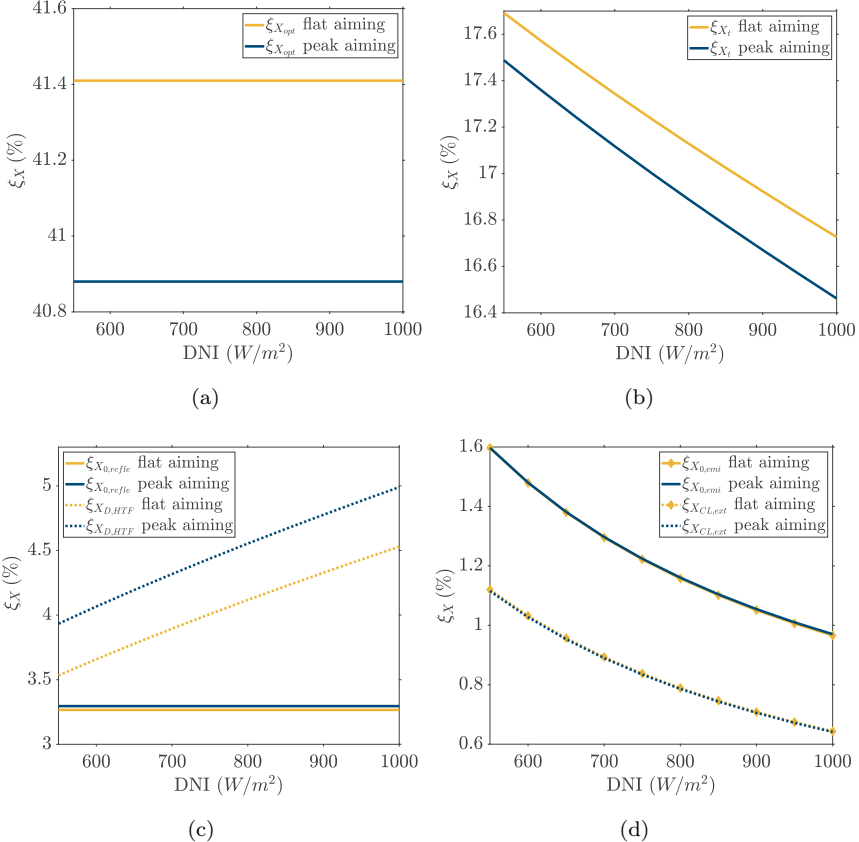


Figure 2.13: Breakdown of the percentage exergies evolution with the DNI for flat and peak aiming strategies.

shown for this DNI and aiming modification study, Figure 2.13. For a fixed DNI, the exergy from the Sun, X_S , is the same regardless the aiming since both cases have the same field layout. Regarding the main discrepancies between the flat and peak aiming strategies observed in the percentage dissection, the flat one presents a higher exergy destruction in the heliostat field, $\xi_{X_{opt}}$. Such outcome is due to the lesser mirrors efficiency, η_{field} , respect to the peak aiming caused by the greater spillage losses, as a result of going for a more homogeneous heat flux distribution on the receiver surface, especially in the axial direction. Thus, the heat arriving from the heliostat field to the receiver is greater in the peak alternative, being the option with the greater HTF mass flow as well, around a 1.35% in all of the DNI scenarios. The exergy destruction due to the tube radiation heat absorption, ξ_{X_t} , is greater again for the flat aiming scenario. Looking at the terms in Eq. 2.27, there are contradictory effects between them

that eventually lead to the result obtained for this loss. The lesser radiation reaching the receiver in the flat case (see Figures 2.5 and 2.10) contributes to a temperature profile with lower values. It is also more homogeneous and does not present excessively hot spots in the flat configuration, opposite to the peak one, where the aiming leads to a highly uneven temperature distribution (see Figure 2.11). The emissivity E_i and heat exchanged by the surfaces Q_{ij} presents the same trend in the two configurations, both qualitative and quantitative but, in this case, the quantitative differences are tiny. On the other hand, the maximum efficiency ratio, ψ_i , is found to be overall greater for the flat aiming. Moving on, the flat aiming alternative has a lesser exergy destruction in the heat transfer from the inner tube wall to the HTF, $\xi_{X_{D,HTF}}$, precisely due to the lower overall temperature distribution; such descend in the tube outer temperature affects also the tube inner wall temperature, lessening the temperature gradient between the tube inner wall and the HTF, since the latter presents virtually the same temperature profile evolution through the receiver in both configurations. Also, the heat Q_{abs} is slightly higher in the peak case since more HTF mass flow rate circulates through the tubes. Thus, the first two exergy destruction sources mentioned are the ones responsible for the lesser exergy efficiency in the combined operation of the heliostat field and the receiver when using the flat aiming strategy in comparison to the peak one. Meanwhile, the exergy loss in the HTF plays in favour of the flat aiming configuration. In addition, both components of ξ_{X_0} , $\xi_{X_{0,refl}}$ and $\xi_{X_{0,emi}}$, as well as $\xi_{X_{CL,ext}}$ are almost identical for these two strategies, as depicted in Figures 2.13(c) and 2.13(d). Looking at the exergy efficiency expression (Eq. 2.33), the greater heat absorbed by tubes in the peak aiming scenario as well as the higher temperatures of the tube wall contribute to a better performance of the peak alternative. The total entropy generated, although greater (4.498×10^4 W/K opposite to 4.0822×10^4 W/K), is not enough to counteract such previously mentioned advantages gained from the heat absorbed and tube wall temperature. The greater entropy generation is found in the temperature gradient between the inner tube wall and the HTF, being one order of magnitude greater than the entropy generated in the tube wall conduction and three orders of magnitude greater than the one due to the pressure drop.

Given the great difference observed in the exergy loss due to the heliostat field, $\xi_{X_{opt}}$, between both aimings, the exergy efficiency of just the receiver is depicted in Figure 2.14. This would be the exergy gain in the HTF over the exergy arriving from the heliostat field: $\eta_{X,receiver} = 100 \frac{X_{HTF}}{X_S - X_{opt}}$. Such

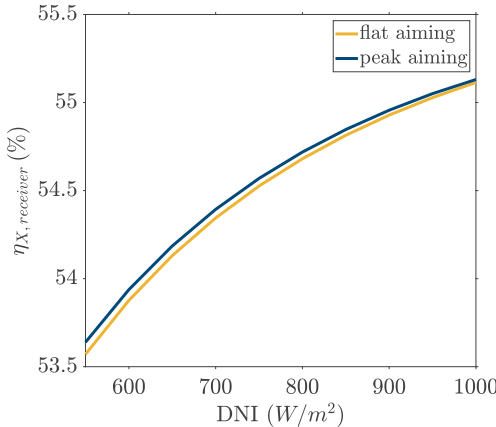


Figure 2.14: Exergy efficiency of the SPT receiver for flat and peak aiming strategies under different DNI.

Figure highlights that the receiver on its own is virtually independent from the aiming strategy selected: the improvements in the exergy losses from one aiming option are counteracted by a poorer performance of other of its losses. For instance, in the peak aiming case, the higher $\xi_{X_{D,\text{HTF}}}$ with respect the flat one is compensated with the lesser ξ_{X_t} . However, the strategy is indeed relevant for the whole plant, as seen for the global η_X , that considers the heliostat field as well (Figure 2.12), making the $\xi_{X_{\text{opt}}}$ the defining factor that cannot be disregarded by only analysing the receiver exergy efficiency.

2.4.3 Ambient temperature influence

Until now, the ambient temperature has not been considered, remaining fixed regardless the DNI, showing an improvement in the exergy efficiency the higher the DNI is. However, the surroundings temperature is not decoupled from the DNI and is indeed a relevant factor in the exergy analysis: as mentioned earlier, lower surroundings temperatures result in greater exergies since the ability of a substance or process to produce work lasts until it is in thermal equilibrium with the ambient. It can be observed from multiple meteorological data that an increase of the DNI at a certain location typically comes with a growth of the ambient temperature. Thus, the increase of the exergy efficiency associated with a higher DNI may be counteracted if the surroundings temperature increases enough.

With all of this, Figure 2.15 provides the evolution of the exergy efficiency

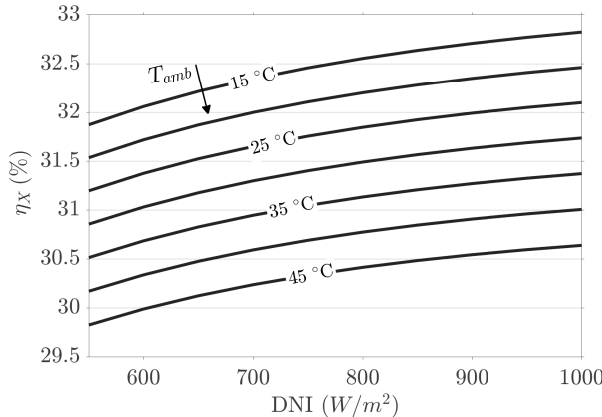


Figure 2.15: Exergy efficiency evolution with the DNI for different ambient temperatures.

with the DNI level for different ambient temperatures. The aiming strategy is the flat one, as selected for the base case. On the other hand, the thermal efficiency, depicted earlier in Figure 2.12(b) remains unchanged regardless the surroundings temperature so it is not the best indicator to compare different locations.

As expected, the isothermals follow a decreasing tendency the greater the ambient temperature is and its relevance in the exergy efficiency is not negligible. Then, for instance, it is preferable in terms of exergy efficiency a location with a DNI of 800 W/m² and an average surroundings temperature of 25 °C rather than another with a DNI of 900 W/m² and an average surroundings temperature of 30 °C. The goal should be finding a location with a moderate/high average DNI level and the lowest ambient temperature as possible. Moreover, lower DNI results in lower tube wall temperatures, relaxing the thermal stress. Meanwhile, for a fixed DNI level, the tube wall temperature distribution is virtually the same regardless the surroundings temperature, with the tiny divergences being due to the higher convection losses with lower ambient temperatures.

A good instance of low ambient temperatures and low/moderate DNI would be the location of the PROMES laboratories, at the French side of the Pyrenees. The 1500 m altitude of the location favours its low average temperatures, with the coldest months having average maximum temperatures around 4 °C and average maximum DNI over 450 W/m² and the hottest ones with average temperatures between 13 and 20 °C and average maximum DNI around

650 W/m². Particularly interesting is the case of Ouarzazate, in the Moroccan dessert, with average maximum temperatures of around 17 °C in winter and DNI over 850 W/m². However, during the summer months, the maximum average DNI is around 800 W/m² and temperatures reach up to 38 °C. Examples of high surroundings temperatures and high DNI would be the location of the Ashalim SPT plant, at Israel, or the Crescent Dunes SPT plant at Nevada, US, both placed at warm and arid regions. The worst case presented for PROMES (during its summer months) resembles to the best scenarios for these locations, occurring in winter. However, in summer, temperatures over 30 °C and DNI of over 830 W/m² are typically reached. Almost 900 W/m² can be reached in August at Crescent Dunes. Lastly, Noor Energy 1, at Dubai presents moderate DNI, with an average value of around 730 W/m², influenced by its dusty location. On the other hand, it suffers from extremely high temperatures, ranging from maximum average temperatures of 23 °C in winter to maximum average temperatures over 40 °C in summer, given its proximity to the equatorial line. The meteorological data commented has been obtained from (European Commision, 2020).

The breakdown for the percentage exergy losses is depicted in Figure 2.16 for different ambient temperatures under the flat aiming strategy scenario. Since the evolution with the DNI of the different losses has already been depicted in Figure 2.13 for flat aiming and 25 °C, and given that it is the same for the rest of the ambient temperatures, only the results for a DNI of 900 W/m² are shown. The biggest difference between the cases is the exergy loss due to the radiation heat absorbed by the tubes, that grows greatly with the ambient temperature. The same thing happens with the exergy destruction due to the internal convection in the HTF and friction with the tube wall, although the differences are not that big. The losses $\xi_{X_{0,\text{refe}}}$ remain the same regardless the ambient temperature, while the losses $\xi_{X_{0,\text{emi}}}$ increase slightly with the surroundings temperature, as well as $\xi_{X_{\text{CL},\text{ext}}}$, although they can be considered negligible. Thus, the two main sources of exergy losses are also the ones suffering from the greater growth with the ambient temperature. The maximum efficiency ratio, ψ (Eq. 2.21), decreases with the surroundings temperature, which makes the $\xi_{X_{0,\text{emi}}}$ diminish as well since it has a direct dependence with it (Eq. 2.26). The reduction of $\xi_{X_{\text{CL},\text{ext}}}$ can be explained by looking at Eq. 2.29, where the term $1-T_{\text{ref}}/T_j$ decreases the higher the ambient temperature. The convective losses are diminished as well the higher the ambient temperature is, but the differences obtained for one surroundings temperature or the other are quite

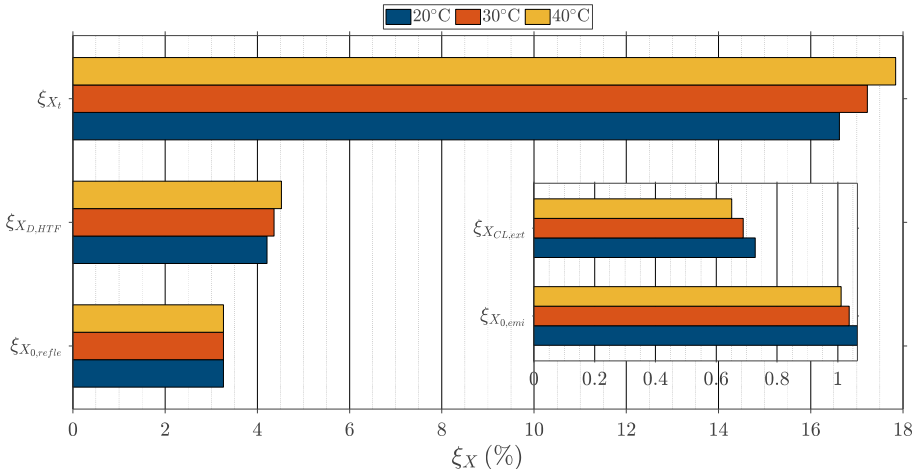


Figure 2.16: Breakdown of the percentage exergies evolution with the DNI for different ambient temperatures.

small. On the other hand, $\xi_{X_{wall,t}}$ and $\xi_{X_{D,HTF}}$ have a direct dependence on the ambient temperature (Eqs. 2.30 and 2.31), while ξ_{X_t} (Eq. 2.28) presents the combination of the term $1-T_{ref}/T_j$ and the maximum efficiency ratio, resulting in a greater loss the higher the temperature.

2.5 Conclusions

A method to obtain the different exergies present in the SPT plants, from the heliostat field to the receiver subsystem, has been introduced. The analysis considers the circumferential thermal gradients in the receiver tubes, providing an accurate solution to a problem so highly sensitive to the temperature of the surfaces involved. Prior the exergy study, the thermal resolution of the receiver also takes into account the structural limits of the material selected for the tubes, in terms of pressure and corrosion, in order to minimize the entropy generation through the tube wall by selecting the lower thickness admissible.

With the method showcased, the exergy analysis has been performed for a typical receiver configuration, resulting in an exergy efficiency of 32.5%. The heliostat field exergy destruction, $\xi_{X_{opt}}$, is found to be the most prominent exergy loss, being a 41.41%. However, for a fixed field layout, its value can only be altered with the modification of the aiming strategy, regardless the ambient conditions and receiver design. Such outcome is due to mirrors efficiency because of the spillage losses: the strategies going for a more homogeneous heat

flux distribution on the receiver surface suffer from greater spillage than those showing greater flux peaks. Regarding the receiver, the exergy loss due to the emissions and absorptions in the tubes, ξ_{X_t} , is the greatest (16.84% in this configuration), followed by the ones due to the internal heat transfer convection, fouling resistance and friction of the HTF with the tube walls, $\xi_{X_{D,HTF}}$ (4.35%). Both are highly dependent on the tube walls temperature distributions. As for the heat escaping through the ambient, ξ_{X_0} , its value is quite similar to $\xi_{X_{D,HTF}}$ in this case, a 4.28%. Its dissection shows that it is mainly due to heat coming from the ambient and being reflected back to it (around two thirds), with the heat emitted by the tubes and rear wall resulting less relevant. The effects of the external convection and the influence of the rear wall are considerably lesser than the rest, being 0.69% and 0.21% respectively. The exergy destruction due to the tube wall conduction was minimized by selecting the minimum admissible thickness, resulting in just a 0.17%.

In order to get a better sense of the importance of the different exergy losses present in the balance, several parameters were varied with respect the original case. Although great exergy efficiency divergences were not expected due to the non-modification of the two focal temperatures (the Sun temperature and the HTF one), various conclusions regarding the individual exergy losses sources were reached. It has been seen that with the degradation of the optical properties of the coating, which is an inevitable phenomena happening in this kind of receivers due to the demanding thermal conditions, the exergy efficiency drops over a 1% every 5% of the degradation of the optical properties. Also, the effects of the absorptivity have been proven to be more relevant than the ones of the emissivity, that barely counteracts the former one. The variation of the absorptivity alone dropped the exergy efficiency from the initial 32.05% to around less than a 27% in the worst case studied (20% degradation), while the modification of the emissivity alone resulted in an exergy efficiency of 32.2%, providing an improvement of just a 0.15%. Hence, it is concluded that the efforts when selecting the coating must focus on the absorptivity and not so much on the emissivity and repainting tasks may be needed over time if the coating material, which typically degrades between a 0.25%/year and 0.75%/year, is not stable enough during the plant lifecycle. Regarding the aiming strategy, the peak alternative is the one with the greater exergy efficiency, despite the greater entropy generation through the tube wall, around a 0.45% greater than in the flat case. This is almost compensated with the improvement of ξ_{X_t} for the peak aiming over the flat (around 0.23%), resulting in exergy efficiencies almost

similar when looking just the receiver. Thus, the difference made by the optical efficiency of the heliostat field is determinant to favour the peak configuration since constitutes a lower exergy loss by itself (40.88% instead of 41.41%) while also providing a greater heat flux to the receiver. However, structural limits should be considered when resorting to these highly aggressive alternatives. Moving on, higher levels of DNI result in greater exergy efficiencies, but the effect of the site temperature should not be disregarded, making more attractive locations with moderately high DNI and lower ambient temperatures over those with the higher DNI and higher surroundings temperatures associated. In this case, the exergy efficiency provides answers over the thermal efficiency, since the latter is not affected by the ambient temperature of the location. For a fixed DNI level, an increase of 5 °C in the ambient temperature results in a drop of over a 0.35% in the exergy efficiency, being the divergences more notable when comparing different DNI and surroundings temperature combinations.

Nomenclature

A	surface area (m^2), absorptivity matrix	k	thermal conductivity (W / (mK))
a_1	elbow angle coefficient	L	length of the duct (m)
C	cross section area (m^2)	lc	lifecycle of the plant (years)
C_p	specific heat at constant pressure (J / (kgK))	m	number of axial divisions per flow path
cr	corrosion ratio (m/year)	\dot{m}	mass flow (kg/s)
D	receiver diameter (m)	n	number of circumferential divisions in half the cross section
d	duct diameter (m)	N_{fp}	number of HTF flow paths
E	emission (W), emission matrix	N_p	number of panels in the receiver
E_1	joint efficiency factor coefficient	N_t	number of tubes
F	view factor	p	perimeter (m)
fr	Darcy friction factor	Q	heat power (W)
h	convective heat transfer coefficient (W / (m^2K))	q	heat flux (W/m^2)
K	expansion or contraction resistance coefficient	R	reflectivity matrix, resistance (Km^2/W)
		R_0	elbows curvature radius (m)
		Re	Reynolds number

T	temperature (K)		coefficient ($\text{W}/(\text{m}^2\text{K})$)
th	thickness	X	exergy (W)
TOL	admissible calculation tolerance in the iterative process	z	axial coordinate
U	global heat transfer		

Greek letters

α	absorptivity	ξ	percentage of exergy loss (%)
ΔP	pressure drop (Pa)	ρ	reflectivity, HTF density (kg/m^3)
ΔS	entropy (W/K)	σ	Stefan-Boltzmann constant
ΔT	temperature difference (K)		($\text{W}/(\text{m}^2\text{K})$), tensile (Pa)
Δz	axial divisions height (m)	Φ	view factors matrix
ε	emissivity	ψ	maximum efficiency ratio
η	efficiency (%)		
θ	circumferential coordinate		

Subscripts

0	ambient surface	hel	heliostats
abs	absorbed	in	inlet
adm	admissible	int	internal
amb	ambient	L	losses
C	convection	m	mirrors
con	contraction	min	minimum
corr	corrosion	$n+1$	rear wall surface
D	destruction	net	net
d	duct	opt	optical
deliv	delivered	out	outlet
emi	emitted	press	pressure
exp	expansion	R	radiation
ext	external	rec	recalculated
field	heliostat field	ref	reference
film	HTF region in contact with the tube internal wall	refle	reflected
foul	fouling	S	Sun
g	ground	t	tube
gen	generation	thermal	energy efficiency
		tot	whole receiver

wall tube wall

Abbreviations

CSP	concentrating solar power	LCOE	levelized cost of electricity
DNI	direct normal irradiation (W/m ²)	SPT	solar power tower
ECGM	energy coarse grid model	XCGM	exergy coarse grid model
HTF	heat transfer fluid		

References

- ASME 2013 ASME Boiler and Pressure Vessel Code. American Society of Mechanical Engineers.
- ASSELINEAU, C.A., COVENTRY, J. & PYE, J. 2018 Exergy analysis of the focal-plane flux distribution of solar-thermal concentrators. *Applied Energy* 222, 1023–1032.
- BEJAN, A. 1978 General criterion for rating heat-exchanger performance. *International Journal of Heat and Mass Transfer* 21 (5), 655–658.
- BEJAN, A. 1982 Second-Law Analysis in Heat Transfer and Thermal Design. *Advances in Heat Transfer* 15 (C), 1–58.
- BELLOS, E. & TZIVANIDIS, C. 2017 A detailed exergetic analysis of parabolic trough collectors. *Energy Conversion and Management* 149, 275–292.
- BELLOS, E. & TZIVANIDIS, C. 2019 Alternative designs of parabolic trough solar collectors. *Progress in Energy and Combustion Science* 71, 81–117.
- BERGER, X., BURIOT, D. & GARNIER, F. 1984 About the equivalent radiative temperature for clear skies. *Solar Energy* 32 (6), 725–733.
- CANDAU, Y. 2003 On the exergy of radiation. *Solar Energy* 75 (3), 241–247.
- COCCO, D., PETROLLESE, M. & TOLA, V. 2017 Exergy analysis of concentrating solar systems for heat and power production. *Energy* 130, 192–203.
- CONROY, T., COLLINS, M.N. & GRIMES, R. 2019 A review of steady-state thermal and mechanical modelling on tubular solar receivers. *Renewable and Sustainable Energy Reviews* 119.

EUROPEAN COMMISION 2020 Photovoltaic geographical information system. https://re.jrc.ec.europa.eu/pvg{_}tools/en/tools.html, accessed: 10/06/2020.

FLESCH, J., MAROCCO, L., FRITSCH, A., NIEDERMEIER, K. & WETZEL, T. 2020 Entropy Generation Minimization Analysis of Solar Salt, Sodium, and Lead-Bismuth Eutectic as High Temperature Heat Transfer Fluids. *Journal of Heat Transfer* 142 (4), 1–10.

GNIELINSKI, V.V. 1976 Neue Gleichungen für den Wärme- und Stoffaustausch in turbulent durchströmten Rohren und Kanälen, *Forsch. Ing. Wes.* 41 (1), 8–16 (1975). English Translation: New equations for heat and mass transfer in turbulent pipe and channel flow. *Int. Chem. Eng* 16 (2), 359–368.

GÓMEZ-HERNÁNDEZ, J., GONZÁLEZ-GÓMEZ, P.A., BRIONGOS, J.V. & SANTANA, D. 2018 Influence of the steam generator on the exergetic and exergoeconomic analysis of solar tower plants. *Energy* 145, 313–328.

HERNÁNDEZ-JIMÉNEZ, F., SORIA-VERDUGO, A., ACOSTA-IBORRA, A. & SANTANA, D. 2019 Exergy recovery from solar heated particles to supercritical CO₂. *Applied Thermal Engineering* 146, 469–481.

Ho, C.K., MAHONEY, A.R., AMBROSINI, A., BENCOMO, M., HALL, A. & LAMBERT, T.N. 2012 Characterization of pyromark 2500 for high-temperature solar receivers. *ASME 2012 6th International Conference on Energy Sustainability, ES 2012, Collocated with the ASME 2012 10th International Conference on Fuel Cell Science, Engineering and Technology* 136 (PARTS A AND B), 509–518.

Ho, C.K. & PACHECO, J.E. 2014 Levelized Cost of Coating (LCOC) for selective absorber materials. *Solar Energy* 108, 315–321.

IDEL'CHIK, I.E. 1960 *Handbook of hydraulic resistance*, 3rd edn. USA: Begell House.

KOUTA, A., AL-SULAIMAN, F., ATIF, M. & MARSHAD, S.B. 2016 Entropy, exergy, and cost analyses of solar driven cogeneration systems using supercritical CO₂ Brayton cycles and MEE-TVC desalination system. *Energy Conversion and Management* 115, 253–264.

- KUMAR, A., SHARMA, M., THAKUR, P., THAKUR, V.K., RAHATEKAR, S.S. & KUMAR, R. 2020 A review on exergy analysis of solar parabolic collectors. *Solar Energy* 197, 411–432.
- MCCONOHY, G. & KUIZENGA, A. 2014 Molten nitrate salts at 600 and 680°C: Thermophysical property changes and corrosion of high-temperature nickel alloys. *Solar Energy* 103, 242–252.
- NOVALES, D., ERKOREKA, A., DE LA PEÑA, V. & HERRAZTI, B. 2019 Sensitivity analysis of supercritical CO₂ power cycle energy and exergy efficiencies regarding cycle component efficiencies for concentrating solar power. *Energy Conversion and Management* 182, 430–450.
- ÖZTÜRK, H.H. 2004 Experimental determination of energy and exergy efficiency of the solar parabolic-cooker. *Solar Energy* 77 (1), 67–71.
- PADILLA, R.V., FONTALVO, A., DEMIRKAYA, G., MARTINEZ, A. & QUIROGA, A.G. 2014 Exergy analysis of parabolic trough solar receiver. *Applied Thermal Engineering* 67 (1-2), 579–586.
- PETELA, R. 1964 Exergy of Heat Radiation. *Journal of Heat Transfer* 86 (2), 187–192.
- PETELA, R. 2003 Exergy of undiluted thermal radiation. *Solar Energy* 74 (6), 469–488.
- PETELA, R. 2005 Exergy analysis of the solar cylindrical-parabolic cooker. *Solar Energy* 79 (3), 221–233.
- PYE, J., ZHENG, M., ASSELINEAU, C.-A. & COVENTRY, J. 2014 An exergy analysis of tubular solar-thermal receivers with different working fluids. *International Conference on Concentrating Solar Power and Chemical Energy Systems (SolarPACES 2014)*, Beijing pp. 1–10.
- RODRÍGUEZ-SÁNCHEZ, M.R., SÁNCHEZ-GONZÁLEZ, A., MARUGÁN-CRUZ, C. & SANTANA, D. 2015 Flow patterns of external solar receivers. *Solar Energy* 122, 940–953.
- RODRÍGUEZ-SÁNCHEZ, M.R., SORIA-VERDUGO, A., ALMENDROS-IBÁÑEZ, J. A., ACOSTA-IBORRA, A. & SANTANA, D. 2014 Thermal design guidelines of solar power towers. *Applied Thermal Engineering* 63 (1), 428–438.

- ROMEO, E., ROYO, C. & MONZÓN, A. 2002 Improved explicit equations for estimation of the friction factor in rough and smooth pipes. *Chemical Engineering Journal* 86 (3), 369–374.
- SÁNCHEZ-GONZÁLEZ, A., RODRÍGUEZ-SÁNCHEZ, M.R. & SANTANA, D. 2018 Aiming factor to flatten the flux distribution on cylindrical receivers. *Energy* 153, 113–125.
- SCANNAPIECO, J.F. 1968 Irradiation of thermal control coatings, Final report. *Tech. Rep.* NASA-CR-94684, DOC.-68SD4224. General Electric Co.; Missile And Space Div., Philadelphia, PA, United States.
- SIEBERS, D. & KRAABEL, J. 1984 Estimating convective energy losses from solar central receivers. *Tech. Rep.* SAND-84-8717. Sandia National Laboratories, Albuquerque, NM, and Livermore, CA, United States.
- TIAN, Y. & ZHAO, C.Y. 2013 A review of solar collectors and thermal energy storage in solar thermal applications. *Applied Energy* 104, 538–553.
- WADE, W.R. & SLEMP, W.S. 1962 Measurements of total emittance of several refractory oxides, cermets, and ceramics for temperatures from 600 degrees F to 2,000 degrees F. *Tech. Rep.* NASA-TN-D-998; AD-272614. National Aeronautics and Space Administration (NASA), Langley Field, VA, United States.
- ZAVOICO, A.B. 2001 Solar Power Tower - Design Basis Document. *Tech. Rep.* SAND2001-2100. Sandia National Laboratories, Albuquerque, NM and Livermore, CA, United States.

Calculation of the elastic stresses and deflections in solar central receiver tubes

Contents

3.1	Introduction	70
3.2	Elastic stress calculation in cylindrical tubes	74
3.2.1	Yield criterion	75
3.2.2	Radial and hoop thermal stress	76
3.2.3	Axial stresses	78
3.3	Central receiver with a non-symmetrical temperature distribution	82
3.4	Results and discussion	84
3.4.1	Initial verification: Analytical vs numerical model	85
3.4.2	Guided tube	90
3.5	Conclusions	95
	References	97

Summary

The aim of the design of central solar receivers is to withstand the high non-uniform solar-heat-flux and temperature during the solar-power-plant lifetime. This high non-uniform tube temperature causes high thermal stress, producing creep and fatigue damage. Therefore, it is necessary to obtain an accurate estimation of the tube stresses during the receiver operation. In the same way, to ensure the panel integrity, the frontal and lateral tube deflections must be obtained to avoid excessive panel bowing and warpage, respectively.

The huge number of simulations needed to perform the creep-fatigue analysis precludes the use of high time-consuming CFD-FEM simulations. To resolve this drawback, a reliable, accurate and fast procedure to obtain the tube

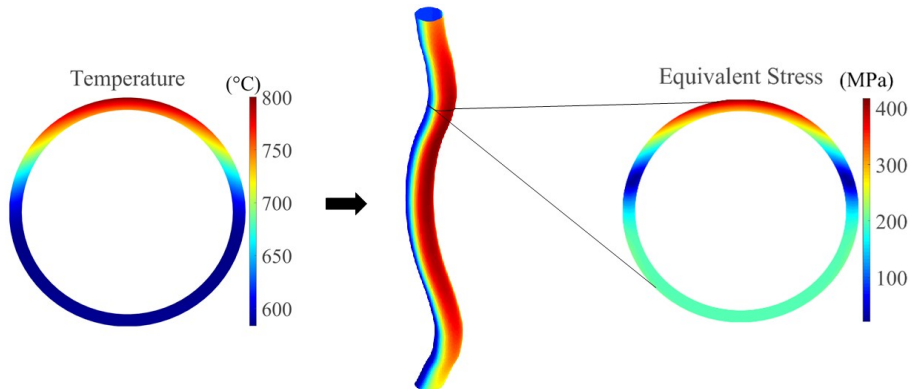


Figure 3.1: Graphical abstract.

stresses, using analytical stress estimation, is proposed. The procedure considers the temperature dependence of the thermo-mechanical properties.

The temperature-dependent hoop stress is estimated using the solution for constant mechanical properties whereas the radial stress is estimated taking constant the Young modulus only. The temperature-dependent axial-bending stress is obtained using the non-homogeneous beam equation subjected to the movement restriction produced by tube clips. When the tube displacement is restricted by tube clips, the equivalent stress difference is less than 2% taking temperature-dependent properties and slightly higher than 10% for constant properties. The proposed stress estimation is enough accurate to perform a reliable fatigue-creep analysis and two order of magnitude faster than the CFD-FEM simulations.

Finally, the tube deflection and displacement, restricted by tube clips, are derived straightforward using the temperature-dependent tube curvature and the beam theory.

3.1 Introduction

Experience gained from solar power tower (SPT) receivers testing and operation has proven that bowing and warpage deformations reduce their receiver life, being the cracks the most critical outcome of these two phenomena. The tubes back to front thermal gradients cause their bowing in such direction, while the lateral thermal gradients do the same in the respective direction; the clips are placed periodically to prevent the bowing of the tubes, but they do

not completely avoid it and the stresses in the tubes increase due to the mechanical restrictions they impose (Montoya *et al.*, 2018). The tubes also suffer from cyclic fatigue, as consequence of the nightly periods of inactivity and the clouds interference in the solar flux incident on the receiver during the daytime operation (Liao *et al.*, 2014). Hence, the important role of the tube temperature makes essential to study the thermal and mechanical behaviour of the tubes in order to improve the receiver design and solve the inconveniences that cause the early receiver failure. This has lead numerous authors to develop a variety of models to analyse it. In that process, they have had to deal with the issue of high computational costs while trying to obtain the most precise approximations of the tube behaviour. Two types of models can be distinguished: the detailed ones, based on CFD and FEM simulations and the simplified models, analytic codes.

In the field of thermal models, the detailed ones are computationally expensive so the simulation of the whole receiver is avoided. Among the vast variety of instances of the application of these models in the SPTs field, Yang *et al.* (2012) studied the heat transfer occurring in a single tube receiver, noticing the importance of the temperature in the tube inner wall to prevent the salts decomposition and the uneven temperature distribution of the tube wall and salt. Fritsch *et al.* (2017) developed a FEM model of a single receiver tube with constant heat transfer coefficients and 1D fluid elements, obtaining a good agreement with a more detailed CFD model. Maytorena & Hinojosa (2019) studied the direct steam generation in a tubular receiver of a SPT plant affected by non-uniform concentrated solar radiation using a CFD model to analyse one tube of the receiver. CFD models have also been used to simulate new receiver geometries, like the design presented by Garbrecht *et al.* (2013), consisting in hexagonal pyramid shaped elements.

Several progresses have been made in the field of simplified thermal models, whose lesser computational costs makes them ideal to simulate the whole receiver. The model developed by Jianfeng *et al.* (2010) considered only a single pipe of an external receiver under unilateral concentrated radiation to study its efficiency. Singer *et al.* (2010) developed an iterative model, *receiver design algorithm* (RDA), that calculates the receiver efficiency matrix, evaluating the losses at the effective radiation temperature considering its variation in the axial coordinate, but neglecting the circumferential ones. Then Xu *et al.* (2011) modified the model by Singer *et al.* (2010) in order to design a molten salt cavity receiver, focusing on the exergy analysis.

In their work, Rodríguez-Sánchez *et al.* (2014a) developed two analytical models that included circumferential divisions of the tubes in addition to the axial ones, allowing a much more precise characterization of the tube temperature distribution. These two models are the *homogeneous wall temperature model* (HTM) and the *homogeneous heat flux model* (HHFM), both named after the initial hypothesis considered in the discretized tube cells. They take into account adjacent tubes but only one tube per panel was considered, assuming that all of the tubes in the same panel receive the same heat flux. This work was later further developed to consider every tube in the receiver Rodríguez-Sánchez *et al.* (2018), resulting in the *fine grid model* (FGM) that has been found to be even more precise than the previous two when it comes to the tube temperature prediction. Since this model takes into account the fact that the incident flux in the tubes is not symmetrical, the FGM allows to study the bending of the tubes not only in the radial direction, allowing to analyse the possible collisions between adjacent tubes.

As for the mechanical studies, there has been a great interest on analysing the thermal stress and deformation problem in cylinders. Gatewood (1941) discussed the thermal stresses and displacements in long hollow cylinders subjected to a bidimensional temperature gradient. Timoshenko & Goodier (1951), starting from the plane strain case, studied the thermal stresses and displacements in unidimensional and bidimensional problems in different geometries. After developing the plane strain results, they presented the results for generalized plane strain (GPS) by changing the boundary conditions. Then Goodier (1957) compiled some of the cases presented in Timoshenko & Goodier (1951). Goodier stated that the variations with temperature of the linear thermal expansion coefficient need to be considered. Noda *et al.* (2003) studied the thermal stresses in beams, including the problem of non-homogeneous properties. For quick thermal stresses estimations, Babcock & Wilcox Company (1984) presented a simplified equation that takes into account the thermal gradients across the cross section and the temperature difference between two sides of the tubes.

That knowledge of the thermal stresses and displacements in hollow cylinders has later been applied in the concentrating solar power (CSP) field to aid the design of the receiver. In these works, different boundary conditions for the tubes have been studied. With an uniform heat flux in a billboard panel, Conroy *et al.* (2018) studied the thermal stresses for different tube diameters and materials as part of a creep-fatigue analysis. The tubes were allowed to expand axially and to bend freely. Intermediate supports influence is not taken into

account. They also analyzed the stresses due to the internal pressure that the tubes withstand, which were considerably low compared to the thermal stresses. Logie *et al.* (2018) considered that the tubes cannot bend freely, studying the case of GPS. Marugán-Cruz *et al.* (2016) studied as well thermal stresses in the plane strain scenario using a numerical model, concluding that the temperature distribution is needed for the whole tube, discarding the 1D models, and finding variations in the stress results depending on the Biot number. Uhlig *et al.* (2018) used a FEM model to analyse the stresses in the inlet panel of a central receiver under the conditions of the cases of the filling process and the solar operation. In the field of parabolic through collectors, Khanna *et al.* (2014) also studied analytically the stresses and bending of the absorber tube supported along its length in different spots, considering two different supporting arrangements. These tubes are place horizontally and are typically longer than the ones in the SPT receiver, but their further work (Khanna & Sharma, 2015) is useful to remark how the number of supports considered affects tube deflection, which they also tested experimentally (Khanna *et al.*, 2016). The importance of considering the periodic supports of the tubes in the STP receiver is presented by Montoya *et al.* (2018). They studied the stresses with a 3D thermo-elastic model, concluding that the mechanical restrictions affect the axial stress component, causing it to be up to three times higher than the one appearing in a non-restricted tube.

With everything presented above, it is seen the need to create an analytical model to study the stresses due to thermal gradients and mechanical constraints in external solar receivers. In the first Section of this Chapter, a simplified analytic method to obtain the elastic thermal stresses and displacements in the receiver tubes is presented, resulting in a low computational cost, considering the thermal gradients, the periodical supports of the tube and temperature dependent properties for the tube material. In Section 3.3, the characteristics of the receiver that will be studied are described. In Section 3.4 the analytical method is verified with the numerical one for a single axial division of a tube under free bending conditions. For the analytical method, the cases of temperature dependant properties and temperature independent properties have been compared. After that, a whole tube of the receiver is studied with the analytical model. The deflection of the tube and the maximum equivalent stress in it are obtained. The chosen boundary conditions that constrain the receiver tubes recreate their real operating conditions: they are allowed to expand axially and they have their bending prevented in certain spots by a series of equally spaced

supports, called clips, placed along their length. These periodical supports reduce the overall bending of the tube but induce mechanical stresses due to the reaction forces that appear in them when the tube is trying to bend in these spots. A real heat flux distribution is considered by using the FluxSPT software presented in (Sánchez-González *et al.*, 2018). The temperature distribution has been obtained using the FGM (Rodríguez-Sánchez *et al.*, 2018), being asymmetrical in the cross section and suffering from variations in z , appearing bowing in both x and y directions. Finally, Section 3.5 discusses the conclusions of this Chapter.

3.2 Elastic stress calculation in cylindrical tubes

An analytical methodology for the calculation of the elastic stresses for a single cylindrical tube, of inner radius a and outer radius b is presented. The tube is under the boundary condition of free thermal axial expansion and its bending is restricted in certain spots along its length by the periodic placement of supports, so-called clips. These clips allow the tube displacement in z and the rotation of the tube cross section in the plane of the support, Figure 3.2.

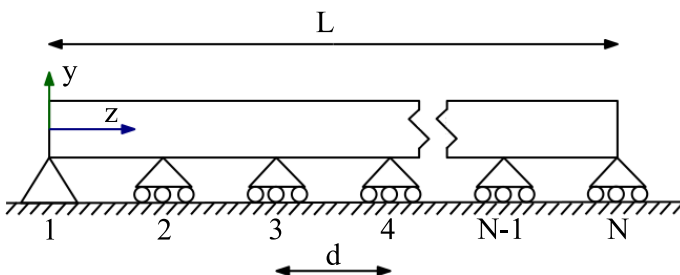


Figure 3.2: Support arrangement and boundary conditions.

The tube studied is discretized in vertical divisions, along the z axis, and every one of these divisions is discretized in radial r and circumferential θ cells, as depicted in Figure 3.3. Since the case of study is a tube, most of the equations presented in this Chapter are expressed in cylindrical coordinates. However, there are equations that are typically written in cartesian coordinates. Given that the tube studied has non-homogeneous properties, two coordinate origins were selected: the one corresponding to the centroid (x, y, z), and the one related to the neutral axis (x^*, y^*, z). The neutral axis is the tube axis along which there are no longitudinal strain, and therefore the length of each vertical

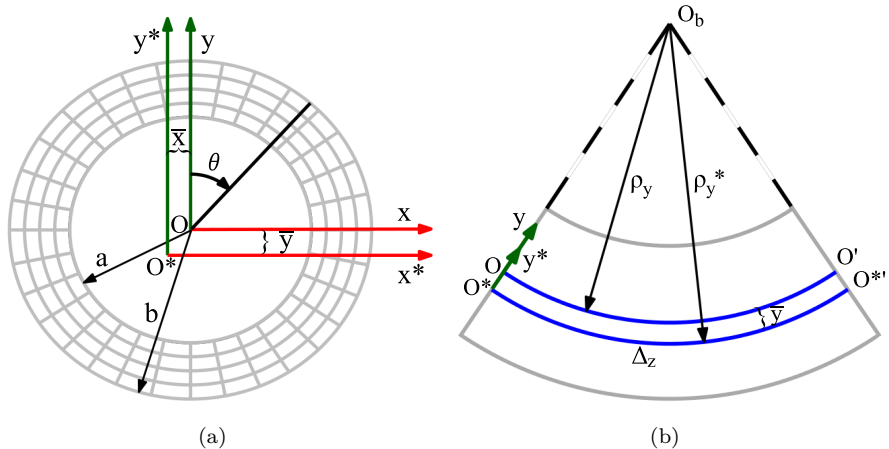


Figure 3.3: (a) Grid of calculation in the cross section and coordinates origins in the centroid (x, y, z) and in the neutral axis (x^*, y^*, z). (b) Deflection of a tube axial division.

division (Δz) remains the same, during bending. It is presented in Figure 3.3(b) delimited by the origins of its coordinate system in two different cross sections: O^* and O'^* . The bending radius of each axial division can be written in terms of the neutral axis, ρ_y^* (and ρ_x^* for the x^* axis), and in terms of the centroid, ρ_y (ρ_x for the x axis).

3.2.1 Yield criterion

Among the criterions to determine the admissible stresses in ductile materials, to prevent failure and serve as an indicator of a good design, the most commonly used are the Von Mises yield criterion (Maximum Distortion Energy Theory) and the Tresca yield criterion (Maximum Shear Stress Theory). The Von Mises or equivalent stress in the tubes, studied in this Chapter, is calculated in cylindrical coordinates as

$$\sigma_{VM} = \sqrt{\frac{(\sigma_r - \sigma_\theta)^2 + (\sigma_\theta - \sigma_z)^2 + (\sigma_z - \sigma_r)^2}{2} + 3\tau_{r,\theta}^2}, \quad (3.1)$$

since $\tau_{r,z}$ and $\tau_{z,\theta}$ are equal to zero due to the assumption of GPS. This null shear stresses calculation is not altered by the addition of supporting clips.

The Tresca criterion, more conservative than the Von Mises one, takes into account only the maximum shear stress. Therefore, it is obtained as

$$\sigma_{Tresca} = \max(|\sigma_1 - \sigma_2|, |\sigma_2 - \sigma_3|, |\sigma_3 - \sigma_1|). \quad (3.2)$$

Thus, in order to guarantee the integrity of the tubes of the receiver by using these criterions, it is necessary to obtain the different stress components that the tubes withstand.

3.2.2 Radial and hoop thermal stress

Due to a steady heat flux, the tube is subjected to a temperature field that depends on the r and θ coordinates but remains constant in the z one for a certain small-sized cell. The temperature profile in the cross section can be split in the temperature variation in r , $T_r(r)$, and the temperature variation in θ , $T_\theta(r, \theta)$:

$$\begin{aligned} T(r, \theta) &= T_r(r) + T_\theta(r, \theta) = \\ &= T_r(r) + \sum_{n=1}^{\infty} [(A_n r^n + B_n/r^n) \cos(n\theta) + (C_n r^n + D_n/r^n) \sin(n\theta)], \end{aligned} \quad (3.3)$$

where $T_r(r)$ is the mean temperature of all the cells at r . Using this and the general expression, in cylindrical coordinates, for the thermal conduction in a cylinder whose thermal conductivity is constant and under a steady state, obtained from the Laplace equation (Necati Özisik, 1993), the temperature profile can be expressed as a harmonic Fourier series for each set of cells in a certain axial division, see Appendix A.

Splitting the temperature distribution in the addition of $T_r(r)$, and $T_\theta(r, \theta)$, the thermal stress problem can be studied as the superposition of both contributions (Goodier, 1957). It is an unidimensional problem while working with T_r and a bidimensional one while doing so with T_θ . Such methodology is also valid if only the inner and outer temperature profiles are known, see Appendix A.

The stresses due to the radial temperature field, T_r , are:

$$\sigma_{T_r,r}(r, \theta) = \frac{E}{1 - \nu} \left[\left(1 - \frac{a^2}{r^2} \right) \frac{1}{2} \bar{\alpha} T - \frac{1}{r^2} \int_a^r \alpha_r T_r r dr \right], \quad (3.4)$$

$$\sigma_{T_r,\theta}(r, \theta) = \frac{E}{1 - \nu} \left[\left(1 + \frac{a^2}{r^2} \right) \frac{1}{2} \bar{\alpha} T + \frac{1}{r^2} \int_a^r \alpha_r T_r r dr - \alpha_r T_r \right]. \quad (3.5)$$

Here, α is the linear thermal expansion coefficient and can be evaluated for the temperature of each cell, E is the Young modulus, and ν is the Poisson coefficient. In the development of such equations, the Young modulus and the Poisson coefficient have been considered constant for a whole set of cells in a

certain axial division in order to obtain the stresses expressions due $T_r(r)$. The subscript r in α indicates that it has been evaluated for the radial temperature field. The mean product of α and the temperature field is:

$$\bar{\alpha}T = \frac{2}{b^2 - a^2} \int_a^b \alpha T r dr. \quad (3.6)$$

On the other hand, the stresses due to the circumferential temperature profile, T_θ , are:

$$\sigma_{T_{\theta},r}(r, \theta) = \frac{r (B_1 \cos \theta + D_1 \sin \theta)}{a^2 + b^2} \frac{\alpha E}{2(1 - \nu)} \left(1 - \frac{a^2}{r^2}\right) \left(1 - \frac{b^2}{r^2}\right), \quad (3.7)$$

$$\sigma_{T_{\theta},\theta}(r, \theta) = \frac{r (B_1 \cos \theta + D_1 \sin \theta)}{a^2 + b^2} \frac{\alpha E}{2(1 - \nu)} \left(3 - \frac{a^2 + b^2}{r^2} - \frac{a^2 b^2}{r^4}\right), \quad (3.8)$$

$$\tau_{r,\theta}(r, \theta) = \frac{r (B_1 \sin \theta - D_1 \cos \theta)}{a^2 + b^2} \frac{\alpha E}{2(1 - \nu)} \left(1 - \frac{a^2}{r^2}\right) \left(1 - \frac{b^2}{r^2}\right). \quad (3.9)$$

The stresses $\sigma_{T_{\theta},r}$, $\sigma_{T_{\theta},\theta}$ and $\tau_{r,\theta}$ are obtained assuming that the mechanical properties are constant. This is not the case in real applications, being more common to work with materials with temperature dependent properties, which will result in a small deviation in the results, depending on how influential such properties variations are. However, these divergences are admissible since these stresses are an order of magnitude lower compared to the axial stress. Also, the complexity of the general expressions of these equations, obtained from the Navier equations for three-dimensional thermoelastic problems (Eslami *et al.*, 2013), makes the previous simplification preferable.

Superimposing the solutions presented above, the radial and hoop thermal stresses, $\sigma_{T,r}$ and $\sigma_{T,\theta}$, are

$$\sigma_{T,r}(r, \theta) = \sigma_{T_{\theta},r} + \sigma_{T_{\theta},\theta}, \quad (3.10)$$

$$\sigma_{T,\theta}(r, \theta) = \sigma_{T_{\theta},\theta} + \sigma_{T_{\theta},\theta}. \quad (3.11)$$

In the absence of mechanical stresses in the radial and circumferential direction, the final stresses are equal to the thermal ones: $\sigma_r = \sigma_{T,r}$, $\sigma_\theta = \sigma_{T,\theta}$.

3.2.3 Axial stresses

For a certain axial division of the tube, the stresses in the z axis can be expressed as

$$\sigma_z(r, \theta) = \sigma_{M,z} + \sigma_{T,z}. \quad (3.12)$$

The first term is related to the mechanical stresses due to the expansion in the axial direction and the bending of the tube, that in this case is understood as a beam. It is directly tied to the boundary conditions of the tube studied.

The second term comes from the application of the Hook law. It is related to the thermal stresses in the tube cross section obtained in Section 3.2.2, as presented by Goodier (1957).

The tube is considered to be non-homogeneous and so the properties of the beam material are temperature dependent. See Appendix B for homogeneous properties. In case of non-homogeneous beams, is more appropriate to work with the neutral axis coordinate system (x^*, y^*, z) , instead of the one placed in the centroid (x, y, z) , see Figure 3.3. Its placement is such that takes into account the weighted section quantities, where E_0 is the reference Young modulus, which can be regarded as the one for the homogeneous properties case:

$$\begin{aligned} A^* &= \int_A \frac{E}{E_0} dA, \\ x^* &= x + \bar{x} = x + \frac{1}{A^*} \int_A \frac{E}{E_0} x dA, \\ y^* &= y + \bar{y} = y + \frac{1}{A^*} \int_A \frac{E}{E_0} y dA. \end{aligned} \quad (3.13)$$

The first term in Eq. 3.12, $\sigma_{M,z}$, is introduced by Noda *et al.* (2003) for a free bending beam so an additional stress in the expression they present must be considered, the one due to the beam supports. The complete term for the instance studied in this Chapter results as

$$\sigma_{M,z}(r, \theta) = -\alpha ET + \frac{E}{E_0} \frac{P_M + P_T}{A^*} + \frac{E}{E_0} \left(y^* \frac{E_0}{\rho_y^*} + x^* \frac{E_0}{\rho_x^*} \right). \quad (3.14)$$

In this case, the properties are evaluated for the temperature of each cell. The term $\sigma_{M,z}$ shown in Eq. 3.14 includes:

- The stresses due to the local thermal expansion.
- The stresses due to mechanical forces, P_M , trying to expand the tube. In this case, they are null due to the free axial expansion hypothesis.
- The stresses due to a virtual axial force P_T that appears if the tube is free to expand in order to counteract the expansion axial force.
- The stresses due to the bending moments in the tube.

Being:

$$P_T = \int_A \alpha ET dA, \quad (3.15)$$

$$\rho_x^* = \frac{I_x^* I_y^* - I_{xy}^{*2}}{M_y^* I_x^* - M_x^* I_{xy}^*} E_0, \quad \frac{I_x^* I_y^* - I_{xy}^{*2}}{M_x^* I_y^* - M_y^* I_{xy}^*} E_0, \quad (3.16)$$

$$I_x^* = \int_A \frac{E}{E_0} y^{*2} dA, \quad I_y^* = \int_A \frac{E}{E_0} x^{*2} dA,$$

$$I_{xy}^* = \int_A \frac{E}{E_0} x^* y^* dA. \quad (3.17)$$

The moment inducing axial stresses via the bending radii, Eq. 3.16 is the addition of a thermal bending moment and a mechanical bending moment,

$$M^* = M_T^* + M_M. \quad (3.18)$$

It presents two components, one in the x^* axis (or x), M_x^* , and one in the y^* axis (or y), M_y^* . Therefore, this moment results in the following stresses:

- The stresses due to a virtual thermal bending moment that considers the free rotation of the ends of the tube, being able to bend freely. It constitutes the moment annulment (MA) when the tube is not restricted. This is valid as long as the Bernoulli-Euler hypothesis is true, fulfilling that the normal plane to the bending radius of the neutral axis before the deformation remains plane and normal to the neutral axis after the deformation.

The thermal bending moment can be calculated as

$$M_{T,x}^* = \int_A \alpha ET y^* dA, \quad M_{T,y}^* = \int_A \alpha ET x^* dA. \quad (3.19)$$

- The stresses produced by the mechanical bending moment due to the reaction forces in the supports of the tube. Notice that the mechanical moment has been written with the centroid coordinate system, since it is independent of the coordinate system chosen due to the fact that it is caused by a force contained in the cross section plane. It allows us to consider the halfway scenarios between:
 - The free thermal bending of the tube, that would result in this part of the term being zero, given the absence of intermediate supports.
 - The tube being kept completely straight, GPS. This part of the term would counteract completely the stresses due to the virtual thermal bending moment.

The mechanical moments due to the supports are obtained as

$$\begin{aligned} M_{M,x}(z) &= \sum_{j=1}^N [R_{j,y}(z - (j-1)d)^+], \\ M_{M,y}(z) &= \sum_{j=1}^N [R_{j,x}(z - (j-1)d)^+]. \end{aligned} \quad (3.20)$$

Here + indicates that only the positive values are considered, being the parenthesis result substituted by zero in the rest of the cases. There are N reaction forces R_j , equal to the number of supports, including the ones placed at both ends. These forces, just as the mechanical moments, are independent from the coordinate system chosen since the z coordinate at which the reactions occur is common to both the centroid system and the neutral axis system.

The reaction forces R_j can be obtained knowing that the displacement at the supports, which are placed spaced a distance d from each other, is null. The equation governing the displacement is calculated as

$$\frac{d^2\delta(z)}{dz^2} = -\frac{1}{\rho(z)}. \quad (3.21)$$

Solving such differential equation, the tube displacement is obtained (Eq. 3.22), which is zero at the supporting points. Each axial division of the tube is subject to thermal and mechanical moments that differ from one to another, so the number of different bending radii (m) in the tube is equal to the number

of axial divisions considered to study it. Like the equation for the mechanical moments, the expression for deformation will present two forms, one for each axis of the cross section: δ_x and δ_y .

$$\begin{aligned} \delta(z) = & -\frac{z^2}{2\rho_{T,1}} - \sum_{i=2}^m \frac{(z - (i-1)\Delta z)^{2,+}}{2} \left(\frac{1}{\rho_{T,i}} - \frac{1}{\rho_{T,i-1}} \right) \\ & - \sum_{j=1}^N \frac{R_j(z - (j-1)d)^{3,+}}{6} + K_1 z + K_2. \end{aligned} \quad (3.22)$$

Here ρ_T is the thermal bending radius depending only on the thermal bending moments, not the mechanical ones, see Eqs. 3.23. To represent consistently the displacement in the whole beam, the thermal bending radius has been referred to the centroid (x, y) of the cross section instead of the neutral axis (x^*, y^*) and is calculated as

$$\begin{aligned} \rho_{T,x} = \rho_{T,x}^* - \bar{x} &= \frac{(I_y^* I_x^* - I_{xy}^{*2}) E_0}{I_x^* M_{T,y}^* - I_{xy}^* M_{T,x}^*} - \frac{1}{A^*} \int_A \frac{E}{E_0} x \, dA, \\ \rho_{T,y} = \rho_{T,y}^* - \bar{y} &= \frac{(I_y^* I_x^* - I_{xy}^{*2}) E_0}{I_y^* M_{T,x}^* - I_{xy}^* M_{T,y}^*} - \frac{1}{A^*} \int_A \frac{E}{E_0} y \, dA. \end{aligned} \quad (3.23)$$

Note that the thermal bending radii ρ_T corresponds to the bending radii ρ in the case of MA, as studied by Conroy *et al.* (2018). In the case of the GPS, with the tube bending prevented, the bending radius is infinite since it remains straight, (Logie *et al.*, 2018).

The constants K_1 and K_2 in Eq. 3.22 are calculated by adding two more equations to the system. These two equations are the ones for the null sum of reaction forces and null sum of mechanical moments. Additionally, once the reactions R_j and the constants K_1 and K_2 are known, the displacement along the whole tube can be obtained,

$$\delta(z) = 0 \text{ in } z = 0, d, 2d, \dots, (N-1)d,$$

$$\begin{aligned} \sum_{j=1}^N R_j &= 0, \\ \sum_{j=1}^N R_j(N-1)d &= 0. \end{aligned} \quad (3.24)$$

On the other hand, the second part of Eq. 3.12, the stresses in the tube cross section are

$$\sigma_{T,z}(r, \theta) = \nu(\sigma_r + \sigma_\theta). \quad (3.25)$$

The stresses in the r and θ coordinates were obtained separately in the previous section, Eq. 3.10 and Eq. 3.11. With all of this, the axial stresses considering variable properties of the tube can be expressed as

$$\sigma_z(r, \theta) = \nu(\sigma_r + \sigma_\theta) - \alpha ET + \frac{E}{E_0} \frac{P_T}{A^*} + \frac{E}{E_0} \left(y^* \frac{E_0}{\rho_y^*} + x^* \frac{E_0}{\rho_x^*} \right). \quad (3.26)$$

3.3 Central receiver with a non-symmetrical temperature distribution

The receiver analysed (Figure 3.4), with a nominal thermal power of 120 MWt, is a cylindrical external tubular receiver of 10 m high and 8.4 m of diameter. The cylindrical frame is surrounded by 18 vertical panels, each one of them being constituted by 62 tubes that are connected by an inlet and outlet collector. The tube external diameter is 2.21 cm, with a thickness of 1.2 mm. The separation between tubes belonging to the same panel is the 8% of their external diameter. This distance falls inside the range of typical values, between 1 to 2.5 mm according to Litwin (2002). They are manufactured in Inconel 625, whose properties are obtained from the ASME BPVC Code (ASME, 2010) and they are covered with a black Pyromark coating, to increase the insolation absorptance (Persky & Szczesniak, 2008). The tubes are guided by a series of clips, placed periodically along its whole length in order to avoid an excessive bending and warpage. The separation between clips is 2 m, making it a total of 6 supports in each tube.

The heat transfer fluid (HTF) used in this receiver is solar salt, with an inlet temperature of 290°C and an outlet temperature of 565°C. The properties of the HTF have been calculated with the equations presented by Zavoico (2001). The mass flow rate of the solar salt is a fixed value since the receiver thermal power and inlet and outlet temperatures for the salt have been restricted. The solar salt is divided into two flow paths, one East-oriented and the other West-oriented. In both paths the salt changes its flow direction alternatively from panel to panel (the red panels in Figure 3.4 represent the upwards flow and the

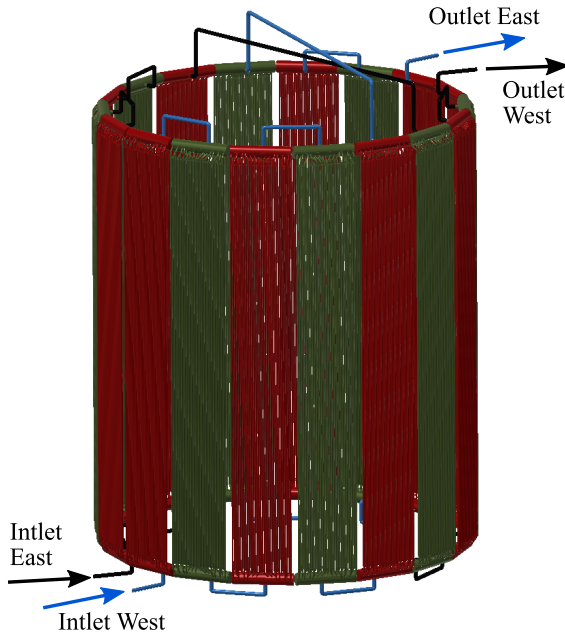


Figure 3.4: Schematic of the receiver studied.

green ones the downwards flow), with a cross between paths at the sixth panel. The solar noon of the Spring Equinox has been chosen as the design point.

The operating conditions in a SPT plant imply that the tubes are subject to a non-symmetrical temperature field with respect the y axis. This is due to the fact that the heat flux being reflected from the heliostats field to the receiver tubes is not uniform on the surface of any of them and will cause them to bend not only in the y axis direction but also in the x , which may lead to undesired contact between adjacent tubes of a panel. The temperature profile asymmetry is greater in the first and last tubes from each panel. This is especially significant when studying the inlet vertical division of the last tube or the outlet division from the first tube of a panel. Such temperature asymmetry for those axial cells is not only due to the non-symmetrical heat flux received but also because the HTF flows in the opposite direction in adjacent panels, as depicted in Figure 3.5. The HTF goes through panel a, then through panel b. When referring to the last (62a) and initial (1b) tubes of two adjacent panels, on one side they find a tube from the same panel (61a for tube 62a or 2b for tube 1b), with the HTF flowing in the same direction and with a temperature evolution very similar. However, on the other side they find a tube from another

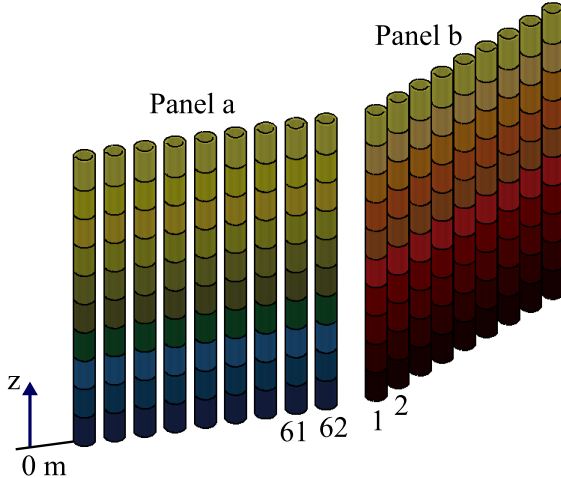


Figure 3.5: Schematic temperature profile evolution of the HTF. The HTF is heated as it flows through the panels tubes, from panel a to panel b.

panel with the HTF flowing in the opposite direction (1b and 62a) and at a very different temperature.

3.4 Results and discussion

The results of the analytical method and the numerical simulations are compared for a non-uniform heat flux over the receiver design that was presented in Section 3.3. The case of free bending is studied in just one axial division in order to verify the behaviour of the analytical model during operation. Then, once the correct performance of analytical method has been proven in that scenario, the influence in the stresses of the support clips guiding the tubes is studied, as well as the bending of the tube.

The tube selected in both cases is the final one of the first panel, facing North, belonging to the Eastern or Western flow paths indistinctly, since the design point selected presents N-S symmetry. This panel is chosen due to the fact that the two Northern panels are the ones presenting the most asymmetrical heat flux with respect the y axis for the design point of this study. As stated in Section 3.3, among the tubes of a same panel, the initial and final are the ones suffering for a greater temperature asymmetry. Since the first tube of this particular panel finds the tube belonging to the adjacent panel at the same thermal conditions (N-S symmetry), the last tube of the panel has been

preferred.

The non-symmetrical heat flux scenario is studied for a receiver similar to the Gemasolar one, using the thermal FGM developed by Rodríguez-Sánchez *et al.* (2018). This allows us to obtain the different stresses and displacements that such heat flux causes in the receiver tubes. Evolving from the *coarse grid model* (CGM) presented in (Rodríguez-Sánchez *et al.*, 2014b)—that included vertical and circumferential divisions of the tubes but only takes into account one representative tube per panel—, Rodríguez-Sánchez *et al.* (2018) developed a *fine grid model* (FGM) including all of the tubes in the receiver. The initial data for the model are the geometry of the receiver, the ambient conditions, the incident radiation in each cell, calculated with FluxSPT, and the mass flow rate and inlet temperature of the salts. An initial estimation for the wall temperature of the tube is required. Calculating the radiation losses, the external and internal convection losses and the fouling resistance, the mean temperature of the fluid in each axial division of the tube can be obtained. The outlet salts temperature must be checked since the limit is set at 565°C. The wall temperature is recalculated and this process is repeated until the salts leave the receiver at the desired temperature.

3.4.1 Initial verification: Analytical vs numerical model

In order to compare the results of the analytical and numerical methods, a single tube under free bending conditions (with the stress term of MA) is initially analysed. In this case, since the effect of the clips is not considered, only one axial division of 0.5 m is selected, Figure 3.6, instead of the whole tube. This is so for simplification reasons, necessary when using the numerical method.

The Abaqus model was built with 8-node linear solid elements. The calculation was carried out by means of a static analysis using Abaqus/standard. Only thermal loads were applied introducing the temperature field obtained from the FGM to Abaqus. The default boundary conditions were used since the tube was allowed to freely expand. A mesh sensitivity analysis was conducted for a 2D tube case varying the number of elements through the tube thickness from 4 to 24 and keeping the aspect ratio equal to 1. Based on this analysis the mesh size was set to 12 elements through tube thickness, which obtained a stress variation lower than 1% compared to the finest mesh size.

When deciding what vertical division to study, two possibilities were presented: the one with the greater asymmetry, providing bending moments in both x and y axis, or the one with the greater temperature gradient, so the

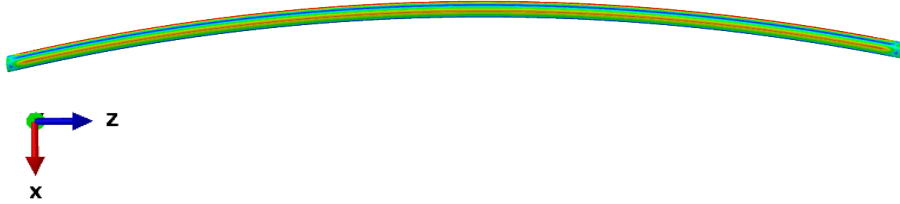


Figure 3.6: Axial division of the receiver tube under free bending conditions.

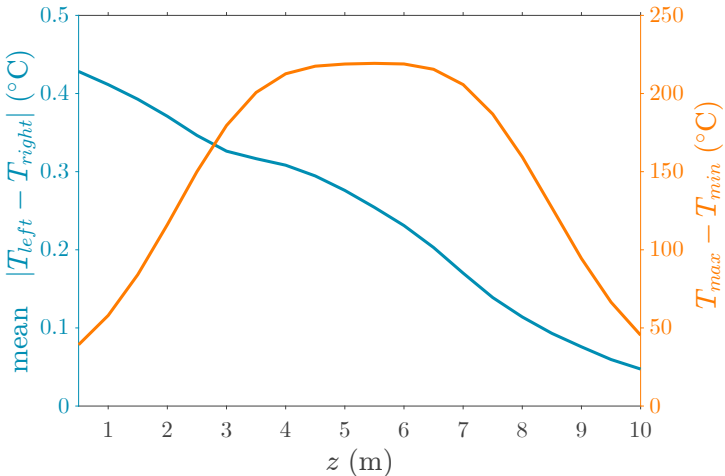


Figure 3.7: Average temperature difference between the right and left halves of the tube cross section along the tube length, representing the asymmetry (blue solid line). Maximum temperature gradient in the cross section along the tube length (orange solid line).

maximum stresses are studied, Figure 3.7. Since this is a verification of the stresses and the goal is not yet to study the bending of the tube in both x and y directions, the section presenting the greater temperature gradient, placed at the middle length of the tube (Figure 3.7), is selected as the representative case.

Using the outer and inner temperature distribution obtained from the thermal model, the whole temperature profile in the selected z section of such tube is calculated (Figure 3.8). It is obtained both for the analytical expressions and FEM simulations considering that the thermal conductivity of the tube differs among cells of a different θ coordinate but is constant in the radial cells, $k = k(\theta)$. This allows us to use the stress equations developed in Section 3.2 under the assumption of constant thermal conductivity, because the heat flux,

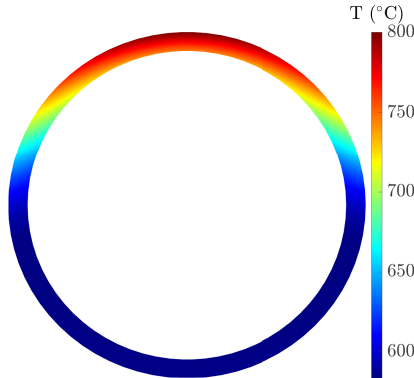


Figure 3.8: Cross sectional temperature distribution.

modifying the temperature field, is considered to have only in the radial component at a certain θ coordinate.

For the temperature distribution of Figure 3.8, the different stresses have been calculated with the analytical and numerical method. Using the analytical method, these stresses have been obtained for temperature dependent (Case A) properties of the tubes material according to ASME (2010) with the considerations regarding certain properties depending on the stress component presented in Section 3.2 and using Eqs. 3.9 - 3.12. The temperature independent properties scenario (Case B) has also been studied, using the Eqs. in Appendix B, evaluating the material properties in the whole cross section at its mean temperature. In this case the temperature distribution differs slightly from the one presented in Figure 3.8, a maximum of $5.3\text{ }^{\circ}\text{C}$, since the thermal conductivity is considered constant in the whole cross section. On the other hand, the numerical results have been calculated using temperature dependent properties.

The analytical results for both scenarios are compared with the numerical results by depicting the difference between the numerical results (FEM) and the analytical ones (subscripts v for variable properties and c for constant properties) over the maximum stress in each case obtained with the numerical method. These results are depicted in Figures from 3.9 to 3.12. The maximum stress in each case are: 2.37 MPa for σ_r , 78.74 MPa for σ_{θ} , 182.82 MPa for σ_z and 165.64 MPa for σ_{VM} .

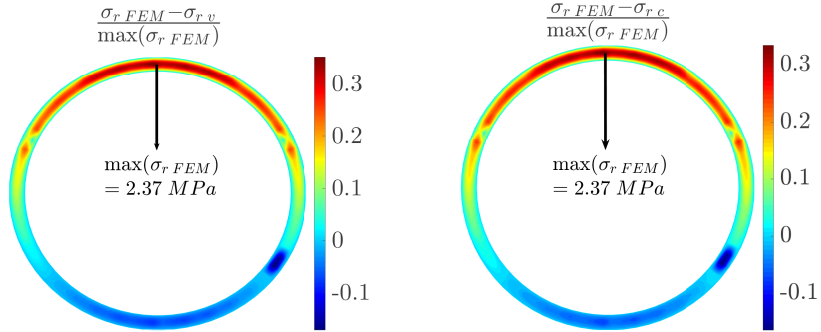


Figure 3.9: σ_r stress for variable properties (left panel) and constant properties (right panel).

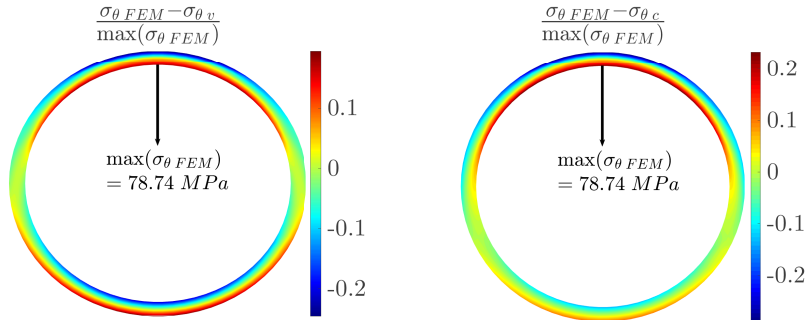


Figure 3.10: σ_θ stress for variable properties (left panel) and constant properties (right panel).

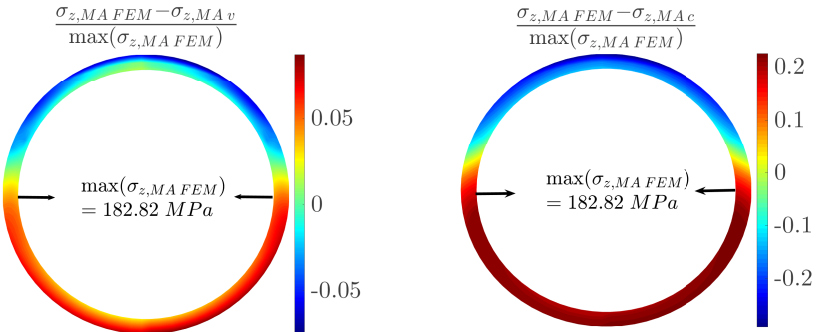


Figure 3.11: $\sigma_{z,MA}$ stress for variable properties (left panel) and constant properties (right panel).

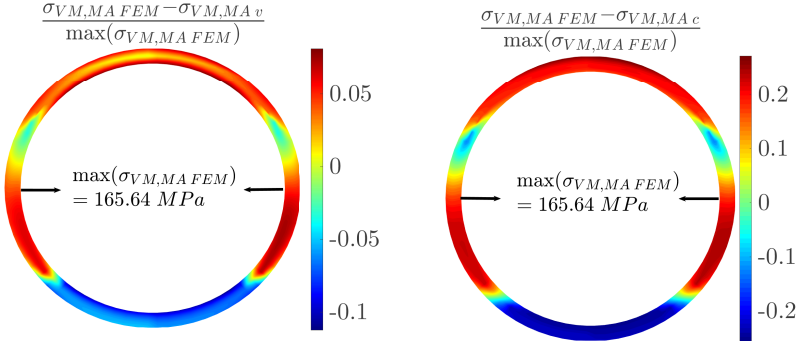


Figure 3.12: $\sigma_{VM,MA}$ stress for variable properties (left panel) and constant properties (right panel).

It can be seen that the analytical method using variable properties, Case A, allows a precise calculation of the tube axial and equivalent stresses, since the results barely differ from the ones obtained with the numerical method. However, the simplification of using constant properties in the analytical model, Case B, should be discarded given that for the most critical stress for the tube endurance (σ_z and σ_{VM}) the deviation is four times higher than the one resulting of taking into account temperature dependant properties: the difference over the maximum stress is just above a 5% with temperature dependent properties and over a 20% when they are temperature independent. Such high difference is undesirable especially when obtaining the rupture time to estimate the receiver lifespan, since it depends on the logarithmic stress as presented by Eno *et al.* (2008).

The small deviations in Case A are due to the fact that the expressions for the stress in the cross section, σ_r , σ_θ and τ , consider most of the properties involved as constant, with just the exception of the thermal expansion coefficient and thermal conductivity in the stress due to the radial temperature profile, $\sigma_{T,r,r}$ and $\sigma_{T,r,\theta}$, likewise was presented in Section 3.2.2. However, the axial stress $\sigma_{M,z}$ does indeed take into account the temperature dependence of the mechanical and thermal properties of the material, as developed in Section 3.2.3. Given the accuracy of the axial stress obtained with temperature dependent properties, the Von Mises stress is not affected by the errors in the cross section stress since the axial component is the most prominent.

Besides the accuracy obtained with the analytical method with variable properties, the computational cost is considerably less than in the FEM simu-

lations: 5.5 seconds against to 1800 seconds. The analytical simulations were performed with a standard PC of 8 GB of RAM and Intel® Core™ i7-7700 CPU @ 3.6 GHz 3.6 GHz processor, while the numerical ones were performed using a workstation of 128 GB @ 2666 GHz of RAM and Intel® Xeon® Silver 4114 CPU 2.2 GHz 2.2 GHz processor.

Therefore, when considering the variable properties proposed in this Chapter, the analytical model is a fast and reliable alternative to study the stress in the receiver, which would simplify a further creep-fatigue analysis and allow a more precise prediction of the receiver lifespan.

3.4.2 Guided tube

Once the accuracy of the analytical expressions has been proven, the whole tube selected in Section 3.4 can be studied using the analytical method. This will save us a considerable time with respect to the numerical simulations for the whole tube. It also allows us to obtain the stresses and displacements accurately, as checked in the previous Section.

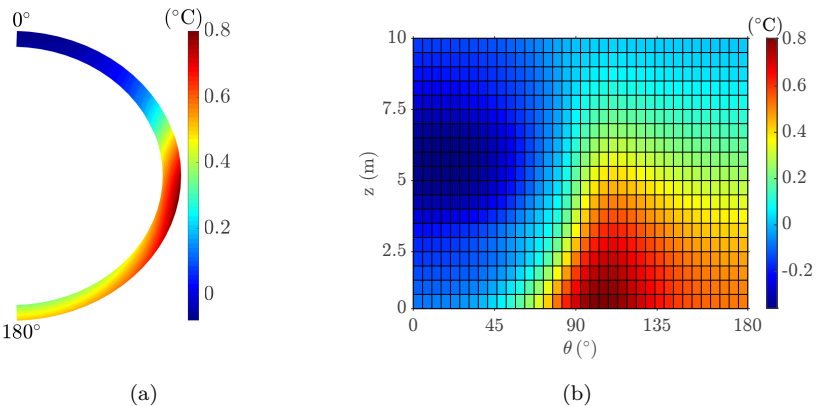


Figure 3.13: (a) Temperature difference between the right and left halves of the first axial division cross section and (b) Temperature difference between the right and left halves of the tube outer wall.

The tube is now considered to be guided with the clip supports, emulating the ones in real life operating receivers of SPTs. The number of clips selected is 6. The receiver is subject to the non-symmetrical temperatures field discussed in Sections 3.3 and 3.4, so bending in both cross section axis is expected for the tube studied. This asymmetry is greater at tube inlet, as established in

Section 3.3. The temperature difference between the right half of the tubes cross section (from 0° to 180° , with the sun at 0°) and the left half is illustrated in Figure 3.13(a) for the first axial division. The decrease of such asymmetry with the z coordinate can be seen in Figure 3.13(b), that depicts the temperature difference between the right half of the tube outer wall and the left one, for the tubes whole length.

However, the temperature field asymmetry and the temperature dependent properties considered for the material do not result in a remarkable shift of the neutral axis respect to the centroid axis. The distances between axes of both coordinate systems are: $\bar{x} = -0.54 \cdot 10^{-19}$ m and $\bar{y} = 0.31 \cdot 10^{-18}$ m. Hence, in this case, the neutral axis coincides with the centroid axis.

Tube displacement

The displacements in axis x and y are depicted in Figure 3.14 for both constant and variable properties of the tube material. Notice that the use of constant properties of the tube translates in an underestimation of the bending which should be avoided, specially when trying to determine if a collision between adjacent tubes can occur studying δ_x , and therefore warpage.

For the deviation in axis y , δ_y , the inclusion of clips dramatically reduces the bending, going from 1.5 m when the tube is only fixed at its ends to 2.71 mm in the case of clips every 2 m (Figure 3.14(a)). This diminishing is especially relevant to avoid undesirable great deformations of the tubes.

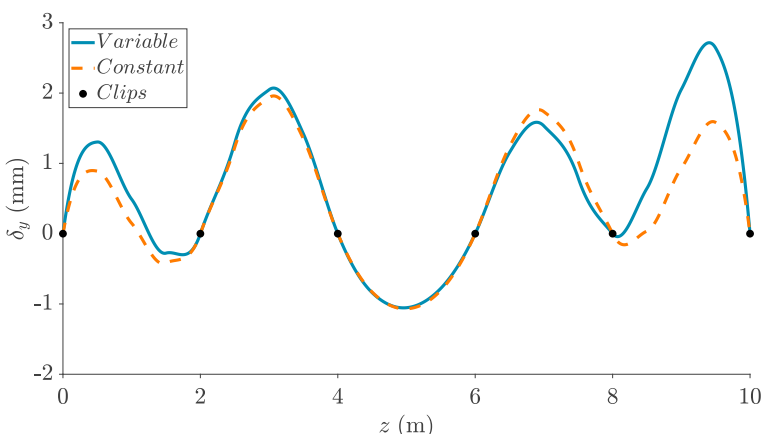


Figure 3.14: (a) Tube bending in the y axis.

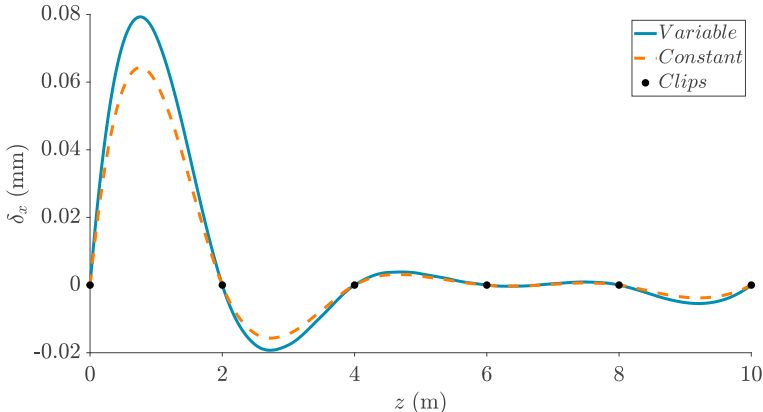


Figure 3.14: (b) Tube bending in the x axis (cont.).

Regarding the deflection in axis x , as stated in Section 3.3, the distance between adjacent tubes in a panel is 1.8 mm. The maximum this tube bends towards its neighbour in the same panel is 0.02 mm (Figure 3.14(b)). As for the contact with tube from the next panel, the tube studied bends towards it a maximum of 0.08 mm in the lower part of its length, so contact does not occur on the right side of the tube cross section either. Therefore, and since the tube with the maximum asymmetry is the one studied, it can be concluded that with this configuration of clips and this aiming strategy there is no contact between tubes for the heat flux distribution coming from the heliostats studied.

Maximum equivalent stress

Following the two main criteria to determine the equivalent stress in ductile materials, Von Mises and Tresca, the maximum ones for each axial division are presented in this section.

The maximum Von Mises equivalent stress has been calculated for the whole tube, both using variable properties and constant properties, Figure 3.15. It can be seen that the maximum stress is obtained with an undesirable underestimation in the case of constant properties, following the tendency present in the calculation of the displacements of the tube. The maximum stresses appear at the tube middle length, where the thermal gradients are greater, as depicted earlier, and correspond to the side of the tube facing the heliostats field. The addition of the mechanical constraints of the clips increases the Von Mises equivalent stress from the MA case, at which the tube bends freely, being

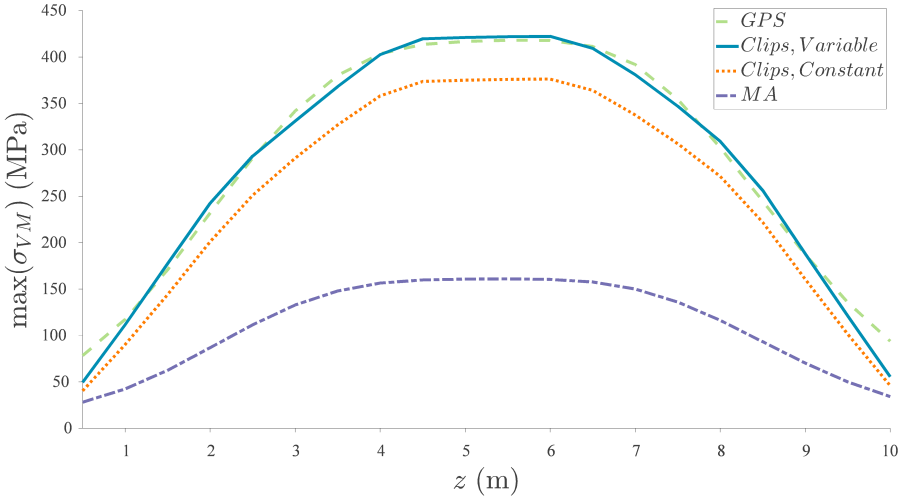


Figure 3.15: Maximum Von Mises stress for the tube with clips, considering variable and constant properties. Maximum von Mises stress in the case of GPS and MA.

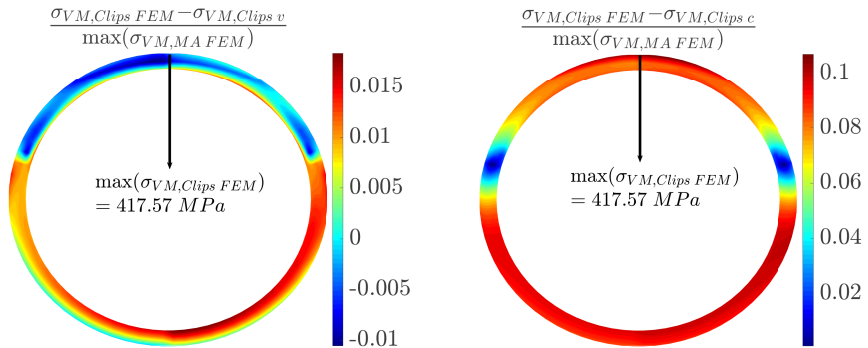


Figure 3.16: $\sigma_{VM,clips}$ stress for variable properties (left panel) and constant properties (right panel).

the extreme scenario the GPS one, where the tube is kept completely straight with an infinite number of clips. For the distribution of clips considered, the maximum Von Mises stress resembles to the GPS one, being lower at some points but higher in others due to the high reaction forces appearing in the support spots. This close resemblance to the case of the tube being kept completely straight matches the displacements presented in Section 3.4.2, which are small compared to the length of the tube. As it can be seen in Eqs. 3.9, 3.10 and 3.11, τ , σ_r and σ_θ do not vary with the different boundary conditions scenarios (GPS, MA and clips). However, the inclusion of the clips increases

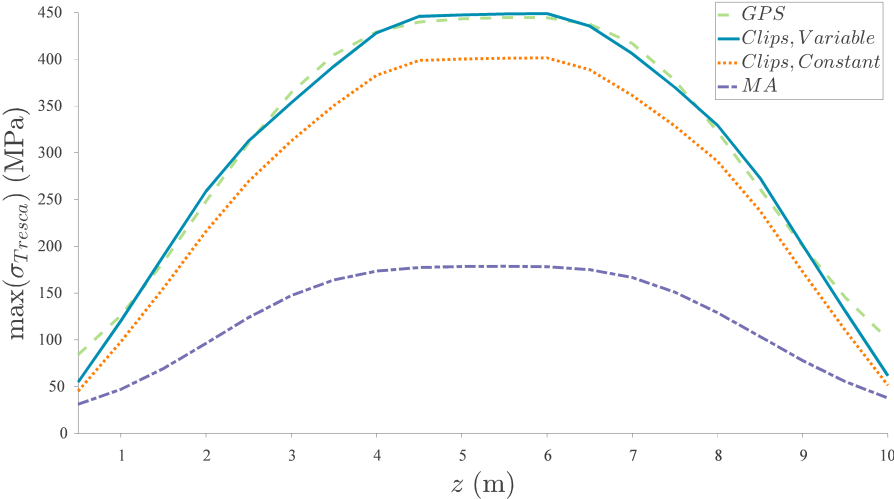


Figure 3.17: Maximum Tresca stress for the tube with clips, considering variable and constant properties. Maximum Tresca stress in the case of GPS and MA.

the axial stress, Eq. 3.14, which is the main responsible for the value of the Von Mises stress, given its entity in comparison to the cross section stress. Since the increment of the axial stress is due to the reaction forces introduced by the supports, such calculation can be expected to be the same in the FEM simulations and in the analytical ones. Therefore, the overall difference between the results of the numerical and analytical simulations is considerably less in the case of the tube with clips, Figure 3.16, than what it was for the free bending tube. The maximum difference is less than a 2% with respect the maximum stress in the case of temperature dependent properties and just over a 10% for the temperature independent scenario. Also, in comparison to the MA case, the location of the maximum Von Mises stress shifts from the inner lateral face of the tube to the outer front (facing the heliostats), while the maximum axial stress shifts from the inner lateral face to the inner rear side (facing the receiver structure).

To obtain the Tresca equivalent stress, the stresses σ_r , σ_θ and σ_z have been used since the shear stress $\tau_{r,\theta}$ is at least one order of magnitude lower than the normal stresses. With a stress tensor of such characteristics, the principal stresses σ_1 , σ_2 and σ_3 in Eq. 3.2, are virtually equivalent to the normal stresses in the cross section, σ_r , σ_θ and σ_z . For the Tresca equivalent stress, Figure 3.17, the difference between the case of dependent and independent properties is also noticeable. As expected, it is a more restrictive criterion than the Von Mises

one. The tendencies in all the cases studied for the Tresca equivalent stress are the same that the ones obtained for the Von Mises stress though, presenting the maximum values at the centre of the tube.

The underestimation of the equivalent stress resulting from considering temperature independent properties of the material would induce great receiver lifetime overestimation, which may lead to an early unexpected failure.

3.5 Conclusions

An analytical method to study the thermal elastic stresses and the bending of the tubes of an external tubular receiver of SPT plants has been presented. With these analytical equations the stress and displacement calculations can be performed under different assumptions: from the free bending case (MA) to the GPS. The interest of these analytical expressions lies in the consideration of temperature dependant properties and the inclusion of the clips without needing a high computational time.

The analytical model proposed in this Chapter constitutes a fast and accurate alternative to numerical models, which are more complex and time-consuming. The comparison for the moment annulment case showed that the hoop, radial and axial stress difference with respect the numerical results, using the proposed estimation, is around 10%, 30%, 5%, respectively when considering temperature dependent properties. The high difference in the cross section stress does not affect greatly the equivalent stress since the highest component is the axial one, which presents the smallest difference. The difference for the Von Mises equivalent stress is just above a 5%. As a consequence of this, a more complete creep-fatigue analysis can be easily undertaken. On the other hand, the simplification of temperature independent properties in the analytical model presents severe deviations, therefore its use is ill-advised, at least for the case analysed.

The boundary conditions for SPTs of external tubular receivers is the intermediate between the free bending and the GPS, where the tube is guided with a series of supports periodically placed along its length, called clips. These supports prevent the displacement in the x and y coordinates, but allow the axial displacement. Therefore, the clip supports reduce greatly the tube deflection, preventing the collision with adjacent tubes and their permanent deformation. Again, taking into account variable properties is crucial in order to not underestimate these displacements in comparison to keeping the properties as tem-

perature independent. The maximum Von Mises stresses with clips gravitates towards the values obtained for the GPS case. In this scenario, the maximum Von Mises stress still differs greatly when using constant properties, resulting in lower values along the whole tube. However, there is an improvement, from a 20% of difference in the MA case to a 10% in the clips case. The difference with respect to the numerical method is also reduced using variable properties, with the difference being lower than a 2%, in comparison to the MA results since the stress due to the clips are coincident in the numerical and analytical simulations. Such small deviation with the analytical method and temperature dependent properties makes it suitable to study the stress in external tubular receivers. The differences observed for the Von Mises stress between when using temperature dependent and independent properties are also present in the Tresca equivalent stress, a more conservative criterion than the Von Mises one. Since the creep and fatigue analysis depend on these equivalent elastic stresses, the use of constant properties is discouraged as it would lead to an overestimation of the receiver lifespan.

Nomenclature

A	tube cross section area (m^2)	N_p	number of panels in the receiver
a	tube inner radius (m)	N_t	number of tubes in a panel
b	tube outer radius (m)	O	coordinate system origin
D	receiver diameter (m)	P	force (N)
d	clips separation (m)	R	reaction forces on the supports (N)
E	Young modulus (GPa)	r	radial coordinate (m)
H	receiver height (m)	T	temperature (K)
I	tube inertia moment (m^4)	\bar{T}	mean temperature (K)
L	tube length (m)	th	tube thickness (m)
M	bending moment (Nm)	x, y, z	cartesian coordinates
m	tube axial divisions		
N	number of supports		

Greek letters

α	linear thermal expansion coefficient (1/K)	Δz	axial cell lenght (m)
		δ	tube displacement

θ	circumferential coordinate ($^{\circ}$)	σ	normal stress (MPa)
ν	Poisson ratio	τ	shear stress (MPa)
ρ	bending radius (m)		

Subscripts

0	reference value	r	radial component
c	analytical results with constant properties	T	thermal component, temperature
e	external surface	v	analytical results with variable properties
FEM	numerical model results	VM	Von Mises
i	inner surface	x, y	cross section components
M	mechanical component	z	axial component
MA	free bending results	θ	circumferential component
max	maximum		
min	minimum		

Superindexes

+	only positive values are considered	*	non-homogeneous properties
---	-------------------------------------	---	----------------------------

Abbreviations

CFD	computational fluid dynamics	HTF	heat transfer fluid
CGM	coarse grid model	HTM	homogeneous wall temperature model
CSP	concentrating solar power	MA	bending moment annulment
FEM	finite element method	PPA	power purchase agreements
FGM	fine grid model	RDA	receiver design algorithm
GPS	generalized plane strain	SPT	solar power tower
HHFM	homogeneous heat flux model		

References

ASME 2010 Asme boiler and Pressure Vessel Code, Section II part D. american society of mechanical engineers.

BABCOCK & WILCOX COMPANY 1984 Molten Salt Receiver Subsystem Research Experiment Phase 1 -Final Report, Volume 1- Technical. *Tech. Rep.* SAND82-8178. Barberton, OH, United States.

CONROY, T., COLLINS, M.N., FISHER, J. & GRIMES, R. 2018 Levelized cost of electricity evaluation of liquid sodium receiver designs through a thermal performance, mechanical reliability, and pressure drop analysis. *Solar Energy* 166, 472–485.

ENO, D.R., YOUNG, G.A. & SHAM, T.-L. 2008 A Unified View of Engineering Creep Parameters. In *ASME Pressure Vessels and Piping Division Conference (PVP2008), Chicago, IL, United States, July 27-31*, pp. 777–792. Chicago: ASME.

ESLAMI, M.R., HETNARSKI, R.B., IGNACZAK, J., NODA, N., SUMI, N. & TANIGAWA, Y. 2013 *Theory of Elasticity and Thermal Stresses*, 1st edn., *Solid Mechanics and Its Applications*, vol. 197. Dordrecht: Springer.

FRITSCH, A., UHLIG, R., MAROCCO, L., FRANTZ, C., FLESCH, R. & HOFF-SCHMIDT, B. 2017 A comparison between transient CFD and FEM simulations of solar central receiver tubes using molten salt and liquid metals. *Solar Energy* 155, 259–266.

GARBRECHT, O., AL-SIBAI, F., KNEER, R. & WIEGHARDT, K. 2013 CFD-simulation of a new receiver design for a molten salt solar power tower. *Solar Energy* 90, 94–106.

GATEWOOD, B.E. 1941 XXIII. Thermal stresses in long cylindrical bodies. *The London, Edinburgh, and Dublin Philosophical Magazine and Journal of Science* 32 (213), 282–301.

GOODIER, J.N. 1957 Thermal Stress and Deformation. *Journal of Applied Mechanics* 24, 467–474.

JIANFENG, L., JING, D. & JIANPING, Y. 2010 Heat transfer performance of an external receiver pipe under unilateral concentrated solar radiation. *Solar Energy* 84 (11), 1879–1887.

KHANNA, S., KEDARE, S.B. & SINGH, S. 2014 Deflection and stresses in absorber tube of solar parabolic trough due to circumferential and axial flux variations on absorber tube supported at multiple points. *Solar Energy* 99, 134–151.

- KHANNA, S. & SHARMA, V. 2015 Effect of number of supports on the bending of absorber tube of parabolic trough concentrator. *Energy* 93, 1788–1803.
- KHANNA, S., SHARMA, V., KEDARE, S.B. & SINGH, S. 2016 Experimental investigation of the bending of absorber tube of solar parabolic trough concentrator and comparison with analytical results. *Solar Energy* 125, 1–11.
- LIAO, Z., LI, X., XU, C., CHANG, C. & WANG, Z. 2014 Allowable flux density on a solar central receiver. *Renewable Energy* 62, 747–753.
- LITWIN, R.Z. 2002 Receiver System: Lessons Learned From Solar Two. *Tech. Rep.* SAND2002-0084. Sandia National Laboratories, Albuquerque, NM, and Livermore, CA, United States.
- LOGIE, W.R., PYE, J.D. & COVENTRY, J. 2018 Thermoelastic stress in concentrating solar receiver tubes: A retrospect on stress analysis methodology, and comparison of salt and sodium. *Solar Energy* 160, 368–379.
- MARUGÁN-CRUZ, C., FLORES, O., SANTANA, D. & GARCÍA-VILLALBA, M. 2016 Heat transfer and thermal stresses in a circular tube with a non-uniform heat flux. *International Journal of Heat and Mass Transfer* 96, 256–266.
- MAYTORENA, V.M. & HINOJOSA, J.F. 2019 Effect of non-uniform concentrated solar flux on direct steam generation in vertical pipes of solar tower receivers. *Solar Energy* 183 (December), 665–676.
- MONTOYA, A., RODRÍGUEZ-SÁNCHEZ, M.R., LÓPEZ-PUENTE, J. & SANTANA, D. 2018 Numerical model of solar external receiver tubes: Influence of mechanical boundary conditions and temperature variation in thermoelastic stresses. *Solar Energy* 174, 912–922.
- NECATI ÖZİSİK, M. 1993 *Heat Conduction*, 2nd edn. New York: Wiley-Interscience.
- NODA, N., HETNARSKI, R.B. & TANIGAWA, Y. 2003 *Thermal Stresses*, 2nd edn. New York, London: Taylor & Francis.
- PERSKY, M.J. & SZCZESNIAK, M. 2008 Infrared, spectral, directional-hemispherical reflectance of fused silica, Teflon polytetrafluoroethylene polymer, chrome oxide ceramic particle surface, Pyromark 2500 paint, Krylon 1602 paint, and Duraflect coating. *Applied Optics* 47 (10), 1389.

- RODRÍGUEZ-SÁNCHEZ, M.R., MARUGÁN-CRUZ, C., ACOSTA-IBORRA, A. & SANTANA, D. 2014a Comparison of simplified heat transfer models and CFD simulations for molten salt external receiver. *Applied Thermal Engineering* 73 (1), 991–1003.
- RODRÍGUEZ-SÁNCHEZ, M.R., MARUGÁN-CRUZ, C., ACOSTA-IBORRA, A. & SANTANA, D. 2018 Thermo-mechanical modelling of solar central receivers: Effect of incident solar flux resolution. *Solar Energy* 165, 43–54.
- RODRÍGUEZ-SÁNCHEZ, M.R., SORIA-VERDUGO, A., ALMENDROS-IBÁÑEZ, J. A., ACOSTA-IBORRA, A. & SANTANA, D. 2014b Thermal design guidelines of solar power towers. *Applied Thermal Engineering* 63 (1), 428–438.
- SÁNCHEZ-GONZÁLEZ, A., RODRÍGUEZ-SÁNCHEZ, M.R. & SANTANA, D. 2018 Aiming factor to flatten the flux distribution on cylindrical receivers. *Energy* 153, 113–125.
- SINGER, C., BUCK, R., PITZ-PAAL, R. & MÜLLER-STEINHAGEN, H. 2010 Assessment of Solar Power Tower Driven Ultrasupercritical Steam Cycles Applying Tubular Central Receivers With Varied Heat Transfer Media. *Journal of Solar Energy Engineering* 132 (4), 041010.
- TIMOSHENKO, S. & GOODIER, J.N. 1951 *Theory of Elasticity*, 2nd edn. New York: McGraw-Hill Book Company.
- UHLIG, R., FRANTZ, C., FLESCH, R. & FRITSCH, A. 2018 Stress analysis of external molten salt receiver. In *AIP Conference Proceedings of the SolarPACES 2017 conference on concentrating solar power and chemical energy systems, Santiago, Chile*, vol. 2033, pp. 040040 1–8. AIP Publishing.
- XU, C., WANG, Z., LI, X. & SUN, F. 2011 Energy and exergy analysis of solar power tower plants. *Applied Thermal Engineering* 31 (17-18), 3904–3913.
- YANG, X., YANG, X., DING, J., SHAO, Y. & FAN, H. 2012 Numerical simulation study on the heat transfer characteristics of the tube receiver of the solar thermal power tower. *Applied Energy* 90 (1), 142–147.
- ZAVOICO, A.B. 2001 Solar Power Tower - Design Basis Document. *Tech. Rep. SAND2001-2100*. Sandia National Laboratories, Albuquerque, NM and Livermore, CA, United States.

Material selection for solar central receiver tubes

Contents

4.1	Introduction	102
4.2	Methodology	106
4.2.1	Heliostat field and thermal model	106
4.2.2	Elastic stresses and strains model	107
4.2.3	Lifetime model	108
4.2.4	Levelized cost of alloy (LCOA)	113
4.3	Case of study	114
4.3.1	Receiver characteristics	114
4.3.2	Alloys characteristics	115
4.3.3	Design day and field aiming	123
4.4	Results and discussion	124
4.4.1	Maximum aiming factor allowable	124
4.4.2	Creep-fatigue results: lifetime analysis	129
4.4.3	Receiver costs	142
4.5	Conclusions	145
References		149

Summary

The severe conditions at which solar power tower central receivers operate and the high capital investment required motivate the lifetime analysis of an external cylindrical tubular receiver working with molten salts. Five alloy alternatives—Haynes 230, alloy 316H, Inconel 625, 740H and 800H—for the manufacturing of such tubes are studied using an analytical low-computational cost methodology.

The required creep and fatigue data of these alloys, available in the literature, is compiled in this Chapter through the obtaining of the needed coefficients for the followed methodology.

A great operation limitation of the alloys is the film temperature, to avoid corrosion issues. The most permissive are Haynes 230, 740H and 800H (650 °C), followed by Inconel 625 (630 °C) and alloy 316H (600 °C). This, as well as trying to avoid surpassing twice the yield strength, translate in great divergences in terms of power production: 24% and 65% less in the last two. Then, the lifetime analysis for a clean design day is performed, where the inclusion of the stress relaxation becomes critical for an accurate damage prediction; alloys 316H and 800H suffer from stress reset during their operation and thus, do not benefitting from the global stress relaxation phenomenon. For various plant lifespan forecasts, the most lasting and economically beneficial, considering also the energy production, is 740H. Then the levelized cost of alloy, with respect 740H, of Haynes 230, Inconel 625 and alloy 316H is 0.01, 0.09 and over 0.25, respectively. Incoloy 800H exhibits a poor endurance during its operation.

4.1 Introduction

Given the elevated cost of the central receiver (IRENA, 2016), the demanding conditions that it must endure, such as high heat fluxes and the cyclic operation, and the inability to use sensors to measure the operation parameters, it has become evident that the development of models as precise as possible is paramount to successfully analyse it and properly predict its correct behaviour under certain operating conditions.

Several codes consider the effect of creep, fatigue or creep-fatigue interaction while dealing with providing design guidelines for power boilers (ASME, 2014), such as the R5 British Code (British Energy Generation, 2003), the ASME BPVC Section III, Subsection NH (ASME, 2004) or the ASME FFS-1 (ASME, 2007). These present different approaches regarding the consideration of the creep-fatigue interaction, the yield criterion selection or the cyclic hardening/softening, among other aspects.

When the solar power tower (SPT) technology emerged, the criterion widely accepted to analyse the lifetime of the different plant components, such as the receiver or the steam power generator, was the ASME Code Case (CC) N-47 (ASME, 1980). For instance, it was used at Solar Two project as reference to obtain the strains and fatigue lifetime (Zavoico, 2001). Other example found in

the literature of the application of the N-47 CC in the analysis of solar receivers is (Babcock & Wilcox Company, 1984), where the creep and fatigue damages were studied in selected points of a molten salt cavity receiver, with tubes made of Incoloy 800H, resulting that the creep was negligible in comparison with the fatigue damage and the most critical points were found to be the ones under the greatest heat flux and lower heat transfer fluid (HTF) temperature. There is another instance in the work of Grossman & Jones (1990), where a cavity type molten salt receiver, which was constructed for a 30-year lifetime according to the N-47 and made of Incoloy 800, was studied after a year of testing at SANDIA National Laboratories. From the analysis it was concluded that the damage obtained was excessively high due to the lack of the appropriate material data available in the code and the operating conditions selected. Lastly, Kistler (1987) performed a fatigue analysis of a solar central receiver in alloy 316 working with sodium as HTF and using measured weather data as reference. In these last two cases (Grossman & Jones, 1990; Kistler, 1987), the creep damage was considered negligible from the start, being the fatigue mechanism the one regarded as the most relevant in terms of studying the receiver lifetime. Nonetheless, the N-47 CC was conceived for nuclear applications, which meant that it relies on high security margins to assure the reliability of the installation, given the potential damage it can cause in the event an issue occurs. Thus, given the less restrictive conditions in SPT plants, the safety margins of this code were soon found excessive for its use in solar applications, which carried severe economic penalties (Berman *et al.*, 1979). Also, the N-47 code case only provided fatigue and creep curves for four types of alloys: 304, 316, Incoloy 800H and 2 1/4 Cr-1 Mo steel (Grossman & Jones, 1990).

Seeing the need for a specific code for solar components, the N-47 CC was simplified by Berman *et al.* (1979) to make the creep and fatigue damage study more adequate for such technology. Then, Narayanan *et al.* (1985) performed a lifetime analysis of a molten salt receiver made of alloys type 304, type 316 and Incoloy 800, following the modified version (Berman *et al.*, 1979) of the N-47 code case. The authors considered aspects such as the start-up, the shut down and cloud passages, and the receivers were able to last the expected lifetime of 30 years. Nevertheless, there is no information regarding the stress analysis, performed with a FEA software. A methodology based on the ASME Section III Subsection NH slightly modified is presented by González-Gómez *et al.* (2021), allowing to obtain the stresses under elastic-plastic regime, considering the stress relaxation effect on the material as well. The analysis included, per-

formed for a clean design day of a Haynes 230 molten salt receiver, compares the results obtained with the presented models against FEA simulations, proving the fitness of the proposed methodology.

As for receivers working with other HTFs, Conroy *et al.* (2018a) studied the creep and fatigue damage in a sodium billboard receiver made of different alloys (304, 316 and 800H) following the ASME BPVC: Section III - Subsection NH, slightly modified; the authors found that the first two are more economically appealing despite their worse performance and reliability in comparison with Incoloy 800H. They also demonstrated the importance of the aiming strategy selection in guaranteeing the receiver integrity (Conroy *et al.*, 2018b). Fork *et al.* (2012) analyzed a central receiver made of 617 alloy working with air as HTF, resulting that creep was the critical damage mechanism over the fatigue one. They used two methods to obtain the damage in the receiver, one based in a modification of the ASME BPVC: Section III - Subsection NH and another one using measured creep-fatigue data. They highlight the influence of the safety factors in the lifetime estimation, which can vary orders of magnitude, and claim that the method selected may result in the underestimation of the fatigue or the creep damages. Lastly, regarding the sCO₂ technology, in which creep becomes a major issue due to the extremely high operating temperatures and pressures, Neises *et al.* (2014) performed an analytical lifetime analysis of the receiver, made of Haynes 230, for different thicknesses and heat fluxes, but they neglected the circumferential variations of the tube wall temperature. Similarly, a sCO₂ receiver in Haynes 230 was also analytically studied by Nithyanandam & Pitchumani (2016) for different incident heat fluxes, tube thickness, tube inner radius and mass flow rate. However, the analysis for the creep and fatigue damages was performed separately, in terms of the rupture time due to the creep phenomenon and the number of allowable cycles due to fatigue, and not considering their interaction. Ortega *et al.* (2016) performed a FEA structural analysis of an Inconel 625 sCO₂ receiver tube section, obtaining the accumulated fatigue and creep damage, showing that the former is significantly lower.

In this Chapter, an integral analysis of a molten salt receiver is performed, considering five different alloy alternatives for their manufacturing: Haynes 230, 316H, Inconel 625, Inconel 740H and Incoloy 800H. As mentioned earlier, Incoloy 800H and 316H were used in the Solar One and Solar Two pilot plants respectively, while the remaining alloys exhibit outstanding mechanical and corrosive properties in the operation range of SPT receivers (Special Metals Corp., 2013; Haynes International, 2020; De Barbadillo, 2017), motivating

their selection. The lifetime of these molten salt receivers is estimated using the analytic method proposed in (González-Gómez *et al.*, 2021). Performing an hourly analysis of a selected design day, the aim is to conclude which alloy is the most adequate to be used as the constructive material of the SPT central receiver tubes. This is determined in terms on its predicted lifetime but regarding as well the thermal efficiency and thermal power that can be obtained from its safe operation, which varies among these materials mainly due to their different resistance to the corrosive effects of the molten salts, and seeing how the disparate lifespans obtained for these alloys affect the receiver costs. To achieve it, previously developed thermal, mechanical and lifetime models have been used. Aiming for a precise solution, aspects such as the circumferential variation of the tube wall temperature (Rodríguez-Sánchez *et al.*, 2014*b*), the tube materials properties temperature dependence—as seen in Chapter 3—, or the stress relaxation due to creep during hold time (González-Gómez *et al.*, 2021, 2019; Wang *et al.*, 2017) are regarded. Moreover, the creep and fatigue behaviour of the alloys selected is obtained by fitting experimental data available in the literature to the lifetime model equations, providing a compilation of parameters and coefficients that allows the characterization of these materials for future works.

Thus, this Chapter is organized as follows: the heliostat field and thermal model, the elastic stress model and the lifetime one are presented in the various divisions of Section 4.2, which permit the calculation of the receiver performance and operation from different angles, all of them relevant to properly design it. Moreover, the leveled cost of alloy metric (LCOA), adequate for the economic analysis, is described. Then, the case of study is presented in Section 4.3, encompassing the receiver general geometrical and constitutive specifications, as well as the design day chosen and the heliostat field characteristics. The characteristics of the selected alloys, as well as their corresponding creep-fatigue coefficients are also presented in this section. After that, the results for the receiver studied are introduced in Section 4.4. First, the different aiming strategies are set for the receiver, resulting from performing thermal and elastic stresses analyses. Then, the elastic-plastic stresses and the stress relaxation that lead to the final creep stress are obtained. Closing this Section, the lifetime prediction for the different receivers and the cost analysis are presented. Lastly, the conclusions constitute Section 4.5.

4.2 Methodology

The receiver lifetime calculation is performed with the creep and fatigue damage assessment, which relies on the upstream calculation of the stresses and strains on the receiver tubes, which in turn depend on the temperature distribution on the tubes and the heat flux reflected by the solar field. These lifetime predictions are key to determine the receiver costs for a certain operation lifespan.

Consequently, the methodology that leads to the final estimation of the receiver lifetime is presented in this Section, which includes the thermal and structural analysis of the receiver. Then, the LCOA metric, that allows the comparison of the different alloys alternatives in terms of their cost and energy production, is included.

4.2.1 Heliostat field and thermal model

A clear sky model, based on the Daneshyar-Paltridge-Proctor one (Reno *et al.*, 2012) and that takes into account the solar altitude, allows the obtaining of the ideal direct normal irradiance (DNI), which is symmetrical with respect the solar noon.

With such DNI, the heat flux on the receiver surface is calculated by using the software tool FluxSPT. Its programming code, developed by Sánchez-González & Santana (2015), follows an optical model based on the convolution-projection method. This tool allows to consider various aiming strategies on the receiver surface, permitting to obtain a flat distribution or a more pointed one, which is defined by the aiming factor k . The aiming factor determines the target point assigned for each heliostat and ranges from 0, which would result in an open aiming (aiming to the top and bottom ends of the receiver), to 3, which is close to be equivalent to an equatorial aiming. In that span, a flat aiming can be found, which would result in the most homogeneous heat flux distribution on the receiver surface as possible (Sánchez-González *et al.*, 2018). Apart from the heat flux on the receiver, this optical model also provides the optical efficiency of the aiming strategy selected, being greater the higher the k is (and thus, the more equatorial the aiming is).

Having the heat flux distribution on the receiver surface, the thermal analysis can be undertaken. It has been proven that the circumferential divisions of the tubes cannot be disregarded when aiming a precise solution (Rodríguez-Sánchez *et al.*, 2014a). It is also relevant to consider the various reflections among the surfaces involved in the radiative exchange in order to obtain an ac-

curate temperature distribution on the tubes. The thermal model is the ECGM (Energy Coarse Grid Model) presented in Chapter 2, although the thickness is considered fixed so the cases studied can be compared from the most similar initial design point as possible. In the calculations, one tube representative per panel is studied, assuming that all the tubes in a panel are under the same heat flux distribution. The thermal analysis results in the tubes temperature distribution, $T(\theta, r, z)$, as well as the thermal power and thermal efficiency of the receiver.

4.2.2 Elastic stresses and strains model

Once the temperature distribution on the receiver tubes is obtained, the elastic stresses and strains on them are calculated with the analytic method detailed in Chapter 3. The methodology considers the temperature dependence of the tube material properties. Such dependence has proven to have a significant impact in the stress calculation over the independent properties consideration and thus it should be taken into account.

At a fixed z , the model is based on the separation of the temperature profile in a circumferential distribution, and a radial one. The decomposition of the temperature in these two profiles allows us to tackle the problem as the superimposition of the thermal stresses obtained for both cases (Goodier, 1957). Thus, the thermal stresses in the radial and circumferential coordinates are obtained considering the contribution of both effects: $\sigma_{T,r}^E = \sigma_{T_r,r}^E + \sigma_{T_\theta,r}^E$ and $\sigma_{T,\theta}^E = \sigma_{T_r,\theta}^E + \sigma_{T_\theta,\theta}^E$. Then, the one corresponding to the axial coordinate is obtained by means of the Hooke law as $\sigma_{T,z}^E = \nu (\sigma_{T,r}^E + \sigma_{T,\theta}^E)$. These loads can be classified as secondary stresses according to ASME (2004).

Nevertheless, the thermal gradient on the tube surface not only causes the thermal stresses already presented, but also the deflection of the tubes. To avoid their excessive bending in the radial direction and towards the adjacent tubes, which would lead to hot spots in the potential contact areas, their displacement is restricted with a series of supports, called clips. However, the downside is that these clips introduce mechanical stresses in the axial coordinate, $\sigma_{M,z}^E$.

Besides the thermal and mechanical stresses, the pressure drop of the HTF inside the tubes also contributes to the solicitations that they must endure

(Timoshenko & Goodier, 1951), being the primary stresses:

$$\begin{aligned}\sigma_{P,r}^E(r) &= P_i \frac{a^2}{b^2 - a^2} \left(1 - \frac{b^2}{r^2} \right), \\ \sigma_{P,\theta}^E(r) &= P_i \frac{a^2}{b^2 - a^2} \left(1 + \frac{b^2}{r^2} \right), \\ \sigma_{P,z}^E(r) &= P_i \frac{a^2}{b^2 - a^2}.\end{aligned}\quad (4.1)$$

Thus, the total stresses on the receiver tubes due to the thermal, mechanical and pressure solicitations are

$$\begin{aligned}\sigma_r^E &= \sigma_{T,r}^E + \sigma_{P,r}^E, \\ \sigma_\theta^E &= \sigma_{T,\theta}^E + \sigma_{P,\theta}^E, \\ \sigma_z^E &= \sigma_{T,z}^E + \sigma_{M,z}^E + \sigma_{P,z}^E.\end{aligned}\quad (4.2)$$

In the case of cylindrical external receivers, the dominant stress component, σ_z , is one and two orders of magnitude in comparison to σ_θ and σ_r , respectively, as observed in the analysis of Chapter 3. Given the small entity of the shear stress, a fairly accurate approximation is to consider the normal stresses as equivalent to the principal stresses. Then, the elastic strains, ε_r , ε_θ and ε_z , are obtained according to the Hooke law.

Lastly, with the stress and strain components being known and under the generalized plane strain scenario, the Von Mises equivalent stress and strain are:

$$\sigma_{\text{eq}}^E = \sqrt{\frac{(\sigma_r^E - \sigma_\theta^E)^2 + (\sigma_\theta^E - \sigma_z^E)^2 + (\sigma_z^E - \sigma_r^E)^2}{2} + 3(\tau^E)^2}, \quad (4.3)$$

$$\varepsilon_{\text{eq}}^E = \frac{\sqrt{2}}{3} \sqrt{(\varepsilon_r^E - \varepsilon_\theta^E)^2 + (\varepsilon_\theta^E - \varepsilon_z^E)^2 + (\varepsilon_z^E - \varepsilon_r^E)^2}. \quad (4.4)$$

4.2.3 Lifetime model

Thus, the receiver lifetime is estimated by the calculation of the equivalent operating days (EODs), which are the result of considering the creep and fatigue damage mechanisms on the receiver tubes. Creep damage is present during the hold time while fatigue occurs with the cyclic loading. To approach the estimation of the EODs, the widely used linear damage summation (LDS) model is employed (ASME, 2004). The addition of both creep and fatigue damages must be equal or less than the maximum damage limit allowable,

$$D_L \geq D_c + D_f. \quad (4.5)$$

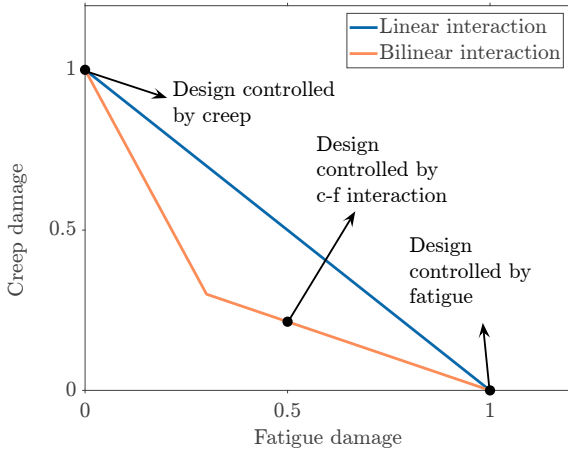


Figure 4.1: Creep-fatigue interaction diagram.

Now, if the creep and fatigue damages are obtained for the design day, d_c and d_f , the EODs are estimated as

$$D_L = d_c \text{ EODs} + d_f \text{ EODs} \rightarrow \text{EODs} = \frac{D_L}{d_c + d_f}. \quad (4.6)$$

On the one hand, the damage limit value varies with the material and it can be equal or less than unity. It depends on the bilinear interaction between the creep and fatigue damages and it is typically presented in a creep-fatigue interaction diagram. However, in the LDS method used in this Chapter, the D_L is considered to have a constant value equal to unity regardless the material used (British Energy Generation, 2003; Chen *et al.*, 2013), becoming the creep-fatigue interaction linear instead of bilinear, Figure 4.1, which is a reasonable assumption for clear-sky days. On the other hand, the calculations of the fatigue and creep damages for the design day, which depend on the equivalent elastic stresses and strains, are presented in the following subsections.

Creep damage

The creep damage calculation is performed with the rupture time, that depends on the effective creep stress, σ_{creep} . This stress is calculated as

$$\sigma_{\text{creep}} = (\sigma_{\text{eq}} - \sigma_{\text{relax}}) / C' \quad (4.7)$$

following the ASME Section III, Division 5. Note that, in this study, if $\sigma_{\text{creep}} > \sigma_{\text{eq}}$, the creep stress is taken as σ_{eq} to avoid an excessive level of conservatism.

Here C' is a safety factor set as 0.9, a value suitable for inelastic analysis involving concentrating solar power (CSP) technologies (Mcmurtrey, 2019; Barua *et al.*, 2020). σ_{eq} is the elastic-plastic equivalent stress. It is obtained by correcting the elastic stress with the Neuber Method, which allows to consider the plasticity effects of the material, with the yield strength, S_y , and twice its value delimiting the different regimes:

- For $\sigma_{\text{eq}}^E \leq S_y$, elastic regime, $\sigma_{\text{eq}} = \sigma_{\text{eq}}^E$
- For $S_y < \sigma_{\text{eq}}^E < 2S_y$, elastic shakedown regime, σ_{eq} is calculated with the Neuber method, in terms of the monotonic stress-strain curve (Glinka, 1985), as

$$\sigma_{\text{eq}}^E \varepsilon_{\text{eq}}^E = \frac{\sigma_{\text{eq}}^2}{E} + \sigma_{\text{eq}} \left(\frac{\sigma_{\text{eq}}}{K} \right)^{\frac{1}{n}}, \quad (4.8)$$

where K and n are the monotonic stress-strain curve parameters: the strength coefficient and the strain hardening exponent respectively, adjusted to experimental data. Their corresponding values for the different alloys studied are presented later in Section 4.3.2, Table 4.4.

Alternatively, when the stress-strain curve can be approximated to a bilinear relation, with two linear regions separated by S_y , it is more accurate to use the Neuber method for an expression that takes into account that linear behaviour of the stress-strain curve (Moftakhar *et al.*, 1995),

$$\sigma_{\text{eq}}^E \varepsilon_{\text{eq}}^E = \sigma_{\text{eq}} \frac{S_y}{E} + \sigma_{\text{eq}} \left(\frac{\sigma_{\text{eq}} - S_y}{H} \right), \quad (4.9)$$

being H the elasto-plastic modulus.

- For $\sigma_{\text{eq}}^E \geq 2S_y$, reverse plasticity regime, the Neuber method relies on the cyclic stress strain curve, since it takes into account the dynamic material hardening experienced in this regime:

$$\frac{\sigma_{\text{eq}}^E \varepsilon_{\text{eq}}^E}{2} = \frac{\sigma_{\text{eq}}^2}{E} + \sigma_{\text{eq}} \left(\frac{\sigma_{\text{eq}}}{K'} \right)^{\frac{1}{n'}}, \quad (4.10)$$

in this case, the cyclic strength coefficient, K' , and the cyclic strain hardening exponent, n' , are likewise compiled in Table 4.4.

On the other hand, σ_{relax} is the stress relaxation. It occurs during hold time under a constant peak strain, causing a decrease in the stress on the material (Yan *et al.*, 2015). If the hold time of the solicitation at high temperature is

high enough, the inelastic nature of creep causes a fraction of the total strain to become permanent. Therefore, the elastic strain decreases, leading to stress relaxation. Neglecting this phenomenon would result in an underestimation of the receiver lifetime (González-Gómez *et al.*, 2021). The stress relaxation is obtained by integrating the creep strain rate model (Norton-Bailey) during the dwell period, giving out the expression

$$\sigma_{\text{relax}} = \sigma_{\text{eq}} - E \left\{ (\sigma_{\text{eq}}/E)^{1-n_r} - (1 - n_r) AE^{n_r} \exp[-Q/(RT)] \frac{t_{\text{stab}}^{m+1}}{m+1} \right\}^{\frac{1}{1-n_r}}. \quad (4.11)$$

Here R is the ideal gases constant ($\text{J}/(\text{mol} \cdot \text{K})$), Q is the creep activation energy (kJ/mol) and t_{stab} is the stabilization time, in seconds. These and the rest of the parameters are included in Table 4.5 for the alloys selected. In this analysis, only the T and the σ_{eq} of the most critical hour during the day—the combination that result in the greatest stress relaxation—are considered to be causing relaxation on the receiver tubes (González-Gómez *et al.*, 2021). This is done for each axial division of the receiver independently, which implies that the critical hour may vary among the axial positions. With such regard, for an hourly study and given the daily cyclic operation of the receiver, the stress relaxation captured in Eq. 4.11 would only “move forward” one hour a day, being needed a total of t_{stab} (expressed in hours in this case) days to achieve such σ_{relax} . After the stabilization time, the tubes relaxation is assumed to be totally fulfilled and that σ_{relax} is then used for all the operation hours during the day to obtain the σ_{creep} according to Eq. 4.7. However, this stress relaxation during cyclic operation would only be able fully deploy for the whole stabilization time, even with the shutdowns and start-ups of the plant, if there is shakedown to elastic cycling. It occurs if the elastic stress σ_{eq}^E is less than the stress reset limit, S_{SR} : the addition of the cold yield strength, $S_{y,\text{cold}}$, and the hot relaxation strength, S_H (Becht IV, 2011). The mentioned S_H is usually taken as $1.25S$, being S the allowable stress available at the ASME BPVC Section II Part D (ASME, 2010). Otherwise, if $\sigma_{\text{eq}}^E > S_{y,\text{cold}} + S_H$, stress reset occurs after the daily shutdown, which means that the initial stress level is restored the following day. This would be equal to having a total t_{stab} of just one hour, given that the stress relaxation would not be daily accumulated. Once the σ_{creep} is known, there are several formulations to obtain the rupture time (Eno *et al.*, 2008). In this study, it is calculated with the Mendelson-Roberts-Manson (M-R-M) parametrization,

$$\log_{10}(t_R) = \beta_0 + \beta_1 \frac{1}{T} + \beta_2 \log_{10}(\sigma_{\text{creep}}) + \beta_3 \log_{10}(\sigma_{\text{creep}}) \frac{1}{T}. \quad (4.12)$$

The M-R-M coefficients are presented in Table 4.6. In Eq. 4.12, σ_{creep} is introduced in MPa while the temperature is in K, resulting in a rupture time expressed in hours. Unlike the Larson-Miller parametrization, the M-R-M one does not have any coefficient fixed to zero, which gives it a good degree of flexibility. It also considers the temperature dependence as reciprocal, which is suitable given that, in most creep mechanisms, the diffusion involved is an Arrhenius-type one (Eno *et al.*, 2008).

Lastly, the creep damage for the design day is obtained by adding the ratios of time intervals, Δt , over their corresponding time to rupture, t_R :

$$d_c = \sum_{i=1}^J \frac{\Delta t_i}{t_{R,i}}. \quad (4.13)$$

A time interval is a period at which the receiver tubes are subjected to a constant creep stress and temperature, resulting in a specific time to rupture. J is the total number of time intervals occurring in the design day.

Fatigue damage

The fatigue damage is estimated after the number of allowable cycles, which varies with the strain range. Thus, the equivalent elastic-plastic strain range is calculated as follows, similarly to the equivalent elastic-plastic stress:

- For $\sigma_{\text{eq}}^E < 2S_y$, $\Delta\varepsilon_{\text{eq}} = \Delta\varepsilon_{\text{eq}}^E$
- For $\sigma_{\text{eq}}^E \geq 2S_y$, the equivalent elastic-plastic stress range ($\Delta\sigma_{\text{eq}}$) is obtained following the Neuber method

$$\Delta\sigma_{\text{eq}}^E \Delta\varepsilon_{\text{eq}}^E = \frac{\Delta\sigma_{\text{eq}}^2}{E} + 2\Delta\sigma_{\text{eq}} \left(\frac{\Delta\sigma_{\text{eq}}}{2K'} \right)^{\frac{1}{n'}}. \quad (4.14)$$

After that, the equivalent plastic strain range ($\Delta\varepsilon_{\text{eq}}^P$) is calculated as (Mao *et al.*, 2016)

$$\Delta\varepsilon_{\text{eq}}^P = 2 \left(\frac{\Delta\sigma_{\text{eq}}}{2K'} \right)^{\frac{1}{n'}}, \quad (4.15)$$

and then the equivalent elastic-plastic strain range ($\Delta\varepsilon_{\text{eq}}$) is obtained as (Kalnins, 2006)

$$\Delta\varepsilon_{\text{eq}} = \frac{\Delta\sigma_{\text{eq}}}{E} + \Delta\varepsilon_{\text{eq}}^P. \quad (4.16)$$

With $\Delta\varepsilon_{\text{eq}}$, the number of allowable cycles is calculated using the implicit Manson-Coffin expression,

$$\frac{\Delta\varepsilon_{\text{eq}}}{2} = \frac{\Delta\varepsilon_{\text{eq}}^E}{2} + \frac{\Delta\varepsilon_{\text{eq}}^P}{2} = \frac{\sigma'_f}{E} N_a^{-c1} + \varepsilon'_f N_a^{-c2}, \quad (4.17)$$

where ε'_f is the fatigue ductility of the material and σ'_f is the fatigue strength coefficient. Their values, as well as the ones of the exponents c_1 and c_2 , are included in Table 4.7 for the alloys studied. A number of cycles low enough to make $\Delta\varepsilon_{\text{eq}}^P \gg \Delta\varepsilon_{\text{eq}}^E$ implies a plastic cyclic straining where $\Delta\varepsilon_{\text{eq}}$ is equivalent to consider only its plastic component, $\frac{\Delta\varepsilon_{\text{eq}}}{2} \approx \frac{\Delta\varepsilon_{\text{eq}}^P}{2} = \varepsilon'_f N_a^{-c2}$. On the contrary, a high number of cycles that satisfies $\Delta\varepsilon_{\text{eq}}^E \gg \Delta\varepsilon_{\text{eq}}^P$ results in an elastic cyclic straining, with $\frac{\Delta\varepsilon_{\text{eq}}}{2} \approx \frac{\Delta\varepsilon_{\text{eq}}^E}{2} = \frac{\sigma'_f}{E} N_a^{-c1}$. As can be perceived from the resulting equations, in the first case fatigue is ductility controlled while in the second case it is strength controlled.

Having the number of allowable cycles, the fatigue damage of the design day is defined as the summation of the ratios between the number of fatigue cycles and their corresponding number of allowable cycles resulting at their respective equivalent strain range conditions

$$d_f = \sum_{j=1}^M \frac{N_j}{N_{a,j}}. \quad (4.18)$$

4.2.4 Levelized cost of alloy (LCOA)

The metric selected to analyze the cost of each alloy as the centric element of the SPT receiver is the leveled cost of alloy (LCOA), obtained as

$$LCOA_i = \frac{C_{\text{alloy},i} - C_{\text{alloy,ref}}}{E_{\text{alloy},i}} + C_{\text{ref}} \left(\frac{1}{E_{\text{alloy},i}} - \frac{1}{E_{\text{ref}}} \right). \quad (4.19)$$

This is a similar approach to the one introduced in (Boubault *et al.*, 2016) for the coating analysis. Since, unlike the coating, the receiver would not be able to work without the tubes, one of the studied receivers (or alloys) needs to be fixed as the reference one. Consequently, the LCOA for such receiver would be zero and the LCOA of the receiver in alloy i is the result of the difference between its LCOE and the LCOE of the reference receiver, with its tubes and headers made of the reference alloy.

Here, $C_{\text{alloy},i}$ is the annualized cost of alloy i and $E_{\text{alloy},i}$ is the annualized energy production of such receiver, considering 300 EODs per year and 11 hours of daily operation. On the other hand, C_{ref} and E_{ref} are the annualized total

cost of the reference receiver and its annualized energy production, respectively, while $C_{\text{alloy,ref}}$ is just the annualized cost of the alloy involved in the reference receiver.

4.3 Case of study

In this Section, the receiver design characteristics are presented. The configurations differ only in the constitutive material of the tubes. The mechanical coefficients required for the receiver lifetime calculation, which vary for the alloys studied, are presented in Section 4.3.2. Such material alternatives will be later analysed under a certain design day, which is introduced in Section 4.3.3.

4.3.1 Receiver characteristics

The external tubular receiver of a SPT plant is studied. It is placed at the top of a 130 m tower and presents an 8.4 m diameter cylindrical structure that frames the panels containing the vertically disposed tubes. In this case, the number of panels, N_p , is fixed in 18 and the external tube radius, b , is set in 1.12 cm. The adjacent tubes of a panel are separated 1.9 mm. All of this results in 61 tubes per panel, N_t . The tubes, seamless, are 1.2 mm thick, th , and 10 m long, L_t . The distance selected between the guiding clips, which prevent the tubes from bending excessively, is 2 m, resulting in a total of 6 clips, considering the ones at both ends. The tubes constituting a panel are connected to their respective inlet and outlet headers, which are 1.49 m long, have an external diameter of 0.163 m and a thickness of 2.8 mm. The receiver tubes are painted with a black Pyromark coating in order to increase their absorptivity, which is 0.95 in the visible spectrum (Zavoico, 2001) and around 0.98 in the infrared spectrum (Ho & Pacheco, 2014). Its infrared emissivity is temperature dependent, with the data available in (Wade & Slemp, 1962). Opposite to this, the frame cylindrical structure is covered with white Pyromark, a ceramic painting with an infrared emissivity of 0.84 (Zavoico, 2001) and high reflectivity: 0.8 in the visible spectrum (Zavoico, 2001) and 0.785 in the infrared one (Scannapieco, 1968). For the tubes manufacturing, five different alloy alternatives are chosen, in order to compare them: 316H, Haynes 230, Inconel 625, Inconel 740H and Incoloy 800H.

The HTF selected is solar salt (60% NaNO₃-40% KNO₃), which is commonly used in most commercial SPT facilities. The solar salt properties as function of the temperature are available in (Zavoico, 2001). There are both a

lower temperature limit, 290 °C, and upper one, 565 °C, to prevent its freezing and decomposition, respectively. The HTF is divided into two parallel flow paths, N-S symmetrical, with no crossover between paths. The salt inlet occurs at the bottom of the two Northern panels, while the outlet happens at the top of the Southern ones. The HTF mass flow through the receiver paths is adjusted to obtain the outlet desired temperature, depending on the heat flux reflected on the receiver surface coming from the heliostat field. Despite having been omitted in the lifetime analysis, all the piping elements need to be considered in order to properly obtain the pressure drop in the receiver, not just the tubes conforming the panels (Rodríguez-Sánchez *et al.*, 2014b). Connecting the receiver tubes to their respective inlet and outlet collectors there are three smoothly bended pipes, presenting two 120° elbows and one of 60°, lengths of 0.7, 1.7 and 0.2 m, and a curvature radius of 0.13 m. Inside these collectors, whose length is 1.4811 m—according to the number of panels of the receiver and diameter of the cylindrical base structure—and its diameter is 162.6 mm, the HTF is modelled to follow a trajectory through two imaginary 90° elbows. Lastly, the connection between adjacent panels occurs through a section with two 90° elbows as well, with lengths of 0.25 m, 0.6 m and 0.17 m diameter, above the 0.1 m minimum recommended (Mehos *et al.*, 2020). The pressure drop of the receiver would be the maximum between the one obtained for each path, considering the pressure drop through the elements presenting an in-series disposition.

4.3.2 Alloys characteristics

General overview

The thermal and mechanical properties of the selected materials are obtained from (ASME, 2010), with the exception of the yield strength, whose reference is specified for each alloy in the following lines:

- Alloy 316H (UNS 31609) is the high carbon variant of the austenitic stainless-steel grade 316 and is adequate for high temperature applications. At room temperature (RT) it presents a yield strength of 205 MPa (Du *et al.*, 2016). In comparison with other alloys selected, it has poorer mechanical properties and corrosion endurance. Moreover, its use at Solar Two showed issues with stress-corrosion cracking (Litwin, 2002). However, its low price, makes it a potentially interesting alternative. Alloy 316H can only be strengthened by cold work, being thermal treatments dis-

carded for its hardening (Ren & Lin, 2019). This alloy requires annealing at 1040 °C or higher, needing a rapid cooling afterwards.

- Inconel 625 (UNS N06625) is an austenitic nickel-based super-alloy. Although far from other options, it has a better corrosion resistance than 316H. Its yield strength is 502 MPa at RT (Mataveli Suave *et al.*, 2016). It presents great thermal and mechanical properties, which led it to be extensively studied in the industry. Working below 650 °C, it is recommended either hot-finished, cold-finished or annealed (Special Metals Corp., 2013) while, above such temperature, annealed or solution-treated are preferred, being the latter desirable for demanding applications in terms of rupture or creep. Moreover, alloy 625 has been found to suffer from grain boundary precipitations after being aged at medium temperatures (~ 650 °C) during low number of cycles (~ 500 h) (Mataveli Suave *et al.*, 2016). This causes it to double its elastic limit and present a perfectly elastic behaviour after the first cycles.
- Inconel 740H (UNS N07740) is an austenitic nickel-base super-alloy extensively used in steam cycles boilers. More recently it has been promoted to sCO₂ cycles, showing an excellent corrosion resistance, balanced with creep strength and weldability (De Barbadillo, 2017). Interest has also arisen in its application in CSP tubular receivers (Barua *et al.*, 2020). Its yield strength is the greatest out of the five alloys, with 621 MPa at 40 °C (Barua *et al.*, 2020). Regarding heat treatments, Inconel 740H is usually provided as solution annealed and age-hardened (PCC Energy Group, 2020). The annealing is expected to be performed at 1100 °C for at least 30 minutes and a maximum of an hour per thickness inch, with water quenching being advisable after it but not mandatory. On the other hand, the aging is done between 760 °C and 815 °C for at least four hours. The forging or hot-rolling of this alloy are both recommended to be done in a range from 870 °C and 1190 °C. Its price is its main drawback, being the most expensive out of the set studied.
- Incoloy 800H (UNS N08810) is an austenitic nickel-based alloy recommended for corrosive mediums and high temperatures. It was used to manufacture the steam receiver tubes of the Solar One project and also tested by Sandia National Laboratories in a solar salt receiver, prior the Solar Two project (Kolb, 2011). Despite its high corrosion resistance and moderate cost, it has worse mechanical properties than Inconel 625

(230 MPa of yield stress at 40 °C (ASME, 2010)). This alloy is supplied after a high-temperature annealed treatment, which results in an average grain size of ASTM 5 or coarser and a greater creep and rupture strength than its low-carbon variant (Special Metals Corp., 2004).

- Haynes 230 (UNS N06230) is an austenitic nickel-base superalloy. Traditionally used in gas turbines, it has recently started being implemented in CSP applications, such as SPT and solar dish, given its great corrosion resistance and since it is thermally more stable compared to alternatives such as Inconel 625 and Incoloy 800H. Nevertheless, is one of the most expensive alternatives. Its yield stress is 310 MPa at RT (ASME, 2010). The solution heat-treated for wrought Haynes 230 is done in the temperature range from 1177 °C to 1246 °C, being cooled or water-quenched afterwards. However, annealing in temperatures lower than these range can negatively impact its strength and ductility due to carbide precipitation (Haynes International, 2020).

The selected alloys are used in this Chapter in the form of seamless tubes, which is typically a more expensive option than the welded alternative but more adequate for applications experiencing high temperature creep, such as the SPT receivers. In the manufacturing process of seamless tubes (De Barbadillo *et al.*, 2018), after the primary melt and remelt, the alloy is forged to the tubular round shape form and extruded. Then, the tubes are cold worked, annealed and aged. Finally, they are straightened and tested. The chemical compositions of these alloys are included in Table 4.1. Some elements present an admissible range of values within the corresponding alloy composition, others appear in a minimum quantity or are capped at a maximum value. This leaves a certain element, which varies from alloy to alloy, as the one filling the composition up to the 100%, marked in Table 4.1 as “Balance”.

It is worth noting that the most restrictive temperature in the design phase of the receiver is the film temperature (Rodríguez-Sánchez *et al.*, 2014b). The limiting value not to be surpassed depends on the HTF selected, aiming to avoid its decomposition and also depends greatly on the tube material, since it suffers from corrosion. The maximum film temperature allowable for each alloy studied working with molten salt as HTF, according to literature, can be found in Table 4.2. The 740H alloy, the most recent one out of the five alloys analysed, presents excellent corrosion properties at high temperatures while in contact with combustion gas and coal ashes, which has led it to be widely tested

Table 4.1: Chemical composition (weight %) of the alloys selected.

Element	230 [a ₁]	316H [b ₁]	625 [c ₁]	740H [d ₁]	800H [e ₁]
Ni	57 Balance	10-14	58 min	Balance	30-35
Cr	22	16-18	20-23	24.5	19-23
W	14	-	-	-	-
Mo	2	2-3	8-10	0.1	-
Fe	3 max	Balance	5 max	3 max	39.5
Co	5 max	-	1 max	20	-
Mn	0.5	2 max	0.5 max	1 max	-
Si	0.4	0.75 max	0.5 max	0.15	-
Nb	0.5 max	-	3.15-4.15 (plus Ta)	1.5	-
Al	0.3	-	0.4 max	1.35	0.15-0.6
Ti	0.1 max	-	0.4 max	1.35	0.15-0.6
C	0.1	0.04-0.1	0.1 max	0.03	0.05-0.1
La	0.02	-	-	-	-
B	0.015	-	-	0.006 max	-
P	-	0.045 max	0.015 max	0.03 max	-
S	-	0.03 max	0.015 max	0.03 max	-
Cu	-	-	-	0.5 max	-

and characterized in the supercritical steam field (Lu *et al.*, 2017; Luo *et al.*, 2018; Jena *et al.*, 2018). More recently, interest has been rising involving its application in sCO₂ cycles (De Barbadillo, 2017; De Barbadillo *et al.*, 2018), but little to none tests have been carried out when working with molten salt as HTF. However, the presence of a high Cr percentage on its composition, as well as Ni, Co, Ti and Al, which are known to enhance the corrosion resistance, seems to confirm its adequate behaviour at high temperatures in an oxidation environment due to the molten salt use (De Barbadillo, 2017; Cunat, 2004). Thus, looking at the rest of alloys studied in this Chapter, their composition and the resulting corrosion resistance, the maximum allowable film temperature for the 740H has been set in 650 °C.

Lastly, the costs per kilogram of each material are comprised in Table 4.3.

[a₁] (Haynes International, 2020) [d₁] (PCC Energy Group, 2020)

[b₁] (Atlas Steels, 2011) [e₁] (Special Metals Corp., 2004)

[c₁] (Special Metals Corp., 2013)

Table 4.2: Maximum allowable film temperature for the alloys studied.

Alloy	230	316H	625	740H	800H
T_{film} (°C)	650 [a ₂]	600 [b ₂]	630 [b ₂]	650	650 [c ₂]

Table 4.3: Alloys prices.

Alloy	230	316H	625	740H	800H
Price (\$/kg)	88	5	70	95	23

The cost of alloy 316H, Inconel 625 and Incoloy 800H tubes, in \$/kg, is supplied by Mtsco (Mtsco, 2020) for a wholesale purchase. Moreover, the price of alloy 617 is also provided by Mtsco, which is considered to be equivalent to the 740H cost (Nicol, 2013). On the other hand, the price of Haynes 230 has been obtained via energy consulting.

Mechanical coefficients

The coefficients needed in the equations of Section 4.2.3 have been obtained for the various alloys of this Chapter by adjusting them to the experimental data available in the literature. They are comprised in the tables that follow, which include the references of the experimental data used.

First, Table 4.4 presents the parameters of the stress-strain curves. The monotonic curve, involving the first load cycle, is fitted to the corresponding Ramberg-Osgood expression (Glinka, 1985)

$$\varepsilon = \varepsilon^E + \varepsilon^P = \frac{\sigma}{E} + \left(\frac{\sigma}{K} \right)^{1/n}, \quad (4.20)$$

while the cyclic curve, related to the stabilized hysteresis loop, is fitted to the Ramberg-Osgood form for said cyclic curve (Glinka, 1985; Lopez & Fatemi, 2012),

$$\frac{\Delta\varepsilon}{2} = \frac{\Delta\varepsilon^E}{2} + \frac{\Delta\varepsilon^P}{2} = \frac{\Delta\sigma}{2E} + \left(\frac{\Delta\sigma}{2K'} \right)^{1/n'}. \quad (4.21)$$

The parameters K and n obtained by fitting Eq. 4.20 to the monotonic stress-strain experimental data are used in Eq. 4.8 to calculate the elastic-plastic

[a₂] (McConohy & Kruizinga, 2014)

[b₂] (Miliozzi *et al.*, 2001)

[c₂] (Bradshaw & Goods, 2001)

Table 4.4: Coefficients of the stress-strain monotonic and cyclic curves.

Alloy	T (°C)	K (MPa)	n (-)	K' (MPa)	n' (-)	H (MPa)
230 [a ₃]	427	425.75	0.0642	1455	0.1485	-
	650	303.74	0.0311	760	0.0744	-
316H [b ₃]	427	159.5	0.03	1246.5	0.239	-
	538	138.9	0.029	1849.2	0.269	-
	593	181.1	0.066	777.7	0.15	-
625 [c ₃]	650	-	-	-	-	2332
	750	-	-	-	-	1287.7
740H [d ₃]	650	975	0.0786	-	-	-
	700	899	0.0584	-	-	-
	750	898	0.0635	-	-	-
800H [e ₃]	427	326	0.1316	-	-	-
	538 [f ₃]	-	-	392	0.0559	-
	649	289	0.1305	-	-	-
	760	182	0.1095	-	-	-
	850 [g ₃]	-	-	178	0.058	-

equivalent stress. On the other hand, the coefficients K' and n' resulting from the fitting of Eq. 4.21 to the cyclic stress-strain data are needed in Eqs. 4.10, 4.14 and 4.15. The cyclic parameters for Inconel 740H have not been obtained since its regular operating conditions in a SPT receiver are far from reaching the twice yield strength limit.

For materials showing a bilinear stress-strain interaction, the elasto-plastic modulus, H , needed in Eq. 4.9 to characterize its behaviour is obtained by fitting the stress-strain data above S_y to the expression (Moftakhar *et al.*, 1995)

$$\varepsilon = \frac{S_y}{E} + \frac{\sigma - S_y}{H}, \sigma > S_y. \quad (4.22)$$

Regarding the alloys selected in this Chapter, Inconel 625 is the one satisfying such scenario (Mataveli Suave *et al.*, 2016) and thus the one needing the fit corresponding to Eq. 4.22.

[a₃] (Barrett *et al.*, 2016)[e₃] (Berman *et al.*, 1979)[b₃] (Maiya, 1980)[f₃] (Kaae, 2009)[c₃] (Mataveli Suave *et al.*, 2016)[g₃] (Rao *et al.*, 1996)[d₃] (Barua *et al.*, 2020)

Table 4.5: Coefficients of the Norton-Bailey model.

Alloy	A (1/(Pa ^{n_r} s))	n_r (-)	m (-)	Q (kJ/mol)	t_{stab} (s)
230 [a ₄]	2.688e-45	6.6	0	322 [b ₄]	108,000
316H [c ₄]	2.0644e-68	11.2594	0	537.64	108,000
625 [d ₄]	6.78e-95	13.37	0	447	108,000
740H [e ₄]	5.857e-57	9.6955	0	612.77	108,000
800H [f ₄]	2.615e-46	9.5	0	685.2	108,000

Table 4.5 compiles the coefficients obtained for the Norton-Bailey creep strain model, which are required in Eq. 4.11 to calculate the stress relaxation. The m factor is set to zero, which translates in a simple Norton equation, allowing us to consider secondary creep strain rates. The minimum strain rate (1/s) versus stress (MPa) at a fixed temperature plot is used to fit the stress power law for creep strain model coefficient (n_r) using the power-law creep equation: $\dot{\epsilon} = A_0\sigma^{n_r}$. The experimental data selected from the literature for this matter have been chosen for the minimum fixed temperature found for every alloy, trying for it to be on par with the working temperatures of the receiver. This has resulted in minimum strain rate versus stress data at fixed temperatures of 600 °C for alloy 316H, 625 °C for Inconel 625 and Incoloy 800H and 700 °C for Haynes 230 and Inconel 740H. Then, the plot of the natural logarithm of the minimum creep rate versus the inverted absolute temperature (1/K) at a fixed stress is fitted with the Arrhenius law, $\dot{\epsilon} = A\sigma^{n_r} \exp[-Q/(RT)]$, to give out the creep activation energy (Q) and the constant A . Again, the fixed stress selected for each alloy out of the ones available in the literature try to resemble the stress working conditions of each alloy. On the other hand, the stabilization of the stress relaxation in molten salts receiver, t_{stab} , is typically around 20-30 days (González-Gómez *et al.*, 2021) which, considering just the most significant hour per day, translates in 20-30 hours. In this study, t_{stab} has been set in 30 hours (108,000 seconds). However, if stress reset occurs, the stabilization time would be considered to be equal to one hour for the methodology presented in this Chapter. This is so because only the effects of the maximum daily stress relaxation are considered (which last one hour) and the daily shutdown of the installation under these stress reset conditions implies the annulment of the relaxation achieved during the day for the next start-up.

[a₄] (Boehlert & Longanbach, 2011)[d₄] (Special Metals Corp., 2013)[b₄] (Eno *et al.*, 2008)[e₄] (Zhang & Takahashi, 2018)[c₄] (Whittaker *et al.*, 2012)[f₄] (Special Metals Corp., 2004)

Table 4.6: Coefficients of the M-R-M parametrization.

Alloy	β_0	β_1	β_2	β_3
230 [b ₄]	-26.27	44158	4.72	-11337
316H [e ₃]	-35.27	47957	9.94	-15175
625 [d ₄]	-44.2641	65825	12.2	-20289
740H [a ₅]	-67.74	87260	20.12	-26560
800H [f ₄]	-19.78	36566	-0.9252	-6197

Table 4.7: Fatigue coefficients.

Alloy	T (°C)	σ'_f (%)	ε'_f (%)	c_1 (-)	c_2 (-)
230 [a ₆]	427	0.2	18	0.01	0.45
	538	0.2	45	0.0005	0.6
	649	0.2	45	0.001	0.65
316H [e ₃]	427	0.13	5.6	0.023	0.43
	482	0.1	4.95	0.015	0.46
	593	0.078	4.73	0.009	0.5
625 [b ₆]	705	0.067	3.17	0.01	0.48
	650	0.21	4.56	0.014	0.34
	815	0.15	4.92	0.01	0.39
740H [c ₆]	700	0.3	4.11	0.018	0.34
	540	0.17	37.6	0.025	0.55
	650	0.2	54	0.003	0.68
800H [f ₄]	760	0.11	32.4	0.14	0.6

Then, Table 4.6 comprises the parameters required in Eq. 4.12 to obtain the rupture time with the M-R-M parametrization. The fit is done with the data available in the rupture time versus stress plots for the different test temperatures. Lastly, the fatigue parameters to obtain the number of allowable cycles via Eq. 4.17 are included in Table 4.7. The fitting is done using the experimental half strain range (%) versus cycles to failure charts found in the literature. With the \log_{10} plot, see Figure 4.2, the tangent line to the curve at low number of cycles allows the calculation of c_2 and ε'_f as its slope and the tenth power of its independent coordinate, respectively. On the other hand, the tangent line at high number of cycles does the same for c_1 and σ'_f/E .

[a₅] (PCC Energy Group, 2020)[b₆] (Bui-Quoc *et al.*, 1988)[a₆] (Fahrmann & Srivastava, 2014)[c₆] (Abe, 2015)

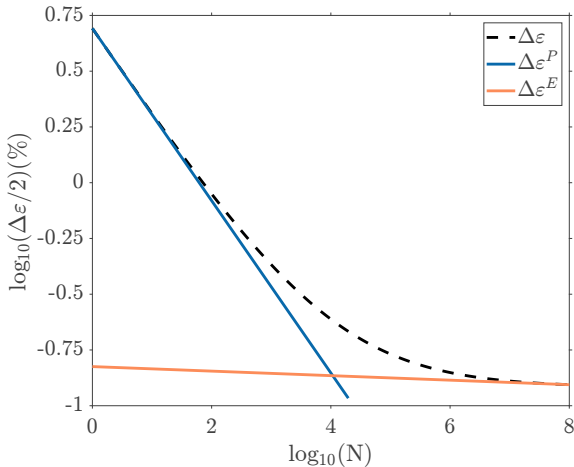


Figure 4.2: Logarithmic half strain range versus number of allowable cycles plot for Inconel 625 at 815 °C, showing the plastic and elastic regions.

4.3.3 Design day and field aiming

The heliostat field is constituted by 2,650 heliostats of 115.8 m^2 , giving a total mirror area of $306,605\text{ m}^2$; the field location selected in FluxSPT is the one corresponding to Gemasolar (Seville, Spain). Thus, the day selected to perform the analysis corresponds to the spring equinox in the Northern Hemisphere. It is a clean day, free of cloud passages and other transient interruptions. It consists of eleven sunlight hours, from 7:00 h to 17:00 h. Its interaction with the heliostat field results in an hourly symmetrical heat flux distribution on the receiver between the two paths: the 7:00 h for the East receiver path is the same than the 17:00 h for the West one, the 8:00 h for the East path corresponds to the 16:00 h for the West half, and so on, being the 12:00 h symmetrical in the N-S direction. The hourly DNI of this design day presents a maximum value of 931.6 W/m^2 at 12:00 h and a minimum of 559.2 W/m^2 at 7:00 h and 17:00 h. Hence, given the receiver location and orientation, the heat flux on its surface during the morning hours is mainly concentrated on the Western half and in the afternoon, it is mostly incident on the Eastern one.

Moreover, the aiming of the heliostat field on the receiver surface can go from an equatorial one to a flat one. To select the appropriate aiming strategy for each receiver configuration it must be considered that there are certain limitations that set the allowable flux density (AFD) on the receiver. These parameters that need to be watched prior the lifetime analysis are: the film

temperature, the salt velocity and the pressure drop from the thermal and hydrodynamic analysis, and the twice yield stress from the stress analysis. As for surpassing the twice yield strength limit, this would mean that the alloys in that situation would work in reverse plasticity regime, leading them to be subjected to dynamic aging and material hardening, increasing the stress amplitude with the number of cycles. Opposite to the elastic shakedown, occurring between S_y and $2S_y$, which causes plastic deformation only in the first one or in a few cycles before the elastic stabilization, the reverse plasticity regime does cause plastic yielding in each cycle, which is ill-advised for the receiver to last as much as expected. Hence, as starting point, the aiming strategy chosen in all the cases is $k = 3$, with the goal of obtaining the maximum thermal power out of the receiver. However, being the most aggressive one and considering the temperature and stresses limitations to guarantee the safe plant operation, it might not be suitable for all the alloys and all the hours. Consequently, the k factor would need to be reduced in the cases where the maximum film temperature or the twice yield strength limit are exceeded.

4.4 Results and discussion

The results from the integral analysis of the receiver are exposed and discussed in the following section. The starting point is to set the maximum aiming factor allowable at each hour for every alloy by performing both the thermal analysis and the elastic stresses one, considering the aforementioned limitations in such regard. Upon having established such hourly aiming strategy, the lifetime analysis is performed in terms of the creep and fatigue damages, which require the obtaining of the elastic-plastic stresses and strains. In the former case, the stress relaxation effects have been included. Lastly, a cost analysis of the receiver is undertaken by establishing a set of expected lifecycles for its operation. The panels substitutions that may be required to fulfil these operation periods, as well as the costs associated with these replacements, are considered in the study.

4.4.1 Maximum aiming factor allowable

First, the receivers studied are characterized using the heliostat field and thermal models presented in Section 4.2.1. The maximum film temperature obtained from such analysis must be kept under the safety limit specified for each alloy, which can be controlled decreasing the aiming factor of the heliostat field.

With the availability of the whole field it was found that two of the five alloys selected were not able to meet the limitation criterion imposed by such maximum film temperature allowable, regardless the aiming factor chosen. Evidently, they are the ones with the most restrictive limitation: 316H and Inconel 625. To be able to properly function with these two receivers, the heliostat field availability was reduced (this means that only a percentage of the heliostat field is aiming to the receiver surface) until the limiting film temperature was not surpassed in any case. The maximum availabilities using the flattest aiming strategy, which changes hourly, in these critical cases and hours are also included in between parenthesis and in italics in Table 4.8. For the scenarios that present no issues, the field availability is not indicated since it is the 100%.

After the thermal analysis is performed, the elastic stresses and strains on the receiver can be obtained following the method presented in Section 4.2.2, using the aiming factors that successfully meet the T_{film} limit, to check the $2S_y$ restraint. These elastic stresses are caused by the circumferential, radial and axial thermal gradients on the tube wall, the mechanical restrictions that, despite allowing its axial displacement, prevent the tubes excessive bending and the pressure stresses caused by the HTF through them. The higher elastic stresses are present in the alloys with the highest T_{film} limit value, which are Haynes 230, Inconel 740H and Incoloy 800H, since that allows more demanding aimings. They are followed by Inconel 625 and in the last place by alloy 316H, with the least permissive T_{film} limit. It was observed that, for the alloys Haynes 230, 316H and Incoloy 800H, the twice yield strength value was surpassed, which means that they worked in reverse plasticity regime. In the case of Haynes 230, this occurred just at 11:00 h, 12:00 h and 13:00 h with the aimings set from the thermal analysis, and just for the first two panels. Thus, it is not extremely critical and it can be successfully reversed by decreasing the aiming strategy factor obtained from the thermal analysis at these specific hours. However, for Incoloy 800H the issue with twice the yield strength is more severe due to its low S_y . In addition, for this alloy, it happens for nearly all the panels and from 7:00 h to 17:00 h, not being feasible to lower that much the equivalent elastic stress by modifying the aiming strategy and the field availability. For alloy 316H, the elastic stress is not as high as the one obtained for Incoloy 800H, being closer to its $2S_y$, but the heliostat field availability was already working quite below its full capacity due to the T_{film} limitation and thus this scenario cannot be avoided for this material neither. Consequently, the final aiming factors leading to the operation under, resulting from considering the

Table 4.8: Hourly maximum aiming strategy factor and heliostat field maximum availability.

Time	230	316H	625	740H	800H
7:00	3	1.8 (72%)	2.5	3	3
8:00	2.3	2.0 (43%)	1.5	2.3	2.3
9:00	2.1	2.2 (35%)	2.2 (73%)	2.0	2.1
10:00	2.1	2.3 (35%)	2.3 (69%)	2.0	2.1
11:00	2	2.3 (34%)	2.3 (73%)	2.2	2.3
12:00	2	2.3 (35%)	2.3 (76%)	2.4	2.4
13:00	2	2.3 (34%)	2.3 (73%)	2.2	2.3
14:00	2.1	2.3 (35%)	2.3 (69%)	2.0	2.1
15:00	2.1	2.2 (35%)	2.2 (73%)	2.0	2.1
16:00	2.3	2.0 (43%)	1.5	2.3	2.3
17:00	3	1.8 (72%)	2.5	3	3

T_{film} and the $2S_y$ restrictions are included in Table 4.8. The aiming strategy is obtained jointly for the Eastern and Western halves, watching the limits of both, instead of proposing a different aiming strategy for each half according to their specific needs dictated by the incident heat flux on them. Therefore, given the symmetry of the DNI with respect solar noon, the strategies result likewise symmetrical, being the Western half the most restrictive one during the morning and the Eastern one during the afternoon.

Now, the resulting evolution of the maximum film temperature, obtained for the final hourly aiming strategies, is presented in Figure 4.3 following the Eastern HTF path. Thus, the first panel is comprehended between $z = 0$ m and $z = 10$ m, panel two between $z = 10$ m and $z = 20$ m, and so on. The behaviour of the Western panel, given the hourly symmetry of the design day with respect the N-S direction, is the same than the Eastern one but inverted with respect time. As mentioned earlier, it can be sensed through this Figure the greater amount of concentrated heat flux on the Eastern half at the afternoon over the morning, given the greater the temperatures on the tube during these hours. Note that the T_{film} for the central hours of the day for Haynes 230 receiver is slightly below its limit since an aiming factor reduction was required after the stress analysis to meet the $2S_y$ limit criterion.

Then, the elastic stresses at the tube crown, which is the most critical spot (as shown in Chapter 3), for the alloys selected at their corresponding aiming

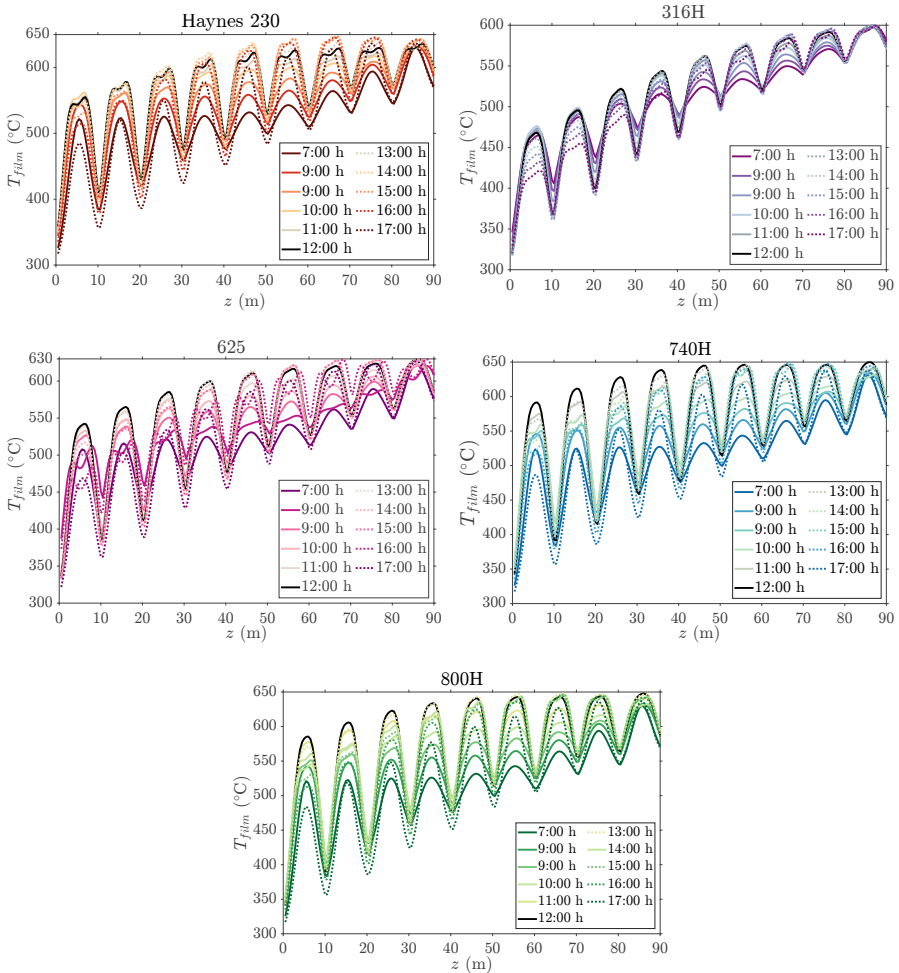


Figure 4.3: Maximum film temperature for every alloy, depicted hourly.

strategy and heliostat availability are presented in Figure 4.4, following again the Eastern HTF path. The hour selected has been the 12:00 h since it is one of the most aggressive, jointly with 11:00 h (and 13:00 h, mirrored), and because of the symmetry between the two flow paths. The twice yield strength value is also included (dashed lines, evaluated at the corresponding temperature for each cell) for the problematic alloys in this regard, showing that Haynes 230 is now below such limit and alloy 316H and Incoloy 800H remain above it.

Once the aiming strategies have been set according to the AFD limits, and before advancing to other stress and lifetime issues, additional receiver criti-

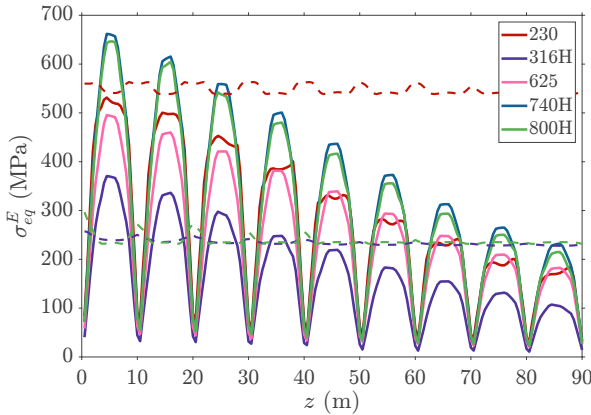


Figure 4.4: Equivalent elastic stress at the tube crown at 12:00 h for the different alloys under the aiming strategies of Table 4.8 and $2S_y$ limit (dashed lines) for alloys Haynes 230, 316H and 800H.

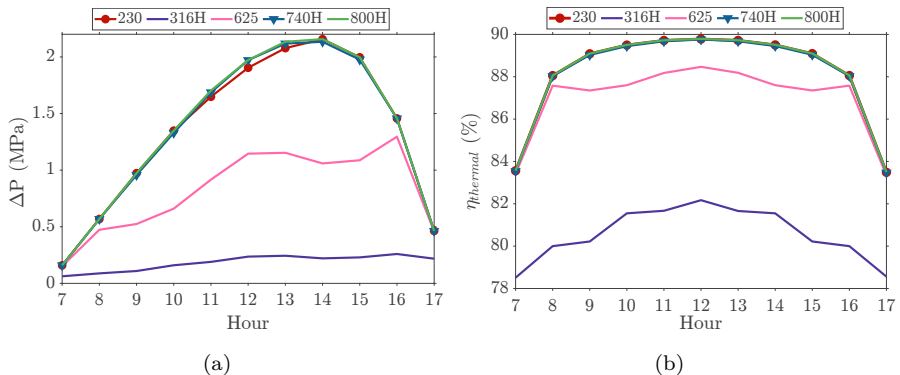


Figure 4.5: Hourly depiction of (a) Pressure drop in the Eastern path and (b) Receiver thermal efficiency.

cal factors need to be watched, such as the pressure drop on the receiver or the maximum HTF velocity. The higher the pressure drop on the receiver, the higher the pumping power required to operate it, causing the increase of the parasitic losses of the plant. An acceptable value for such maximum pressure drop is around 20 bar (Rodríguez-Sánchez *et al.*, 2014*b*), with the receiver studied operating around these conditions in the worst scenarios in such regard (Haynes 230, 740H and 800H). Figure 4.5(a) depicts the hourly results through the Eastern half, with the Western one behaving symmetrically. The velocities of the HTF through the receiver present the same hourly evolution as the pres-

Table 4.9: Receiver thermal power for the design day.

Time	230	316H	625	740H	800H
Thermal power (MWt)	115.97	40.82	89.72	116.18	116.64

sure drop, given their relation; the maximum value is just shy of 6 m/s, also obtained for the alloys with the maximum pressure drop.

Lastly, given that very different aiming strategies and heliostats availabilities must be adopted so the AFD limits are not surpassed, it is useful to provide the thermal efficiency, and thermal power of the set of receivers analyzed. The thermal efficiency in each case is shown in Figure 4.5(b), with the thermal power presenting the same trend. To get a better sense of the difference between each receiver configuration in terms of thermal power, the ones obtained during the design day for the different receivers are comprised in Table 4.9. It is observed that the three alloys with the most similar aiming factors allowable—Haynes 230, 740H and 800H—present both the higher thermal efficiency and thermal power. This can be explained by their higher film temperature limit with respect the rest of the alloys studied. Consequently, the following receiver in terms of such power and efficiency is the one in Inconel 625, with a film temperature limit of 630 °C, and the worst one is 316H alloy, highly penalized by its early thermal corrosion limit.

4.4.2 Creep-fatigue results: lifetime analysis

Equivalent elastic stresses and strains

In the previous section, the equivalent elastic stresses were obtained to set the maximum aiming factor allowable in the receiver surface. Subsequently, it has been checked if the maximum equivalent elastic stress obtained with the hourly aiming configuration of Table 4.8 is below the shakedown stress range, ($\Delta\sigma \leq 2S_y$). In contrast, the stress reset limit ($S_{y,cold} + S_H$) has not been considered as a limiting factor in terms of the aiming strategy selection, but it will determine the way the alloys respond in regard to the stress relaxation. With the final aiming strategy, Haynes 230 exhibits no issues in this aspect, as well as alloys Inconel 625 and Incoloy 740H (see Figure 4.6). On the contrary, both alloys 316H and Incoloy 800H surpass the stress reset limit at certain positions along the flow path and thus these will suffer from stress reset after the daily shutdown of the plant. Even if some z position does not present elastic

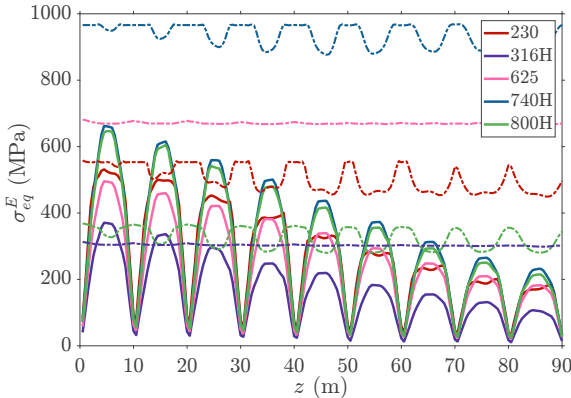


Figure 4.6: Equivalent elastic stress at the tube crown at 12:00 h and the corresponding stress reset limit for each alloy.

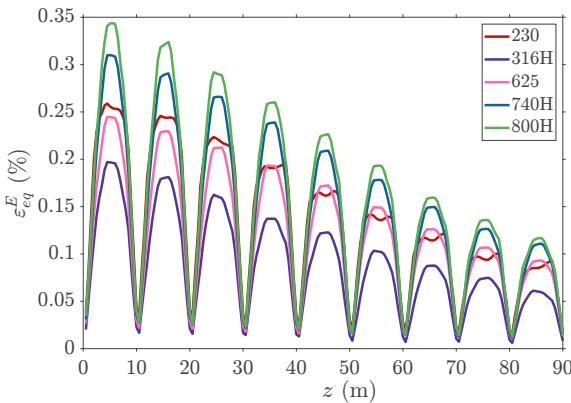


Figure 4.7: Equivalent elastic strain at the tube crown for the different alloys at 12:00 h.

stresses above the stress reset limit at certain hours of the day, if such value is exceeded at least once during the daily operation, such receiver spots are still regarded to work under stress reset. For instance, the alloy 316H receiver only shows stress reset at the central sections of the first two panels (panel one from $z = 0$ m to $z = 10$ m and panel two from $z = 10$ m to $z = 20$ m), while the receiver in 800H presents issues in up to the seventh panel, with at least one spot working under stress reset at a certain time. The rest of the axial positions would relax under the shakedown to elastic cyclic conditions, just as the totality of the Haynes 230, Inconel 625 or Inconel 740H receivers do.

On the other hand, the elastic strains, needed for the fatigue damage calculation, are presented in Figure 4.7, again following the HTF path and at 12:00 h. The maximum strain is roughly a 0.35% for Incoloy 800H, the alloy presenting

the greater ones. This implies that these alloys are way below concerning strain values for fatigue damage.

Equivalent elastic-plastic stresses, stress relaxation and creep stresses

Once the elastic stresses are known, the elastic-plastic stresses are calculated by following the methodology in Section 4.2.3 and using the monotonic and cyclic coefficients, compiled at Table 4.4, obtained for the different alloys by fitting the manufacturers and experimental data available in the literature. Subsequently, the stress relaxation is obtained with such equivalent elastic-plastic stress, which finally gives out the creep stress.

As mentioned during the methodology exposition, the stress relaxation at a certain height working below the stress reset limit remains the same during the whole day since it is evaluated at the T and σ_{eq} combination resulting in the greatest value, out of the ones obtained hourly from the operation of the receiver under the aiming strategies at Table 4.8. Conversely, for the spots of the receivers in alloy 316H and Incoloy 800H above the stress reset limit, the stabilization time results, from a practical point of view, in one hour since they suffer from stress reset after the daily shutdown. Hence, in such scenario, instead of considering the stress relaxation effects during the whole day, they are only accounted after the hour at which the maximum relaxation occurs. With that in mind, the final creep stress is obtained by means of Eq. 4.7. An instance of the stress relaxation behaviour for each alloy is depicted in Figure 4.8. Alloy 316H has been omitted since it barely relaxes due to its mild working conditions.

On the one hand, Figure 4.8(a) shows the stress relaxation influence on the creep stress for Haynes 230, Inconel 625 and Inconel 740H over 40 days. This is enough time to capture the full stress relaxation of these alloys during their cyclic operation, given that their t_{stab} has been set to 30 hours. This is equivalent to 30 days since the relaxation is accumulated just one hour per day considering a continuous exposure to the maximum temperature (González-Gómez *et al.*, 2021). In the three cases, the z position selected to show its relaxation is the one reaching the greatest value in the whole receiver. For Haynes 230, such location is $z = 54$ m (sixth panel) and happens at 14:00 h. Inconel 625 reaches the maximum relaxation at $z = 46$ m (fifth panel) and at 13:00 h. Lastly, Inconel 740H is illustrated with the 12:00 h of $z = 26$ m (third panel). After the t_{stab} , the stress relaxation is considered fully deployed and hence the following days present a constant value of it, having reached the global stress relaxation; then, that is the stress relaxation that would be

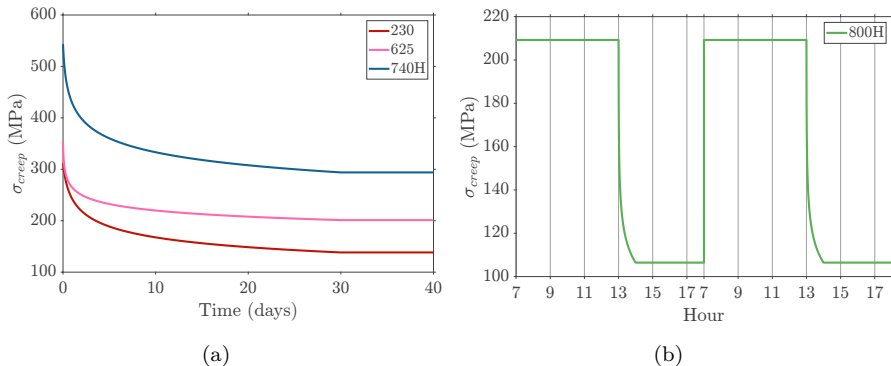


Figure 4.8: (a) Creep stress achieved after full relaxation for Haynes 230, Inconel 625 and Inconel 740H, working under the shakedown to elastic cyclic regime. (b) Creep stress after relaxation for Incoloy 800H, working in stress reset regime, for two consecutive operating days.

finally used in Eq. 4.7 for the corresponding z in each case and during all of the daily operation hours. The same procedure is used for the rest of the axial positions, using their maximum stress relaxation during the day. On the other hand, Figure 4.8(b) depicts an instance of the stress relaxation behaviour under stress reset conditions at the $z = 46$ m (fifth panel) spot of the Incoloy 800H receiver, which coincides with the maximum relaxation obtained on such receiver and indeed works under stress reset. In this case, the operation hours of two consecutive days have been presented to show the stress reset effect. Hence, looking at such Figure, becomes evident that the criterion to set in the spots surpassing S_{SR} is to consider the stress relaxation only after the time at which the maximum relaxation occurs (in the z depicted, from 14:00 h to 17:00 h). The spots that do not fall in the stress reset regime would behave just as the alloys in Figure 4.8(a).

Additionally, to get a better sense of the temperature and stress ranges at which every alloy could be able to benefit from the stress relaxation, the creep stress for the studied alloys is depicted in Figure 4.9 as a function of the temperature and the equivalent stress solicitation. It has been obtained by using Eqs. 4.7 and 4.11 with the coefficients of Table 4.5 at a fixed t_{stab} of 30 hours for all the alloys. It must be noted that when the hold time of the solicitation reaches a high enough value, having a fixed temperature and stress, the stress relaxation becomes constant (Yan *et al.*, 2015). Hence, the stabilization time has been selected to fulfill that for all the alloys. In addition,

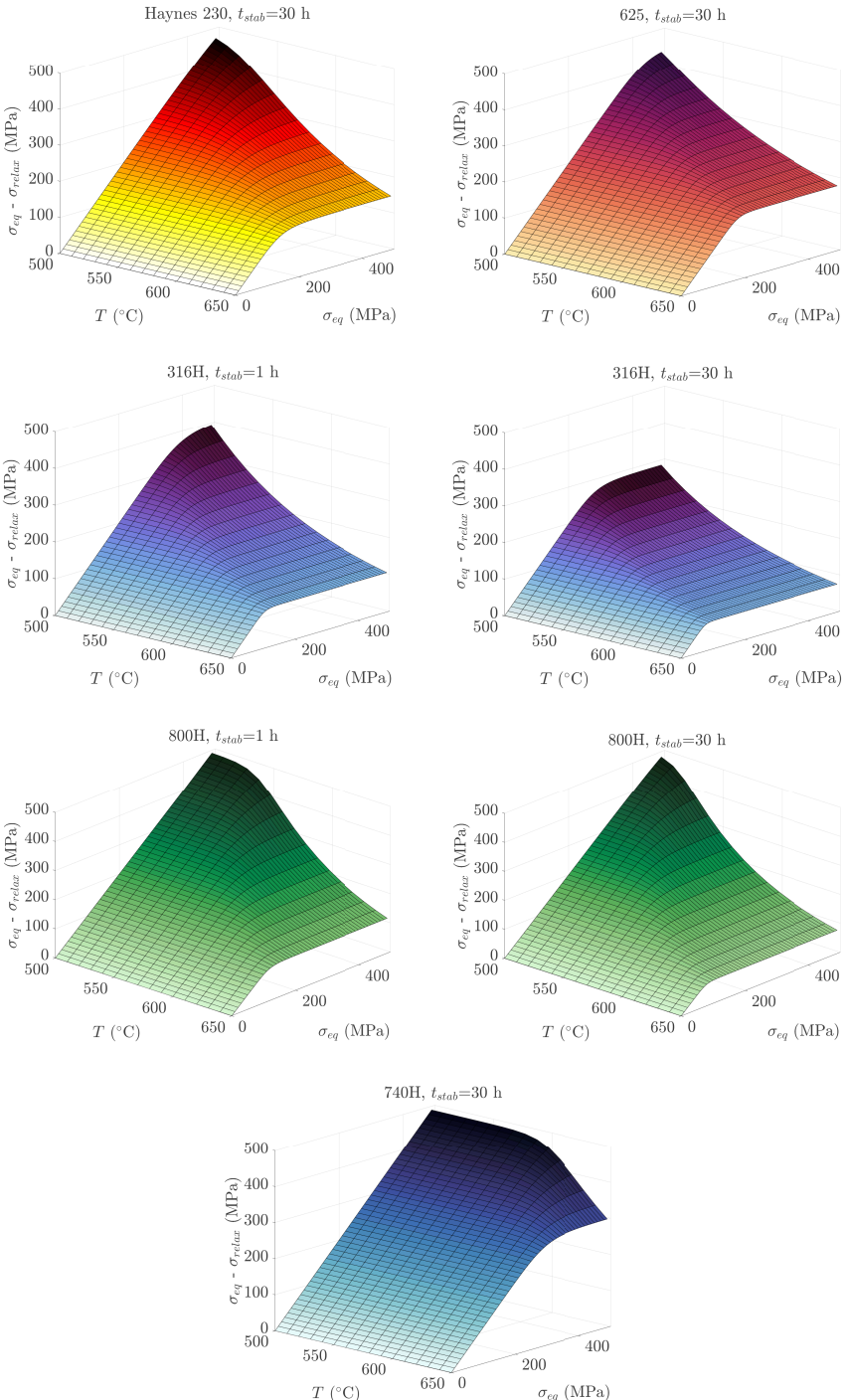


Figure 4.9: Effect of stress relaxation in terms of the creep stress as function of the temperature and elastic-plastic equivalent stress solicitation.

for the two alloys presenting stress reset at certain points, alloy 316H and Incoloy 800H, the creep stress as function of temperature and elastic-plastic equivalent stress has also been depicted for a t_{stab} of 1 hour, capturing how they would behave under such regime. The linear evolution of the resulting $\sigma_{eq} - \sigma_{relax}$ (or σ_{creep}), observed in Figure 4.9 for certain values of the σ_{eq} solicitation at a fixed temperature, implies that the alloy is not suffering stress relaxation at these temperatures and stresses; thus, more aggressive working conditions would be needed for stress relaxation to start happening. It is worth remarking that at a fixed temperature, once the alloy is undergoing through stress relaxation, when increasing σ_{eq} it will continue relaxing in a fashion that implies that σ_{relax} grows proportionally with such solicitation, since the resulting σ_{creep} becomes a constant value. Notable differences can be observed between having a t_{stab} of 1 hour or a t_{stab} of 30 hours, being the latter way more favorable, especially for alloy 316H.

However, it should be noted that the stress relaxation translates in permanent inelastic strains, enlarging the hysteresis loop during hold periods (Jeong *et al.*, 1999) and reducing the alloys fatigue life, although this adverse effect is presumably diminished with the increase of the hold time (Brinkman *et al.*, 1976). Thus, an extremely high stress-relaxation can favour the results of the rupture time in terms of creep, since it reduces the effective creep stress solicitation on the alloy, but it eventually leads to the exhaustion of its ductility (Payten *et al.*, 2013) and an excess of fatigue, which could cause unexpected early failure not predicted by the creep rupture time. Such conditions are obtained when the stress reset limit is surpassed, where the creep-fatigue damages are combined, and the time-to-failure is dramatically reduced.

Subsequently, Figure 4.10 shows the elastic stress, equivalent elastic-plastic stress and creep stress for the alloys studied at the tube crown at 12:00 h as well as 17:00 h (Eastern path), in order to present a better depiction of the ranges of the different stresses during this particular design day. These two hours are the ones with the higher and lower σ_{eq} , respectively. This may seem to contradict the fact that the Eastern side of the receiver is subjected to a higher concentrated heat flux in the afternoon. However, during the first morning hour, the first panel of this half suffers from a higher peak stress than any panel during the last hour of the afternoon, when the stresses result to be overall higher but more evenly distributed, translating in a slightly lower peak stress despite the greater solar radiation incidence. Alloys Haynes 230, Inconel 625 and Inconel 740H relax normally, under the shakedown to elastic cycling regime, in a greater

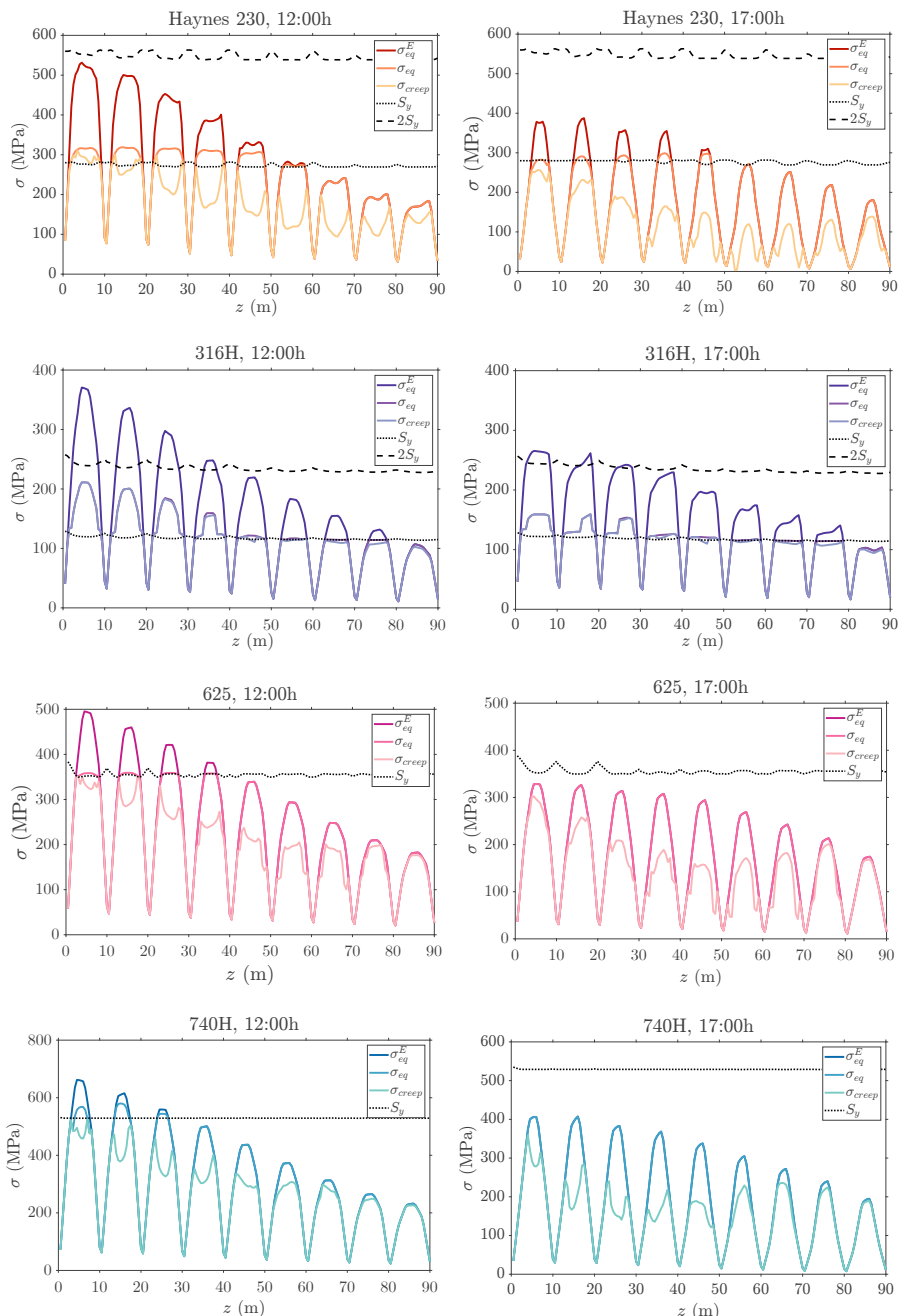


Figure 4.10: Elastic stress, elastic-plastic equivalent stress and creep stress for the alloys studied at the tube crown, at 12:00 h and at 17:00 h.

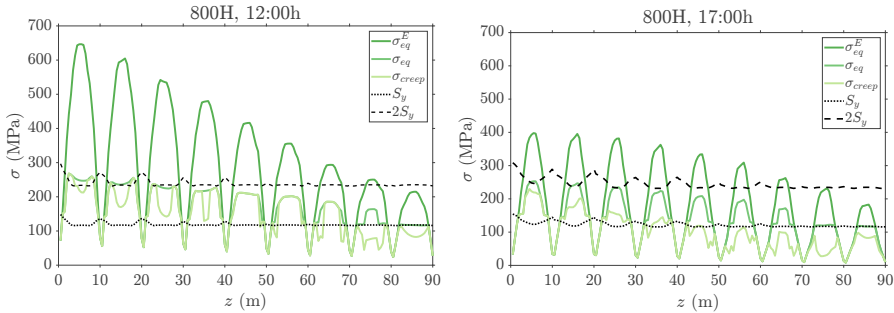


Figure 4.10: Elastic stress, elastic-plastic equivalent stress and creep stress for the alloys studied at the tube crown, at 12:00 h and at 17:00 h (cont.).

or less deal depending on their characteristics and the temperature and elastic-plastic stress conditions at which they operate. On the other hand, alloy 316H barely relaxes due to its low T_{film} limit, which prevents it from reaching high enough temperatures and elastic-plastic stresses. Moreover, the first two panels, with stress reset, relax roughly 1 MPa. In addition, note the behavior of the Incoloy 800H receiver: the creep stress at 12:00 h is the same than the elastic-plastic one at middle length of the fifth, sixth and seventh panels; however, they have indeed relaxed at 17:00 h. The reason for such outcome is that these spots fall under the stress reset conditions (Figure 4.8) and the maximum stress relaxation at these positions occur after midday. This means that since the stress relaxation is only considered for them after the time at which the maximum value occurs and, after the daily shutdown, the following day they will start at their initial stress level, these spots appear not relaxed during the morning hours. Thus, the moment of the maximum stress relaxation is crucial for the alloys with stress reset in this study, since the earlier it happens, the more hours they can benefit from it. In any case such approach errs on the safety side. For the alloys working in the shakedown to elastic cyclic conditions it is irrelevant in such regard since the relaxations is accumulated through the shutdowns and start-ups.

Equivalent operating days

Upon knowing the creep stress, the d_c can be obtained with the methodology presented in Section 4.2.3. A key aspect of such method is the rupture time calculation, in this case using the M-R-M parametrization with the coefficients in Table 4.6 for each alloy. In Figure 4.11, the rupture time of each alloy is

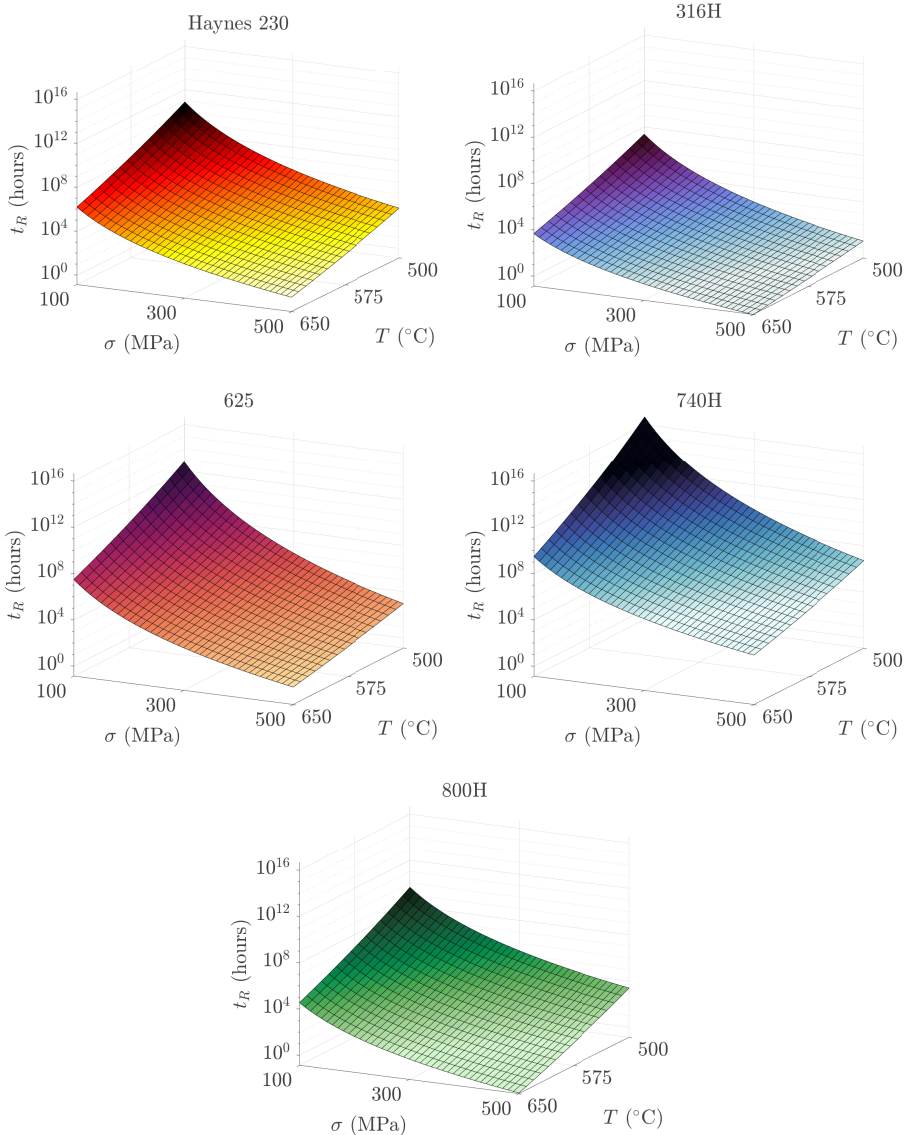


Figure 4.11: Rupture time as function of the creep stress and the temperature.

presented likewise it was previously done with the stress relaxation: as a surface depending on the temperature and the stress (Eq. 4.12). This representation, made for the same temperature and stress ranges for every case, provides a clearer picture of the creep endurance of each material. As it can be seen, Inconel 740H presents the greater creep resistance, followed by Inconel 625.

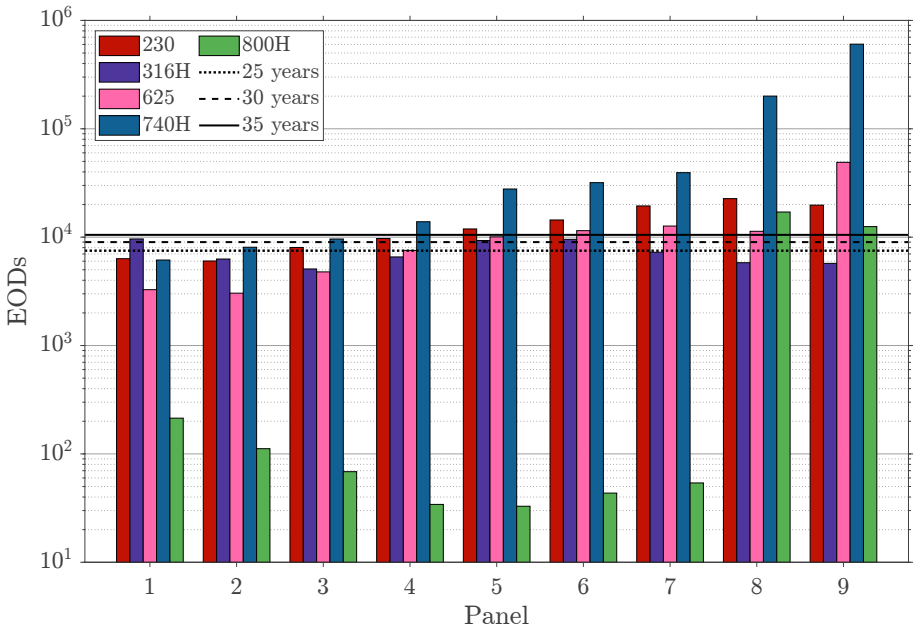


Figure 4.12: EODs for the alloys studied, Eastern path.

The alloys 800H and Haynes 230 show a similar behavior between them, while alloy 316H has the poorest endurance in this regard. Despite the temperature range on the receiver surface is very limited, with the lower bound of around 500 °C and the upper around 650 °C, and despite these are not especially high temperatures, a great descend on the rupture time is experienced when the temperatures increase from the lower to the upper limit, at a fixed stress. Given the high sensitivity to the temperature and stress that the rupture time has, the regard of the stress relaxation results essential in the lifetime estimation.

With both the creep and fatigue damages, the EODs are obtained for each receiver configurations. Figure 4.12 depicts the results for the Eastern path. It should be noted that, for the clean design day, the fatigue damage is negligible in comparison to the creep damage, being the latter the limiting factor. A similar outcome has been previously observed in other works available in the literature (González-Gómez *et al.*, 2021; Conroy *et al.*, 2018a; Ortega *et al.*, 2016). Given the low entity of the fatigue damage in comparison with the creep one, the initial assumption of the D_L as equal to unity is more than reasonable. In Figure 4.12, three reference marks of 25, 30 and 35 years, considering 300 EODs per year, have also been included to analyze the impact of selecting the different alloys in potential plants with different projected lifecycles.

The outcome regarding the EODs obtained highlights the importance of the stress relaxation phenomenon. Looking at the effect that the stress relaxation occasioned in the studied alloys (Figure 4.10, difference between σ_{eq} and σ_{creep}) and given the high sensitivity of the rupture time to the stress applied (Figure 4.11), had this effect not been considered, the lifetime of these receivers would have been dramatically reduced, leading to an excessively conservative result. Haynes 230, Inconel 625 and Inconel 740H are the alloys benefitting the most from the stress relaxation since they are working under elastic cyclic shakedown without stress reset. On the other hand, alloy 800H is highly penalized by the stress reset present at the middle length of the first seven panels, with EODs going from 214 days to just 33. Its last two panels, however, benefit from stress relaxation and can last up to 40 years, considering 300 EODs per year. Lastly, alloy 316H is subjected to low elastic-plastic stresses at being insufficient for the material to relax but still low enough to allow an acceptable overall lifetime of the receiver.

The minimum EODs for each receiver are depicted in Figure 4.13(a). The limiting panels, understood as the ones presenting the lesser EODs, are the first one for Inconel 740H, the second panel for Haynes 230 and Inconel 625, the third panel in the alloy 316H receiver and the fifth panel in the case of Incoloy 800H. Inconel 740H and Haynes 230 are the two alloys with the higher expected lifetime in their corresponding critical panels, around 20 years. Due to their great corrosion resistance, these are also two of the three alloys being able to provide with the highest thermal power (Table 4.9), alongside with 800H, whose poor performance in regard the EODs, the worse out of the five alloys, makes it the least desirable option. Then, alloy 316H is just shy of a 17-year lifetime. Nevertheless, the thermal power it can produce is a 65% less than Haynes 230, 740H and 800H. Lastly, Inconel 625 is the fourth most lasting alloy, with the limiting panel being just over 10 years. Also, it provides around a 24% less thermal power than Haynes, 740H and 800H, but more than twice than alloy 316H.

Subsequently, all the receivers would need panels substitutions to be able to withstand at least a 25-year operation. The total number of panel substitutions, s_p , for each receiver are presented in Figure 4.13(b) for expected lifetimes of 25, 30 and 35 years. The Inconel 740H receiver would need the substitution of the first panel in both path flows (two in total) to last up to 25 years; from that, the substitution of the second panel of each path and the replacement of third ones would be also required for the receiver to operate 30 and 35

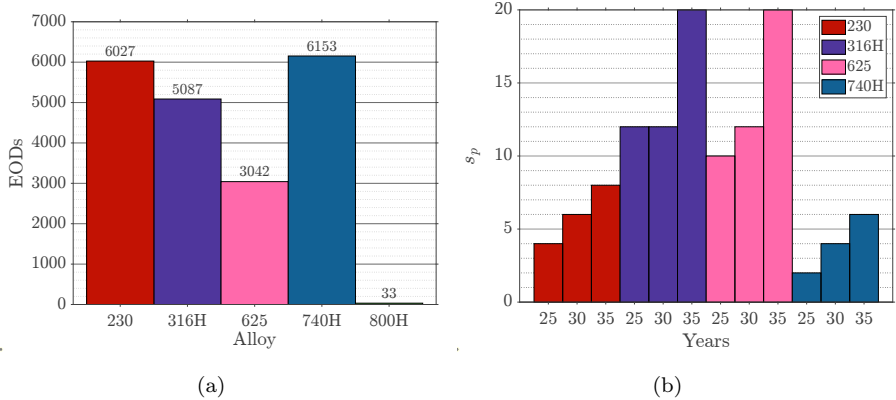


Figure 4.13: (a) Minimum EODs for a receiver panel. (b) Number of total panels substitutions in the different receivers to achieve an operation of 25, 30 and 35 years.

years, respectively. Then, the Haynes 230 receiver needs the substitution of the first two panels of each path (four in total) to operate 25 years; in the same way as the Inconel 740H receiver, the additional replacement of the two third panels and the two fourth panels would be required to reach the 30 and 35-year marks, respectively. Then, alloy 316H demands substitutions for the second, third, fourth, seventh, eighth and ninth panels, making it a total of twelve changes for the whole receiver, to last both 25 and 30 years. When aiming to reach a 35-year lifetime, the first, fifth and sixth panels (and thus, the whole receiver) need replacement as well, plus a second substitution in the third panel. Lastly, despite the limiting panel of Inconel 625 lasting less EODs than 316H, it requires a total of five panel changes per path flow, ten in the whole receiver, when aiming for a 25-year operation: two in the first two panels and just one on its third panel. However, it should be noted that certain panels require multiple substitutions for this 25-year goal, which alloy 316H does not experience until the 35-year operation limit. Then, in order to last 30 years, the additional replacement of the two fourth panels is required. For the 35-year mark, the substitution of the fifth panel is needed as well, joined by a third replacement of panels 1 and 2 and a second change of panel 3. Incoloy 800H has been excluded from Figure 4.13(b) since it would need a total of 830 s_p among the first seven panels of each path just to reach the 25-year mark.

Additionally, it must be noted that exceeding the $2S_y$ value entails the appearance of large plastic deformations, which can jeopardize the receiver integrity. For such reason, given the alarmingly high elastic stresses at which

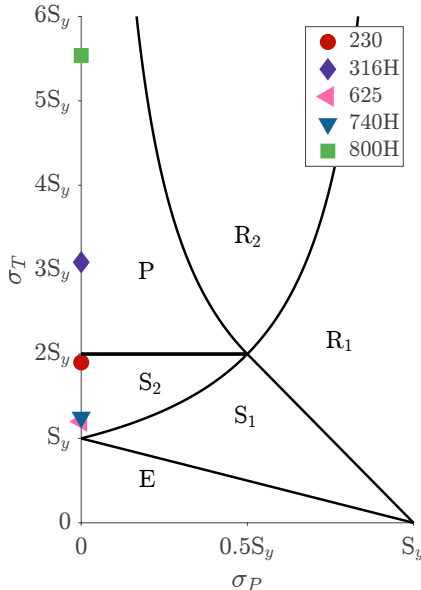


Figure 4.14: Stress regimes diagram with the most critical regimes found for each alloy.

Incoloy 800H and alloy 316H are working, way over $2S_y$, their installation is ill-advised. For instance, the first four panels of the receiver in alloy 316H surpass such limit despite presenting acceptable EODs. Moreover, such receiver also needs to operate with unusually low aiming factors and heliostat availabilities in order to fulfill the maximum T_{film} admissible and so avoid the molten salts corrosive effects on its inner wall, leading it to undesirable low thermal efficiency and power. Looking back, lower carbon variants of these two (and thus, with a poorer creep and rupture properties), Incoloy 800 and alloy 316, were the ones used in Solar Two and Solar One respectively, without promising results: Incoloy 800 suffered from multiple cracks and alloy 316 was advised to be replaced with an advanced higher nickel alloy.

Related to the regimes at which the alloys operate, Figure 4.14 shows where each alloy is located at the Bree diagram (Bree, 1967) in terms of the higher elastic stress that they experience. This diagram depicts the stress regimes that the materials can present as a function of the thermal and pressure stresses with respect their yield strength S_y . Given that the pressure stresses (primary stresses) in the receiver tubes are almost negligible with respect the thermal ones (secondary stresses), none of the cases studied fall inside the ratcheting region, being the elastic (E), the elastic shakedown (S_2) and the plastic cyclic

regime (P) the only ones relevant in this study.

With all of that in mind, the high lifetime obtained for Inconel 740H makes it the best candidate. Haynes 230 can match it if the elastic limits are watched. Inconel 625 also presents fairly good results, but its lower corrosion resistance causes it to have a lower thermal efficiency and supply less thermal power than the other two alternatives.

4.4.3 Receiver costs

To obtain the cost of a SPT receiver expected to last the lifetime periods discussed in the previous section, the prices of the different alloys, included in Table 4.3, involved in the manufacturing of receiver tubes and headers are multiplied by their weight, the number of them constituting a panel (61 tubes, two headers) and the total panels needed for that specific lifespan, which are the initial amount plus the number of substitutions required during such period, Figure 4.13(b). Also, there are other items whose cost is directly associated with the durability of the receiver tubes, since they need to be replaced with them, such as the coating paint or the different weldings in the tubes. These are relevant in the cost analysis of the receiver from the tubes point of view, especially when dealing with the uneven amount of panel substitutions occurring among the various alloys options. The cost of the Pyromark 2500 ceramic painting is estimated to be around 287 \$/m² (Ho & Pacheco, 2014). Moreover, the cost of its initial application on the receiver tubes and expected reapplications during the receiver lifetime is dissected in (Boubault *et al.*, 2017), including aspects such as the preparation of the coating and substrate, the application of the coating and other treatments required. These costs (2017) have been adjusted to inflation in this analysis. On the other hand, the cost of weldings of the tubes to clips and headers, as well as the cost of the nozzles installation in each header are available in (Kelly *et al.*, 2010), all of them referred to as specialty costs. Each tube is connected to two nozzles and is welded to two headers and six clips. The welding of the tubes-to-header require 1.5 man-hours, the tubes-to-clip ones need 1 hour, and the nozzles demand 2 man-hours, with the cost estimated to be of 65 \$/man-hour (2010); this has also been adjusted to inflation, giving a cost of 77.35 \$/man-hour.

Table 4.10: Receiver costs.

Alloy	Life (yrs)	Thermal power (MWt)	Alloy price (\$/kg)	Total N_p	Total alloy cost (\$)	Total coating cost (\$)	Total specialty cost (\$)	Total receiver cost (\$)	Ratio (\$/MWt)
230	25	115.97	88	22	918,554	580,081	1,349,448	2,848,082	24,559
	30	40.82	5	24	1,002,058	664,755	1,472,125	3,138,939	27,067
	35			26	1,085,563	749,429	1,594,802	3,429,795	29,575
316H	25	89.72	70	30	63,429	684,554	1,840,157	2,588,140	63,404
	30			30	63,429	743,110	1,840,157	2,646,696	64,838
	35			38	80,344	906,139	2,330,865	3,317,348	81,268
625	25			28	883,057	658,436	1,717,479	3,258,973	36,324
	30			30	946,133	743,110	1,840,157	3,529,399	39,338
	35			38	1,198,435	906,139	2,330,865	4,435,439	49,436
740H	25			20	812,523	553,962	1,226,771	2,593,256	22,321
	30	116.18	95	22	893,775	638,637	1,349,448	2,881,860	24,805
	35			24	975,027	723,311	1,472,125	3,170,463	27,289

The costs related to having to shut-down the plant to undertake the panels substitutions are omitted since, with the forecast of their expected lifetime, they can be scheduled in advance to take place in unfavorable operation conditions, such as a series of winter days. If considered, these would penalize the Inconel 625 receiver over the rest of alternatives in the 25, 30 and 35-year lifespans since it presents panels that need to be replaced more than once. Alloy 316 would be penalized only in the 35-year alternative. For the rest of the cases, even if the panels would need to be replaced at different times, a synchronized substitution could be programmed as well.

As the result of all the above, a summary of the different aspects considered in the present costs comparison is shown in Table 4.10, having omitted the Incoloy 800H receiver due to its poor results, as commented in Section 4.4.2. Moreover, the ratio of the receiver cost over the thermal power that such receiver can produce in the design day is included. Given the disparity found in the operating conditions that these receivers can endure, it is a suitable metric to compare them. The general costs distribution is around a 30% due to the alloy cost, around a 20% due to the coating and a 46-50% due to the specialty costs. The only exception is the alloy 316H receiver, given the extraordinary low price of such material. However, despite that low alloy price, such receiver is highly penalized by the multiple panel substitutions that it must face to fulfill the various expected lifetimes; hence, its total cost ends up being similar to the cost of the receiver in 740H, the most enduring material but also the most expensive one, and even surpasses it for a 35-year operation. Just one step above these two is the receiver in Haynes 230. The most expensive receiver, the one in Inconel 625, is also handicapped by the various panel substitutions. Moreover, its alloy price is not that far from the most expensive alternatives. Nevertheless, if the thermal power of these receivers is considered, the one in alloy 316H is unarguably the worst performing, followed by the Inconel 625 receiver and the ones in Haynes 230 and Inconel 740H, with the last two being almost on par.

As for the obtaining of the LCOA of the studied receivers, the Inconel 740H alternative has been chosen as the reference receiver for being the one providing the lowest cost/power ratio. The LCOA results and the values of the terms involved in Eq. 4.19 are included in Table 4.11, with the ones involving the reference receiver appearing in italics. The results show that Haynes 230 LCOA is sustained over the studied lifetime periods. On the contrary, alloy 316H one descends over time, while Inconel 625 presents a minimum in the 30-

Table 4.11: LCOA of the receiver alternatives.

Reference		740H			
Alloy	Life (yrs)	$C_{\text{alloy},i}$ (\$/yr)	$E_{\text{alloy},i}$ (MWh/yr)	C_{ref} (\$/yr)	LCOA (\$/MWh)
230	25	36,742		103,730	0.01
	30	33,402	382,701	96,062	0.01
	35	31,016		90,585	0.01
316H	25	2,537		103,730	0.28
	30	2,114	134,706	96,062	0.26
	35	2,296		90,585	0.25
625	25	35,322		103,730	0.09
	30	31,538	296,076	96,062	0.08
	35	34,241		90,585	0.09
740H	25	32,501		103,730	0
	30	29,793	383,394	96,062	0
	35	27,858		90,585	0

year mark. Overall, looking at both the LCOA and the cost over thermal power ratio, the extension of the plant operation does not alter the global tendencies in between receivers, being the results very robust in such regard: the best alternative is always the Inconel 740H receiver, followed by the Haynes 230 one, and the worst is the alloy 316H receiver.

4.5 Conclusions

A set of SPT molten-salt cylindrical central receivers has been analysed from the lifetime point of view and the costs this implies, them being made of different alloys commonly used in the present or similar applications: 316H, Haynes 230, Inconel 625, 740H and 800H. The analytical model used for that end allows us to estimate the creep-fatigue damage and it is based on experimental data available in the literature. Also, as a part of this study, the corresponding coefficients needed in such model have been obtained for each alloy by fitting the mentioned data.

The analysis is performed for the same clean design day in all the cases, with an hourly time resolution. However, the limitation of the film temperature to avoid the salt excessive corrosive effects, and the look for the elastic shakedown

regime working conditions (elastic stresses below $2S_y$), imposes the need of using different aiming strategies, and even heliostat field availability, for each receiver, causing a disparity in the thermal power these receivers can offer. Especially critical is the case of the 316H alloy, whose low maximum admissible T_{flim} set its thermal power to be around just one third of the maximum one obtained for the set of receivers. For the same reason, the next receiver on the list in terms of thermal power is the Inconel 625, being the Haynes 230, the 740H and the 800H receivers the best alternatives in this regard.

Upon having established the aiming strategies, the effective creep stresses can be obtained, taking into account the stress relaxation in each case, which enables us to obtain the creep damage on the receiver more accurately. In this case, the receivers in alloys 316H and 800H have the great disadvantage of working under stress reset conditions ($\sigma_{\text{eq}}^E > S_{y,\text{cold}} + S_H$), not being able to accumulate stress relaxation over the daily plant shutdowns. On the other hand, the fatigue damage is negligible in all the receivers due to the clean design day with no transient interruptions. Then, the lifetime results show the clear dominance of the 740H receiver over the rest. Its limiting panel lasts just over 20 and a half years and is the receiver requiring the least amount of panel substitutions to fulfill an operating lifetime of 25, 30 and 35 years. The next best performing receiver is the Haynes 230 one, also lasting just shy of 20 years but requiring the substitution of two more panels with respect the 740H one in each lifecycle mark. Then, alloy 316H receiver is the one needing the greatest number of panel substitutions for the 25-year operation and is at par with the Inconel 625 receiver for the 30 and 35-year ones. The minimum EODs for the former are 5,087 (around 17 years) and requires multiple substitutions of the same panel just once and for the 35-year lifetime scenario. On the other hand, the Inconel 625 receiver limiting panel lasts only 3,042 (just over 10 years), below half the projected plant lifetime in all the cases. Thus, some of its panels require more than one substitution, even for the 25-year operation, with some of them needing a triple replacement to last up to 35 years. Lastly, the Incoloy 800H receiver performs poorly, with the least lasting panel operating during just 33 EODs.

A cost analysis is lastly fulfilled, considering just the receiver elements affected by the panel substitutions—receiver tubes, headers, coating, weldings and nozzles—given the great differences observed in this regard among the receivers. This analysis is also motivated by the big gap in terms of thermal power they can supply. With these aspects in mind, both Inconel 740H and Haynes 230

receivers validate their suitability over the rest, in terms of total receiver cost over thermal power and of their LCOA, despite being the two most expensive alloys. Moreover, the Inconel 625 receiver overtakes the alloy 316H one, with the latter penalized by its low thermal power and despite the former being more expensive and presenting a lower minimum EODs mark.

Nomenclature

A	tube cross section area (m^2), stress relaxation constant $(1 / (Pa^{n_r} s))$	N	constant fatigue cycles
a	tube inner wall radius (m)	n	monotonic strain hardening exponent
b	tube outer wall radius (m)	n'	cyclic strain hardening exponent
C	cost (\$/year)	N_p	number of panels
C'	creep stress safety factor	n_r	stress power law for creep strain model
c_1, c_2	Manson-Coffin equation exponents	N_t	number of tubes per panel
D	total damage	P_i	tube internal pressure (Pa)
d	design day damage	Q	creep activation energy (J/mol)
E	Young modulus (Pa), thermal energy (MWh/year)	R	ideal gas constant (J / (molK))
H	elasto-plastic modulus (Pa)	r	radial coordinate, radius (m)
J	number of creep damage intervals	S	allowable stress (Pa)
K	monotonic strength coefficient (Pa)	S_H	hot relaxation strength (Pa)
K'	cyclic strength coefficient (Pa)	s_p	number of panels substitutions
k	aiming factor	S_{SR}	stress reset limit (Pa)
L_t	tube length (m)	S_y	yield strength (Pa)
M	total number of fatigue cycles	t	time (s)
m	Norton-Bailey experimental	th	thickness (m)
		T	temperature (K)
		z	axial coordinate (m)

Greek letters

β	M-R-M parametrization coefficients	$\eta_{thermal}$	thermal efficiency (%)
ΔP	pressure drop (Pa)	θ	circumferential coordinate ($^{\circ}$)
Δt	time interval (s)	ν	Poisson coefficient
ε	strain (%)	σ	normal stress (Pa)
$\dot{\varepsilon}$	strain rate (1/h)	σ'_f	fatigue strength (%)
ε'_f	fatigue ductility (%)	τ	shear stress (Pa)

Subscripts

a	allowable	L	limit
c	creep	M	mechanical stress component
cold	room temperature	P	pressure stress component
creep	effective creep stress	R	rupture
eq	Von Mises equivalent stress/strain	ref	reference receiver
		relax	relaxation
f	fatigue	stab	stabilization
film	HTF region in contact with the tube inner wall	T	thermal stress component

Superindexes

E	elastic stress
P	plastic stress

Abbreviations

AFD	allowable flux density	DNI	direct normal irradiance
ASTM	American society for testing and materials	(W/m ²)	
ASME	American society of mechanical engineers	ECGM	energy coarse grid model
BPVC	boiler and pressure vessel code	EODs	equivalent operating days
CC	code case	FEA	finite element analysis
CSP	concentrating solar power	FFS	fitness for service
		HTF	heat transfer fluid
		LCOA	levelized cost of alloy
		LCOE	levelized cost of energy

LDS	linear damage summation	RT	room temperature
M-R-M	Mendelson-Roberts-Manson	sCO ₂	supercritical carbon dioxide
NH	ASME nuclear CC (former N-47)	SPT	solar power tower
PCC	Precision Castparts Corp.	UNS	unified numbering system

References

- ABE, F. 2015 Research and Development of Heat-Resistant Materials for Advanced USC Power Plants with Steam Temperatures of 700 °C and Above. *Engineering* 1 (2), 211–224.
- ASME 1980 ASME Boiler and Pressure Vessel Code. Code Cases: Nuclear Components Code Case N-47. American Society of Mechanical Engineers.
- ASME 2004 ASME Boiler and Pressure Vessel Code, Section III, Division 1, Subsection NH. American Society of Mechanical Engineers.
- ASME 2007 ASME FFS-1. Fitness-For-Service. American Society of Mechanical Engineers.
- ASME 2010 Asme boiler and Pressure Vessel Code, Section II part D. american society of mechanical engineers.
- ASME 2014 ASME Design Guidelines for the Effects of Creep, Fatigue & Creep-Fatigue Interaction. STP-PT-070. American Society of Mechanical Engineers.
- ATLAS STEELS 2011 Grade data sheet 316, 316L and 316H. http://www.atlassteels.com.au/documents/Atlas_Grade_datasheet_316_rev_Jan_2011.pdf, accessed: 30/04/2020.
- BABCOCK & WILCOX COMPANY 1984 Molten Salt Receiver Subsystem Research Experiment Phase 1 -Final Report, Volume 1- Technical. *Tech. Rep.* SAND82-8178. Barberton, OH, United States.
- BARRETT, P.R., AHMED, R., MENON, M. & HASSAN, T. 2016 Isothermal low-cycle fatigue and fatigue-creep of Haynes 230. *International Journal of Solids and Structures* 88-89, 146–164.
- BARUA, B., McMURTRY, M.D., RUPP, R.E. & MESSNER, M.C. 2020 Design Guidance for High Temperature Concentrating Solar Power Components.

- Tech. Rep. ANL-20/03. Argonne National Laboratory, Argonne, IL, United States.
- BECHT IV, C. 2011 Elevated temperature shakedown concepts. *Journal of Pressure Vessel Technology, Transactions of the ASME* 133 (5), 051203–1–5.
- BERMAN, I., GANGADHARAN, A.C., GUPTA, G.D. & NARAYANAN, T.V. 1979 An interim structural design standard for solar energy applications. Tech. Rep. SAND79-8183. Sandia National Laboratories, Albuquerque, NM, United States.
- BOEHLERT, C.J. & LONGANBACH, S.C. 2011 A comparison of the microstructure and creep behavior of cold rolled HAYNES® 230 alloy and HAYNES® 282 alloy. *Materials Science and Engineering A* 528 (15), 4888–4898.
- BOUBAULT, A., HO, C.K., HALL, A., LAMBERT, T.N. & AMBROSINI, A. 2016 Levelized cost of energy (LCOE) metric to characterize solar absorber coatings for the CSP industry. *Renewable Energy* 85, 472–483.
- BOUBAULT, A., HO, C.K., HALL, A., LAMBERT, T.N. & AMBROSINI, A. 2017 Durability of solar absorber coatings and their cost-effectiveness. *Solar Energy Materials and Solar Cells* 166, 176–184.
- BRADSHAW, R.W. & GOODS, S.H. 2001 Corrosion of Alloys and Metals by Molten Nitrates. Tech. Rep. SAND 2000-8727. Sandia National Laboratories, Albuquerque, NM, and Livermore, CA, United States.
- BREE, J. 1967 Elastic-plastic behaviour of thin tubes subjected to internal pressure and intermittent high-heat fluxes with application to fast-nuclear-reactor fuel elements. *Journal of Strain Analysis* 2 (3), 226–238.
- BRINKMAN, C.R., STRIZAK, J.P. & BOOKER, M.K. 1976 Time-dependent strain-controlled fatigue behavior of annealed 2 1/4 Cr-1 Mo steel for use in nuclear steam generator design. *Journal of Nuclear Materials* 62, 181–204.
- BRITISH ENERGY GENERATION 2003 R5, Issue 3 assessment procedure for the high temperature response of structures.
- BUI-QUOC, T., GOMUC, R., BIRON, A., NGUYEN, H.L. & MASOUNAVE, J. 1988 Elevated Temperature Fatigue-Creep Behavior of Nickel-Base Superalloy IN 625. In *Low Cycle Fatigue* (ed. H. Solomon, G. Halford, L. Kaisand & B. Leis), pp. 470–484. ASTM International.

- CHEN, X., SOKOLOV, M.A., SHAM, S., ERDMAN, D.L., BUSBY, J.T., MO, K. & STUBBINS, J.F. 2013 Experimental and modeling results of creep-fatigue life of Inconel 617 and Haynes 230 at 850 °C. *Journal of Nuclear Materials* 432 (1-3), 94–101.
- CONROY, T., COLLINS, M.N., FISHER, J. & GRIMES, R. 2018a Levelized cost of electricity evaluation of liquid sodium receiver designs through a thermal performance, mechanical reliability, and pressure drop analysis. *Solar Energy* 166, 472–485.
- CONROY, T., COLLINS, M.N., FISHER, J. & GRIMES, R. 2018b Thermal and mechanical analysis of a sodium-cooled solar receiver operating under a novel heliostat aiming point strategy. *Applied Energy* 230, 590–614.
- CUNAT, P.-J. 2004 Alloying elements in stainless steel and other chromium-containing alloys. EuroInox, pp. 1–24.
- DE BARBADILLO, J.J. 2017 INCONEL alloy 740H. In *Materials for Ultra-Supercritical and Advanced Ultra-Supercritical Power Plants*, 1st edn., chap. 14, pp. 469–510. Woodhead Publishing.
- DE BARBADILLO, J.J., BAKER, B.A., GOLLIHUE, R.D. & MCCOY, STEPHEN A. 2018 Properties of inconel alloy 740H for high pressure steam and supercritical CO₂ applications. In *ASME Symposium on Elevated Temperature Application of Materials for Fossil, Nuclear, and Petrochemical Industries (ETAM2018)*, Seattle, WA, United States, pp. 6741 1–11.
- DU, B.C., HE, Y.L., ZHENG, Z.J. & CHENG, Z.D. 2016 Analysis of thermal stress and fatigue fracture for the solar tower molten salt receiver. *Applied Thermal Engineering* 99, 741–750.
- ENO, D.R., YOUNG, G.A. & SHAM, T.-L. 2008 A Unified View of Engineering Creep Parameters. In *ASME Pressure Vessels and Piping Division Conference (PVP2008)*, Chicago, IL, United States, July 27–31, pp. 777–792. Chicago: ASME.
- FAHRMANN, M.G. & SRIVASTAVA, S.K. 2014 Low cycle fatigue behaviour of HAYNES 230 alloy. *Materials at High Temperatures* 31 (3), 221–225.
- FORK, D.K., FITCH, J., ZIAEI, S. & JETTER, R.I. 2012 Life Estimation of Pressurized-Air Solar-Thermal Receiver Tubes. *Journal of Solar Energy Engineering* 134 (4), 041016–1–11.

GLINKA, G. 1985 Calculation of inelastic notch-tip strain-stress histories under cyclic loading. *Engineering Fracture Mechanics* 22 (5), 839–854.

GONZÁLEZ-GÓMEZ, P.A., GÓMEZ-HERNÁNDEZ, J., BRIONGOS, J.V. & SANTANA, D. 2019 Lifetime analysis of the steam generator of a solar tower plant. *Applied Thermal Engineering* 159, 113805.

GONZÁLEZ-GÓMEZ, P.A., RODRÍGUEZ-SÁNCHEZ, M.R., LAPORTE-AZCUÉ, M. & SANTANA, D. 2021 Calculating molten-salt central-receiver lifetime under creep-fatigue damage. *Solar Energy* 213, 180–197.

GOODIER, J.N. 1957 Thermal Stress and Deformation. *Journal of Applied Mechanics* 24, 467–474.

GROSSMAN, J.W. & JONES, W.B. 1990 Evaluation of thermal cycling creep-fatigue damage for a molten salt receiver. In *ASME international solar energy conference, Miami, FL, United States*.

HAYNES INTERNATIONAL 2020 Haynes ® 230 ® alloy. <http://haynesintl.com/docs/default-source/pdfs/new-alloy-brochures/high-temperature-alloys/brochures/230-brochure.pdf>, accessed: 12/03/2020.

HO, C.K. & PACHECO, J.E. 2014 Levelized Cost of Coating (LCOC) for selective absorber materials. *Solar Energy* 108, 315–321.

IRENA 2016 The Power to Change: Solar and Wind Cost Reduction Potential to 2025. *Tech. Rep.* June. Internation Renewable Energy Agency, Abu Dhabi.

JENA, P.S.M., SINGH, R.K., MAHANTA, L., PASWAN, S. & SAHU, J.K. 2018 Low cycle fatigue behaviour of nickel base superalloy IN 740H at 760°C: Influence of fireside corrosion atmosphere. *International Journal of Fatigue* 116, 623–633.

JEONG, C.Y., NAM, S.W. & GINSZTLER, J. 1999 Activation processes of stress relaxation during hold time in 1Cr-Mo-V steel. *Materials Science and Engineering A* 264, 188–193.

KAAE, J.L. 2009 High-temperature low-cycle fatigue of Alloy 800H. *International Journal of Fatigue* 31, 332–340.

- KALNINS, A. 2006 Fatigue analysis in pressure vessel design by local strain approach: Methods and software requirements. *Journal of Pressure Vessel Technology, Transactions of the ASME* 128 (1), 2–7.
- KELLY, B., IZYGON, M. & VANT-HULL, L. 2010 Advanced Thermal Energy Storage for Central Receivers with supercritical coolants. *Tech. Rep.* DOE/GO18149. Abengoa Solar Inc., Lakewood, CO, United States.
- KISTLER, B.L. 1987 Fatigue analysis of a solar central receiver design using measured weather data. *Tech. Rep.* SAND86-8017. Sandia National Laboratories, Albuquerque, NM, United States.
- KOLB, G.J. 2011 An Evaluation of Possible Next-Generation High Temperature Molten-Salt Power Towers. *Tech. Rep.* SAND2011-9320. Sandia National Laboratories, Albuquerque, NM, United States.
- LITWIN, R.Z. 2002 Receiver System: Lessons Learned From Solar Two. *Tech. Rep.* SAND2002-0084. Sandia National Laboratories, Albuquerque, NM, and Livermore, CA, United States.
- LOPEZ, Z. & FATEMI, A. 2012 A method of predicting cyclic stress-strain curve from tensile properties for steels. *Materials Science & Engineering A* 556, 540–550.
- LU, J.-T., LI, Y., YANG, Z., HUANG, J.-Y., ZHU, M. & GU, Y. 2017 Fireside Corrosion Behaviors of Inconel 740H Superalloy in Various SO₂ Contents. In *Energy Materials 2017. The Minerals, Metals & Materials Series*, 1st edn., pp. 193–201. Cham, Switzerland: Springer.
- LUO, K., LI, C., XUE, F., LIU, Y., ZHANG, L. & ZHANG, G. 2018 Oxidation and Hot Corrosion Behavior of Inconel 740H Alloy at High Temperature. In *High Performance Structural Materials. Proceedings of Chinese Materials Conference (CMC) 2017* (ed. Yafang Han), pp. 557–565. Singapore: Springer Singapore.
- MAIYA, P.S. 1980 Cyclic stress-strain curves and cyclic-hardening behavior for types 304 and 316 stainless steel and Incoloy alloy 800H. *Tech. Rep.* ANL-80-100. Argonne National Laboratory, Argonne, IL, United States.
- MAO, J., TANG, D., BAO, S., LUO, L. & GAO, Z. 2016 High temperature strength and multiaxial fatigue life assessment of a tubesheet structure. *Engineering Failure Analysis* 68, 10–21.

- MATAVELI SUAVE, L., CORMIER, J., BERTHEAU, D., VILLECHASE, P., SOULA, A., HERVIER, Z. & HAMON, F. 2016 High temperature low cycle fatigue properties of alloy 625. *Materials Science and Engineering A* 650, 161–170.
- MC CONOHY, G. & KUIZENGA, A. 2014 Molten nitrate salts at 600 and 680°C: Thermophysical property changes and corrosion of high-temperature nickel alloys. *Solar Energy* 103, 242–252.
- MCMURTREY, M.D. 2019 Creep-fatigue Behavior and Damage Accumulation of a Candidate Structural Material for Concentrating Solar Power Solar Thermal Receiver. *Tech. Rep. INL/EXT-19-55551-Rev000*. Idaho National Laboratory, Idaho Falls, ID, United States.
- MEHOS, M., PRICE, H., CABLE, R., KEARNEY, D., KELLY, B., KOLB, G. & MORSE, F. 2020 Concentrating Solar Power Best Practices Study. *Tech. Rep. NREL/TP-5500-75763*. National Renewable Energy Laboratory, Solar Dynamics LLC, Golden, CO, United States.
- MILIOZZI, A., GIANNUZZI, G.M., TARQUINI, P. & LA BARBERA, A. 2001 Fluido termovettore: dati di base della miscela di nitrati di sodio e potassio. *Tech. Rep. ENEA/SOL/RD/2001/07*. ENEA, Rome, Italy.
- MOFTAKHAR, A., BUCZYNSKI, A. & GLINKA, G. 1995 Calculation of elasto-plastic strains and stresses in notches under multiaxial loading. *International Journal of Fracture* 70 (4), 357–373.
- MTSCO 2020 Mt stainless steel. <http://www.mtstainlesssteel.com>, accessed: 05/12/2020.
- NARAYANAN, T.V., RAO, M.S.M. & CARLI, G. 1985 Structural Design and Life Assessment of a Molten Salt Solar Receiver. *Journal of Solar Energy Engineering* 107 (3), 258–263.
- NEISES, T.W., WAGNER, M.J. & GRAY, A.K. 2014 Structural Design Considerations for Tubular Power Tower. In *International Conference on Energy Sustainability (ES2014)*, Boston, MA, United States, pp. 6603 1–7. National Renewable Energy Laboratory.
- NICOL, K. 2013 Status of advanced ultra-supercritical pulverised coal technology. *Tech. Rep. CCC/229*. IEA Clean Coal Centre, London, UK.

- NITHYANANDAM, K. & PITCHUMANI, R. 2016 Thermal and structural investigation of tubular supercritical carbon dioxide power tower receivers. *Solar Energy* 135, 374–385.
- ORTEGA, J., KHIVSARA, S., CHRISTIAN, J., HO, C., YELLOWHAIR, J. & DUTTA, P. 2016 Coupled modeling of a directly heated tubular solar receiver for supercritical carbon dioxide Brayton cycle: Optical and thermal-fluid evaluation. *Applied Thermal Engineering* 109, 970–978.
- PAYTEN, W.M., SNOWDEN, K.U. & DEAN, D.W. 2013 Effects of prior stress relaxation on the prediction of creep life using time and strain based methods. *Journal of Pressure Vessel Technology* 135, 041201–1–8.
- PCC ENERGY GROUP 2020 Inconel® Alloy 740H: A Superalloy Specifically Designed for Advanced Ultra Supercritical Power Generation. <http://www.specialmetals.com/files/PCCEG740HWhitePaper.pdf>, accessed: 07/04/2020.
- RAO, K.B.S., SCHUSTER, H. & HALFORD, G.R. 1996 Mechanisms of high-temperature fatigue failure in alloy 800H. *Metallurgical and Materials Transactions A* 27 (4), 851–861.
- REN, W. & LIN, L. 2019 Consideration of Thermal Embrittlement in Alloy 316H for Advanced Non-Light Water Reactor Applications. *Pressure Vessels and Piping Conference (PVP2019), San Antonio, TX, United States*, vol. 6B: Materials and Fabrication. V06BT06A016.
- RENO, M.J., HANSEN, C.W. & STEIN, J.S. 2012 Global horizontal irradiance clear sky models : implementation and analysis. *Tech. Rep.* SAND2012-2389. Sandia International Laboratories, Albuquerque, NM, United States.
- RODRÍGUEZ-SÁNCHEZ, M.R., MARUGÁN-CRUZ, C., ACOSTA-IBORRA, A. & SANTANA, D. 2014a Comparison of simplified heat transfer models and CFD simulations for molten salt external receiver. *Applied Thermal Engineering* 73 (1), 991–1003.
- RODRÍGUEZ-SÁNCHEZ, M.R., SORIA-VERDUGO, A., ALMENDROS-IBÁÑEZ, J. A., ACOSTA-IBORRA, A. & SANTANA, D. 2014b Thermal design guidelines of solar power towers. *Applied Thermal Engineering* 63 (1), 428–438.

- SÁNCHEZ-GONZÁLEZ, A., RODRÍGUEZ-SÁNCHEZ, M.R. & SANTANA, D. 2018
Aiming factor to flatten the flux distribution on cylindrical receivers. *Energy* 153, 113–125.
- SÁNCHEZ-GONZÁLEZ, A. & SANTANA, D. 2015 Solar flux distribution on central receivers: A projection method from analytic function. *Renewable Energy* 74, 576–587.
- SCANNAPIECO, J.F. 1968 Irradiation of thermal control coatings, Final report. *Tech. Rep.* NASA-CR-94684, DOC.-68SD4224. General Electric Co.; Missile And Space Div., Philadelphia, PA, United States.
- SPECIAL METALS CORP. 2004 INCOLOY alloy 800H & 800HT.
<https://www.specialmetals.com/assets/smc/documents/alloys/incoloy/incoloy-alloys-800h-800ht.pdf>, accessed: 14/04/2020.
- SPECIAL METALS CORP. 2013 INCONEL alloy 625. <https://www.specialmetals.com/assets/smc/documents/alloys/inconel/inconel-alloy-625.pdf>, accessed: 12/04/2020.
- TIMOSHENKO, S. & GOODIER, J.N. 1951 *Theory of Elasticity*, 2nd edn. New York: McGraw-Hill Book Company.
- WADE, W.R. & SLEMP, W.S. 1962 Measurements of total emittance of several refractory oxides, cermets, and ceramics for temperatures from 600 degrees F to 2,000 degrees F. *Tech. Rep.* NASA-TN-D-998; AD-272614. National Aeronautics and Space Administration (NASA), Langley Field, VA, United States.
- WANG, R.Z., ZHANG, X.C., GONG, J.G., ZHU, X.M., TU, S.T. & ZHANG, C.C. 2017 Creep-fatigue life prediction and interaction diagram in nickel-based GH4169 superalloy at 650 °C based on cycle-by-cycle concept. *International Journal of Fatigue* 97, 114–123.
- WHITTAKER, M.T., EVANS, M. & WILSHIRE, B. 2012 Long-term creep data prediction for type 316H stainless steel. *Materials Science and Engineering A* 552, 145–150.
- YAN, X.L., ZHANG, X.C., TU, S.T., MANNAN, S.L., XUAN, F.Z. & LIN, Y.C. 2015 Review of creep-fatigue endurance and life prediction of 316 stainless steels. *International Journal of Pressure Vessels and Piping* 126, 17–28.

- ZAVOICO, A.B. 2001 Solar Power Tower - Design Basis Document. *Tech. Rep.* SAND2001-2100. Sandia National Laboratories, Albuquerque, NM and Livermore, CA, United States.
- ZHANG, S. & TAKAHASHI, Y. 2018 Creep and Creep-Fatigue Deformation and Life Assessment of Ni-Based Alloy 740H and Alloy 617. *Pressure Vessels and Piping Conference (PVP 2018), Prague, Czech Republic*, vol. 6A: Materials and Fabrication. V06AT06A060.

Assessment of time resolution for the receiver lifetime estimation

Contents

5.1	Introduction	160
5.2	Methodology	163
5.2.1	Models employed	163
5.2.2	Calculation procedure	167
5.3	Characteristics studied	168
5.3.1	Heliostat field and receiver description	168
5.3.2	Cases of study	170
5.4	Results and discussion	172
5.4.1	Time resolution analysis	172
5.4.2	Design day analysis	182
5.5	Conclusions	187
	References	190

Summary

The present Chapter assesses the impact of the time resolution and design day selection in the lifetime estimation of a solar power tower molten-salt external tubular receiver working during clean-day conditions. Thus, a global analysis of the receiver is performed, starting from the aiming strategy selection of the heliostat field; in that regard, the receiver operation limits are set in order to keep a low enough film temperature and to avoid the stress reset that would prevent the stress relaxation accumulation over the receiver cyclic operation. The time steps selected for their relevance testing are: 60, 30, 15, 5 and 1 minute during the spring equinox, as well as just the solar noon conditions. The latter

greatly underpredicts the receiver lifetime with respect the 1-min case, being consequently early discarded. As for the rest, the most-damaged panel lifetime is underestimated over a 18% and a 16% using the 60 and 30-minute time steps, dropping under a 5.5% for the 15-min one. Finer resolutions allow a more precise heliostat field aiming strategies selection, decreasing the peak fluxes on the receiver. Resolutions from 15 to 5-min offer a good compromise between accuracy and computational cost. Lastly, selecting a set of 8 representative days for the year, equally-spaced in solar height, opposite to just the spring equinox offers more accurate results since the latter underestimates the whole receiver lifetime, which can result excessively conservative. The summer solstice is the least-damaging day, with the lifetime decreasing as approaching the winter one, as long as the tank filling is achieved.

5.1 Introduction

A rather usual approach when undertaking the lifetime analysis of solar technology components is to consider 10,000 fatigue cycles and 100,000 hours of operation, which is equivalent to 30 years of operation with nearly 1 cycle a day (Babcock & Wilcox Company, 1984) and about 9 to 10 hours of operation per day (Neises *et al.*, 2014). Thus, from the early works in the matter to more recent ones, there is a wide variety of studies in the literature addressing whether the receiver can withstand the creep and fatigue damages when operating during for such horizon and number of cycles (Conroy *et al.*, 2019). Kistler (1987) and Grossman & Jones (1990) performed the analysis of solar central receivers taking into account these 10,000 cycles and 100,000 hours, following the N-47 code case for nuclear applications. Both studies also took into account cloud transients and considered the creep damage negligible. Kistler used measured weather data to establish different types of fatigue cycles depending on the heat flux variations due to these cloud transients, advising the use of a security factor of 2 for the number of cycles, given the uncertainties present in these studies. Babcock & Wilcox Company (1984) also considered the 10,000 cycles to perform the analysis of a cavity type receiver in Incoloy 800H working with molten salt following the N-47 code case, regarding the creep negligible as well.

Nonetheless, since the security margins of the N-47 are deemed excessive when analyzing solar technology components, Berman *et al.* (1979) proposed an interim design code based on some simplifications of the N-47 code case,

making it more suitable for the present field. Following such methodology, Narayanan *et al.* (1985) performed the analysis for a molten salt receiver in 304 and 316 alloys, also including cloud cover cycles besides the daily start-up cycles. Nevertheless, the creep and fatigue material data available at the time was limited and the result of short-term tests. Also based on such interim design code and taking into account the cycle and hours recommendations for 30 years, the works of Neises *et al.* (2014) and Nithyanandam & Pitchumani (2016) analyze sCO₂ receivers, both made of Haynes 230, for various design configurations. However, the former is a preliminary study that did not consider circumferential variations of the heat flux in the selected tube nor its plastic deformations; this last aspect is also disregarded in (Nithyanandam & Pitchumani, 2016). Conroy *et al.* (2018a) performed a design optimization study of a sodium billboard receiver. They also analyzed the relevance of the aiming strategy on the receiver lifetime (Conroy *et al.*, 2018b). In both works, the lifetime analysis was done following the rules of ASME B&PV Section III: Subsection NH (ASME, 2004). They evaluated the creep damage by differentiating the creep loading conditions establishing direct normal irradiation (DNI) levels every 50 W/m², from 0 to 1000 W/m². On the other hand, they also set different fatigue cycles. Real 1-minute DNI data was then used to determine the time spent in each DNI level, as well as the cycle type and frequency. However, elastic stresses were considered for the creep damage and the apparition of stress reset disregarded. More recently, (González-Gómez *et al.*, 2021) also followed the ASME B&PV Section III: Subsection NH to study the lifetime of a molten salt solar power tower (SPT) receiver considering 60-minute time intervals, taking the clean spring equinox as design day. In their work, they took into account the plastic deformations of the tubes as well as the stress relaxation effect, which is paramount to avoid the underestimation of the receiver lifetime, although the aiming strategy of the heliostat field into the receiver was not modified during the operation, which penalizes the receiver thermal production rates.

While in the lifetime estimation field the focus has not been yet put on establishing the time resolution and the design day selection impact, some studies have approached such issue from a thermal and economic perspective, or performed the analysis for finer time resolutions than the hour basis. Meybodi *et al.* (2017) used a multi-year Australian solar database to analyse the time resolution impact on the power production and costs of a parabolic trough with molten salt storage plant. Selecting 5, 15, 30 and 60-minute time steps, they concluded that the 5-minute one provided the most realistic prediction, while

the 60-minute one fell in the opposite side. In between, the 15 and 30-minute steps provided quite realistic results for simplified analysis. Guédez *et al.* (2014) performed a thermoeconomic analysis of the thermal storage system integration in a concentrating solar power (CSP) plant in order to optimize the peak power production, considering 10-minute time steps. Given the variability of the solar resource during the day, a trend of integrating CSP with concentrating photovoltaic (CPV) is also arising. In this regard, the work of Cocco *et al.* (2016) analysed the dispatchability improvement of combining both technologies by performing a minute-by-minute analysis of two design days selected as representative: a summer and a winter day. Lastly, Zurita *et al.* (2020) also studied a CSP-PV hybrid plant from the capacity factor and leveled cost of energy (LCOE) point of view and asses the role that the time resolution selected to perform the analysis plays in the results. Their study was performed for three different days selected as representative: a clear-sky day, a variable day with high DNI and high-frequency transients, and a variable day with low DNI. The LCOE and capacity factor deviation for the 60-minute time step with respect the 1-minute one was around 5.2% and just shy of 6%, respectively.

Additionally, the experience gained from the commercial scale central receiver technologies suggests that the use of hourly DNI data fails to correctly predict the annual performance, being advisable to use 15 minutes or finer data, with 1-minute information being potentially the best alternative (Mehos *et al.*, 2020).

As a result of the above, this Chapter aims to assess the time resolution and design day selection impact from the SPT receiver lifetime angle, given the lack of analysis in this regard and the aggressive conditions the receiver faces during its operation. Moreover, taking into account the dimension of a central receiver design process, which interacts with other subsystems constituting the whole facility—especially the heliostat field—, an integral analysis of a tubular central receiver is performed for that end. Considering different time steps and design days, the design process starts by selecting the heliostat field aiming configuration on the receiver surface—which determines the heat flux distribution on the receiver—and it concludes with the lifetime estimation under these operation conditions. The interaction of the receiver with the thermal energy storage (TES) system, the molten salts tank, is also regarded, considering the operation of the receiver coupled to the filling of such tank. Hence, the Chapter is organized as follows: first, the various models needed to perform the integral analysis of the receiver are presented in Section 5.2, along with a description of

how the calculation process develops by integrating all these models and taking into account the operation limits of the receiver. Then, the characteristics of the heliostat field, receiver and cases of study are introduced in Section 5.3. From there, Section 5.4 discusses the results obtained for both the time resolution and the design day analyses. Lastly, Section 5.5 provides the conclusions reached in the present study.

5.2 Methodology

This section presents the different models required for the integral analysis performed in this Chapter—optical, thermal, elastic stresses and strains, and lifetime models—as well as how they work together in the calculation procedure, in which some operation limits must be regarded.

5.2.1 Models employed

Optical and thermal models

The optical model chosen, developed by Sánchez-González & Santana (2015), allows us to obtain the heat flux on the receiver surface, as well as the optical efficiency of the heliostat field, based on the convolution-projection method. For that end, the optical model uses the DNI obtained with the Daneshyar-Paltridge-Proctor clear sky model (Reno *et al.*, 2012), which depends on the solar altitude α ,

$$\text{DNI} = 950.2 [1 - \exp(-0.075 \alpha)]. \quad (5.1)$$

Given that the days selected in this study are clear days, the DNI would be symmetrical in time with respect the solar noon.

This optical model allows to select the aiming strategy of the heliostat field into the receiver, which would determine the shape of the heat flux distribution on the receiver surface. The aiming factor, k , is the variable designated for that end; in the present model, it ranges from 3 to 0, being 3 the equatorial aiming, with the heliostats focusing in the middle of the receiver height, and 0 the most “open” aiming, being both the upper and lower ends of the panels the points at which the heliostats aim. It must be noted that, the more equatorial the aiming is, the higher the peak flux on the receiver surface is, enabling greater power production, and the lesser the spillage losses, but it may result too aggressive for the operation limits of the receiver. On the other hand, an open aiming is less

efficient but more conservative in terms of entailing potential receiver issues. Moreover, the shading and blocking losses of the heliostats are considered in the model.

Next, the thermal model uses the heat flux distribution on the receiver surface to obtain the different temperatures of the receiver tubes. The model employed in this Chapter is the coarse grid model (CGM) developed in (Rodríguez-Sánchez *et al.*, 2014), which considers a tube representative per panel and a series of circumferential divisions of the tubes, besides the axial ones, to calculate the radiative heat exchange between the surfaces involved. The inlet and outlet temperatures of the heat transfer fluid (HTF) are set according to the particularities of the HTF in question. Given that the day studied is a clean one, with no transient interruptions and smooth transitions in the DNI, the model relies on the modification of the mass flow through the receiver in order to achieve the fixed outlet desired temperature. Thus, this approach corresponds with the so-called control mode 1 presented by Zurita *et al.* (2020), suitable for the aforementioned conditions; the control mode 2 described in their work would not apply in this study. An aspect to regard after the analysis is performed is the resulting film temperature in the tube (temperature of the inner wall, in contact with the HTF through it), since it is limited depending on both the HTF and the alloy selected for the tubes manufacturing.

The use of the CGM is preferred in this Chapter opposite to the energy coarse grid model (ECGM) developed in Chapter 2 due to its lower computational cost, around 5 times lesser, which is essential given the high number of simulations required for this analysis. The difference between them strives in the radiative exchanges calculation, with the ECGM being more precise since it involves an iterative process until the radiative heats converge. Then, the rest of the calculation process develops in the same way, obviating the minimum tube thickness calculation implemented in the ECGM. Thus, the CGM used in this Chapter underestimates the tube film temperature and the temperature of the tube outer wall around a 3% at their respective critical spots. Although these divergences are undesirable for a fine thermal and exergy analysis, such as the one carried out in Chapter 2, these are assumed admissible in the present damage assessment since the main factor of uncertainties is later introduced by the creep and fatigue experimental coefficients.

Elastic stresses-strains and lifetime models

The elastic stresses and strains on the receiver tubes are obtained upon knowing their temperature distribution, once the thermal analysis has been completed. The model used for such end is the analytical one presented in Chapter 3. It is based on the separation of the temperature profile as the addition of the circumferential and radial components, allowing the superimposition of the thermal stresses resulting from both gradients, and it considers the temperature dependence of the material properties. On the other hand, the mechanical restrictions of the receiver tubes, set to avoid their excessive bending—which could cause collisions between adjacent tubes and the appearance of hot spots—, are also taken into account. Hence, the elastic stresses and strains obtained are due to both the thermal contribution, given the uneven temperature distribution on the tubes surface, and the mechanical one, caused by the displacement restrictions these tubes are subjected to. Moreover, the pressure stress caused by the HTF through the tubes is considered as well, although it can be regarded as negligible in comparison to the thermal and mechanical components.

Subsequently, the analytical lifetime model employed is the one developed by González-Gómez *et al.* (2021) and already presented in Chapter 4. It is based on these elastic stresses and strains to give out the elastic-plastic ones. This model also considers the stress relaxation phenomenon, which occurs during hold time under high temperatures and stresses and can develop during a certain stabilization time, even with the characteristic cyclic operation of this kind of technology, suffering from daily start-ups and shutdowns, as long as the stress reset limit is not surpassed. The creep stresses, σ_c , resulting after the stress relaxation, as well as the temperature, T , at which the tubes operate, are the ones responsible for the daily creep damage during day i , $d_{c,i}$,

$$d_{c,i} = \sum_{n=1}^{J_i} \frac{\Delta t_n}{t_{R,n}}, \quad (5.2)$$

by means of the rupture time calculation, t_R , at the different time intervals, Δt_n ,

$$\log_{10}(t_R) = \beta_0 + \beta_1 \frac{1}{T} + \beta_2 \log_{10}(\sigma_c) + \beta_3 \log_{10}(\sigma_c) \frac{1}{T}. \quad (5.3)$$

Here the different β are the Mendelson-Roberts-Manson (M-R-M) parametrization coefficients, that depend on the alloy selected. On the other hand, the daily

fatigue damage, $d_{f,i}$,

$$d_{f,i} = \sum_{m=1}^{M_i} \frac{N_m}{N_{a,m}}, \quad (5.4)$$

is caused by the strain range, $\Delta\varepsilon_{\text{eq}}$, which determines the number of allowable cycles of the tubes, N_a ,

$$\frac{\Delta\varepsilon_{\text{eq}}}{2} = \frac{\Delta\varepsilon_{\text{eq}}^E}{2} + \frac{\Delta\varepsilon_{\text{eq}}^P}{2} = \frac{\sigma'_f}{E} N_a^{-c1} + \varepsilon'_f N_a^{-c2}, \quad (5.5)$$

where E is the Young modulus, σ'_f is the fatigue strength coefficient and ε'_f is the fatigue ductility.

Then, the addition of the total creep damage, D_c , and the total fatigue damage, D_f , for the studied operation days must be equal or lesser than the damage limit, D_L ,

$$D_L \geq D_c + D_f. \quad (5.6)$$

In this analysis, the linear damage summation (LDS) model (ASME, 2004) is used, considering that both the creep and fatigue damages work independently. It also implies that the damage limit, D_L , is equal to unity regardless the material selected for the tubes manufacturing (British Energy Generation, 2003; Chen *et al.*, 2013), which is a good assumption in clear design days (González-Gómez *et al.*, 2021). Considering just a representative day for the receiver operation, i , the total creep and fatigue damages can be expressed as the daily creep and fatigue damages obtained that day multiplied by the number of equivalent operating days of the receiver (EODs); on the other hand, if a total of I representative days is selected instead, these total damages would be equal to the average daily damages during these I days, multiplied by the total of EODs. Thus, the lifetime of the receiver, expressed in terms of its equivalent operating days, is obtained as

$$D_L = \text{EODs} \sum_{i=1}^I \left(\frac{d_{c,i}}{I} \right) + \text{EODs} \sum_{i=1}^I \left(\frac{d_{f,i}}{I} \right) \rightarrow \text{EODs} = \frac{D_L}{\overline{d_c} + \overline{d_f}} \quad (5.7)$$

These EODs can be converted into years dividing them by the number of operation days considered during a year. In this Chapter, it has been regarded as 365 days since one of the scenarios studied consists of a set of days equally-spaced in solar height through the whole year. However, less days could be taken into account if an estimate of the number of days presenting non-favourable conditions for the start-up is deemed.

5.2.2 Calculation procedure

The criteria established in the optical model for the start-up is that the solar height must be at least 10° (Falcone, 1986). On the other hand, the plant shutdown for each case occurs once the TES tank is completely filled. Prior the final lifetime analysis, it is necessary to determine the aiming strategy of the heliostat field on the receiver surface. For such end, two limiting factors for the AFD are regarded:

- The maximum allowable film temperature, T_{film} , of the alloy selected when in contact with the selected HTF. This restriction is watched to avoid the excessive corrosion of the tubes; in case of Haynes 230 tubes with molten salts flowing through them, such limit is set in 650°C (McConohy & Kruizenga, 2014).
- The stress reset limit, S_{SR} . It is deemed in order to ensure the cyclic accumulation of stress relaxation over the cyclic receiver operation; otherwise, stress reset would occur after the daily shutdown and the tubes would not be able to resume the operation the following day at the relaxed stress level achieved during the previous day. The stress reset limit is determined by the expression $S_{\text{SR}} = S_{y,\text{cold}} + S_H$ (Becht IV, 2011), where $S_{y,\text{cold}}$ is the cold (room temperature) yield strength and S_H is the hot relaxation strength, taken as 1.25 times the allowable stress, S , obtained from the ASME BPVC Section II Part D (ASME, 2010).

Hence, at the beginning of the operation, the k is set as equatorial as possible in all the time steps in order to obtain the maximum thermal power; in the case of the present optical model, the most equatorial aiming factor that can be selected is denoted by $k = 3$. With that, the thermal model is run and the resulting T_{film} is checked to be under the established limit. Should that not be the case, the thermal model is rerun with a lower k , until the criterion is correctly met. Then, the elastic stresses-strains analysis is performed with the temperatures obtained from the thermal model, making sure that the stress reset limit is not surpassed; if the elastic stresses result above the S_{SR} , the aiming factor needs to be lowered again.

Once the k is definitive for the different time moments of the design day chosen, the hours of operation (HOP) needed to fill the molten salts storage tank are obtained. The lifetime analysis is finally undertaken for these aiming factors and the resulting operation hours, using the corresponding temperatures and

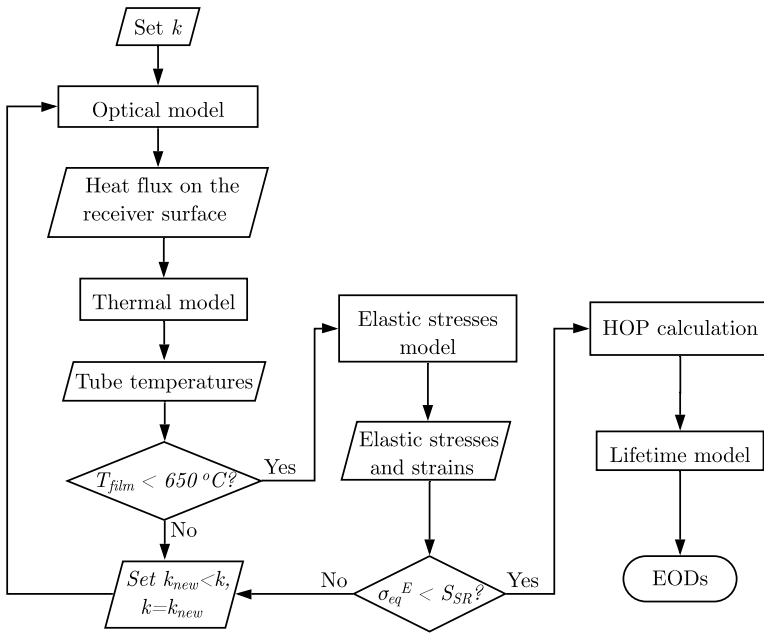


Figure 5.1: Calculation procedure, including the different models used and the operation limits considered.

elastic stresses and strains from the previous models. The present calculation procedure is summarized in Figure 5.1.

5.3 Characteristics studied

5.3.1 Heliostat field and receiver description

The receiver studied is part of a plant with a Gemasolar-like heliostat field (Burgaleta *et al.*, 2011), with 2,650 heliostats of 115.7 m^2 of effective mirror surface each, resulting in a total area of $306,605 \text{ m}^2$. The location of the plant is Seville, Spain, just like Gemasolar, at the latitude of 37.56° .

The tower elevating the central external tubular receiver has a 130 m height. The base structure of the receiver, on the other hand, is an 8.4 m diameter cylinder and serves to frame its panels, set to 18. These panels are constituted by 61 vertically placed identical tubes of 10.5 m long, 2.24 cm of external diameter and a 1.2 mm thickness; their manufacturing is in Haynes 230, whose

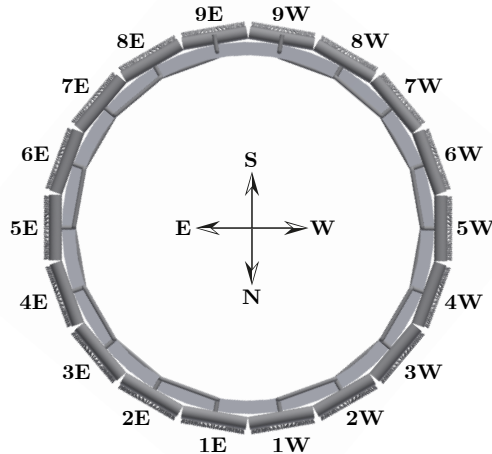


Figure 5.2: Plan view of the receiver schematic representation and the two flow paths.

mechanical properties are obtained from (ASME, 2010) and its creep and fatigue coefficients, required in the lifetime analysis methodology, are compiled in Chapter 4. The tubes are also painted with a black Pyromark coating of high absorptivity, enhancing their optical properties, while the cylindrical structure holding the receiver panels is covered with a reflective material, trying to maximize the heat flux reflected from it to the rear side of the tubes. Both ends of the tubes constituting one panel are welded to such panel respective inlet and outlet headers, which distribute the HTF trough all these tubes and then collect it. Lastly, the tubes are guided along their length by a series of welded supports, or clips, preventing their excessive bending. In this study, the generalized plane strain scenario is considered, which is equivalent to having an infinite number of clips, preventing the tubes bending. As proved in Chapter 3, the elastic stresses results do not diverge greatly when considering clips every 2 m.

The chosen HTF is solar salt (60% NaNO₃-40% KNO₃), whose temperature dependent properties are available in the literature (Zavoico, 2001). For its operation in the SPT receiver, it is taken into account that this HTF has a lower inlet temperature limit set in 290 °C to avoid its freezing, and an upper one of 565 °C, aiming to prevent its decomposition. The HTF mass flow rate entering the receiver is splitted into two parallel flow paths, with the solar salt flowing through each path panels in a serpentine-like fashion, from the North-oriented

face to the Southern one. The inlet is placed at the bottom of the first panel of each path, while the outlet results at the top of their respective last panel. The orientation of the two paths inlet and outlet results in a N-S symmetrical heat flux distribution in both flow paths at solar noon. On the contrary, during the morning hours the Western half receives higher concentrated heat flux while in the evening that is the case for the Eastern one, given that the facility studied is projected for a Northern Hemisphere location.

The TES tank capacity consists of 8,500 ton of molten salt, which allows a continued production during the night hours, after the receiver has ceased its daily operation.

5.3.2 Cases of study

In this study, two distinct issues are tackled relating the receiver lifetime analysis: the time step used and the selection of the design day.

On the one hand, the EODs are obtained for a fixed clean design day, discretized using a set of different time steps in order to determine an accurate enough time resolution but without compromising the computational cost. The design day selected for that end is the spring equinox (Julian day 81) since it is the most commonly used as the representative one (Rodríguez-Sánchez *et al.*, 2018). The solar height for this day at solar noon is 52.44° at the location considered in the present analysis. The time intervals studied are: 60, 30, 15, 5 and 1 minute. The case of just considering the operating conditions at the solar noon for the whole day is also included, since such instant is typically regarded as the design point in simplified approaches. All these time intervals are admissible for the analysis since, given the thermal conductivity and thickness of the tubes, they are greater than the time to reach the quasi-steady state, guaranteeing that the corresponding Fourier number is equal or greater than 0.5 (Taler *et al.*, 2019). For such analysis, all the time step cases are set to start at 7:00 h (solar time) since it is the first o'clock hour at which the receiver can operate, despite more precise resolutions could start earlier (for instance, 6:51 h for the 1-minute time step). This way, the focus is solely on the information loss between time intervals, without the interference of additional data. Additionally, the impact of the time resolution in the TES tank filling will also be studied.

Upon having established the time step, the second goal is to determine whether the use of the spring equinox as the design day is sufficient for the receiver lifetime estimation, opposite to performing the daily analysis in a set

Table 5.1: Days selected for the design day analysis and their maximum solar height.

Day	172	218	238	256	272	290	310	355
α_{max} (°)	75.89	68.98	62.4	55.46	49.02	42.11	35.61	28.99

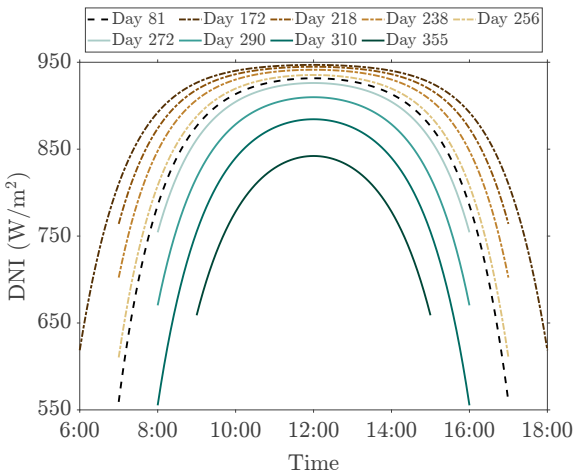


Figure 5.3: DNI for the days analyzed.

of days equidistant in their maximum solar height, the one at the solar noon. Such set consists in 8 days going from the summer solstice (Julian day 172) to the winter solstice (Julian day 355), both included, that can be regarded as representative for the whole year. This approach was presented by Wagner (2008). The selected days for this study are compiled in Table 5.1, including their maximum solar height. In this case, each day will start at their corresponding time, following the start-up criteria detailed in the previous paragraph, regardless of it is not an o'clock time. The plant shutdown is also programmed with the filling of the storage tank.

The DNI of the different days studied in this Chapter, including both the spring equinox and the 8 days set, are depicted in Figure 5.3. Note that the initial and final hour differs from day to day since the depiction starts for each day at the first o'clock hour available according to the start-up criteria. As expected, the DNI level presents its maximum value in the solar solstice, decreasing progressively as the days approach to the winter solstice. The spring equinox is equivalent to the autumn one, and thus its DNI places in the central position with respect the set of 8 days.

5.4 Results and discussion

In this Section, the results obtained for the two cases of study previously introduced are presented. First, the analysis of the different time steps is discussed and then, the results for the set of the 8 evenly spaced days.

5.4.1 Time resolution analysis

Aiming strategy and DNI

Following the calculation procedure, the aiming strategy is established at the different time instants first, considering the film temperature limitation and aiming to avoid the appearance of stress reset. An instance of how different aiming strategies modify the incident heat flux on the receiver surface is presented in Figure 5.4, with the tubes vertically discretized in 20 axial divisions; various time instants are also depicted to show how the peak flux is displaced from the Western half in the morning hours to the Eastern one in the afternoon. Thus, note that each half of the receiver will have different aiming necessities due to the disparate heat flux incidence on their surfaces, being the Western half the most restrictive one in the morning hours and the Eastern one the limiting half during the afternoon. In this Chapter, the aiming strategy is selected individually for each path, instead of watching the both paths limits at once in order to set a single aiming for the whole receiver. However, the Eastern and Western aiming strategy configurations during the day are symmetrical between them with respect noon, given that the day selected is a clear one, also with symmetrical DNI with respect noon. By looking at Figures 5.4(a) and 5.4(b), which depict the same hour, the descend of the peak heat flux with k becomes evident. It can be sensed as well that the decrease of k , besides implying lower peak value, engages a greater tube surface, flattening the flux profile. The most demanding conditions of the Western half in the morning hours with respect the Eastern are also noticeable. Such gap is closed the nearer the solar noon is, the moment at which both halves present the same heat flux distribution; then, in the afternoon, the roles are reversed.

Once the aiming strategies for the different time intervals are set, the resulting peak heat fluxes, q , on the Eastern half of the receiver surface during its operation are depicted in Figure 5.5(a) for the different time steps selected in this study, while their corresponding DNI levels are presented in Figure 5.5(b); due to the aiming strategy symmetry between both halves respect noon, as well as the DNI symmetry, the Western peak fluxes are also symmetrical to the

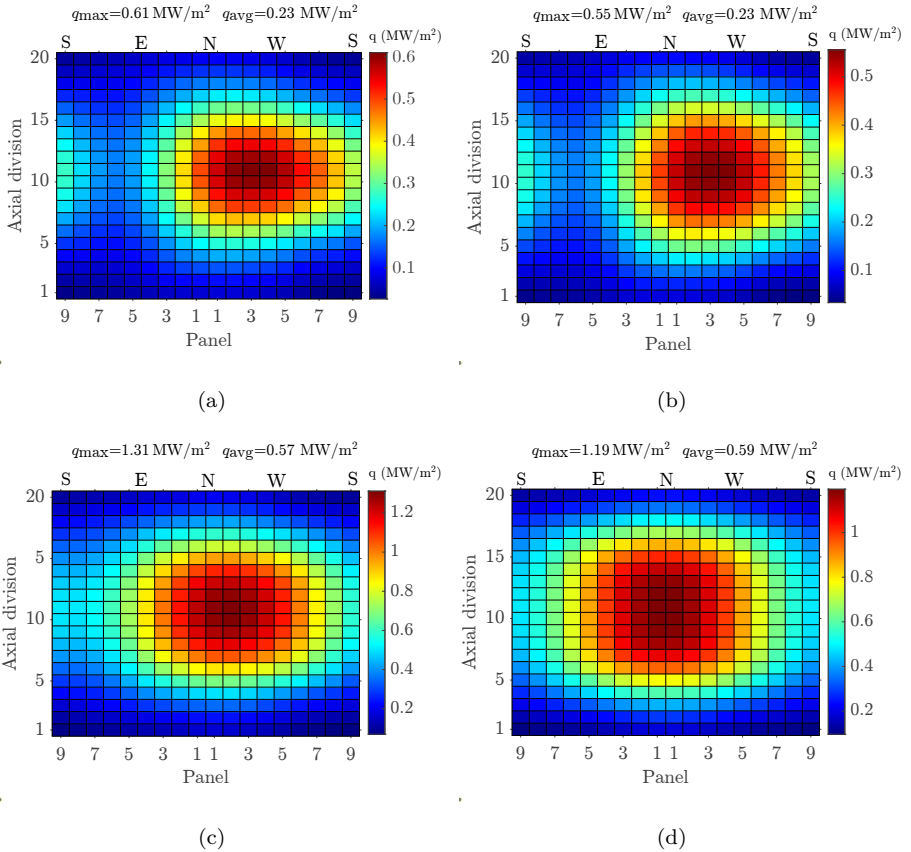


Figure 5.4: Heat flux map on the receiver surface, with its maximum and average value for (a) $k = 3$ at 7:00h, (b) $k = 2.6$ at 7:00h, (c) $k = 2.6$ at 10:00h, (d) $k = 2.3$ at 12:00h.

ones depicted with respect solar noon. As expected, more precise time resolutions provide a smoother transition of the aiming strategies, which can result beneficial since lower aiming factors contribute to reduce the peak flux with respect more equatorial ones. Periods with low DNI admit almost-equatorial aiming strategies, since the peak flux is not extremely critical. However, as soon as the DNI increases, it would be required a more open aiming factor in order to decrease the peak flux on the receiver surface. These required aiming strategies shifts can be sensed in the peak heat flux representation as the saw peaks appearing during the day; a descending saw peak (for instance, the ones represented from 8:00 h to 9:00 h for the 1-min time resolution), that provides a sudden lower peak heat flux, means the setting of a more open aiming factor,

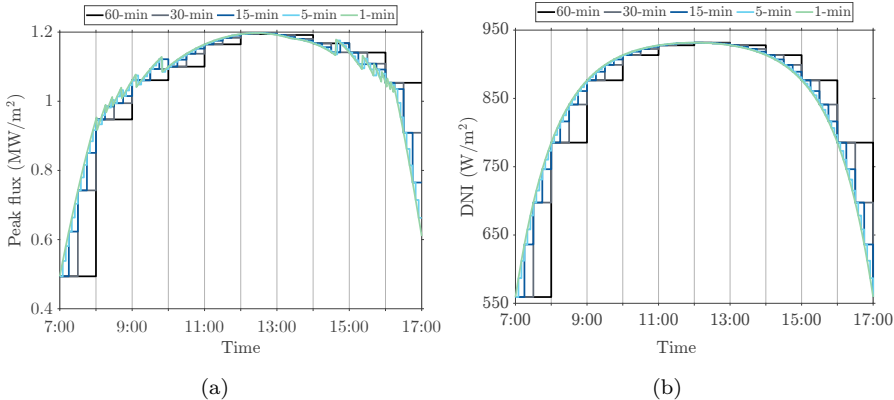


Figure 5.5: (a) Maximum heat flux on the Eastern half and (b) DNI for the different time step cases.

while growing saw peaks (appearing mostly from 15:00 h to 16:00 h), resulting in sudden greater peak fluxes, imply the opposite. On the other hand, note that each time step uses the corresponding DNI level at every “measurement” instant that such resolution allows. For instance, from 7:00 h to 7:59 h, the 60-minute resolution would work the full hour with the DNI level obtained at 7:00 h, while the 1-minute resolution would use a different DNI every minute. Since the DNI grows as the morning hours advance to solar noon, greater time steps present lower values of the DNI with respect more precise time resolutions at the time instants different to the measurement one, until the 11:59 h. The opposite effect occurs during the afternoon hours since the DNI decreases after the solar noon.

Lifetime results: full tank filling

Once the different k have been established after the thermal and mechanical analysis checking, the hours of operation to fill the tank are obtained; these are included in Table 5.2. The time variation in the HOP, from the less precise time step (60-minute) to the more precise one (1-minute) is just of 21 minutes, with the latter needing the least time to fill the tank. In between these time resolutions, the HOP also increases the less precise the resolution is.

The last step of this receiver study is the lifetime analysis, resulting in the obtaining of the EODs for each receiver panel by means of the creep and fatigue damages during these HOP. However, as in any clear design day, the fatigue damage is negligible in comparison to the creep one, being the latter

Table 5.2: HOP for the tank filling considering different time resolutions.

Time step	1-min	5-min	15-min	30-min	60-min	Solar noon
HOP	8h 14min	8h 16min	8h 19min	8h 24min	8h 35min	7h 16min

the main factor dictating the resulting EODs. Figure 5.6 presents an instance of the main intermediate results of the analysis, obtained during the calculation procedure: the outer tube temperatures from the thermal model, the creep stresses—considering stress relaxation—and the creep damage. In this case, the ones depicted correspond to the results for the 5-min time resolution at 12:00 h. The temperature of the tubes is greater towards the center in the vertical direction, where the heliostats are mainly aiming. Such temperature evolves by increasing from the Northern panels to the Southern ones regardless the sun position (in this case, solar noon, results in a symmetrical N-S configuration) since it is greatly affected by the salt heating when circulating through the panels. The stresses also result greater in the central regions of the tubes but, opposite to the temperatures, the most affected panels are the Northern ones. The combination of both temperature and stress result in the creep damage, the main mechanism these tubes must endure during clean design days; in this case, such damage is the accumulated one during the 5 minutes that the time step depicted covers.

On the other hand, the final results of the analysis, the EODs, are presented in Figure 5.7 for the 1, 5, 15 and 60-min time steps, converted to years (considering 365 days) for a more straight-forward understanding. The complete lifetime results are included in Table C.1 of Appendix C for reference, including additional cases of 2 and 7.5 minutes (with HOP of 8 h 14 min and 8 h 16 min, respectively), where the results for the most-damaged panel in each flow path and time step are presented in bold italicics. In the Eastern path, the limiting panel is the first one in all the cases, while in the Western one it shifts from the first panel in the solar noon design point case and in the time steps of 60 and 30 minutes, to the second panel in the rest of the time intervals. Then, the lifetime increases when advancing to the Southern panels, with the expected lifetime decreasing back again in the last one, subjected to the higher tube temperatures. The general trend is for coarser time resolutions to underestimate the receiver panels lifetime, although such trend is reversed in a few instances.

Moreover, the percentage variation of the EODs obtained for the rest of the

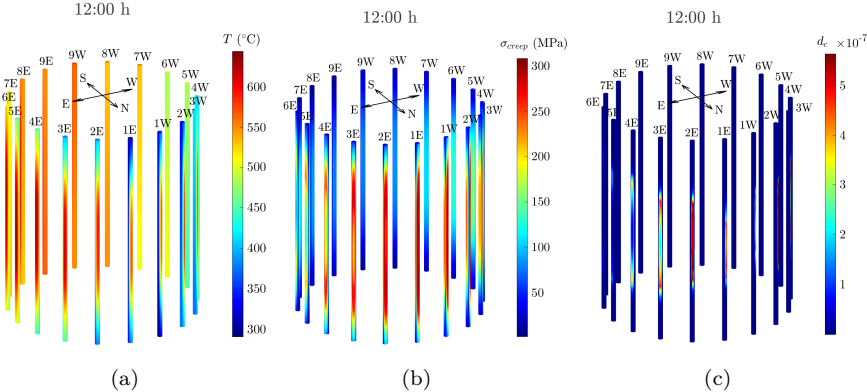


Figure 5.6: Tubes outer temperatures, creep stresses and creep damages for the representative tubes of the 5-min time step at solar noon.

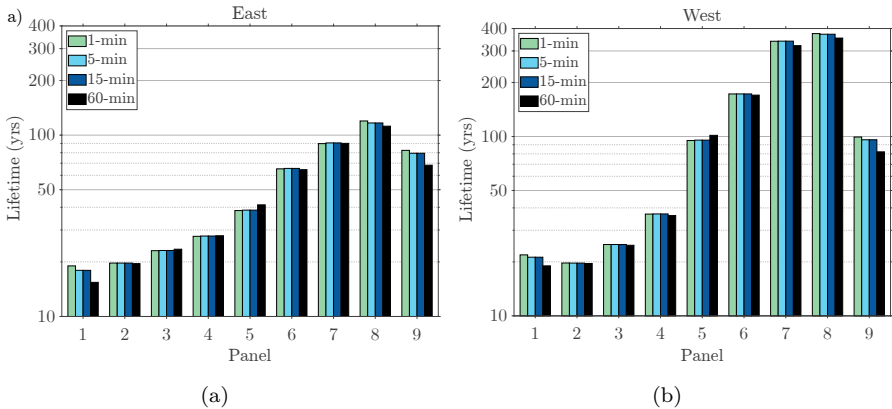


Figure 5.7: Lifetime results for the receiver panels using the 1, 5, 15 and 60-min time steps. (a) Eastern and (b) Western flow paths.

time resolutions with respect the 1-minute one are all included in Table C.2 in order to get a better sense of the time resolution impact in the lifetime prediction. From the examination of the results it can be concluded that selecting just the solar noon as the design point is not an appropriate approach, since it underestimates the lifetime of the panels in over a 40% with respect the 1-minute time step in the best of the cases. The rest of the time resolutions present fairly accurate results in nearly all the panels. The exception is, however, the first panel of both halves, with the time interval of 60 minutes deviating over a 18% and a 13% in the Eastern and Western sides, respectively, and the 30-min time step diverging over a 16% and a 14%. This is not a negligible issue since the first panel of the Eastern half is the limiting one, not only in such flow path

but in the whole receiver. While the underestimation falls in the safety side, it could lead to an overestimation of the plant costs. Apart from these two time intervals, the rest of them fall in divergences under 5.5% in the Eastern half and 3% in the Western one for the aforementioned panel; thus, selecting a time step of 15 minutes or lower would be more appropriate. When comparing both paths panel-by-panel, the Eastern side panels are most damaged than the Western ones overall, regardless the time step selected. This is due to the fact that the receiver operates during the whole morning, when the incident heat flux is greater on the Western half than in the Eastern, which creates the need to adopt aimings that provide a lower heat flux peak in that side in order to meet the operation limits, opposite to the Eastern half, which is able to operate with more equatorial aimings. Then, the receiver shuts down early in the afternoon once the tank is filled, when the heat flux on the receiver surface is more aggressive in the Eastern side and, thus, when that half would be able to benefit from requiring more open aiming strategies. The only exception in this regard is the solar noon case of study since at that time the receiver is under a symmetrical heat flux in the N-S direction. The second panel of both flow paths can also be considered an exception in all the time steps, given the proximity of the results for such panel in both halves of the receiver.

For the 1-minute time step, the thermal power and thermal energy supplied by this receiver in this design day are 119.65 MWt and 985.12 MWh, respectively. The differences observed regarding these matters with respect the 1-minute time resolution are roughly a 3.07% overestimation of the thermal power and a 7.45% overestimation of the thermal energy in the case of the 60-minute time resolution, being the results for the intermediate resolutions below such difference. In the case of the solar noon, the difference in the thermal power increases to an 18.28% but in terms of thermal energy it decreases to a 4.39%, which can be explained by the fact that it operates almost an hour less, sufficient for it to achieve the tank filling.

Lifetime results: fixed HOP

Given the differences observed in the HOP, despite them not being excessive, the analysis has then been performed for a fixed HOP in all the cases, being equal to the one obtained for the 1-minute time step. The case of the solar noon design point has been omitted given its extremely high lack of accuracy and providing that the tank is already filled almost one hour in advance with respect the 1-min time resolution HOP. Thus, the percentage variation with

Table 5.3: Molten salts (Tn) collected for a fixed HOP equal to the one required for tank filling with 1-min time step

Time step	5-min	15-min	30-min	60-min
Tank (Tn)	8,473	8,425	8,341	8,156

respect the 1-minute time step results obtained from this analysis are gathered in Table C.3. The new amount of storaged molten salts they can achieved is presented in Table 5.3, showing a descend up to a 4% in the worst of the cases, resulting from such shorter operation.

Regarding the lifetime, these receivers are able to endure slightly more since the HOP are reduced with respect the tank full filling operation. This translates in a lesser gap with the 1-min time resolution in the cases where the EODs resulting from the tank filling operation were below the ones obtained for the reference time step (negative percentage difference) and a greater gap in the ones that lasted longer (positive percentage difference). Some cases flip from lasting lesser than the reference time resolution panels in the filling operation, to lasting more like; for instance, the second panel of the Eastern path for the 60-minute time step. Nevertheless, for the critical panel in each path, the differences of the rest of the time resolutions with respect the 1-minute one do not vary greatly; the biggest gap-closing in this regard occurs in the first panel of the Western path, going from a -13.16% to a -8.02% using the 60-min time step, which has seen its HOP reduced in 21 min. On the Eastern half, however, it only goes from -18.86% to -18.055%. On the other hand, remarkable deviations are now observed in the rest of the panels of the Eastern half for the 60-minute time resolution, reaching up to a 15.92% difference in the fifth panel.

Further time resolutions remarks

In order to illustrate the differences between time steps, the creep damage in the tube crown (the most critical spot in the tube cross-section) for the 60 and the 1-minute time resolutions are presented in Figure 5.8. The focus has been put into the Eastern path since it is the one presenting the shortest lasting panel. From there, the comparison has been depicted for the 12th axial division ($z = 6.3$ m) of the first panel since it is the location at where the greatest differences between the creep damages of both cases are found the most consistently over the daily operation. In the case of the 60-min time step, the d_c obtained for each hour has been divided by 60 in order to be able

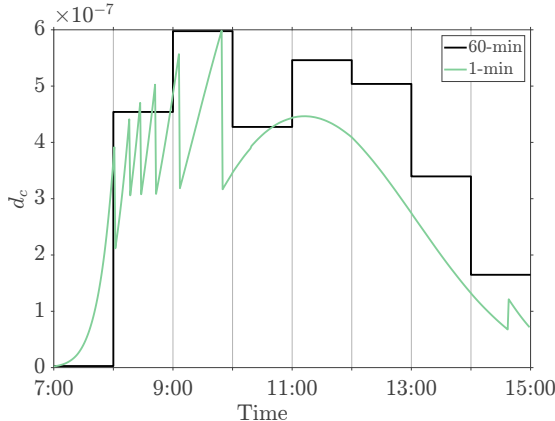


Figure 5.8: Minute by minute creep damage of the 60 and 1-minute time step at the 12th axial division of the first Eastern panel.

to properly compare it with the 1-min time interval results. Figure 5.8 shows that, despite the greater DNI of the 1-min resolution during the morning hours, its creep damage is overall lower during most of the operation, which has to do with the ability to switch with greater precision between aiming factors: decreases earlier than the 60-minute resolution during the morning hours and increases later than it during the afternoon ones. These k changes correspond, in the case of the 1-min resolution, to each d_c peak. As for the 60-min time intervals, the steps depicted are due to sudden modifications both in the k and the DNI, opposite to the smoother DNI of the 1 minute one.

For the cumulated creep damage in one hour, the biggest difference between both time resolutions occurs in the period from 12:00 h to 12:59 h, precisely at the 12th axial division of the Eastern half first panel. Thus, Figure 5.9(a) offers more detail on the results presented in Figure 5.8 by depicting the minute-by-minute ratio of the temperature in the 12th axial division tube crown for the 60-min time step over the 1-min one during such hour, as well as the creep stress ratio, also in the tube crown, and the creep damage ratio; for both time resolutions, the aiming factor is the same and remains constant during that hour. On the other hand, the time period from 7:00 h to 7:59 h is illustrated in Figure 5.9(b) for being the hourly interval at which the cumulated d_c difference between both cases is the greatest favoring the 60-min time step. In this case, the aiming factors also match during the whole hour. Despite temperatures and creep stresses ratios not being far from the unity, which means that the results for both time resolutions are quite similar in such regard, the differences are

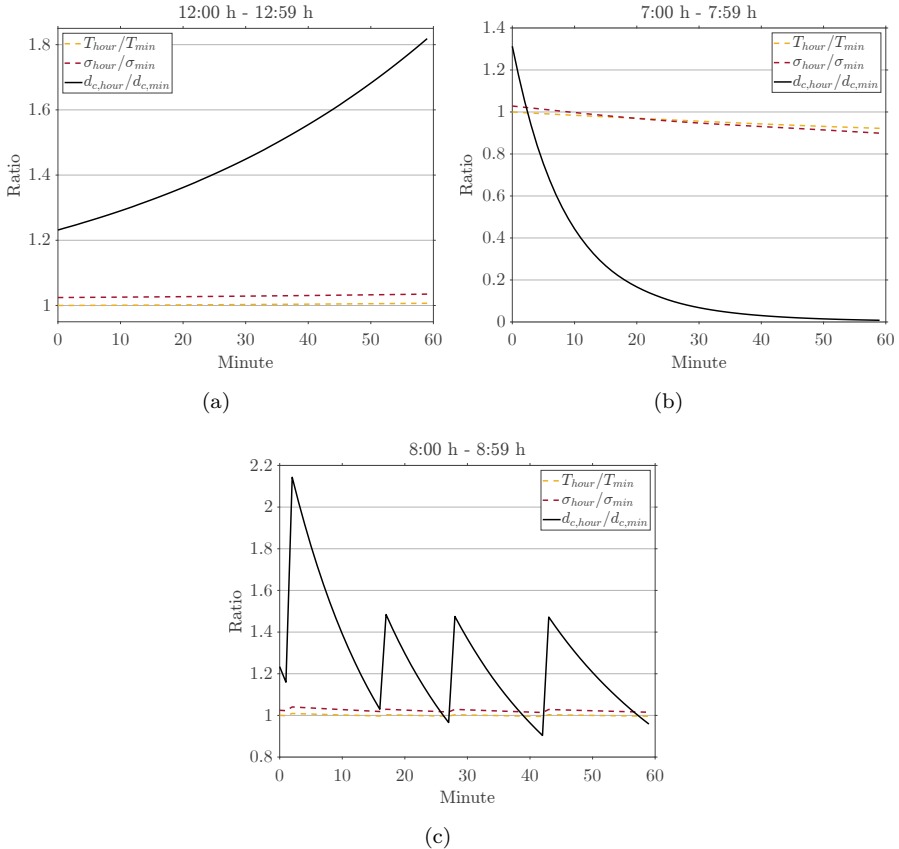


Figure 5.9: Temperature, stress and creep damage minute-by-minute ratio of the 60-minute time resolution over the 1-minute one during (a) 12:00 to 12:59 h, (b) 7:00 to 7:59 h and (c) 8:00 to 8:59 h.

amplified in Eq. 5.3, affecting the outcome of the d_c . It is also worth mentioning that, although the ratio of the d_c from 7:00 h to 7:59 h is extremely favorable to the 60-min time step, the creep damages entity is negligible during most of the hour in comparison with the ones corresponding to the 12:00 h to 12:59 h time period, as already seen in Figure 5.8. Moreover, that behavior when contrasting both creep damages is a rare instance during the daily operation, being the 60-min time step the most damaged during nearly the whole operation. Lastly, Figure 5.9(c) provides an instance of an hour, from 8:00 h to 8:59 h, in which the aiming factor starts matching for both time steps but soon begins progressively decreasing for the 1-minute time resolution. The small discontinuities in the temperature and stress caused by that k modification can be sensed, as well as

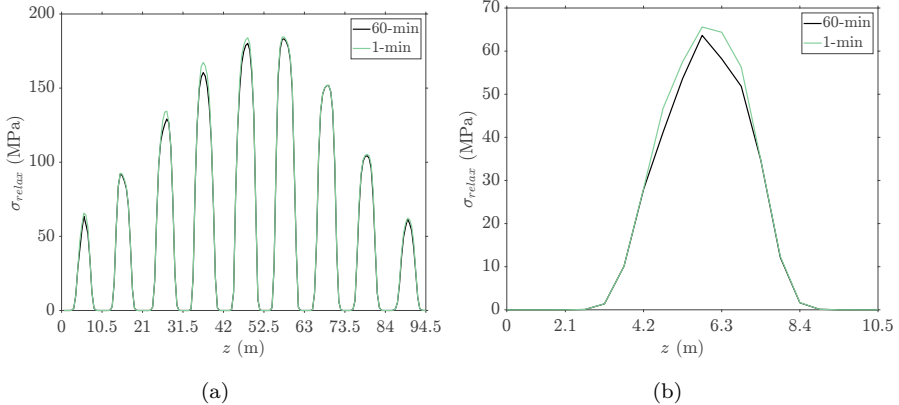


Figure 5.10: Stress relaxation at each axial division (a) in the Eastern path and (b) detail on its first panel.

how they are again amplified when referring to the creep damage.

As it can be perceived in Figures 5.8 and 5.9, there are also divergences in the creep damages at the o'clock instants, despite the DNI and, in some of them, the k of both time resolutions match; this has to do with the different stress relaxation that applies in each case, Figure 5.10, which results in a different creep stress, as observed in Figure 5.9. Note that, for a certain axial division and in the absence of stress reset, the stress relaxation is evaluated as a constant value for the whole day, which would be the maximum stress relaxation for that axial division resulting from all the combinations of temperature and equivalent elastic-plastic stress that occur during the whole daily operation. The biggest differences occur in the center of the panels, which are the spots in the vertical direction under the most aggressive operating conditions. It is not surprising that the stress relaxation somehow varies with the time resolution given the gain/loss of information implied in modifying the time step of the analysis. But, again, despite these disagreements are not that great, this divergence is greatly amplified in the rupture time calculation.

Additionally, in sight of the great relevance that the aiming factor has in the final outcome—and then the peak flux—, and given the fairly accurate results obtained with the 5-min time step for this clean design day, it has been put to test whether the interpolation of its temperature, stresses and strains data to 1-min time intervals provides a good approximation to the 1-min time resolution, the reference one. The interpolated temperatures and elastic stresses and strains are completely accurate during the periods operating at a constant k ; conversely,

Table 5.4: Comparison of the percentage lifetime difference with respect the 1-min results for the 5-min time resolution results and its interpolation to 1-min time intervals.

Case	Percentage lifetime difference (%)								
	Panel 1E	Panel 2E	Panel 3E	Panel 4E	Panel 5E	Panel 6E	Panel 7E	Panel 8E	Panel 9E
5-min	-2.57	0.31	0.27	0.33	0.27	0.68	0.90	0.77	-2.32
Interp	-2.49	0.129	0.026	0.011	-0.004	0.052	-0.003	-0.13	-2.46
Percentage lifetime difference (%)									
Case	Panel 1W	Panel 2W	Panel 3W	Panel 4W	Panel 5W	Panel 6W	Panel 7W	Panel 8W	Panel 9W
	-2.43	0.28	0.08	-0.05	-0.43	0.13	0.14	0.21	-0.16
Interp	-2.55	0.172	0.03	0.008	-0.035	-0.003	-0.051	-0.16	-0.41

small deviations are observed when aiming strategy changes occur since, the coarser the time resolution, the less precise the aiming strategy selection over the operation turns out. With that, the percentage difference of the results from the interpolation with respect the 1-min time step results are compared against the percentage difference of the 5-min time resolution results with respect the reference one in Table 5.4. The interpolated results are closer than the 5-min time step to the reference time resolution ones in nearly all the panels. The results are especially accurate in panels from 3 to 7. The lifetime of the critical panel in each flow path (panel 1 in the Eastern path and panel 2 in the Western) is also more accurately predicted with the interpolation. The exception is the first panel of the Western flow path as well as the ninth panel of both paths. Thus, the interpolation can be indeed considered a good approximation to the more precise 1-minute results when a finer resolution is not feasible or there is a computational cost concern.

5.4.2 Design day analysis

Having performed the time resolution analysis, the time step is set to 5 minutes for the design day analysis. In this case, the lifetime resulting from the receiver operation during a set of days is obtained in order to validate the suitability of selecting just the spring equinox as design day.

Lifetime results for the set of days

Just as in the spring equinox, the k at each time interval is obtained for the set of days. Figure 5.11 depicts the peak flux on the Eastern receiver half during these days, as a result of the aiming strategies adopted during them; again, the Western results are symmetrical with respect the solar noon. During the morning hours of the summer solstice (day 172), the aiming factor in the Eastern half quickly drops due to the demanding conditions encountered this day, decreasing the peak flux with respect other apparently less-harming days. The more the days get further to the summer solstice, the most symmetrical with respect solar noon the aiming strategy behavior becomes. Due to its low DNI, the winter solstice day does not even need to work with the lowest k value adopted during the rest of days. The hours of operation needed to completely fill the tank are included in Table 5.5, as well as the start-up time, according to the criteria established in the optical model, and shutdown time. Note that not all days are able to reach the tank filling due to the more limited sunlight hours and the lower DNI (Figure 5.3).

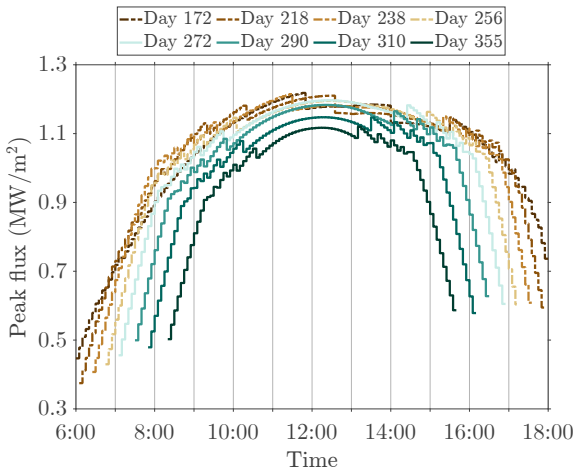


Figure 5.11: Maximum heat flux in the Eastern half for the set of representative days.

Then, the lifetime results for the first two panels of each flow path are presented in Figure 5.12, for being the most damaged two. The critical panel in the Eastern half is the first one, being so in all the days except in the 310 day; on the other hand, the second panel is the limiting one in the Western half in nearly all the days of the set, except the days 272 and 290. The complete lifetime results for this set of days are compiled in Table D.1 and depicted in Figure D.1.

Table 5.5: Hours of operation and tons of molten salt in the tank.

Day	Start	End	HOP	Tank (Tn)
172	6:00	13:52	7h 52min	8,500
218	6:05	14:07	8h 2 min	8,500
238	6:25	14:29	8h 4min	8,500
256	6:45	14:58	8h 13min	8,500
272	7:05	15:34	8h 29min	8,500
290	7:30	16:34	9h 4min	8,293
310	7:50	16:14	8h 24min	7,154.7
355	8:20	15:44	7h 24min	5,758.3
Avg	7:00	15:11	8h 11min	7,963.2

It can be observed that the most favorable day is the summer solstice; it is the most aggressive day in terms of DNI, which means that, in order to meet the T_{film} and $2S_y$ limitations, it requires a more open set of aiming strategies during the operation with respect other days of the year, lowering the peak flux on the receiver surface but yet allowing the tank filling in the least time. From there, the lifetime decreases when moving further from the summer solstice, with the minimum value being found between the last day able to fill the tank (day 272) and the following one (day 290). Then, the lifetime forecast increases back in the last days of the year, despite they some operate even longer than previous days. These are considerably less aggressive days in terms of DNI but that implies that they are allowed to work with more equatorial aimings; yet, that is not sufficient for them to be able to fill the tank. It should be noted that the results in Table D.1, as well as the ones highlighted in Figure 5.12, represent the lifetime estimation for each day individually, as if they were considered the design day on their own. The average lifetime obtained with such set of days, which constitutes the final receiver lifetime prediction when performing the analysis for various days (Eq. 5.7), is also included in Table D.1 and depicted in Figure 5.13. The Eastern half panels present greater lifetime estimation the Southern they are placed; in the Western half, the second and the ninth panel deviate from that trend.

Additionally, since not all the days constituting the set studied achieve the complete tank filling, the case of having a tank with half the capacity is studied next, considering the same start-up hour in each case than in the tank of double the size. The purpose is to understand how the damage mechanism evolves

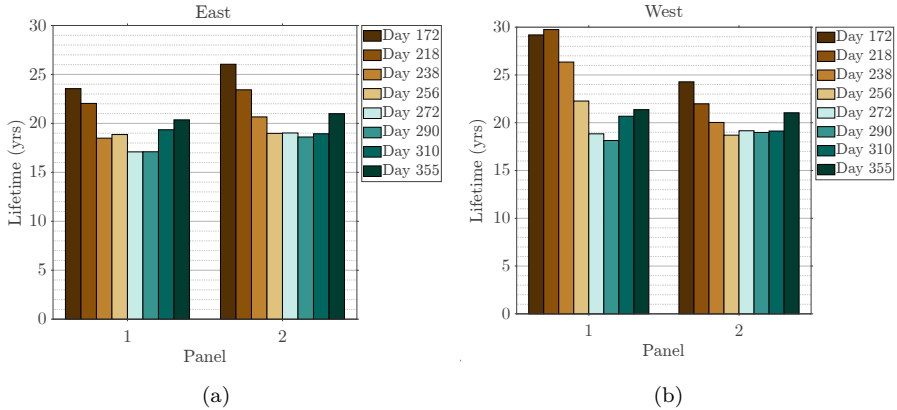


Figure 5.12: Lifetime results of the first two panels from (a) the Eastern and (b) Western halves, for each representative day individually.

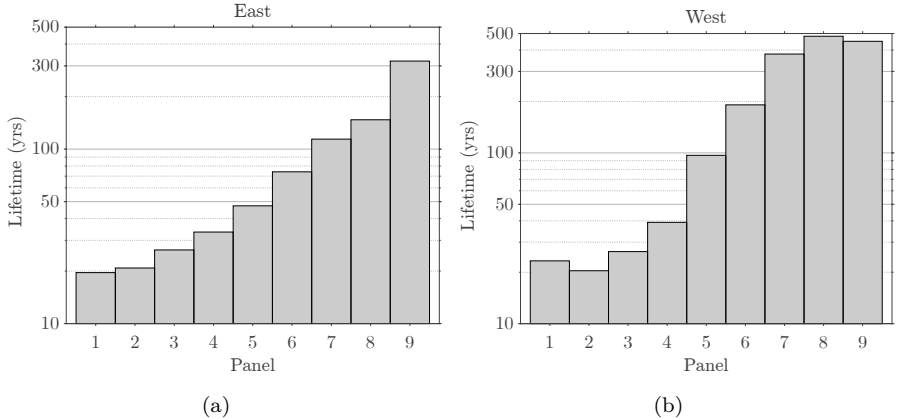


Figure 5.13: Final lifetime results for the set of representative days: (a) Eastern and (b) Western flow paths.

during the year with the ambient conditions, providing these days the opportunity to reach the same goal. The outcome for each day individually is included in Figure 5.14, again for the first two panels of each half. The full results are as well included for reference in Appendix D, in Table D.2 and shown in Figure D.2. Now the trend is clearly descendent from the summer solstice to the winter one, with minor exceptions (note that the start-up hour differs from one day to the other), showing that the less HOP needed during the summer days and the less equatorial aiming strategies that the summer days require in order to meet the safety limits benefits the receiver in terms of lifetime. With respect to the original tank, twice this size, the HOP do not follow the same proportion,

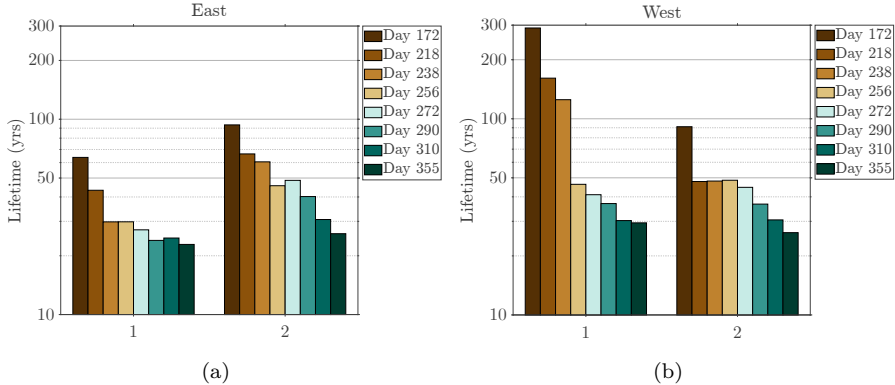


Figure 5.14: Lifetime results of the first two panels from (a) the Eastern and (b) Western halves, considering a salts tank of half the original capacity, for each representative day individually.

being needed more than half the time required for the bigger tank. However, note that the analysis has been performed starting as early in the morning as possible. Looking at the previous results obtained in this Chapter, the receiver would possibly benefit from a late start, not only by requiring less HOP but also from the lower aiming strategies needed at the central hours of the day.

Lifetime estimation using a set of days vs the spring equinox design day

To conclude the design day analysis, the EODs percentage variation, panel-by-panel, between the case of the spring equinox and the case of the representative set of days is depicted in Figure 5.15, considering the full tank filling. Note that the lifetime estimation of the spring equinox, which is equivalent to the autumn one (day 265), falls around the results of the days 256 and 272 (see Table C.1, 5-min time step, and Table D.1); nevertheless, in many of the panels, the spring results are not perfectly framed between them, again most probably due to the different plant start-up schedule that also altered in some occasions the lifetime trend through the set of days.

Looking at the year overall results, the lifetime predicted with the spring equinox is below the one resulting from considering the set of days in all the receiver panels. The differences are mainly more noticeable in the Eastern path. Regarding the critical panel in each path, the Eastern one (panel 1) has its lifetime underestimated in a 9.4% using just the spring equinox while the Western one (panel 2) would last a 7.1% less in that case. The second most-

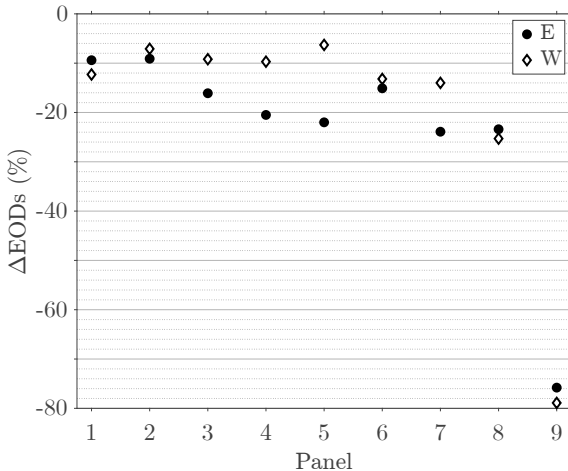


Figure 5.15: Lifetime percentage difference of the spring equinox results with respect the set of days.

damaged panels in each path, which are panel 2 in the Eastern half and panel 1 in the Western side, deviate by a 9.1% and a 12.3%, respectively. Panels from 3 to 8 present an average deviation of a 20.2% in the Eastern side and a 12.9% in the Western half. In both flow paths the final panel lifetime is greatly underestimated, over a 75%.

Even having selecting a precise time resolution, these results heavily suggest that taking just the spring equinox may fall excessively into the security side in terms of lifetime prediction, which would lead to an overestimation of the plant costs.

5.5 Conclusions

This Chapter deals with the impact, in terms of lifetime, that the time resolution and design day selection have when performing an integral analysis of an external tubular central receiver of a SPT plant operating during clean design day conditions. The process starts by obtaining the heliostat field aiming strategy to the receiver during its operation, since it defines the heat flux distribution on the receiver surface. For this matter, it has to be taken into account the safety operation limit marked by the admissible film temperature in the tube, to avoid corrosion. It is also desirable to keep the elastic stresses under the stress reset limit in order to guarantee the stress relaxation full accumulation despite the cyclic receiver operation. Hence, the aiming factor is initially

selected as equatorial as possible but, depending on the DNI and sun position of the different time intervals, it would require modifications in order to meet both considerations, decreasing the peak flux.

The first goal of this Chapter is determining the contribution of finer or coarser time resolutions in the results of the lifetime analysis. The time steps selected are 60 minutes, 30, 15, 5 and 1, as well as the case of considering just the solar noon as design point. Thus, the finer time resolution of this Chapter is the 1-minute one, which will be taken as the reference one. Initially, the lifetime analysis is performed for the filling of an 8,500 Th molten salt storage tank. For being a clean design day, the fatigue damage is negligible in comparison to the creep damage. It is observed that the selection of the solar noon as design point highly underestimates the receiver lifetime, being over a 40% less in the best of the cases, with all the panels being excessively off. The divergences in the rest of the time resolution cases are not that great with respect the reference one in nearly all the panels; the exception is the Eastern first panel (which is also the most critical of the receiver), with divergences progressively decreasing from the -18.86% obtained for the 60-min time step. Looking at the results, the 5-min, or even the 15-min, time step would be desirable for the analysis if aiming for results close to the ones obtained with the finer resolution without compromising the computational cost excessively. On the other hand, the divergences in the receiver thermal power are lesser than a 5% between the 60-minute time step and the 1-minute one. Given that the tank filling approach results in different HOP for each time resolution, the analysis is then performed for a fixed HOP, equal to the time that takes the reference time step to fill the tank. Now, the receiver panels last slightly longer in these time steps that have seen their HOP reduced, closing the gap in the panels that lived lesser than the reference case. However, for these panels that initially lasted longer, the breach in the predicted lifetime increases even more. Despite the critical panels fall in the first of these two scenarios, the divergences are not significantly reduced.

The close examination of the creep damage results shows that the finer aiming strategy selection, and therefore the flux profile and peak value associated, contributes greatly in the lifetime differences. Despite coarser time resolutions work at lower DNI levels during most of the operation, since it prominently takes place during the morning hours, their inability to quickly adapt to more open-less peaker-aiming strategies highly penalizes them in terms of creep damage. The interpolation of the 5-minute time step results to a one-minute basis translates in a lesser deviation with respect the 1-minute time resolution, es-

pecially in the central panels of the receivers, whose lifetime prediction results virtually exact. The critical panel in each path also sees that gap reduced, although it is not that remarkable.

Once the time resolution analysis has been performed, the 5-min time step is selected to perform the design day analysis. This consists in the comparison of the lifetime results for the spring equinox with the average lifetime obtained using a set of 8 days equidistant in maximum solar height. These days cover from the summer to the winter solstice and serve as representative of the year. From their individual examination it is found that the least damaging day is the summer solstice, which is also the fastest to achieve the TES tank filling; then, the lifetime decreases the closer the day is to the winter solstice. The minimum lifetime obtained falls around the last day allowing the tank filling; if all the days are able to fill the tank, the critical day is the winter solstice itself, outcome that is observed for a tank with half the original capacity. The goal of their joint comparison opposite to the spring equinox is determining whether the latter provides a good characterization of the yearly operation by itself. The results show that the receiver lifetime is underestimated when using just the spring equinox as design day. The divergences of the critical panel are over a 9%, while the last panel in both path flows is underestimated in over a 75%.

Hence, looking at the lifetime results obtained through this Chapter, it would be advisable to use moderate time resolutions for a set of representative days in order to avoid an excessive level of conservatism.

Nomenclature

c_1, c_2	Manson-Coffin equation exponents		cycles per day fatigue cycles
D	total damage	N, S	cardinal points
d	daily damage	q	heat flux (W/m^2)
E	Eastern flow path, Young modulus (Pa)	S S_H	allowable stress (Pa) hot relaxation strength (Pa)
I	number of days studied	S_{SR}	stress reset limit (Pa)
J	number of creep damage intervals per day	S_y $S_{y,\text{cold}}$	yield strength (Pa) yield strength at room temperature (Pa)
k	aiming factor	T	temperature (K)
M	number of fatigue damage		

t_R rupture time (h)

W Western flow path

Greek letters

α	solar altitude ($^{\circ}$)	ε	strain (%)
β	M-R-M parametrization coefficients	ε'_f	fatigue ductility (%)
Δt	time interval (s)	σ	stress (Pa)
$\Delta \varepsilon$	strain range (%)	σ'_f	fatigue strength (%)

Subscripts

a	allowable	hour	60-minute time step
avg	average	L	limit
c	creep	max	maximum
eq	equivalent	min	1-minute time step
f	fatigue	relax	relaxation stress
film	inner tube wall		

Superindexes

E	elastic
P	plastic

Abbreviations

ASME	American society of mechanical engineers	EODs	equivalent operating days
BPVC	boiler and pressure vessel code	HOP	hours of operation
CGM	coarse grid model	HTF	heat transfer fluid
CPV	concentrating photovoltaic	LCOE	levelized cost of energy
CSP	concentrating solar power	LDS	linear damage summation
ECGM	energy coarse grid model	M-R-M	Mendelson-Roberts-Manson
DNI	direct normal irradiance (W/m ²)	sCO ₂	supercritical carbon dioxide
		SPT	solar power tower
		TES	thermal energy storage

References

- ASME 2004 ASME Boiler and Pressure Vessel Code, Section III, Division 1, Subsection NH. American Society of Mechanical Engineers.
- ASME 2010 Asme boiler and Pressure Vessel Code, Section II part D. american society of mechanical engineers.
- BABCOCK & WILCOX COMPANY 1984 Molten Salt Receiver Subsystem Research Experiment Phase 1 -Final Report, Volume 1- Technical. *Tech. Rep.* SAND82-8178. Barberton, OH, United States.
- BECHT IV, C. 2011 Elevated temperature shakedown concepts. *Journal of Pressure Vessel Technology, Transactions of the ASME* 133 (5), 051203-1–5.
- BERMAN, I., GANGADHARAN, A.C., GUPTA, G.D. & NARAYANAN, T.V. 1979 An interim structural design standard for solar energy applications. *Tech. Rep.* SAND79-8183. Sandia National Laboratories, Albuquerque, NM, United States.
- BRITISH ENERGY GENERATION 2003 R5, Issue 3 assesment procedure for the high temperature response of structures.
- BURGALETA, J.I., ARIAS, S. & RAMIREZ, D. 2011 Gemasolar, the first tower thermosolar commercial plant with molten salt storage. In *Proceedings of the SolarPACES 2011 conference on concentrating solar power and chemical energy systems, Granada, Spain.*
- CHEN, X., SOKOLOV, M.A., SHAM, S., ERDMAN, D.L., BUSBY, J.T., MO, K. & STUBBINS, J.F. 2013 Experimental and modeling results of creep-fatigue life of Inconel 617 and Haynes 230 at 850 °C. *Journal of Nuclear Materials* 432 (1-3), 94–101.
- COCCO, D., MIGLIARI, L. & PETROLLESE, M. 2016 A hybrid CSP-CPV system for improving the dispatchability of solar power plants. *Energy Conversion and Management* 114, 312–323.
- CONROY, T., COLLINS, M.N., FISHER, J. & GRIMES, R. 2018a Levelized cost of electricity evaluation of liquid sodium receiver designs through a thermal performance, mechanical reliability, and pressure drop analysis. *Solar Energy* 166, 472–485.

- CONROY, T., COLLINS, M.N., FISHER, J. & GRIMES, R. 2018b Thermal and mechanical analysis of a sodium-cooled solar receiver operating under a novel heliostat aiming point strategy. *Applied Energy* 230, 590–614.
- CONROY, T., COLLINS, M.N. & GRIMES, R. 2019 A review of steady-state thermal and mechanical modelling on tubular solar receivers. *Renewable and Sustainable Energy Reviews* 119.
- FALCONE, P.K. 1986 A handbook for solar central receiver design. *Tech. Rep. SAND-86-8009*. Sandia National Laboratories, Livermore, CA, United States.
- GONZÁLEZ-GÓMEZ, P.A., RODRÍGUEZ-SÁNCHEZ, M.R., LAPORTE-AZCUÉ, M. & SANTANA, D. 2021 Calculating molten-salt central-receiver lifetime under creep-fatigue damage. *Solar Energy* 213, 180–197.
- GROSSMAN, J.W. & JONES, W.B. 1990 Evaluation of thermal cycling creep-fatigue damage for a molten salt receiver. In *ASME international solar energy conference, Miami, FL, United States*.
- GUÉDEZ, R., SPELLING, J., LAUMERT, B. & FRANSSON, T. 2014 Optimization of thermal energy storage integration strategies for peak power production by concentrating solar power plants. *Energy Procedia* 49 (0), 1642–1651.
- KISTLER, B.L. 1987 Fatigue analysis of a solar central receiver design using measured weather data. *Tech. Rep. SAND86-8017*. Sandia National Laboratories, Albuquerque, NM, United States.
- MCCONOHY, G. & KRUIZENGA, A. 2014 Molten nitrate salts at 600 and 680°C: Thermophysical property changes and corrosion of high-temperature nickel alloys. *Solar Energy* 103, 242–252.
- MEHOS, M., PRICE, H., CABLE, R., KEARNEY, D., KELLY, B., KOLB, G. & MORSE, F. 2020 Concentrating Solar Power Best Practices Study. *Tech. Rep. NREL/TP-5500-75763*. National Renewable Energy Laboratory, Solar Dynamics LLC, Golden, CO, United States.
- MEYBODI, M. AGHAEI, RAMIREZ SANTIGOSA, L. & BEATH, A.C. 2017 A study on the impact of time resolution in solar data on the performance modelling of CSP plants. *Renewable Energy* 109, 551–563.
- NARAYANAN, T.V., RAO, M.S.M. & CARLI, G. 1985 Structural Design and Life Assessment of a Molten Salt Solar Receiver. *Journal of Solar Energy Engineering* 107 (3), 258–263.

- NEISES, T.W., WAGNER, M.J. & GRAY, A.K. 2014 Structural Design Considerations for Tubular Power Tower. In *International Conference on Energy Sustainability (ES2014), Boston, MA, United States*, pp. 6603 1–7. National Renewable Energy Laboratory.
- NITHYANANDAM, K. & PITCHUMANI, R. 2016 Thermal and structural investigation of tubular supercritical carbon dioxide power tower receivers. *Solar Energy* 135, 374–385.
- RENO, M.J., HANSEN, C.W. & STEIN, J.S. 2012 Global horizontal irradiance clear sky models : implementation and analysis. *Tech. Rep.* SAND2012-2389. Sandia International Laboratories, Albuquerque, NM, United States.
- RODRÍGUEZ-SÁNCHEZ, M.R., MARUGÁN-CRUZ, C., ACOSTA-IBORRA, A. & SANTANA, D. 2018 Thermo-mechanical modelling of solar central receivers: Effect of incident solar flux resolution. *Solar Energy* 165, 43–54.
- RODRÍGUEZ-SÁNCHEZ, M.R., SORIA-VERDUGO, A., ALMENDROS-IBÁÑEZ, J. A., ACOSTA-IBORRA, A. & SANTANA, D. 2014 Thermal design guidelines of solar power towers. *Applied Thermal Engineering* 63 (1), 428–438.
- SÁNCHEZ-GONZÁLEZ, A. & SANTANA, D. 2015 Solar flux distribution on central receivers: A projection method from analytic function. *Renewable Energy* 74, 576–587.
- TALER, J., DZIERWA, P., JAREMKIEWICZ, M., TALER, D., KACZMARSKI, K., TROJAN, M. & SOBOTA, T. 2019 Thermal stress monitoring in thick walled pressure components of steam boilers. *Energy* 175, 645–666.
- WAGNER, M.J. 2008 Simulation and Predictive Performance Modeling of Utility-Scale Central Receiver System Power Plants. PhD thesis, University of Wisconsin, Madison.
- ZAVOICO, A.B. 2001 Solar Power Tower - Design Basis Document. *Tech. Rep.* SAND2001-2100. Sandia National Laboratories, Albuquerque, NM and Livermore, CA, United States.
- ZURITA, A., MATA-TORRES, C., CARDEMIL, J.M. & ESCOBAR, R.A. 2020 Assessment of time resolution impact on the modeling of a hybrid CSP-PV plant: A case of study in Chile. *Solar Energy* 202, 553–570.

Creep-fatigue damage calculation during transient conditions

Contents

6.1	Introduction	196
6.2	Receiver models employed	198
6.2.1	Optical model, aiming strategy and thermal model	198
6.2.2	Elastic stresses and strains model and lifetime model	200
6.3	Configurations analysed	202
6.3.1	Reference design days, and heliostat field and receiver configuration	202
6.3.2	Receiver control modes during transient conditions	203
6.3.3	DNI cases of study	207
6.4	Methodology proposed to calculate the transient operation	208
6.4.1	Clean design day and cloudy day levels characterization	208
6.4.2	Calculating the creep and fatigue damages	210
6.5	Results and discussion	210
6.5.1	DNI database clustering	211
6.5.2	Creep and fatigue damage results for clustered days	215
6.5.3	Damage analysis using the 2018 DNI database	222
6.6	Conclusions	224
	References	227

Summary

The successful deployment of solar power towers (SPTs) lies in the reliable design of solar receivers, assuring the lifetime under high heat flux and cloud

passages. Two main damage mechanisms appear during central-receiver operation: creep, during hold times at high temperatures and stresses, and fatigue, caused by cyclic and transient operation. Nevertheless, early-days molten-salt central-receiver studies focused on the fatigue damage, neglecting the creep. This Chapter aims to determine the extent of each damage on a Haynes 230 receiver. It is analyzed using transient direct normal irradiance (DNI) data of a whole year, controlling the operation to guarantee the receiver preheat and minimize the start-ups. The molten-salt flow-rate during cloud passages or hazy days remains as the clear-sky scheduled one, to avoid tube overheat, preventing salt degradation and stress reset, when the clouds cleared.

The results show that creep dominates, with a minimum share of 73.8% for the transient DNI case. High creep is motivated by the long operating (6 h per day on average), mostly at high DNI, while the low number of average start-ups per day (1.4) do not increase much the fatigue, barely affected by small transients. The use of clear-sky DNI instead of the transient one constitutes a conservative estimation, with the creep greatly increasing, showing a minimum share of 82%. Consequently, the predicted lifetime is lower, going from 45 years to 27.8. Intermediate mass-flow control modes would fall in-between them. Clustering the days according to their DNI features shows that the high-energy days, with high creep, are the most common, highlighting the creep interest and that the fatigue can be estimated taking only the strain range produced by the start-up.

6.1 Introduction

In the early development stages of SPT technology, the attention regarding the damage assessment of the receiver was put on the fatigue analysis (Babcock & Wilcox Company, 1984; Kistler, 1987; Grossman & Jones, 1990) and the creep was considered negligible. It was argued that, for the cavity-type molten-salt receiver analysed in (Babcock & Wilcox Company, 1984), with its tubes forming a membrane wall, the critical spot found was under high heat fluxes and had a low salt temperature, minimizing the creep damage; additionally, the code case initially used, the N-47 for nuclear applications, was though-out for fast breeder reactors, with long hold times at elevated temperatures but few transients, the opposite situation than the faced by solar receivers (Kistler, 1987; Grossman & Jones, 1990). Conversely, the research involving the use of alternative heat transfer fluids (HTFs) for the receiver operation made the receiver

creep-fatigue damage assessment evolve towards the consideration of creep as the main damage mechanism. The air receiver studied by Fork *et al.* (2012) showed a negligible fatigue opposite to creep, with small strain variations resulting in a high number of allowable fatigue cycles. As for the sCO₂, Neises *et al.* (2014) showed that the receiver, under high pressures (~ 25 MPa) and temperatures (outlet of 650 °C), presented a fatigue damage around a 10% of the total, although they only considered an axis-symmetric heat flux distribution over the tubes, which largely reduces the stress. Regarding sodium receivers, a billboard design tested by Conroy *et al.* (2018) in order to evaluate the impact of different sizes (receiver areas from 1 m² to 4 m²) and tubes diameters on the levelized cost of electricity (LCOE) showed also that the creep damage was the restrictive one out of the two damages, with fatigue becoming more relevant for very small receivers. These HTFs have in common their higher admissible temperatures with respect molten salt, allowing greater heat fluxes on the receiver and, thus, increasing the tubes temperatures, which are critical for the creep damage. There are, however, some molten-salt works studying both damages. Narayanan *et al.* (1985) performed the analysis following the modified N-47 CC proposed by Berman *et al.* (1979), taking into account cloud transients and daily start-ups for the fatigue side of the analysis. Nevertheless, the creep assessment approach was a rather simplified one. More recently, González-Gómez *et al.* (2021) proposed a methodology to evaluate creep and fatigue damage on molten-salt receivers, considering the elastic-plastic behaviour of stresses and the stress relaxation, two key aspects in the creep damage analysis. However, the study was performed for clear-sky days, neglecting the effects of cloud transient operation.

The fluctuating nature of solar radiation is an essential feature that accompanies concentrating solar technologies and that needs to be taken into account, from the design point of view to an operation one. Thus, in order to mitigate its fluctuation effects, control strategies on the heliostat field aiming and on the receiver are implemented (Crespi *et al.*, 2018; Augsburger & Favrat, 2013; Zurita *et al.*, 2020; Wagner *et al.*, 2018), which include the preheat of the receiver during the morning start-up and the mid-day ones (Vant-Hull, 2002). To successfully achieve it, the acknowledgement of the solar resource is essential, with the DNI for the upcoming days being the key parameter for the operation mode selection, not only of the receiver but for the whole plant (Rohani *et al.*, 2017). Traditionally, there have been methods to classify days according to their DNI, being the clearness index one of the most common due to its sim-

plicity, with days being either overcast, cloudy, partly cloudy or clear (Liu & Jordan, 1960). However, such approach disregards qualitative features of the DNI, such as the distribution of the solar resource during the day or its variability, that are relevant in the concentrating solar power (CSP) production. Thus, alternative indexes have been proposed in the literature to adequate the classification of the days to the actual operation of the plant, resulting in a higher number of day-groups (Moreno-Tejera *et al.*, 2017), more suitable for CSP analysis (Moreno-Tejera *et al.*, 2018).

With all of the above, this Chapter aims to shed light on the actual share of fatigue and creep damages that a molten-salt central-receiver in Haynes 230 experiences, a gap of knowledge not yet addressed, with previous studies either neglecting the creep damage, using quite simplified models to calculate it, or not contemplating transient operation. Two scenarios are considered for each day: a day with cloud passages interrupting the DNI, providing small transients, and its corresponding clear-sky DNI, with maximum creep damage. These are tested for a set of days during different seasons, exploring how the creep and fatigue damages vary depending on the day-type and stage of the year as well. A final receiver lifetime estimation is carried out with the DNI data of a whole year during both transient and clear-sky operation, showing the damages share as well. In Section 6.2, the various receiver models required to analyse the receiver behaviour are listed. Then, Section 6.3 presents the receiver characteristics, as well as the operation modes considered and the two main cases of study in terms of DNI. Subsequently, the methodology proposed to characterize the receiver during transient conditions is detailed in Section 6.4, with the results presented in Section 6.5 for individuals days of each type and for the whole year study. Lastly, the conclusions of this Chapter are included in Section 6.6.

6.2 Receiver models employed

SPT receivers lifetime is determined by their creep and fatigue damages. Thus, the required model to obtain them is presented, as well as the upstream ones that provide relevant information in that regard, such as the heat flux on the receiver or the temperature distribution.

6.2.1 Optical model, aiming strategy and thermal model

The Daneshyar-Paltridge-Proctor clear-sky model (Reno *et al.*, 2012) is used to obtain the DNI of the clear-sky conditions, DNI_C , as a function of the solar

altitude solely, α ,

$$\text{DNI}_C = 950.2 [1 - \exp(-0.075 \alpha)]. \quad (6.1)$$

With it, the optical model employed, developed by Sánchez-González & Santana (2015), provides the heat flux on the receiver surface, q_{rec} . The heliostat field aiming strategy is specified in the process, which can be from an equatorial one, where the target is mainly the middle length of the receiver, to an open one, with the focus being both receiver ends. The former results in higher peak fluxes, guaranteeing a greater optical efficiency and power production, but can be excessively damaging; on the other hand, the latter provides more gentle operation conditions but lower efficiency. Near sunrise, the heat flux reflected on the receiver increases much faster than other moments of the day due to the shading, the changes of insolation and the cosine efficiency of the heliostats (Vant-Hull, 2002). Consequently, the optical model is set to evaluate the flux on the receiver as long as a minimum α of 10° is guaranteed (Falcone, 1986).

In this work, the main thermal and mechanical limitations regarded for the aiming strategy setting are:

- The tubes film temperature, T_{film} , which depends on the HTF and the tube material, to prevent the tubes from suffering an excessive level of corrosion.
- The stress reset limit, S_{SR} : surpassing it would prevent the desirable global stress relaxation phenomenon (Barua *et al.*, 2020). It is equal to $S_{\text{SR}} = S_{y,\text{cold}} + S_H$ (Becht IV, 2011), with $S_{y,\text{cold}}$ being the yield strength at room temperature and S_H the hot relaxation strength, typically taken as 1.25 times the allowable stress, S , established by the ASME (ASME, 2010). This limit is lower than the twice yield strength, $2S_y$, and thus the reverse plasticity regime of the material, which would lead to greater stress amplitude cycle after cycle due to the material hardening and dynamic aging, is also avoided.

Hence, the aiming strategy is initially selected as equatorial as possible each time and then modified so the allowable flux density (AFD) satisfied by these aspects is met. It is adjusted for each path individually since they are subjected to different heat flux during most of the operation. Upon obtaining the heat flux, the thermal coarse grid model (CGM) developed by Rodríguez-Sánchez *et al.* (2014) provides the tubes temperatures, with the tubes discretized in axial and circumferential divisions.

6.2.2 Elastic stresses and strains model and lifetime model

The tubes temperature distribution is used in the model developed in Chapter 3, taking into account the tubes properties temperature dependence, to obtain the elastic stresses and strains (σ_{eq}^E and $\varepsilon_{\text{eq}}^E$). Then, following the lifetime model fully detailed in Chapter 4, these σ_{eq}^E and $\varepsilon_{\text{eq}}^E$ are transformed into elastic-plastic ones (σ_{eq} and ε_{eq}). Note that the plasticity memory of the material is not regarded, providing a straight-forward as well as conservative calculation approach in such sense. Moreover, the stress relaxation is considered, σ_{relax} , selecting a stabilization time of 30 hours for alloy Haynes 230, which is achievable since the S_{SR} is watched. This results in the final creep stress, σ_c , which is then used to obtain the rupture time due to creep,

$$\log_{10}(t_R) = \beta_0 + \beta_1 \frac{1}{T} + \beta_2 \log_{10}(\sigma_c) + \beta_3 \log_{10}(\sigma_c) \frac{1}{T}, \quad (6.2)$$

where β are the Mendelson-Roberts-Manson (M-R-M) parametrization coefficients, included in Chapter 4. Thus, the creep damage during a certain i day is the addition of the creep damages of all the J time intervals of duration Δt at which that day is discretized,

$$d_{c,i} = \sum_{j=1}^{J_i} \frac{\Delta t_n}{t_{R,n}}. \quad (6.3)$$

Opposite to the creep damage, the fatigue one is defined by the M strain ranges of the receiver tubes occurring over the daily operation. Each of these strain ranges result in a number of allowable cycles, N_a , for the tubes, obtained as

$$\frac{\Delta \varepsilon_{\text{eq}}}{2} = \frac{\Delta \varepsilon_{\text{eq}}^E}{2} + \frac{\Delta \varepsilon_{\text{eq}}^P}{2} = \frac{\sigma'_f}{E} N_a^{-c1} + \varepsilon'_f N_a^{-c2}. \quad (6.4)$$

Its exponents and coefficients are evaluated at the mean temperature of the beginning and end of each fatigue cycle, as established by the ASME Section VIII, Division 2. These parameters are compiled in Table 6.1. The ones for temperatures from 427 to 982 °C were already available in (Fahrmann & Srivastava, 2014) and presented in Chapter 4; nonetheless, considering the shutdown instants, the mean temperature for the evaluation of these coefficients falls outside that range at certain times. Hence, the coefficients corresponding to the temperatures of 24 and 204 °C have been included as well, obtained by fitting the experimental data available in (Barrett *et al.*, 2016).

To consider the creep-fatigue interaction effects, a reduction factor of 4 due to the hold periods is applied to the N_a obtained with Eq. 6.4, which is deemed a

Table 6.1: Fatigue coefficients at different experimental temperatures.

T (°C)	σ'_f/E (%)	c_1 (-)	ε'_f/E (%)	c_2 (-)
24	0.17	0.014	66.5	0.54
204	0.15	0.011	130	0.6
427	0.2	0.01	18	0.45
538	0.2	0.0005	45	0.6
649	0.2	0.001	45	0.65
760	0.2	0.02	45	0.7
871	0.15	0.02	12	0.55
982	0.2	0.02	45	0.8

conservative approach (Radke *et al.*, 2017; Kolb, 2011): $N_{a,s} = N_a(\Delta\varepsilon_{eq,s}, T)/4$. Additionally, the data scattering of the $N_a-\varepsilon$ curve is also regarded, using a 2x factor for the strain calculation, $\Delta\varepsilon_{eq,s} = 2\Delta\varepsilon_{eq}$; as discussed by Chopra & Shack (2003) and Radke *et al.* (2017), it is not a safety factor but rather an approach to account for the effect of aspects such as the load history, the size, surface finish and material variability. There are also divergences in the fatigue life results when translating the ones obtained from the testing of solid specimens into the tubular components used in the receiver design; nevertheless, these differences were found at strain ranges way far from the strain levels appearing during the regular receiver operation (Radke *et al.*, 2017). Thus, and given the lack of knowledge regarding how such effect translates, if any, for considerably lower strain ranges, they are not included in this analysis. It should also be noted that the experimental plots of the strain range versus the number of allowable cycles only reach just below the 10^6 number of cycles (Fahrmann & Srivastava, 2014; Barrett *et al.*, 2016) and so such value is taken as the maximum N_a in this study, regardless the $\Delta\varepsilon_{eq}$ of the receiver tubes being lower than the one providing such value. Hence, the daily fatigue damage is obtained as

$$d_{f,i} = \sum_{m=1}^{M_i} \frac{N_m}{N_{a,s,m}}. \quad (6.5)$$

The fatigue cycles, N_m , are determined using the rainflow counting method available in Matlab (Mathworks, 2017), programmed following the ASTM standard for fatigue cycle counting (ASTM International., 2017). These are either 1 or 0,5 depending on whether they constitute a full or half cycle. The algorithm also provides their corresponding strain range and also takes into account the

cycle comprehended between the minimum and maximum strain values of the whole set.

The total creep and fatigue damages, D_c and D_f , during the receiver lifetime are the addition of all their corresponding daily damages considered. Their combination must be equal or lower than the damage limit, D_L : $D_L \geq D_c + D_f$. Considering the linear interaction of both damage mechanisms, as proposed by the linear damage summation (LDS) model (ASME, 2004), such limit is equal to one, which is acceptable in the case of Haynes 230, as experimentally showed by Chen *et al.* (2013). For a single design day, i , D_c and D_f are equivalent to multiplying $d_{c,i}$ and $d_{f,i}$ by the estimated equivalent operating days (EODs) that determine the receiver lifetime. If various days, I , are regarded, these total damages are the result of the average daily damages multiplied by the total EODs:

$$D_L = \text{EODs} \sum_{i=1}^I \left(\frac{d_{c,i}}{I} \right) + \text{EODs} \sum_{i=1}^I \left(\frac{d_{f,i}}{I} \right) \rightarrow \text{EODs} = \frac{D_L}{\overline{d_c} + \overline{d_f}}. \quad (6.6)$$

6.3 Configurations analysed

6.3.1 Reference design days, and heliostat field and receiver configuration

The characteristic days selected are the spring equinox (Julian day 81, equivalent to the autumn equinox, day 265), the summer solstice (172) and the winter one (355). These are useful to test the receiver during days with different solar altitude, modifying the aiming strategy needs of the receiver. The location studied corresponds to the Gemasolar plant (Seville, Spain), at a latitude of 37.56°. The heliostat field is also the Gemasolar one, with 2,650 heliostats of 115.8 m² of effective mirror surface each, giving a total of 306,605 m² of mirror area. The receiver is a cylindrical external tubular one, with its main characteristics compiled at Table 6.2. The tubes are coated with a black Pyromark painting to enhance their absorptivity, while the rear refractory wall is covered with a high reflectivity paint. These are made of Haynes 230, one of the best alternatives in terms of thermal and mechanical properties, available as temperature dependent in the ASME BPVC Section II, Part D (ASME, 2010). Its creep and fatigue damage coefficients are compiled in Chapter 4, essential for the life service calculation. The tubes are guided by a series of welded supports, called clips, in order to avoid their excessive deflection. In this Chapter,

Table 6.2: Receiver main parameters.

Parameter	Value
Tower height	130 m
Receiver diameter	8.4 m
Number of panels	18
Tubes length	10.5 m
Tubes external diameter	2.24 cm
Tubes thickness	1.2 mm
Tubes separation	1.4 mm
Tubes per panel	61
Number of flow paths	2
Maximum $T_{\text{out, HTF}}$	565 °C
Maximum T_{film}	650 °C

a number of clips is selected such that the generalized plane strain condition prevails and the tubes are unable to bend, as seen in Chapter 3. The HTF is solar salt (60% NaNO₃-40% KNO₃) (Zavoico, 2001), with the admissible bulk temperatures for its SPT use between 290 °C and 565 °C to prevent its freezing and decomposition, respectively. It is divided into two symmetrical flow paths in the N-S direction, flowing in a serpentine-like way. The maximum allowable film temperature, which is the temperature at the tube inner wall, for such HTF and tube material is 650 °C (McConohy & Kruizenga, 2014).

6.3.2 Receiver control modes during transient conditions

The receiver control modes considered in this Chapter can be divided into two categories. The first one determines the operation of the receiver and is defined by the heat fluxes on its surface and the fulfilling of a favorable operation/preheating forecast. The second involves the HTF mass-flow rate. The DNI fluctuation is regarded over time but happening uniformly upon the heliostat field, not considering transient divergences on its spatial distribution at a certain instant. This is a design-oriented approach, a stage at which the DNI data available is only time-dependent, and is the most detrimental regarding power production. Modern facilities, such as Ashalim SPT plant (Minis *et al.*, 2019) are provided with spatial DNI measurement systems, useful at operation stages, but typically not available during the receiver design.

Operation of the receiver

The receiver operation is subject to a minimum heat flux on its surface, $q_{\min,\text{rec}} \geq q_{\min,\text{limit}}$, equal to 40 kW/m^2 , in order to avoid the HTF cooling and potential freezing. The limiting spot is the inlet of the final panel from the Western half during the morning and from the Eastern one during the afternoon. Note that, during the first morning time intervals and late afternoon ones, the aiming strategy selected is equatorial since the T_{film} and S_{SR} limits allow it; this may lead to a delay in the start-up and to shut down in advance since the heat flux is mainly concentrated on the receiver centre, while the critical spots are towards the receiver vertical ends. Thus, more open aiming strategies could be able to provide the $q_{\min,\text{limit}}$ on the receiver sooner than the scheduled ones.

The minimum DNI required to have a $q_{\min,\text{rec}}$ equal to 40 kW/m^2 at each moment of the three characteristic days is presented in Figure 6.1. If such DNI results above the feasible DNI_C , it is omitted and the receiver would not be able to work. Thus, the time frame at which the receiver could operate during these days is marked by the initial and final times of the DNI_{\min} (dashed lines in Figure 6.1). Additionally, to avoid an excessive number of start-ups and shutdowns, the start-up at a certain time that surpasses the $q_{\min,\text{limit}}$ is subject to a favourable forecast during the following 35 minutes after the present time step completion (40 minutes total). If this condition is not met, the receiver remains inoperative to avoid shutting down shortly back again.

Since the receiver is drained after the definitive daily shutdown, it must be preheated prior the first daily start-up to prevent the salt freezing in some spots during the filling operation. The preheating criterion in this analysis is set to obtain a temperature of 400°C at the tube crown front and 380°C in the rear side, following the maximum temperature during preheating recommendation of Vant-Hull (2002). In this study, the successful preheating conditions are achieved if the average heat flux on the receiver surpasses a minimum value, $q_{\text{avg,rec}} \geq q_{\text{avg,limit}}$; $q_{\text{avg,limit}}$ is set equal to 40 kW/m^2 with the current scheduled aiming strategy to guarantee that the heat flux limits of 12 kW/m^2 and 36 kW/m^2 (Vant-Hull, 2002) would be achieved when using more spread aiming-strategy during preheat mode. The process is bound to last 20 minutes prior the start-up, above the Vant-Hull 15-minute early-morning preheat (Vant-Hull, 2002) and the Wagner et. al 12-minute one (Wagner *et al.*, 2018).

Consequently, the start-up at a favourable instant is also subjected to the $q_{\min,\text{rec}} \geq q_{\min,\text{limit}}$, a total 40 minutes favourable forecast ($t + 7\Delta t$) and to a 20-minute preheat ($t - 4\Delta t$). If the $q_{\min,\text{rec}}$ goes back below the $q_{\min,\text{limit}}$ the

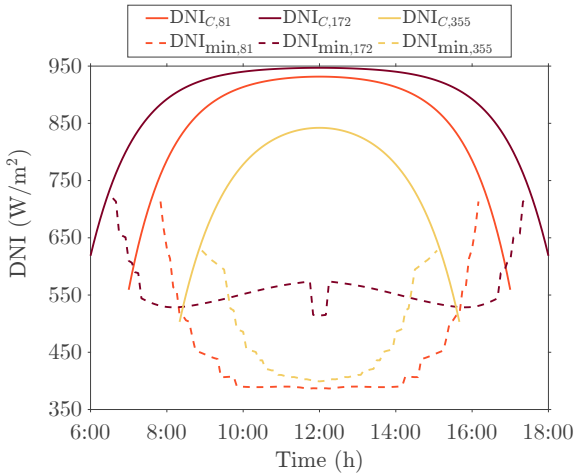


Figure 6.1: DNI to guarantee a minimum heat flux on the receiver equal to 40 kW/m², opposite to the reference DNI.

receiver is either fully shutdown or kept preheating, depending on the forecast ahead and considering that the ramp-up for starting it back up lasts also 20 minutes (Wagner *et al.*, 2018; Vant-Hull, 2002), with the receiver at the same preheating mode. The control diagram resulting from these operation restrictions is shown in Figure 6.2(a), with instances of the different possibilities that can be encountered in a certain day represented in Figure 6.2(b). Initially, it is established whether the receiver operates (mode = 1) or not (mode = 0). The receiver operates if the minimum heat flux on the receiver surpasses the limit set for that end and if was either already operating (o_1) or shutdown but with additional 35 favourable minutes ahead (40 in total) and has already preheated (o_2). The rest of the scenarios lead to the receiver not operating: the minimum heat flux on the receiver does not surpass the threshold of 40 kW/m² (m_1), the receiver was not operating during the previous time instant and the upcoming operation forecast is not favourable (m_2), or the receiver was not operating and had a favourable future operation forecast but it has not been fully preheated yet for the forthcoming start-up (m_3). The mode for these three scenarios is then determined between the preheating ($ph = 1$) or the full shutdown ($ph = 0$). The receiver is in preheating mode if it can preheat and either the preheating (15 additional minutes) and operation forecasts (40 minutes after the preheating completion) are fulfilled (p_1) or if it was already preheating (p_2). On the other hand, the receiver is kept fully shutdown if the average heat

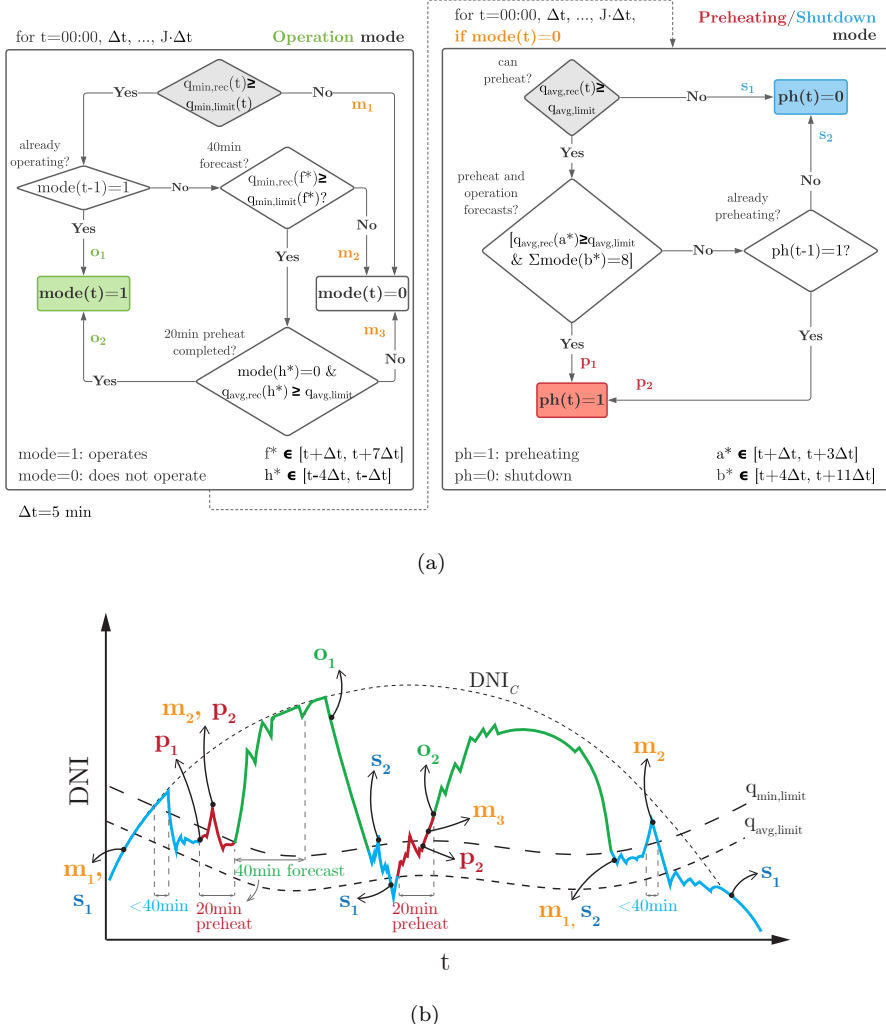


Figure 6.2: (a) Receiver operation control diagram for a given day, with instances of the possible situations represented in (b).

flux is not sufficient in order for the receiver to preheat (s_1) or if it can preheat but the forecasts are not favourable and was not already preheating (s_2).

Mass-flow rate/ HTF outlet temperature control

While upcoming cloud transients can be noted in advance during operation, it is not easy to predict their actual impact since they can differ in various aspects: velocity, transmissivity, shape or direction (Crespi *et al.*, 2018; Augsburger &

Favrat, 2013). Moreover, the delay between the modification of the operation (heliostat aiming, mass-flow rate, etc.) and the actual variation of the HTF outlet temperature, $T_{\text{out,HTF}}$, cannot be disregarded. If the mass flow rate, \dot{m}_{HTF} , is modified during a cloud passage and it suddenly ends, the receiver may then present an insufficient \dot{m}_{HTF} for the cleaner conditions, resulting in a tube overheating and therefore high unexpected damage. Thus, regarding the $T_{\text{out,HTF}}$ and \dot{m}_{HTF} , two control modes are contemplated:

- Mode 1: clean design day conditions, when the DNI matches the clear-sky expected one, the DNI_C . The mass flow for each flow path is adjusted so the $T_{\text{out,HTF}}$, meets the desired value of 565 °C. Hence, the \dot{m}_{HTF} required at each time instant of the given clean day is known beforehand and can be scheduled before the start-up.
- Mode 2: lower DNI with respect to the clean design day. The \dot{m}_{HTF} at each instant is the one that would correspond to the clear-sky conditions, letting the $T_{\text{out,HTF}}$ fluctuate. Moreover, the aiming strategy of the heliostat field continues to be the clear-sky scheduled one. This way, $T_{\text{out,HTF}}$ will never surpass the maximum value established once the cloud passage concludes. A usual approach in commercial scale plants is to decide the storage tank that the salts are sent to based on the $T_{\text{out,HTF}}$ and the storage tank level, since decreasing the temperature in the hot tank leads to a drop of the power cycle efficiency; operators typically continue diverting the HTF towards it as long as the $T_{\text{out,HTF}}$ drops no more than 530 °C (Mehos *et al.*, 2020), although instances such as the work of Zurita *et al.* (2020) admit a greater drop (470 °C).

6.3.3 DNI cases of study

The creep damage on the receiver tubes depends on the temperature and stresses during hold times while fatigue depends on the strain ranges. Thus, in order to properly sense the fatigue influence during transient operation, two major DNI scenarios are presented for a certain day:

- Considering its actual transient DNI (case TR), providing several strain ranges during the day. The \dot{m}_{HTF} control combines the modes 1 and 2 described in Section 6.3.2, depending on whether the transient DNI matches the clear-sky one (mode 1) or not (mode 2) at each time. Consequently, during mode 2, the tube temperatures at times with lower DNI with respect the clear-sky one would be lower than the ones obtained with a

strategy seeking to obtain a $T_{\text{out,HTF}}$ closer to the target one (using a lower \dot{m}_{HTF}). Thus, this case provides the minimum creep but takes into account the effect of the small cloud passages when calculating the fatigue damage.

- Assuming its corresponding DNI_C, (case C), an ideal DNI scenario that would provide the maximum creep as possible on the receiver tubes but disregards the effect of small cloud passages in the fatigue damage. The operation schedule of the receiver is obtained considering its actual DNI, not the clear-sky one assumed for the subsequent damage calculation of this case, which results in the same hours of operation and start-ups for both C and TR cases. On the other hand, the mass-flow rate control corresponds solely to mode 1 for being a clear-sky DNI.

Additionally, a case with the same cloud interruptions than during the TR variant but with perfect \dot{m}_{HTF} control, adjusting the \dot{m}_{HTF} at every instant in order to guarantee a $T_{\text{out,HTF}} = 565$ °C, will also be briefly addressed in the results section labelled as case P.

6.4 Methodology proposed to calculate the transient operation

6.4.1 Clean design day and cloudy day levels characterization

As the starting point, the optical, thermal and mechanical analyses are performed for the clear-sky DNI of the three characteristic days during their corresponding solar hours (α of at least 10°): 7:00-17:00 (day 81), 6:00-18:00 (day 172) and 8:20-15:40 (day 355). The analyses are carried out for 5-min Δt since these offer an accurate assessment of the solar data without greatly compromising the computational cost, as addressed in Chapter 5. The aiming strategy is selected according to the AFD limits; once it is definitive, the heat flux on the receiver, the tubes temperatures, and σ_{eq}^E and $\varepsilon_{\text{eq}}^E$ are obtained with the corresponding models. Moreover, since the clear-sky DNI corresponds to mode 1 of Section 6.3.2, the \dot{m}_{HTF} is calculated as well with the thermal model and will be the scheduled HTF flow for the day regardless the real DNI level (this is cases C and TR), unless the receiver is shutdown. The interest in the lifetime model lies on the σ_{relax} , which will be the one regarded for the rest of DNI

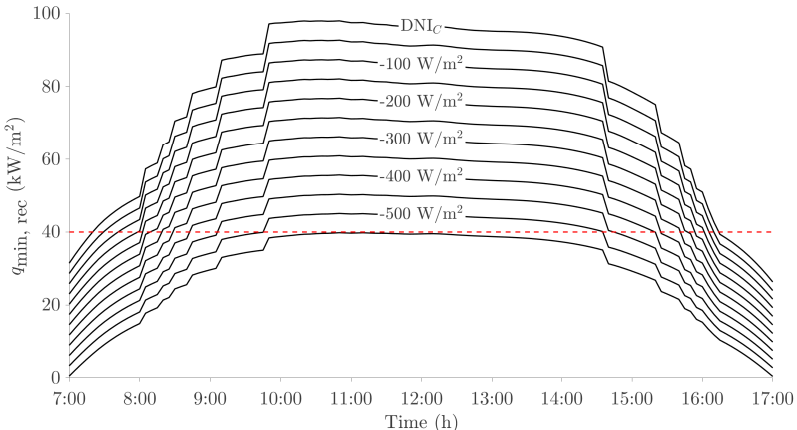


Figure 6.3: Minimum heat flux on the receiver surface for the DNI layers during the spring equinox day (81). The limiting 40 kW/m^2 appears in dashed lines.

levels as well, with the assumption of an already accomplished global stress relaxation.

Then, the different DNI levels for the design days are characterized. They have been selected as equidistant layers in decrements of 50 W/m^2 with respect their corresponding DNI_C . Thus, the optical model runs with the new DNI, resulting from subtracting the fixed value to Eq. 6.1, but using the clear-sky aiming strategy previously scheduled, providing the heat flux on the receiver surface under these new conditions. The thermal model works in the $T_{\text{out,HTF}}$ operation mode 2, using the mass flow calculated during the clear-sky conditions. The elastic stresses and strains model works as usual.

The DNI descends are considered up to a DNI level that provides a $q_{\min,\text{rec}}$ just below the $q_{\min,\text{limit}}$ threshold. For the day 81, the descend is up to -550 W/m^2 , resulting in 12 data layers (Figure 6.3), the day 172 reaches the -500 W/m^2 mark (11 layers), and the day 355 requires decrements up to -450 W/m^2 (10 layers). In that way, the existence of interpolation data when fitting the cloudy day of choice is guaranteed, avoiding the data extrapolation.

To summarize, the data library for each flow path during a certain day is constituted by:

- σ_{relax} for all the axial divisions of the flow path, corresponding to the values of the clear-sky day (1-D array).
- \dot{m}_{HTF} scheduled according to the clear-sky conditions for the day and its

DNI_C values, both at every time step (1-D arrays).

- $q_{\min,\text{rec}}$, $q_{\text{avg},\text{rec}}$ and $T_{\text{out,HTF}}$ at every time step in which the day is discretized and the various DNI layers (2-D arrays).
- Tube temperature, σ_{eq}^E and $\varepsilon_{\text{eq}}^E$ at the front side of the tube crown (the critical spot of the tubes (González-Gómez *et al.*, 2021)) for all the axial divisions at the different time steps and DNI layers (3-D arrays).

6.4.2 Calculating the creep and fatigue damages

The suitability of the data libraries for interpolation has been tested, with the verification being performed inside the time window satisfying that $q_{\min,\text{rec}} \geq q_{\min,\text{limit}}$ without surpassing the clear-sky DNI (Figure 6.1). The greatest divergences are found at the centre of the tubes, with the maximum temperature difference around 0.25 °C (0.04% of error), the elastic strain one around 2×10^{-5} (2% of error) and the elastic stress around 4 MPa (around 2% of error). The $T_{\text{out,HTF}}$ with respect the original data is around 0.04 °C, while the minimum heat flux one is in an order of magnitude of 10^{-14} , both differences being negligible.

Now, for a given transient DNI, the initial step is to obtain the $q_{\min,\text{rec}}$ at each Δt by interpolating the data of the $q_{\min,\text{rec}}$ library with the actual DNI of the day. Then, following the control diagram depicted in Figure 6.2(a), the operation modes schedule is obtained. According to each mode, i.e: regular operation, preheating or full shut-down, the tubes temperatures, σ_{eq}^E and $\varepsilon_{\text{eq}}^E$ can be calculated for each axial division and time interval with the interpolation of their corresponding libraries to the transient DNI, as well as the $T_{\text{out,HTF}}$ progress during the day. Then, the lifetime model is used, obtaining the creep and fatigue damages on the receiver, which can also provide an estimation of its lifetime.

6.5 Results and discussion

The methodology presented serves to analyse the damages of the two major cases of study addressed for different types of days and stages of the year. Thus, a DNI database for a whole year is clustered depending on the DNI features of each day, with their spatial distribution during the year also being considered, in order to test both the transient hazy days and clear-sky DNI approaches for the damage calculation, showing the relevance of each damage mechanism.

6.5.1 DNI database clustering

The DNI database used is the synthetically generated DNI for the year 2018 by the Group of Thermodynamics and Renewable Energies (GTER) of the University of Seville, obtained with the methodology presented by Larrañeta *et al.* (2018), using their collected measured data in Seville (37.4° N, 6.01° W) from 2002 to 2015. Such data have been classified according to the clustering technique proposed by Moreno-Tejera *et al.* (2017). It is based on three key aspects of the DNI to take into consideration when involved in CSP technologies:

- The transmittance index (Skartveit & Olseth, 1992), k_b , to quantify the daily energy level, resulting in days with high, medium, low or null energy. It is defined as the ratio between the daily irradiation (H_{TR}) and the daily irradiation during clear-sky conditions (H_C),

$$k_b = \frac{H_{\text{TR}}}{H_C}. \quad (6.7)$$

- The variability index, VI, initially proposed for the global horizontal irradiance (GHI) by Stein *et al.* (2012) is used in this Chapter for the DNI, the radiation component of interest in CSP applications (Moreno-Tejera *et al.*, 2017). This metric compares the length of the DNI curve with the curve during clear-sky conditions as

$$VI = \frac{\sum_{j=2}^J \sqrt{(DNI_{\text{TR},j} - DNI_{\text{TR},j-1})^2 + \Delta t^2}}{\sum_{j=2}^J \sqrt{(DNI_{C,j} - DNI_{C,j-1})^2 + \Delta t^2}}, \quad (6.8)$$

with $DNI_{\text{TR},j}$ being the DNI at a certain time step j and $DNI_{C,j}$ the DNI at the same instant during the clear-sky day. It measures the DNI changes due to cloud passages. Having a series of days, their VI is normalized with the greater value obtained for the set, preventing this index have a greater weight than the other two. The VI index determines days with high, medium and low variability.

- The morning fraction index, F_m , proposed by Moreno-Tejera *et al.* (2017) determines the temporal distribution of the DNI during the day. It is the ratio of accumulated DNI during the morning ($H_{\text{TR,mh}}$), from the sunrise to the solar noon, and the total daily DNI (H_{TR}),

$$F_m = \frac{H_{\text{TR,mh}}}{H_{\text{TR}}}. \quad (6.9)$$

Then, the days are assigned a time fraction, F_t , as:

$$\begin{aligned} \text{if } F_m \leq 0.3, F_t &= 1, \\ \text{if } 0.3 < F_m < 0.7, F_t &= 0.5, \\ \text{if } F_m \geq 0.7, F_t &= 0. \end{aligned} \quad (6.10)$$

Days with a $F_t = 1$ present their DNI mainly during the afternoon hours, a $F_t = 0$ means that the daily DNI is concentrated during the morning, while a $F_t = 0.5$ indicates a balanced day.

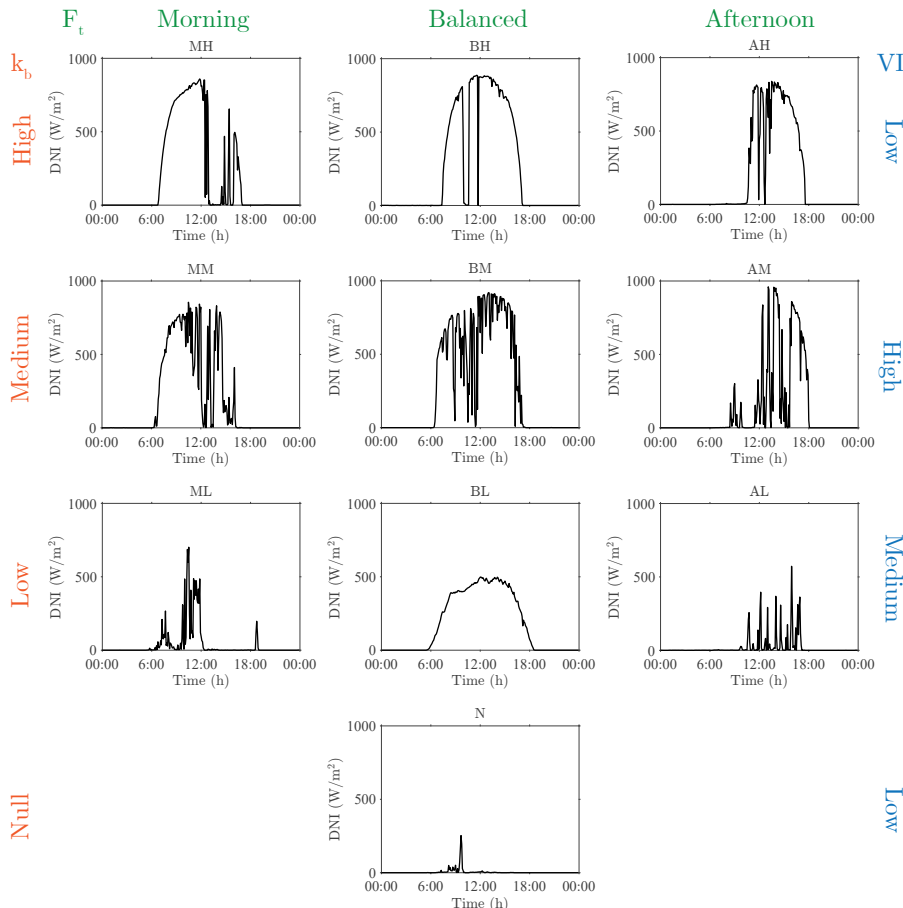


Figure 6.4: Day-types cluster classification according to their DNI features.

These indexes are useful to characterize the different features of the DNI without duplication (Moreno-Tejera *et al.*, 2017), providing both qualitative

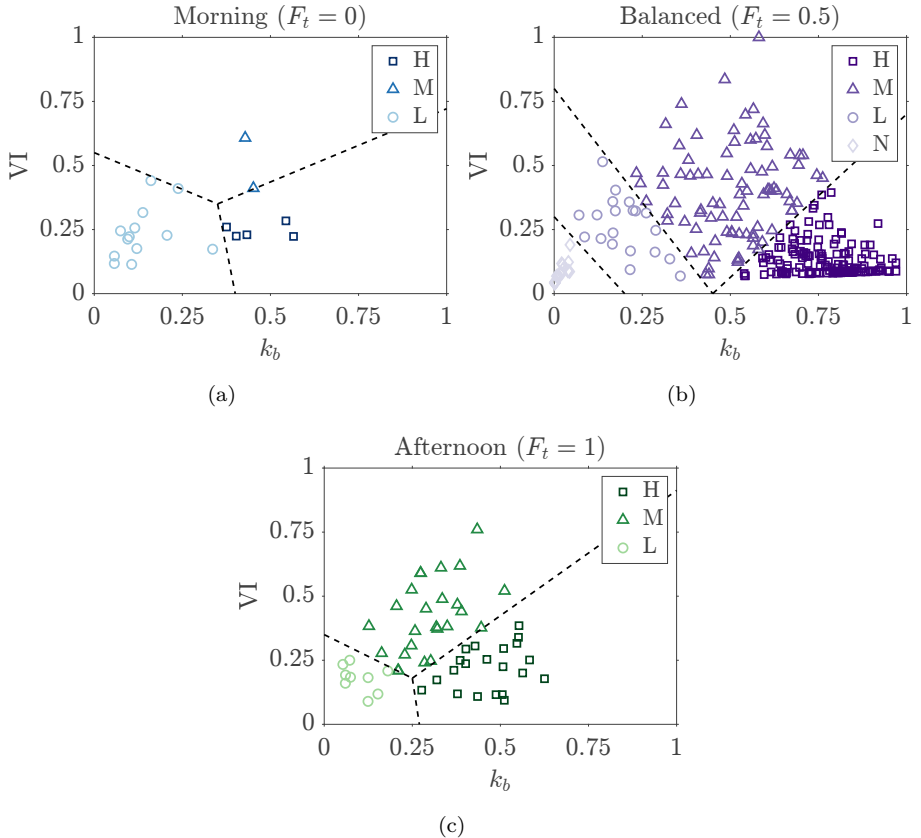
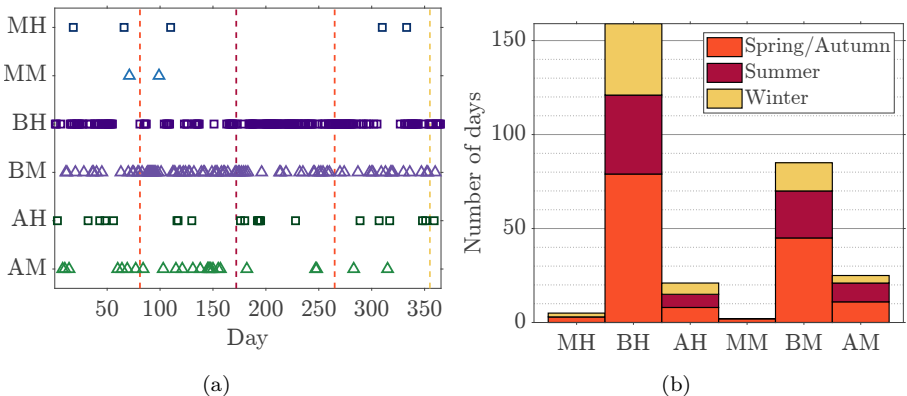


Figure 6.5: Arrangement of the 2018 year into the cluster groups.

and quantitative information of the state of the sky. It is a more suitable approach for CSP analysis than the commonly-used clear sky index, a simple approach but providing less valuable information (Moreno-Tejera *et al.*, 2018). Thus, the days clustering resulted in the 10 day-types compiled in Figure 6.4. The columns present the days arranged according to their DNI temporal distribution, i.e: Morning (M), Balanced (B) and Afternoon (A), while the rows do the same in terms of energy level: High (H), Medium (M), Low (L) and Null (N). Hence, for instance, a day with the energy mainly during the afternoon and with a medium energy level is labelled as “AM”. Regarding the variability, it was found that high energy days present low variability, medium energy days showed high variability, and low and null energy days present medium/low variability. Moreover, the rows of “Low” and “Null” energy can be regarded as just one group since such low DNI levels do not provide sufficient energy for the

Table 6.3: Number of each day-type during the year 2018.

	Morning	Balanced	Afternoon	Total
High	5	159	21	185
Medium	2	85	25	112
Low	13	20	9	42
Null		26		26
Total	20	290	55	

**Figure 6.6:** (a) Distribution of the high and medium energy day-type through the year and (b) number of days of each type during each season.

CSP operation. Despite alternative rearrangements of these clusters have been later proposed (Moreno-Tejera *et al.*, 2018), in the present study, only days with high and medium energy are considered relevant for their operation and damage analysis, and remain as the 6 individual groups originally presented, with no further combinations or divisions.

The clustering of the database employed results in the groups depicted in Figure 6.5, where the dashed lines represent the limit of each cluster in accordance to (Moreno-Tejera *et al.*, 2017), which were obtained using the Partitioning Around Medoids k-medoid algorithm to a 13-year database. For a better understanding, the number of each of the day-type during 2018 are presented in Table 6.3. The most repeated one is the BH (over a 53%), followed by the BM (over a 28%). The MH and MM days are at scarce, with just five and two occurrences, respectively. Between the low and null energy days, the receiver remains shut down for 68 days. The most frequent energy-type of days are the high ones. That same cluster classification was done for the data of the year

2015, obtaining 7 less shut-down days, 4 less of high energy and 11 more of medium energy, showing a good agreement in terms of day-distribution density.

Given they are the relevant day-type for the analysis, the distribution of the high and medium energy days throughout the year is depicted in Figure 6.6(a), with the reference days of the spring equinox (and autumn), summer solstice and winter solstice, highlighted in dashed lines. Consequently, each day-type occurrence can be assigned a season, Figure 6.6(b) in order to perform a full-year damage analysis using the spring equinox, summer solstice and winter solstice as reference days; for instance, the days between the 127 (average of day 81 and 172) and 219 (average between 172 and 265) are compared to the clear-sky DNI of the summer solstice (172).

6.5.2 Creep and fatigue damage results for clustered days

For the 6 high and medium energy days, one day per season—the spring equinox (equivalent to the autumn one), the summer solstice and the winter one—, is selected, giving a total of 18 scenarios. For the 18 configurations, the transient DNI data to analyse have been chosen from days as near as possible to the three reference clear-sky days.

Then, the actual DNI (from the database) of the chosen days is rescaled according to their assigned DNI_C , in order to provide working conditions at the two $T_{out,HTF}$ (Section 6.3.2) when analysing the TR scenario, as would occur in any pre-scheduled real cloudy day. Nevertheless, for some day-type, the same DNI data was adapted for the three reference clear-sky days given the scarcity of meaningful days of that type; such was the case of the two morning types: the transient DNI corresponding to the day 310 was adapted to the three DNI_C for the MH type while the same was done for the DNI of day 71, representative of the MM day-type. These were the two less frequent day-type and their distribution through the season fell mainly at spring, Figure 6.6(b). The transient DNIs adapted to each DNI_C are depicted in Figure 6.7 for the 18 cases, as well as their corresponding clear-sky DNI and the operation schedule according to the control diagram of Figure 6.2. Moreover, note that the cases with the DNI corresponding to the same real day (the already cited MH and MM with the days 310 and 71, respectively) can serve of instances of the same day but with a forecast for a lower (or greater) clear-sky DNI. This would emulate, for instance, the descent in the typical expected clear-sky DNI of the studied day due to the atmospheric attenuation caused by rains during the previous week.

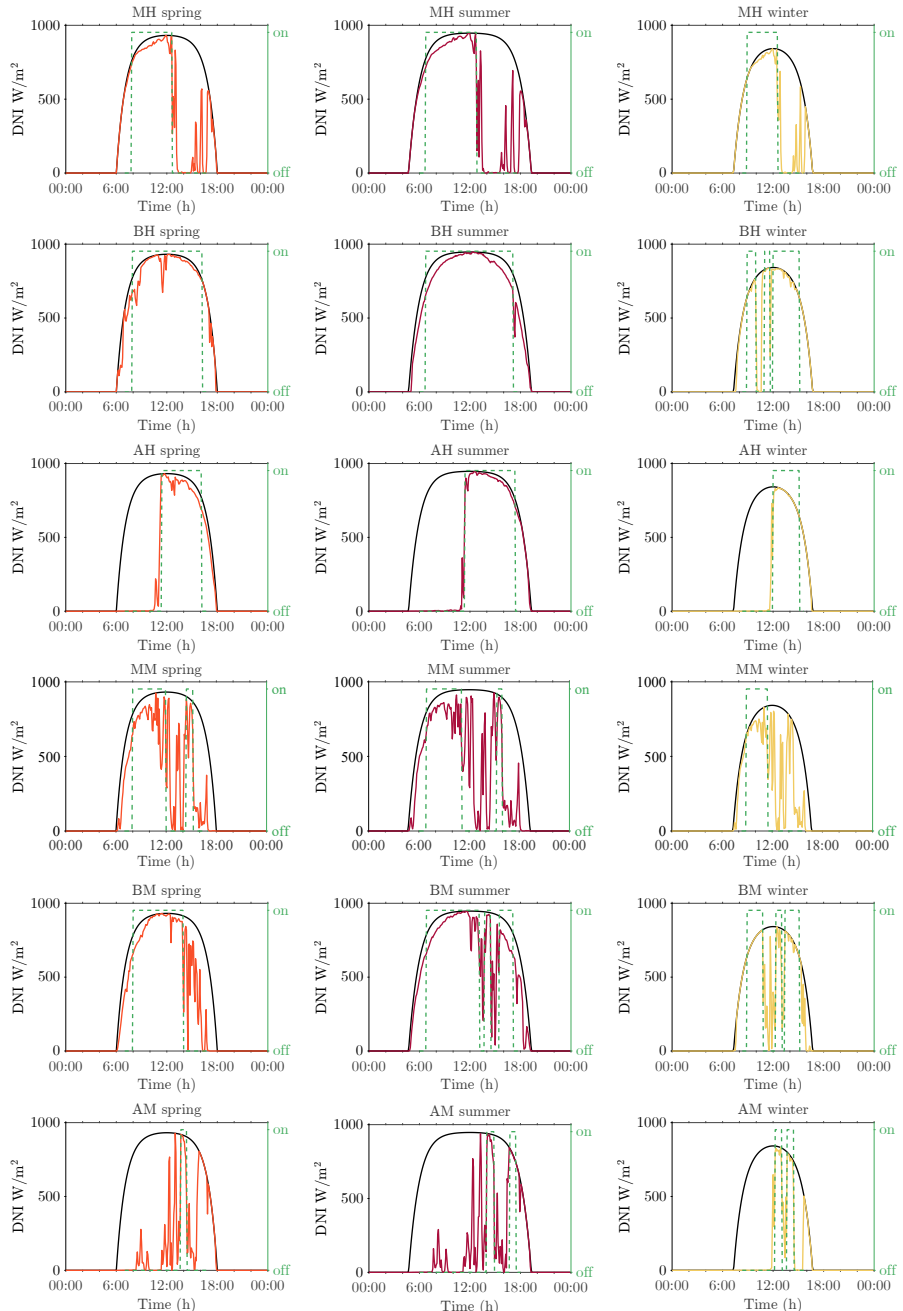


Figure 6.7: Transient DNI for the day-type analyzed, with their clear-sky reference DNI and their operation windows.

Subsequently, the creep and fatigue damages are calculated for these 18 scenarios under the two main DNI cases: with cloud transients, TR, and clean, C, Figure 6.8. The damages have been depicted for the Eastern and Western halves of the receiver (E and W notation), with 9 panels each. The results can be analysed from the three DNI features angle:

- Regarding the energy level (k_b), high-energy days are the most harmful ones despite the lesser fatigue cycles they present with respect to the medium-energy days. This is because the high heat fluxes lead to an increase of tube surface temperature and hence creep damage, which is the main cause of lifetime consumption on the receiver. For these days, the maximum fatigue damage ratio over the total occurs in the first panels, with the greatest rate being a 35%. In Southern panels, the fatigue share decreases, with minimum values around 2.5% of the total. Looking at the medium-energy days, fatigue gains relevance, with its share increasing up to an 88% in the first panel. However, this has to do with the lower creep damage on the receiver motivated by the lower heat fluxes rather than being caused by a great increase of the fatigue damage.
- Conversely, it is found a growth of the fatigue damage in days with multiple start-ups, which are a result of a high variability index (VI); this can be sensed by looking at the cases of BM-summer and winter, MM-spring or BH and AM during winter, for instance, whose fatigue is up to 2 times the fatigue during days with one start-up.
- As for the energy time distribution classification, the balanced day is the most damaging compared to the morning and afternoon days, with both salt paths behaving similarly, especially for instances with symmetric DNIs. During the morning days, the Western panels are subjected to more damage than the Eastern ones since most of the radiation is concentrated in the Western half. Nevertheless, the demanding heat fluxes force the aiming strategy of that half to switch to a more open one earlier than the Eastern half, causing the Eastern first panel to be more damaged than the Western one; the opposite occurs during the afternoon days.

Note that, despite the growth of the fatigue damage in some of the days with high variability, the creep plummeting during medium-energy days translates in an overall lower damage in the receiver than during the high-energy ones. The differences over the year are sensed through the three seasons, with summer

providing high and uniform damages in the whole receiver, and spring and winter being more North oriented, with the latter damaging the receiver the least.

As for the two major DNI cases, clear-sky (C) and transient (TR), Figure 6.8 shows greater receiver damages when considering the C scenarios. Such outcome is related also with the creep damage, being from 1.2 to 8 times greater in first panel during clear-sky conditions than during cloudy days, given the higher heat fluxes on the receiver, increasing the tubes temperature and stress. On the other hand, the fatigue damage presents low differences between the TR and C cases. In both transient and clear scenarios such difference is mainly due to the cycle computed with the minimum and maximum strains of the day. The strain range due to the maximum and minimum values is quite similar between the transient DNI and the clear-sky one, although the latter is slightly greater in some cases because of the higher clear-sky tubes temperatures, showing an increase on the clear-sky fatigue damage between a 6% and 3% with respect the transient one. If the maximum and minimum strain values coincide for the C and TR scenarios, the fatigue damage of case TR is slightly greater than the one in case C due to the small cloud transients occurring. Hence, it should be taken into account that the clear-sky scenario does not properly show the fatigue behaviour of the receiver. Nevertheless, these small cloud transients are found far from meaningful, being the already mentioned minimum and maximum strains and the number of start-ups the most relevant aspects in such regard. Lastly, the differences between the clear-sky and transient damages are greater for the spring and summer reference days due to the greater clear-sky DNI with respect winter, increasing the creep damage. Additionally, the damages differences between C and TR cases are lower during the high-energy days than during medium-energy days, precisely due to the proximity of the transient DNI to the clear-sky one as well.

It should be considered that the damage results may change depending on the operation strategy implemented; for instance, setting a greater time period with a favourable forecast to operate could mean a lesser number of start-ups and so the diminishing of both the fatigue and creep damages due to the forced inactivity of the receiver. Nevertheless, to take the feasible operation hours of the cloudy day and to evaluate them at the clear sky conditions would always lead to more conservative results than using the actual transient DNI due to the creep effect and the little relevance the small transients have in the fatigue damage. Keeping the same hours of operation and with the AFD control, the

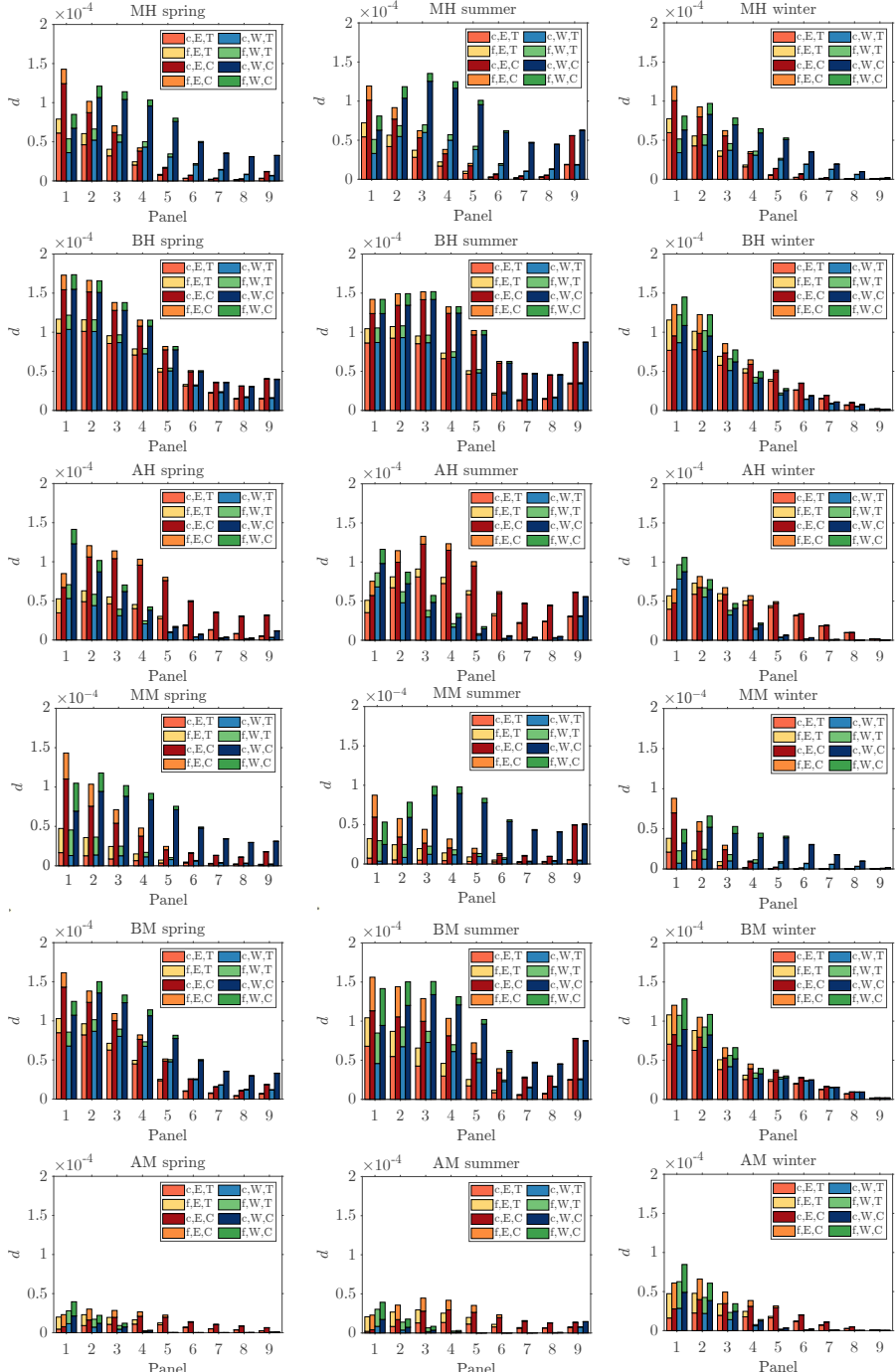


Figure 6.8: Creep (c) and fatigue (f) damages for the cases of study. Both receiver halves have been included (E and W), as well as the results for clear-sky DNI (C) during the receiver operation, opposite to the transient actual DNI (TR).

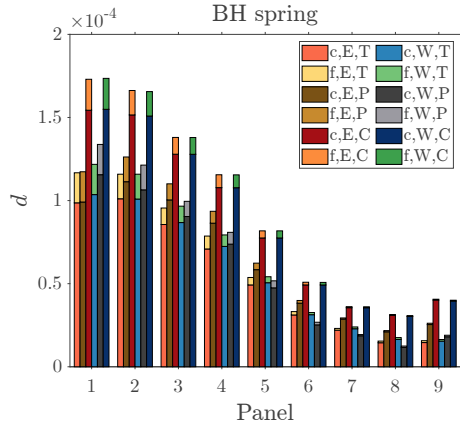


Figure 6.9: Creep and fatigue damages for the TR, C and P DNI and mass-flow rate control cases.

transient and clear-sky results are the two ends of the possible spectrum of results regarding the modification of the \dot{m}_{HTF} strategy. This is because, in this Chapter, the \dot{m}_{HTF} during transient operation is kept the same than clear-sky conditions scheduled one at the expense of the $T_{\text{out,HTF}}$. Hence, under the same heat flux, this results in lower tubes temperatures and, thus, lower creep with respect an operation adjusting the \dot{m}_{HTF} to provide a $T_{\text{out,HTF}}$ closer to the 565 °C goal. That is, for instance, the perfect mass flow rate control scenario (P) mentioned earlier, whose results for the BH day of spring are depicted in Figure 6.9 opposite to the C and TR cases. At the critical panels it shows a greater creep than the TR case, as expected, but it is still much lower than case C one. The fatigue damage is practically the same than the one for case TR, being under the same transient DNI. Note that the only difference between the alternatives TR and P is the \dot{m}_{HTF} strategy, while case C differs in the DNI with respect case TR and in the DNI and \dot{m}_{HTF} with respect case P.

On the other hand, the outlet temperature during the receiver operation and the HTF mass flow through it are shown in Figure 6.10 for the 18 cases. Many of the winter days present an average HTF outlet temperature close to the reference one (565 °C). For instance, the ones during the BH and AH days: 561.3 °C and 562.18 °C, respectively. Nevertheless, the lower clear-sky DNI implies a lower heat flux on the receiver surface, and thus, these winter days have a scheduled mass flow lower than the spring and summer ones, with maximum daily average HTF outlet temperatures of 553.45 °C (MH) and 556.14 °C (AH), respectively. Consequently, the average thermal power for the winter days is

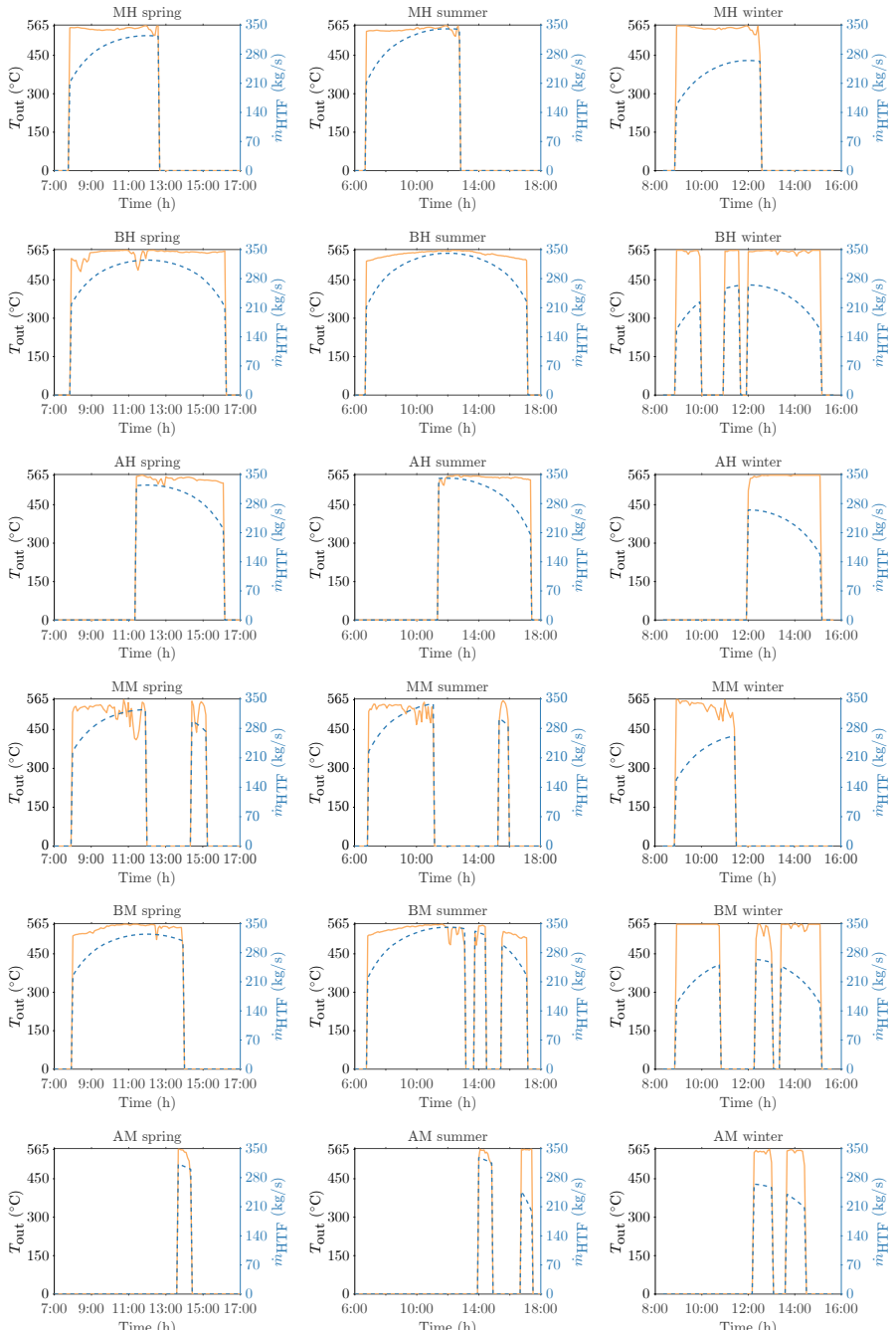


Figure 6.10: HTF outlet temperature during the transient operation and total HTF mass flow rate through the receiver.

lower than during spring and summer. The greater daily average thermal power is yielded by the three high-energy day-type during the summer solstice, with results between 124 MWt and 121.5 MWt; the average of the winter days, on the other hand, falls below 100 MWt. The greatest energy production is achieved during the BH day of summer due to its long operation, more than 10 and a half hours, with a reasonably high average outlet temperature, 549.7 °C, and mass-flow rate, 307.1 kg/s, yielding 1.26 GWh.

6.5.3 Damage analysis using the 2018 DNI database

For the whole year analysis, the DNI of each day in the database is likewise designated a DNI_C (days 81, 172 or 355) according to their corresponding season, Figure 6.6. The operating hours resulting from the operation control are presented in Figure 6.11, along with the number of start-ups each day.

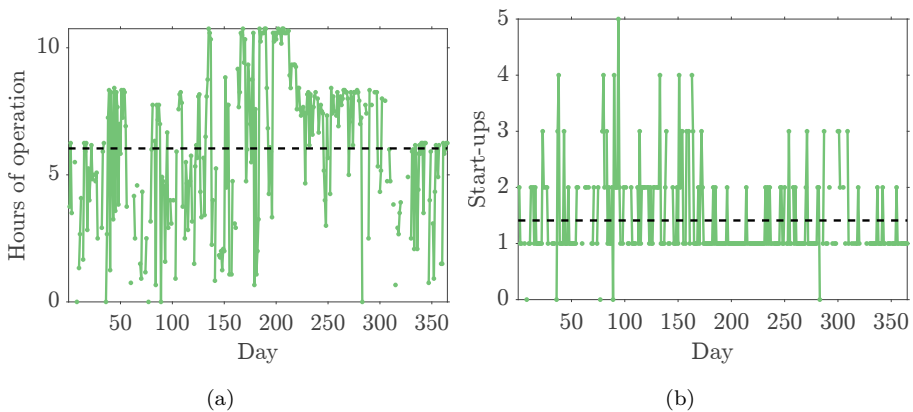


Figure 6.11: (a) Hours of operation and (b) number of start-ups of the high and medium energy days of 2018. Average results in dashed lines.

The average hours of operation and start-ups are 6.04 hours and 1.41 times, respectively, per high and medium energy days; these are a significant number of hours to provide a great creep damage, while the low number of start-ups indicates that the fatigue one will not be greatly augmented by such factor. The BH-type, the most prominent one throughout the year, presents an average operation of 7.9 hours. The rest of them are quite behind, with an average of 4.46 hours during the BM days (the second most prominent), 4.37 hours for the AH days, 3.71 for the MM (with just two instances during the year), and lastly, the AM day-type with an average of just 1.6 hour-average during its 25 days.

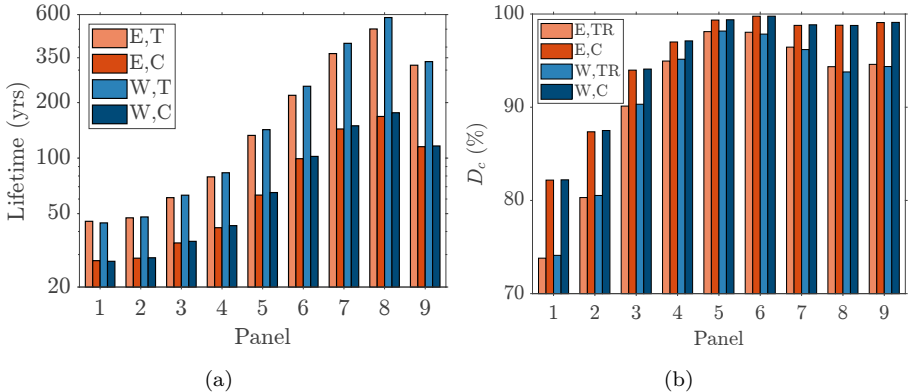


Figure 6.12: (a) Lifetime estimation considering the high and medium energy days of 2018 and (b) annual creep damage percentage under the transient DNI and the clear-sky one.

As for the start-ups, just the BM and MM day-type are above the average, with 1.82 and 2 start-ups, respectively.

Then, the damage analysis for the whole year is performed considering these high and medium energy days at their corresponding reference season. The limiting lifetime results for each receiver panel, obtained towards the middle length of the tubes, are included in Figure 6.12(a) for the C and TR DNI assumptions, with the clear-sky case operating the hours obtained for the actual transient DNI, as usual. Such Figure shows a quite similar outcome between both receiver halves in the two DNI cases, manifesting the dominance of the balanced days over the rest which, as noted in the previous Section, lead to an almost equal damage when comparing both flow paths panel-by-panel. As expected, the greater creep damages for the clear-sky DNI observed in the individual cases earlier presented translate likewise for the whole year analysis. In the first panel, which remains the most critical one, the lifetime drops from 45.4 years to 27.8, showing that using the clear-sky conditions are way off the real results, but yet they constitute a conservative approach for a quick lifetime estimation of the receiver.

On the other hand, for the most damaged spot of each panel, the contribution of the annual creep damage to the annual total one is depicted in Figure 6.12(b). It highlights again the greater relevance of the creep damage over the fatigue one, especially from panels 3 to 9. The lowest creep damage weight is found at first panel for both the TR and C DNI cases. Regarding the

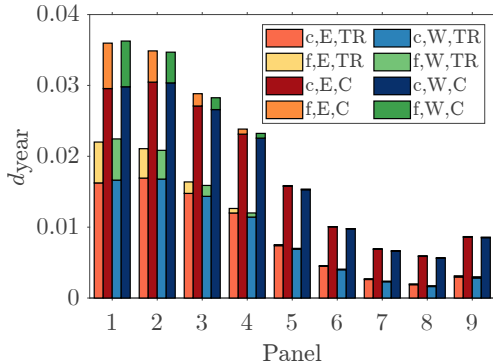


Figure 6.13: Annual creep and fatigue damages for the Eastern and Western panels of the receiver under the transient DNI and the clear-sky one.

cloudy days DNI, it is a 73.8% of the total, with the creep damage being 2.8 times the fatigue one. The greatest average creep damage through the year is inflicted by the set of BH days, which is amplified given they account for more than half of the year, followed by the BM ones, the second most common type. On the other hand, the days with greater average fatigue, which are mainly medium-energy non-balanced days, are less frequent. As for the clear-sky DNI, the creep damage share increases in all the panels, being over an 82% at the most damaged point of the receiver. Such increments have to do with the creep damage increase with respect the transient DNI case while the fatigue damage remains almost constant, as depicted in Figure 6.13, and, thus, being even more diluted.

As stated in the previous section, a different $\dot{m}_{\text{HTF}}/T_{\text{out,HTF}}$ strategy, such as the P one, would be in the middle ground of the results of Figures 6.12 and 6.13.

6.6 Conclusions

The creep and fatigue damages on a molten-salt receiver are investigated. Hence, two major DNI cases are selected in order to test the influence of cloud passages and hazy days on the fatigue damage and the total damage on the receiver: clear-sky DNI and the actual transient DNI considering a fixed HTF mass flow rate, letting its outlet temperature fluctuate. Thus, they constitute the possible cases on the receiver of maximum creep and minimum creep with cloud transient interruptions, respectively.

These two scenarios are initially compared for different day-type and seasons. The results show the salient influence of the creep damage over the fatigue one, with the latter being mainly due to the strain range corresponding to the minimum and maximum values during the day. It is found that the fatigue damage is aggravated with multiple daily start-ups but the small transients during a day result negligible. Moreover, the comparison of the transient and clear-sky results even shows a greater fatigue damage for the former in some of the day-type at the first panel (up to a 6% in some cases), which has to do with the increase of the maximum strain of the cycle due to the higher clear-sky heat fluxes on the receiver. Nevertheless, for a maximum strain range equal for both TR and C DNIs, the small transients during TR do indeed yield slightly greater fatigue, although such increase is not relevant. Using the same transient DNI of the TR case but a mass flow rate strategy aiming to increase the HTF outlet temperature results in a greater creep, but it is still far from the clear-sky one. Thus, the cases of clear-sky DNI and transient DNI with the outlet temperature fluctuating constitute the upper and lower limits of the damage on the receiver, being other transient scenarios with a different mass flow rate controls in between.

Regarding the DNI features of the different days, the fatigue damage share is up to a 35% during high energy days, while in the less-common medium energy ones it increases up to an 88%. Nevertheless, this has to do with a considerable drop in the creep damage due to the lower heat fluxes on the receiver. Thus, during the most demanding days, the dominant damage mechanism is creep, with fatigue only gaining relevance during days with a great descend of the former rather than being motivated by a growth of its own. The most harmful day-type is the one with their energy evenly distributed throughout the day and presenting a high-energy level, followed by the medium-energy ones. These happen to be the most common during the year, as the full-year data analysis shows, favoring the grater creep damage share in the total.

For the whole year analysis, the average number of start-ups during the year is 1.4 per day, while the average hours of operation are around 6. The creep damage for the transient DNI is above 73% in the critical first panel, above 80% in the second panel, and above the 90% mark for the rest. The lifetime of both receiver halves is practically the same, with a minimum value of 45.43, due to the abundance of balanced days, opposite to the morning and afternoon ones. The clear-sky DNI results show how the fatigue damage is even more diluted than in the transient analysis, with the creep increasing (a minimum

share above 82%) and, therefore, the lifetime of the receiver resulting more conservative: 27.8 years.

Nomenclature

A	energy mainly during the afternoon	\dot{m}	mass flow rate (kg/s)
B	energy balanced during the day	m	non-operation mode
C	clear-sky operation	L	low energy level
c_1, c_2	fatigue exponents	N	fatigue cycles, null energy level
D	total damage	P	operation mode
d	damage		transient conditions and a perfect mass-flow rate control
\bar{d}	average damage for a set of days	p, ph	preheat mode
E	Eastern flow path, Young modulus (Pa)	q	heat flux (W/m^2)
F_m	morning fraction index	S	allowable stress (Pa)
F_t	time fraction index	s	shutdown mode
H	daily irradiation, high energy level	S_H	hot relaxation strength (Pa)
I	total number of days studied	S_{SR}	stress reset limit (Pa)
J	number of time intervals per day	S_y	yield strength (Pa)
k_b	transmittance index	$S_{y,cold}$	yield strength at room temperature (Pa)
M	number of fatigue cycles per day, energy mainly during the morning, medium energy level	T	temperature (K)
		t	time
		TR	transient conditions
		t_R	rupture time (h)
		VI	variability index
		W	Western flow path

Greek letters

α	solar altitude ($^\circ$)	ε	strain (%)
β	Mendelson-Roberts-Manson parametrization coefficients	ε'_f	fatigue ductility (%)
Δt	time interval duration (min)	σ	stress (Pa)
$\Delta \varepsilon$	strain range (%)	σ'_f	fatigue strength (%)

Subscripts

<i>a</i>	allowable		hours
avg	average	max	maximum
<i>C</i>	clear-sky	min	minimum
<i>c</i>	creep	out	outlet
eq	equivalent	rec	receiver
<i>f</i>	fatigue	relax	relaxation stress
film	inner tube wall	<i>s</i>	using reduction and data scattering factors
<i>L</i> , limit	limit		
mh	morning half of the solar	year	annual aggregated damage

Superindexes

<i>E</i>	elastic
<i>P</i>	plastic

Abbreviations

AFD	allowable flux density	EODs	equivalent operating days
ASME	American society of mechanical engineers	GHI	global horizontal irradiance
ASTM	American society for testing and materials	GTER	thermodynamics and renewable energies group
BPVC	boiler and pressure vessel code	HTF	heat transfer fluid
CC	code case	LCOE	levelized cost of energy
CGM	coarse grid model	LDS	linear damage summation
CSP	concentrating solar power	M-R-M	Mendelson-Roberts-Manson
DNI	direct normal irradiance (W/m ²)	sCO ₂	supercritical carbon dioxide
		SPT	solar power tower

References

- ASME 2004 ASME Boiler and Pressure Vessel Code, Section III, Division 1, Subsection NH. American Society of Mechanical Engineers.
- ASME 2010 Asme boiler and Pressure Vessel Code, Section II part D. american society of mechanical engineers.

ASTM INTERNATIONAL. 2017 ASTM E1049-85: Standard Practices for Cycle Counting in Fatigue Analysis. West Conshohocken, PA.

AUGSBURGER, G. & FAVRAT, D. 2013 Modelling of the receiver transient flux distribution due to cloud passages on a solar tower thermal power plant. *Solar Energy* 87 (1), 42–52.

BABCOCK & WILCOX COMPANY 1984 Molten Salt Receiver Subsystem Research Experiment Phase 1 -Final Report, Volume 1- Technical. *Tech. Rep.* SAND82-8178. Barberton, OH, United States.

BARRETT, P.R., AHMED, R., MENON, M. & HASSAN, T. 2016 Isothermal low-cycle fatigue and fatigue-creep of Haynes 230. *International Journal of Solids and Structures* 88-89, 146–164.

BARUA, B., McMURTREY, M.D., RUPP, R.E. & MESSNER, M.C. 2020 Design Guidance for High Temperature Concentrating Solar Power Components. *Tech. Rep.* ANL-20/03. Argonne National Laboratory, Argonne, IL, United States.

BECHT IV, C. 2011 Elevated temperature shakedown concepts. *Journal of Pressure Vessel Technology, Transactions of the ASME* 133 (5), 051203–1–5.

BERMAN, I., GANGADHARAN, A.C., GUPTA, G.D. & NARAYANAN, T.V. 1979 An interim structural design standard for solar energy applications. *Tech. Rep.* SAND79-8183. Sandia National Laboratories, Albuquerque, NM, United States.

CHEN, X., SOKOLOV, M.A., SHAM, S., ERDMAN, D.L., BUSBY, J.T., MO, K. & STUBBINS, J.F. 2013 Experimental and modeling results of creep-fatigue life of Inconel 617 and Haynes 230 at 850 °C. *Journal of Nuclear Materials* 432 (1-3), 94–101.

CHOPRA, O.K. & SHACK, W.J. 2003 Review of the margins for ASME code fatigue design curve - effects of surface roughness and material variability. *Tech. Rep.* NUREG/CR6815, ANL-02/39. Argonne National Laboratory, Argonne, IL, United States.

CONROY, T., COLLINS, M.N., FISHER, J. & GRIMES, R. 2018 Levelized cost of electricity evaluation of liquid sodium receiver designs through a thermal performance, mechanical reliability, and pressure drop analysis. *Solar Energy* 166, 472–485.

- CRESPI, F., TOSCANI, A., ZANI, P., SÁNCHEZ, D. & MANZOLINI, G. 2018 Effect of passing clouds on the dynamic performance of a CSP tower receiver with molten salt heat storage. *Applied Energy* 229 (January), 224–235.
- FAHRMANN, M.G. & SRIVASTAVA, S.K. 2014 Low cycle fatigue behaviour of HAYNES 230 alloy. *Materials at High Temperatures* 31 (3), 221–225.
- FALCONE, P.K. 1986 A handbook for solar central receiver design. *Tech. Rep. SAND-86-8009*. Sandia National Laboratories, Livermore, CA, United States.
- FORK, D.K., FITCH, J., ZIAEI, S. & JETTER, R.I. 2012 Life Estimation of Pressurized-Air Solar-Thermal Receiver Tubes. *Journal of Solar Energy Engineering* 134 (4), 041016–1–11.
- GONZÁLEZ-GÓMEZ, P.A., RODRÍGUEZ-SÁNCHEZ, M.R., LAPORTE-AZCUÉ, M. & SANTANA, D. 2021 Calculating molten-salt central-receiver lifetime under creep-fatigue damage. *Solar Energy* 213, 180–197.
- GROSSMAN, J.W. & JONES, W.B. 1990 Evaluation of thermal cycling creep-fatigue damage for a molten salt receiver. In *ASME international solar energy conference, Miami, FL, United States*.
- KISTLER, B.L. 1987 Fatigue analysis of a solar central receiver design using measured weather data. *Tech. Rep. SAND86-8017*. Sandia National Laboratories, Albuquerque, NM, United States.
- KOLB, G.J. 2011 An Evaluation of Possible Next-Generation High Temperature Molten-Salt Power Towers. *Tech. Rep. SAND2011-9320*. Sandia National Laboratories, Albuquerque, NM, United States.
- LARRAÑETA, M., FERNANDEZ-PERUCHENA, C., SILVA-PÉREZ, M.A. & LILLO-BRAVO, I. 2018 Methodology to synthetically downscale DNI time series from 1-h to 1-min temporal resolution with geographic flexibility. *Solar Energy* 162 (October), 573–584.
- LIU, B.Y.H. & JORDAN, R.C. 1960 The interrelationship and characteristic distribution of direct, diffuse and total solar radiation. *Solar Energy* 4 (3), 1–19.
- MATHWORKS 2017 Rainflow counting method. <https://mathworks.com/help/signal/ref/rainflow.html>, accessed: 21/03/2021.

- McCONOHY, G. & KUIZENGA, A. 2014 Molten nitrate salts at 600 and 680°C: Thermophysical property changes and corrosion of high-temperature nickel alloys. *Solar Energy* 103, 242–252.
- MEHOS, M., PRICE, H., CABLE, R., KEARNEY, D., KELLY, B., KOLB, G. & MORSE, F. 2020 Concentrating Solar Power Best Practices Study. *Tech. Rep. NREL/TP-5500-75763*. National Renewable Energy Laboratory, Solar Dynamics LLC, Golden, CO, United States.
- MINIS, N., ROSENBLUTH, E., HAYUT, R. & AM-SHALLEM, M. 2019 Spatial DNI measurement for accurate solar flux control in Megalim 121 MWe solar receiver power plant. *AIP Conference Proceedings* 2126 (July), 030037.
- MORENO-TEJERA, S., SILVA-PÉREZ, M.A., RAMÍREZ-SANTIGOSA, L. & LILLO-BRAVO, I. 2017 Classification of days according to DNI profiles using clustering techniques. *Solar Energy* 146, 319–333.
- MORENO-TEJERA, S., SILVA-PÉREZ, M.A., RAMÍREZ-SANTIGOSA, L. & LILLO-BRAVO, I. 2018 Evaluation of classification methods according to solar radiation features from the viewpoint of the production of parabolic trough CSP plants. *Renewable Energy* 121, 429–440.
- NARAYANAN, T.V., RAO, M.S.M. & CARLI, G. 1985 Structural Design and Life Assessment of a Molten Salt Solar Receiver. *Journal of Solar Energy Engineering* 107 (3), 258–263.
- NEISES, T.W., WAGNER, M.J. & GRAY, A.K. 2014 Structural Design Considerations for Tubular Power Tower. In *International Conference on Energy Sustainability (ES2014)*, Boston, MA, United States, pp. 6603 1–7. National Renewable Energy Laboratory.
- RADKE, E.F., DEWEES, D.J., WASYLUK, D.T. & TANZOSH, J.M. 2017 Creep-fatigue design applied to molten salt solar receivers. In *ASME 2014 Symposium on Elevated Temperature Application of Materials for Fossil, Nuclear, and Petrochemical Industries (ETAM2014)*, Seattle, WA, United States, pp. 1032 232–247.
- RENO, M.J., HANSEN, C.W. & STEIN, J.S. 2012 Global horizontal irradiance clear sky models : implementation and analysis. *Tech. Rep. SAND2012-2389*. Sandia International Laboratories, Albuquerque, NM, United States.

- RODRÍGUEZ-SÁNCHEZ, M.R., SORIA-VERDUGO, A., ALMENDROS-IBÁÑEZ, J. A., ACOSTA-IBORRA, A. & SANTANA, D. 2014 Thermal design guidelines of solar power towers. *Applied Thermal Engineering* 63 (1), 428–438.
- ROHANI, S., FLURI, T.P., DINTER, F. & NITZ, P. 2017 Modelling and simulation of parabolic trough plants based on real operating data. *Solar Energy* 158, 845–860.
- SÁNCHEZ-GONZÁLEZ, A. & SANTANA, D. 2015 Solar flux distribution on central receivers: A projection method from analytic function. *Renewable Energy* 74, 576–587.
- SKARTVEIT, A. & OLSETH, J.A. 1992 The probability density and autocorrelation of short-term global and beam irradiance. *Solar Energy* 49 (6), 477–487.
- STEIN, J.S., HANSEN, C.W. & RENO, M.J. 2012 The variability index: A new and novel metric for quantifying irradiance and PV output variability. *World Renewable Energy Forum, WREF 2012, Including World Renewable Energy Congress XII and Colorado Renewable Energy Society (CRES) Annual Conference* 4 (May), 2764–2770.
- VANT-HULL, L.L. 2002 The role of "allowable flux density" in the design and operation of molten-salt solar central receivers. *Journal of Solar Energy Engineering, Transactions of the ASME* 124 (2), 165–169.
- WAGNER, M.J., HAMILTON, W.T., NEWMAN, A., DENT, J., DIEP, C. & BRAUN, R. 2018 Optimizing dispatch for a concentrated solar power tower. *Solar Energy* 174, 1198–1211.
- ZAVOICO, A.B. 2001 Solar Power Tower - Design Basis Document. *Tech. Rep.* SAND2001-2100. Sandia National Laboratories, Albuquerque, NM and Livermore, CA, United States.
- ZURITA, A., MATA-TORRES, C., CARDEMIL, J.M. & ESCOBAR, R.A. 2020 Assessment of time resolution impact on the modeling of a hybrid CSP-PV plant: A case of study in Chile. *Solar Energy* 202, 553–570.

General conclusions

Solar power tower (SPT) technology is gaining relevance in the renewable alternatives landscape due to its numerous benefits. Yet, it is still far from the maturity of other renewable options, with room for improvement regarding its design, operation and overall cost. Research on testing facilities and current-commercial plants reports warn from the harmful operation conditions the receiver must endure, with high non-uniform heat fluxes and cyclic operation, and its implications on the project. Additionally, the study of the receiver subsystem using analytical models is found to be the most efficient and suitable approach, given its low computational cost opposite to numerical models, which eases the task of performing a global analysis, and the difficulties found in the sensors placement of real-scale receivers. Hence, this dissertation has been focused on the study of the damage mechanisms threatening the receiver during its regular operation, creep and fatigue, from an analytical point of view, considering as well its previous thermal and mechanical characterization.

The thermal study of the receiver is presented in Chapter 2 as well as the subsequent methodology to perform a high-resolution exergy analysis. The latter is conducted considering the heliostat field and the receiver subsystems, showing that the heliostat field is the main factor driving exergy losses; it can only be altered by changing its aiming strategy—and, thus, its optical efficiency—, being advisable strategies as equatorial as possible. Nevertheless, the mechanical limits of the receiver should be watched. Regarding the receiver, the exergy destruction is mainly caused by the multiple emissions and absorptions happening at the tubes. Moreover, the coating degradation is investigated, showing that the efforts should be directed into providing an absorptivity as great as possible, while the emissivity plays a negligible role; consequently, repainting tasks are found to be a good practice due to its exergy implications. In addition, locations with moderate DNI and low ambient temperature are more appealing exergy-wise than sites with outstanding DNI levels and high ambient

temperatures.

Then, an analytical methodology to calculate the elastic stresses and strains on the receiver tubes, as well as their bending, is proposed in Chapter 3, taking into account the temperature dependance of the tubes material properties. Its accuracy is proved against numerical results. It is found that the disregard of such temperature dependance translates in considerable deviations in the stresses and bending results, constituting an ill-advised practice since it could lead to errors in the subsequent damage analyses. The supports guiding the tubes greatly reduce their bending opposite to a free bending situation. On the other hand, the equivalent stresses obtained with a finite number of supports highly resemble to the ones yielded by the generalized plane strain case, equivalent to an infinite number of supports, constituting a feasible simplification for further calculations.

An initial approach to the creep and fatigue damages investigation is conducted in Chapter 4, where different alloys alternatives for the receiver tubes manufacturing—alloy 316H, Haynes 230, Inconel 625, Inconel 740H and Incoloy 800H—are studied in terms of their expected lifetime due to the creep and fatigue effects during a certain clean design day, on an hourly basis. The coefficients to calculate the damages for the different alloys have been obtained through the fitting of experimental data existing in the literature and are compiled in such Chapter. Since the receiver mechanical limits are regarded when setting the heliostat field aiming strategy, with the target of it being as equatorial as possible, the disparate alloys properties lead to great differences in the power production these receivers can offer. Nevertheless, some of the alternatives are not able to dodge the stress reset limit and, thus, are unable to achieve the desirable global stress relaxation. As a consequence, the lifetime analysis results show a great penalty to those not fulfilling the global stress relaxation, which is specially noticeable in the case of Incoloy 800H, whose poor results lead to its early discard. Alloy 316H is barely affected by its absence, forced to operate with extremely low heat fluxes, at the expense of a low power production, due to its poor corrosion resistance. The best alternative is Inconel 740H, followed by Haynes 230, with outstanding lifetime results thanks to the stress relaxation, and yielding the highest power productions. The Inconel 625 receiver endures slightly lesser than alloy 316H, but it is able to offer considerably more thermal power. Thus, the cost metric proposed, the levelized cost of alloy (LCOA), takes into account the costs involved in the panel replacement for each alternative, not only due to the tubes themselves but also regarding weldings and

coating paintings, among others, and the power production yielded. In this regard, Inconel 740H and Haynes 230 lead almost on par, followed by Iconel 625. Alloy 316H is highly penalized by its low power production.

In Chapter 5, the influence of the time resolution in the lifetime analysis is investigated during clear-sky days, setting the thermal energy storage tank filling as the receiver shut-down criterion for the day, which gives the receiver hours of operation. The results obtained for the spring equinox show that selecting just the solar noon, a common approach in the literature, highly underestimates the receiver lifetime. The time resolution of 5 minutes is established as the most appropriate due to its accurate results with respect to the 1-minute one and its lower computational cost. The differences are essentially due to the precision of the aiming strategy shift over time, allowing the alternatives with finer control to reduce earlier the peak fluxes during the morning hours, when the majority of the operation takes place in this study. As for working with just the spring equinox, its results are found to be more restrictive than the ones obtained with an analysis of a set of days representative for the year, advising against its single use as well.

The damage analysis is performed during transient conditions in Chapter 6. The receiver operation is subjected to a favourable forecast for operation and a previous preheat. The mass-flow rate and aiming strategy during transients remain the clear-sky scheduled ones. Thus, two DNI cases are tested, the clear-sky day and the transient one, using a whole-year DNI database, clustering the days in different day-type and seasons. Creep damage is the most harmful mechanism endangering the receiver integrity, with fatigue being essentially caused by the strain range of the minimum and maximum values during the day, and aggravated by the appearance of multiple start-ups during the daily operation. Hence, small transients are negligible in terms of fatigue damage. Given the relevance of creep, high energy days are the most harmful ones, opposite to days with high DNI variability, typically with medium energy levels. For that same reason, the clear-sky study is considerably more restrictive than the transient one. These constitute both ends of damage spectrum, showing maximum and minimum creep damages, respectively. Transient days with a finer control on the mass-flow rate, aiming to increase the HTF outlet temperature, fall in between.

APPENDIX
A

Appendix A: Fourier series coefficients

The coefficients of the Fourier series (Eq. 3.3), calculated as presented by Bijlaard *et al.* (1968), result

$$B_1 = \frac{\pi}{4} \frac{\int_a^b \int_0^\pi T_\theta \left(r^2 - \frac{b^2 + a^2}{2} \right) \cos\theta dr d\theta}{b^2 - a^2 - (b^2 + a^2) \ln(b/a)}, \quad (\text{A.1})$$

$$A_1 = \frac{2}{b^2 - a^2} \left[\frac{2}{\pi} \int_a^b \int_0^\pi T_\theta \cos\theta dr d\theta - B_1 \ln(b/a) \right], \quad (\text{A.2})$$

$$D_1 = \frac{\pi}{4} \frac{\int_a^b \int_0^\pi T_\theta \left(r^2 - \frac{b^2 + a^2}{2} \right) \sin\theta dr d\theta}{b^2 - a^2 - (b^2 + a^2) \ln(b/a)}, \quad (\text{A.3})$$

$$C_1 = \frac{2}{b^2 - a^2} \left[\frac{2}{\pi} \int_a^b \int_0^\pi T_\theta \sin\theta dr d\theta - D_1 \ln(b/a) \right], \quad (\text{A.4})$$

when the inner A.5 and outer A.6 temperature profiles are known,

$$T_i(\theta) = A'_0 + \sum_{n=1}^{\infty} A'_n \cos n\theta + B'_n \sin n\theta, \quad (\text{A.5})$$

$$T_e(\theta) = A''_0 + \sum_{n=1}^{\infty} A''_n \cos n\theta + B''_n \sin n\theta. \quad (\text{A.6})$$

Here, A'_0 and A''_0 are the mean values of the internal temperature, \bar{T}_i (at $r = a$), and external, \bar{T}_e (at $r = b$), respectively, calculated as

$$\bar{T}_i = \frac{1}{2\pi} \int_0^{2\pi} T_i(\theta) d\theta, \quad (\text{A.7})$$

$$\bar{T}_e = \frac{1}{2\pi} \int_0^{2\pi} T_e(\theta) d\theta. \quad (\text{A.8})$$

The equivalence of the coefficients in Eq. 3.3 with the ones in Eqs. A.5 and A.6 can be easily obtained by substituting $r = a$ and $r = b$ in the circumferential temperature profile Fourier series (Eq. 3.3):

$$\begin{aligned} \left(A_1 a + \frac{B_1}{a} \right) \cos\theta + \left(C_1 a + \frac{D_1}{a} \right) \sin\theta &= A'_1 \cos\theta + B'_1 \sin\theta : \\ A'_1 &= A_1 a + \frac{B_1}{a}, \end{aligned} \quad (\text{A.9})$$

$$B'_1 = C_1 a + \frac{D_1}{a}. \quad (\text{A.10})$$

$$\begin{aligned} \left(A_1 b + \frac{B_1}{b} \right) \cos\theta + \left(C_1 b + \frac{D_1}{b} \right) \sin\theta &= A''_1 \cos\theta + B''_1 \sin\theta : \\ A''_1 &= A_1 b + \frac{B_1}{b}, \end{aligned} \quad (\text{A.11})$$

$$B''_1 = C_1 b + \frac{D_1}{b}. \quad (\text{A.12})$$

Nomenclature

A, B, C, D	Fourier series coefficients	T	temperature (K)
a	tube inner radius (m)	\bar{T}	mean temperature (K)
b	tube outer radius (m)		
r	radial position (m)		

Subscripts

e	external surface	θ	circumferential component
i	inner surface		

References

- BIJLAARD, P.P., DOHRMANN, R.J. & DUKE, J.M. 1968 Thermal Stress Analysis of Nonuniformly Heated Cylindrical Shell and Its Application to a Steam Generator Membrane Wall. *Journal of Engineering Power* 1 (90), 73–81.

Appendix B: Stresses calculation for homogeneous properties

Since the thermal conductivity is considered constant in the whole vertical division of the tube, the stresses of Eqs. 3.4 and 3.5 can be rewritten as:

$$\sigma_{T_r,r}(r,\theta) = K_r \frac{\alpha_r E}{2(1-\nu)} \left[-\ln \frac{b}{r} - \frac{a^2}{b^2 - a^2} \left(1 - \frac{b^2}{r^2} \right) \ln \frac{b}{a} \right], \quad (\text{B.1})$$

$$\sigma_{T_r,\theta}(r,\theta) = K_r \frac{\alpha_r E}{2(1-\nu)} \left[1 - \ln \frac{b}{r} - \frac{a^2}{b^2 - a^2} \left(1 + \frac{b^2}{r^2} \right) \ln \frac{b}{a} \right]. \quad (\text{B.2})$$

Here K_r is

$$K_r = \frac{\bar{T}_i - \bar{T}_e}{\ln(b/a)} \quad (\text{B.3})$$

As for the circumferential temperature field contribution, Eqs. 3.7, 3.8 and 3.9 can be simplified as:

$$\sigma_{T_\theta,r}(r,\theta) = K_\theta \frac{\alpha E}{2(1-\nu)} \left(1 - \frac{a^2}{r^2} \right) \left(1 - \frac{b^2}{r^2} \right), \quad (\text{B.4})$$

$$\sigma_{T_\theta,\theta}(r,\theta) = K_\theta \frac{\alpha E}{2(1-\nu)} \left(3 - \frac{a^2 + b^2}{r^2} - \frac{a^2 b^2}{r^4} \right), \quad (\text{B.5})$$

$$\tau_{r,\theta}(r,\theta) = K_\tau \frac{\alpha E}{2(1-\nu)} \left(1 - \frac{a^2}{r^2} \right) \left(1 - \frac{b^2}{r^2} \right), \quad (\text{B.6})$$

being K_θ and K_τ two constants dependent on the coefficients of the Fourier series, see Appendix A, for the complete temperature field, Eq. 3.3:

$$K_\theta = \frac{r}{a^2 + b^2} (B_1 \cos \theta + D_1 \sin \theta), \quad (\text{B.7})$$

$$K_\tau = \frac{r}{a^2 + b^2} (B_1 \cos\theta - D_1 \sin\theta). \quad (\text{B.8})$$

Therefore, the contribution of the stresses in the cross section for the axial stress is, which corresponds to the second term of Eq. 3.12:

$$\begin{aligned} \sigma_{T,z}(r, \theta) &= K_r \frac{\nu \alpha_r E}{2(1-\nu)} \left[1 - 2 \ln \left(\frac{b}{r} \right) - \frac{2a^2}{b^2 - a^2} \ln \left(\frac{b}{a} \right) \right] \\ &\quad + K_\theta \frac{\nu \alpha E}{2(1-\nu)} \left(2 - \frac{a^2 + b^2}{r^2} \right). \end{aligned} \quad (\text{B.9})$$

Now that the tube is considered to be homogeneous, with properties independent of the temperature, the virtual force P_T that appears when the tube is free to expand axially is constant $P_T = \int_A \alpha ET dA = E\bar{\alpha}T$. Thus, the first term in Eq. 3.12 can be written as:

$$\sigma_{M,z}(r, \theta) = E(\bar{\alpha}T - \alpha T) + E \left(r \cos\theta \frac{E}{\rho_y} + r \sin\theta \frac{E}{\rho_x} \right). \quad (\text{B.10})$$

For the bending radius, since E is assumed constant instead of temperature dependent, the numerator is the product EI , where I is the tube inertia moment, resulting from integrating $\int_A r^2 dA$. For a cylindrical tube:

$$I_x = Iy = \frac{\pi(b^4 - a^4)}{4}, \quad (\text{B.11})$$

$$\rho_x = \frac{I_x E}{M_y}, \quad \rho_y = \frac{I_y E}{M_x}. \quad (\text{B.12})$$

Here M_x and M_y are the moments on the tube, constituted by the thermal moments and the mechanical moments. The mechanical term is the one presented in Eq. 3.20 and remains unchanged since it does not depend on the tube material. The thermal moment working with constant properties changes though, being obtained as:

$$M_{T,x}(z) \int_A \alpha E Tr \cos\theta dA, \quad M_{T,y}(z) \int_A \alpha E Tr \sin\theta dA. \quad (\text{B.13})$$

With all of this, the final stresses in z can be rewritten as:

$$\begin{aligned} \sigma_z(r, \theta) &= K_r \frac{\nu \alpha_r E}{2(1-\nu)} \left[1 - 2 \ln \left(\frac{b}{r} \right) - \frac{2a^2}{b^2 - a^2} \ln \left(\frac{b}{a} \right) \right] \\ &\quad + K_\theta \frac{\nu \alpha E}{2(1-\nu)} \left(2 - \frac{a^2 + b^2}{r^2} \right) + E(\bar{\alpha}T - \alpha T) \\ &\quad + E \left(r \cos\theta \frac{E}{\rho_y} + r \sin\theta \frac{E}{\rho_x} \right). \end{aligned} \quad (\text{B.14})$$

And since the thermal expansion coefficient is constant, it can be regrouped as:

$$\begin{aligned}\sigma_z(r, \theta) = & K_r \frac{\alpha E}{2(1-\nu)} \left[1 - 2\ln\left(\frac{b}{r}\right) - \frac{2a^2}{b^2-a^2} \ln\left(\frac{b}{a}\right) \right] \\ & + K_\theta \frac{\nu \alpha E}{2(1-\nu)} \left(2 - \frac{a^2+b^2}{r^2} \right) - E \alpha T_\theta \\ & + E \left(r \cos\theta \frac{E}{\rho_y} + r \sin\theta \frac{E}{\rho_x} \right).\end{aligned}\quad (\text{B.15})$$

Nomenclature

A	tube cross section area (m^2)	M	bending moment (Nm)
a	tube inner radius (m)	P	force (N)
B, D	Fourier series coefficients	r	radial coordinate (m)
b	tube outer radius (m)	T	temperature (K)
E	Young modulus (GPa)	x, y, z	cartesian coordinates
I	tube inertia moment (m^4)		
K	constant		

Greek letters

α	linear thermal expansion coefficient (1/K)	ρ	bending radius (m)
θ	circumferential coordinate ($^\circ$)	σ	normal stress (MPa)
ν	Poisson ratio	τ	shear stress (MPa)

Subscripts

e	external surface		temperature
i	inner surface	x, y	cross section components
M	mechanical component	z	axial component
r	radial component	θ	circumferential component
T	thermal component,		

Appendix C: Time resolution analysis extended results

Table C.1: Lifetime results for the different time steps with receiver operating until the tank filling.

Time step	Lifetime (yrs)									
	Panel 1E	Panel 2E	Panel 3E	Panel 4E	Panel 5E	Panel 6E	Panel 7E	Panel 8E	Panel 9E	
Solar noon	10.92	11.58	12.29	13.32	15.72	20.31	24.14	31.02	36.15	
60-min	15.42	19.56	23.49	27.87	41.26	64.49	90.05	112.03	68.28	
30-min	15.93	19.86	23.14	27.87	38.81	65	90.42	108.611	73.67	
15-min	17.96	19.70	23.12	27.78	38.58	65.55	90.57	116.7	79.45	
7.5-min	18.22	19.76	23.06	27.64	38.31	64.93	89.67	117.35	81.05	
5-min	18.52	19.76	23.12	27.76	38.48	65.63	90.58	117.63	80.51	
2-min	19.01	19.7	23.07	27.7	38.46	65.37	90.06	117.02	80.23	
1-min	19.01	19.7	23.06	27.67	38.37	65.18	89.77	116.73	82.42	
Lifetime (yrs)										
Time step	Panel 1W	Panel 2W	Panel 3W	Panel 4W	Panel 5W	Panel 6W	Panel 7W	Panel 8W	Panel 9W	
	10.92	11.58	12.29	13.32	15.72	20.32	24.14	31.02	36.15	
Solar noon	10.92	19	19.58	24.75	36.24	101.5	170.1	321.06	353.86	82.11
60-min	18.65	19.78	24.95	37.12	96.74	172.47	340.11	371.92	84.69	
30-min	21.23	19.68	24.99	37	95.44	172.72	340.2	371.75	95.9	
15-min	21.34	19.75	24.95	36.83	94.53	172.19	338.63	375.48	97.09	
7.5-min	21.34	19.77	25.01	36.92	94.56	172.93	340.18	375.62	99.19	
5-min	21.89	19.72	25	36.95	95.09	172.8	339.89	375.23	99.45	
2-min	21.88	19.71	24.99	36.94	94.97	172.7	339.69	374.83	99.35	

Table C.2: Percentage lifetime variation with respect the 1-minute time step, with the receiver operating until the tank filling.

Percentage lifetime difference (%)										
Time step	Panel 1E	Panel 2E	Panel 3E	Panel 4E	Panel 5E	Panel 6E	Panel 7E	Panel 8E	Panel 9E	
Solar noon	-42.58	-41.19	-46.69	-51.86	-59.03	-68.83	-73.11	-73.42	-56.14	
60-min	-18.86	-0.67	1.88	0.72	7.53	-1.07	0.31	-4.02	-17.16	
30-min	-16.21	0.82	0.34	0.73	1.14	-0.28	0.72	-6.96	-10.62	
15-min	-5.50	0.02	0.24	0.39	0.55	0.54	0.89	-0.02	-3.61	
7.5-min	-4.17	0.33	0.01	-0.09	-0.17	-0.40	-0.11	0.53	-1.67	
5-min	-2.57	0.31	0.27	0.33	0.27	0.68	0.9	0.77	-2.32	
2-min	0.01	0.03	0.06	0.11	0.22	0.28	0.32	0.25	-2.65	

Percentage lifetime difference (%)										
Time step	Panel 1W	Panel 2W	Panel 3W	Panel 4W	Panel 5W	Panel 6W	Panel 7W	Panel 8W	Panel 9W	
Solar noon	-50.10	-41.24	-50.82	-63.94	-83.45	-88.24	-92.89	-91.72	-63.62	
60-min	-13.16	-0.66	-0.99	-1.89	6.88	-1.5	-5.48	-5.59	-17.36	
30-min	-14.73	0.35	-0.18	0.49	1.87	-0.13	0.12	-0.77	-14.76	
15-min	-2.94	-0.15	-0.01	0.18	0.50	0.02	0.15	-0.82	-3.47	
7.5-min	-2.44	0.20	-0.16	-0.28	-0.46	-0.29	-0.31	0.17	-2.28	
5-min	-2.43	0.28	0.08	-0.05	-0.43	0.13	0.14	0.21	-0.16	
2-min	0.06	0.01	0.02	0.04	0.13	0.06	0.06	0.11	0.1	

Table C.3: Percentage lifetime variation with respect the 1-minute time step. The receiver operates a fixed HOP corresponding to the 1-minute time step tank filling.

Percentage lifetime difference (%)										
Time step	Panel 1E	Panel 2E	Panel 3E	Panel 4E	Panel 5E	Panel 6E	Panel 7E	Panel 8E	Panel 9E	
60-min	-18.05	3.53	5.81	6.13	15.92	13.36	14.16	15.32	-7.01	
30-min	-15.80	2.42	2.12	3.17	4.53	3.91	6.51	2.15	-5.31	
15-min	-5.38	0.43	0.74	1.1	1.53	1.87	2.8	1.8	-1.84	
7.5-min	-4.14	0.43	0.13	0.07	0.06	-0.09	0.32	0.95	-1.24	
5-min	-2.53	0.43	0.41	0.53	0.54	1.04	1.4	1.27	-1.84	

Percentage lifetime difference (%)										
Time step	Panel 1W	Panel 2W	Panel 3W	Panel 4W	Panel 5W	Panel 6W	Panel 7W	Panel 8W	Panel 9W	
60-min	-8.02	2.52	0.15	-1.01	8.69	0.98	-2.58	0.31	-9.97	
30-min	-12.44	1.39	0.26	0.91	2.51	1.03	1.55	2.02	-11.18	
15-min	-2.33	0.11	0.1	0.29	0.67	0.34	0.57	-0.07	-2.16	
7.5-min	-2.3	0.26	-0.14	-0.25	-0.42	-0.22	-0.22	0.35	-1.97	
5-min	-2.25	0.35	0.11	-0.02	-0.39	0.23	0.26	0.43	0.2	

 APPENDIX
D

Appendix D: Set of days lifetime analysis extended results

Table D.1: Lifetime of the receiver panels for the set of representative days and average results.

Day	Lifetime (yrs)									
	Panel 1E	Panel 2E	Panel 3E	Panel 4E	Panel 5E	Panel 6E	Panel 7E	Panel 8E	Panel 9E	
172	23.55	26.04	31.58	41.17	54.88	98.11	129.77	135.38	38.73	
218	22.04	23.43	27.94	37.29	52.77	91.77	147.04	115.42	37.87	
238	18.49	20.66	24.49	31.26	43.19	76.02	126.54	150.28	53.00	
256	18.86	18.98	22.42	27.06	37.32	62.72	91.59	114.81	72.37	
272	17.09	19.02	22.50	26.97	38.53	59.66	87.78	111.10	92.77	
290	17.10	18.61	24.96	29.76	47.04	62.11	88.81	110.88	135.39	
310	19.35	18.94	27.49	34.05	52.59	66.68	104.09	169.27	276.87	
355	20.36	20.99	30.07	40.18	52.16	75.80	137.07	271.06	1,849.8	
Avg	19.6	20.83	26.43	33.47	47.31	74.11	114.09	147.28	319.60	
Day	Lifetime (yrs)									
	Panel 1W	Panel 2W	Panel 3W	Panel 4W	Panel 5W	Panel 6W	Panel 7W	Panel 8W	Panel 9W	
172	29.19	24.28	27.32	41.44	103.17	281.38	411.32	240.86	42.44	
218	29.75	21.98	25.57	38.62	93.99	204.14	355.19	217.10	48.86	
238	26.35	20.03	24.13	36.73	87.94	176.10	386.97	236.99	50.66	
256	22.27	18.70	23.72	35.48	88.55	164.34	335.41	365.69	76.27	
272	18.84	19.16	24.39	35.72	95.60	169.13	318.23	373.28	111.8	
290	18.14	18.98	26.27	37.60	100.57	188.94	367.45	504.00	187.5	
310	20.68	19.13	28.74	41.26	107.92	159.94	388.73	742.50	446.9	
355	21.37	21.04	31.19	46.75	96.32	184.84	470.33	1,175.5	2,637	
Avg	23.32	20.41	26.42	39.20	96.76	191.10	379.20	482.00	450.2	

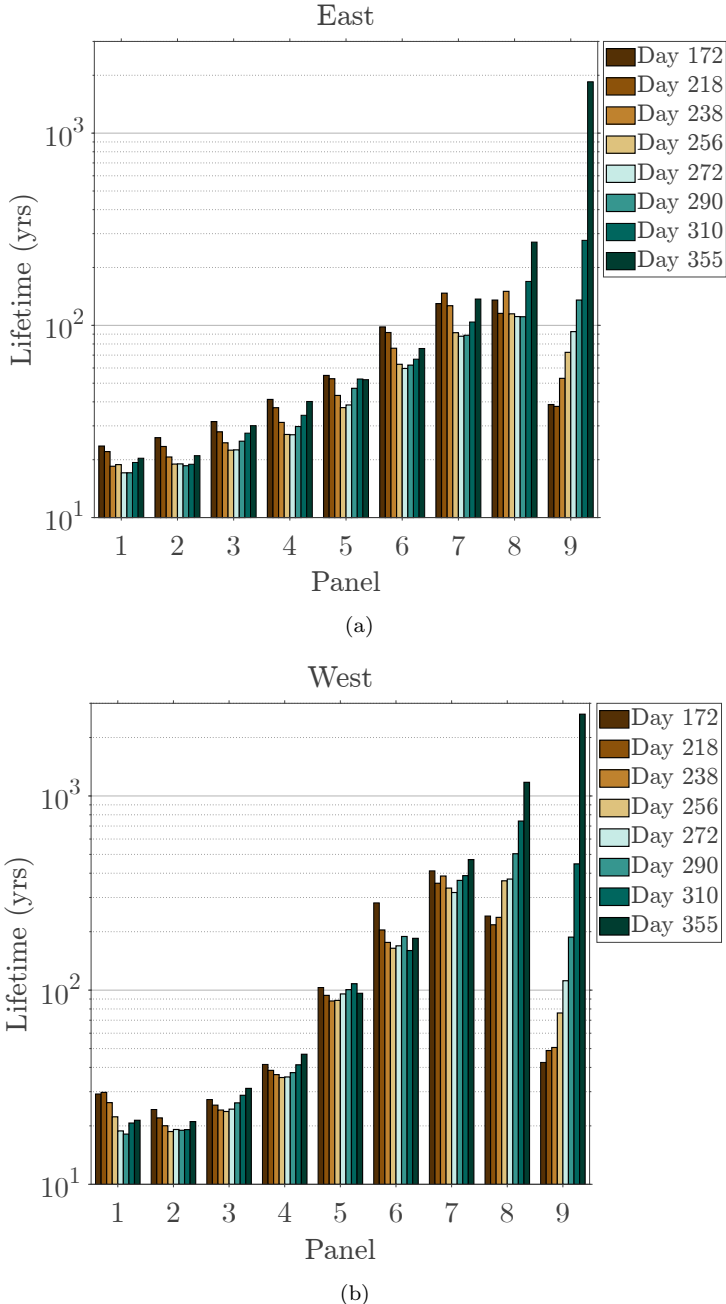


Figure D.1: Lifetime of the receiver panels during the set of representative days, in order to achieve the tank filling. (a) Eastern and (b) western flow paths.

Table D.2: Lifetime for the receiver panels during the filling operation of a tank with half the salts capacity.

Day	HOP	Lifetime (yrs)									
		Panel 1E	Panel 2E	Panel 3E	Panel 4E	Panel 5E	Panel 6E	Panel 7E	Panel 8E	Panel 9E	
172	4h 22min	63.77	93.54	129.1	156.78	202.58	276.62	266.47	149.66	62.15	
218	4h 30min	43.29	66.44	86.3	107.21	136.61	191.94	199.67	116.01	71.46	
238	4h 29min	29.82	60.51	93.63	132.98	207.20	293.38	321.79	128.66	75.15	
256	4h 31min	29.84	45.67	83.31	118.84	237.87	323.14	338.86	240.78	90.25	
272	4h 30min	27.15	48.65	74.12	99.22	228.71	291.80	361.92	364.44	130.32	
290	4h 38min	23.97	40.19	61.16	83.91	194.60	276.52	409.72	524.01	522.28	
310	4h 51min	24.65	30.66	45.44	71.08	168.08	227.30	375.82	1,334.4	1,787.4	
355	5h 14min	22.86	25.94	35.76	47.13	77.64	139.44	290.15	1,053.7	4,187.4	
Avg	4h 38min	33.17	51.45	76.11	102.15	181.66	252.52	320.55	488.96	865.8	
Lifetime (yrs)											
Day	HOP	Panel 1W	Panel 2W	Panel 3W	Panel 4W	Panel 5W	Panel 6W	Panel 7W	Panel 8W	Panel 9W	
		290.3	91.08	93.05	147.66	879.75	5,124.2	3,295.98	611.44	74.48	
172	4h 22min	161.1	47.88	75.67	129.35	730.30	3,174.8	3,783.27	746.00	79.23	
218	4h 30min	125.1	48.14	70.83	120.29	702.05	2,380.8	3,417.25	886.45	80.25	
238	4h 29min	46.33	48.60	61.69	99.05	576.22	1,309.9	2,205.28	1,124.96	142.40	
256	4h 31min	41.01	44.72	56.39	85.28	491.76	1,018.2	1,588.18	1,896.61	313.68	
272	4h 30min	36.96	36.73	47.00	67.63	280.90	655.27	1,174.09	2,371.49	624.16	
290	4h 38min	30.27	30.51	40.51	58.66	190.80	298.22	858.75	2,744.88	1,373.82	
310	4h 51min	29.47	26.27	34.70	51.34	113.72	221.15	649.55	2,466.45	4,652.12	
355	5h 14min	95.07	46.74	59.98	94.91	495.69	1,772.8	2,121.54	1,606.04	917.52	

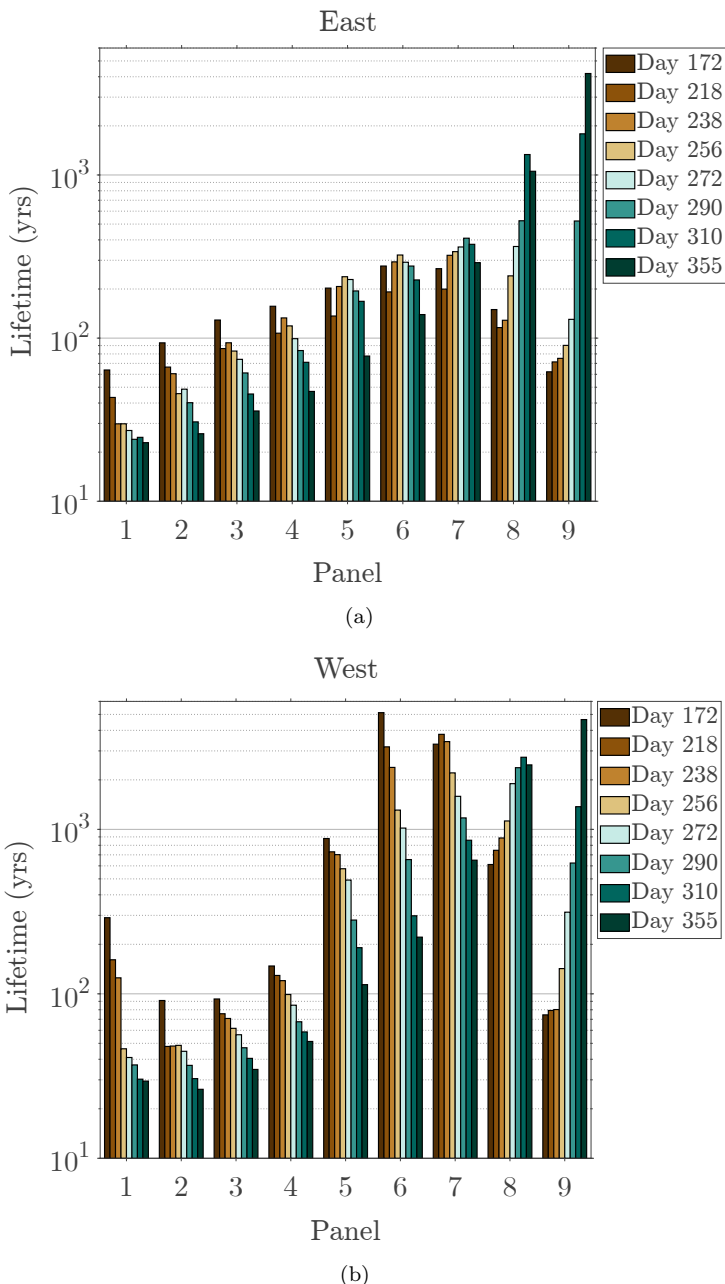


Figure D.2: Lifetime of the receiver panels during the set of representative days, in order to achieve half the tank filling. (a) Eastern and (b) western flow paths.

Alphabetical list of references

- ABE, F. 2015 Research and Development of Heat-Resistant Materials for Advanced USC Power Plants with Steam Temperatures of 700 °C and Above. *Engineering* 1 (2), 211–224.
- ASHBY, M.F. 1983 Mechanisms of deformation and fracture. *Advances in Applied Mechanics*, vol. 23, pp. 117–177. Elsevier.
- ASME 1980 ASME Boiler and Pressure Vessel Code. Code Cases: Nuclear Components Code Case N-47. American Society of Mechanical Engineers.
- ASME 2004 ASME Boiler and Pressure Vessel Code, Section III, Division 1, Subsection NH. American Society of Mechanical Engineers.
- ASME 2007 ASME FFS-1. Fitness-For-Service. American Society of Mechanical Engineers.
- ASME 2010 Asme boiler and Pressure Vessel Code, Section II part D. american society of mechanical engineers.
- ASME 2013 ASME Boiler and Pressure Vessel Code. American Society of Mechanical Engineers.
- ASME 2014 ASME Design Guidelines for the Effects of Creep, Fatigue & Creep-Fatigue Interaction. STP-PT-070. American Society of Mechanical Engineers.
- ASSELINEAU, C.A., COVENTRY, J. & PYE, J. 2018 Exergy analysis of the focal-plane flux distribution of solar-thermal concentrators. *Applied Energy* 222, 1023–1032.
- ASTM INTERNATIONAL. 2017 ASTM E1049-85: Standard Practices for Cycle Counting in Fatigue Analysis. West Conshohocken, PA.
- ATLAS STEELS 2011 Grade data sheet 316, 316L and 316H. http://www.atlassteels.com.au/documents/Atlas_Grade_datasheet_316_rev_Jan_2011.pdf, accessed: 30/04/2020.

- AUGSBURGER, G. & FAVRAT, D. 2013 Modelling of the receiver transient flux distribution due to cloud passages on a solar tower thermal power plant. *Solar Energy* 87 (1), 42–52.
- BABCOCK & WILCOX COMPANY 1984 Molten Salt Receiver Subsystem Research Experiment Phase 1 -Final Report, Volume 1- Technical. *Tech. Rep.* SAND82-8178. Barberton, OH, United States.
- BARRETT, P.R., AHMED, R., MENON, M. & HASSAN, T. 2016 Isothermal low-cycle fatigue and fatigue-creep of Haynes 230. *International Journal of Solids and Structures* 88-89, 146–164.
- BARUA, B., McMURTREY, M.D., RUPP, R.E. & MESSNER, M.C. 2020 Design Guidance for High Temperature Concentrating Solar Power Components. *Tech. Rep.* ANL-20/03. Argonne National Laboratory, Argonne, IL, United States.
- BAUER, T., PFLEGER, N., BREIDENBACH, N., ECK, M., LAING, D. & KAESCHE, S. 2013 Material aspects of Solar Salt for sensible heat storage. *Applied Energy* 111, 1114–1119.
- BECHT IV, C. 2011 Elevated temperature shakedown concepts. *Journal of Pressure Vessel Technology, Transactions of the ASME* 133 (5), 051203–1–5.
- BEJAN, A. 1978 General criterion for rating heat-exchanger performance. *International Journal of Heat and Mass Transfer* 21 (5), 655–658.
- BEJAN, A. 1982 Second-Law Analysis in Heat Transfer and Thermal Design. *Advances in Heat Transfer* 15 (C), 1–58.
- BELLOS, E. & TZIVANIDIS, C. 2017 A detailed exergetic analysis of parabolic trough collectors. *Energy Conversion and Management* 149, 275–292.
- BELLOS, E. & TZIVANIDIS, C. 2019 Alternative designs of parabolic trough solar collectors. *Progress in Energy and Combustion Science* 71, 81–117.
- BENOIT, H., SPREAFICO, L., GAUTHIER, D. & FLAMANT, G. 2016 Review of heat transfer fluids in tube-receivers used in concentrating solar thermal systems: Properties and heat transfer coefficients. *Renewable and Sustainable Energy Reviews* 55, 298–315.
- BERGER, X., BURIOT, D. & GARNIER, F. 1984 About the equivalent radiative temperature for clear skies. *Solar Energy* 32 (6), 725–733.

- BERMAN, I., GANGADHARAN, A.C., GUPTA, G.D. & NARAYANAN, T.V. 1979 An interim structural design standard for solar energy applications. *Tech. Rep.* SAND79-8183. Sandia National Laboratories, Albuquerque, NM, United States.
- BIJLAARD, P.P., DOHRMANN, R.J. & DUKE, J.M. 1968 Thermal Stress Analysis of Nonuniformly Heated Cylindrical Shell and Its Application to a Steam Generator Membrane Wall. *Journal of Engineering Power* 1 (90), 73–81.
- BOEHLERT, C.J. & LONGANBACH, S.C. 2011 A comparison of the microstructure and creep behavior of cold rolled HAYNES® 230 alloy and HAYNES® 282 alloy. *Materials Science and Engineering A* 528 (15), 4888–4898.
- BOUBAULT, A., HO, C.K., HALL, A., LAMBERT, T.N. & AMBROSINI, A. 2016 Levelized cost of energy (LCOE) metric to characterize solar absorber coatings for the CSP industry. *Renewable Energy* 85, 472–483.
- BOUBAULT, A., HO, C.K., HALL, A., LAMBERT, T.N. & AMBROSINI, A. 2017 Durability of solar absorber coatings and their cost-effectiveness. *Solar Energy Materials and Solar Cells* 166, 176–184.
- BRADSHAW, R.W. & GOODS, S.H. 2001 Corrosion of Alloys and Metals by Molten Nitrates. *Tech. Rep.* SAND 2000-8727. Sandia National Laboratories, Albuquerque, NM, and Livermore, CA, United States.
- BREE, J. 1967 Elastic-plastic behaviour of thin tubes subjected to internal pressure and intermittent high-heat fluxes with application to fast-nuclear-reactor fuel elements. *Journal of Strain Analysis* 2 (3), 226–238.
- BRINKMAN, C.R., STRIZAK, J.P. & BOOKER, M.K. 1976 Time-dependent strain-controlled fatigue behavior of annealed 2 1/4 Cr-1 Mo steel for use in nuclear steam generator design. *Journal of Nuclear Materials* 62, 181–204.
- BRITISH ENERGY GENERATION 2003 R5, Issue 3 assessment procedure for the high temperature response of structures.
- BUI-QUOC, T., GOMUC, R., BIRON, A., NGUYEN, H.L. & MASOUNAVE, J. 1988 Elevated Temperature Fatigue-Creep Behavior of Nickel-Base Superalloy IN 625. In *Low Cycle Fatigue* (ed. H. Solomon, G. Halford, L. Kaisand & B. Leis), pp. 470–484. ASTM International.

- BURGALETA, J.I., ARIAS, S. & RAMIREZ, D. 2011 Gemasolar, the first tower thermosolar commercial plant with molten salt storage. In *Proceedings of the SolarPACES 2011 conference on concentrating solar power and chemical energy systems, Granada, Spain.*
- CANDAU, Y. 2003 On the exergy of radiation. *Solar Energy* 75 (3), 241–247.
- CHEN, X., SOKOLOV, M.A., SHAM, S., ERDMAN, D.L., BUSBY, J.T., MO, K. & STUBBINS, J.F. 2013 Experimental and modeling results of creep-fatigue life of Inconel 617 and Haynes 230 at 850 °C. *Journal of Nuclear Materials* 432 (1-3), 94–101.
- CHOPRA, O.K. & SHACK, W.J. 2003 Review of the margins for ASME code fatigue design curve - effects of surface roughness and material variability. *Tech. Rep. NUREG/CR6815, ANL-02/39.* Argonne National Laboratory, Argonne, IL, United States.
- COCCO, D., MIGLIARI, L. & PETROLLESE, M. 2016 A hybrid CSP-CPV system for improving the dispatchability of solar power plants. *Energy Conversion and Management* 114, 312–323.
- COCCO, D., PETROLLESE, M. & TOLA, V. 2017 Exergy analysis of concentrating solar systems for heat and power production. *Energy* 130, 192–203.
- CONROY, T., COLLINS, M.N., FISHER, J. & GRIMES, R. 2018a Levelized cost of electricity evaluation of liquid sodium receiver designs through a thermal performance, mechanical reliability, and pressure drop analysis. *Solar Energy* 166, 472–485.
- CONROY, T., COLLINS, M.N., FISHER, J. & GRIMES, R. 2018b Thermal and mechanical analysis of a sodium-cooled solar receiver operating under a novel heliostat aiming point strategy. *Applied Energy* 230, 590–614.
- CONROY, T., COLLINS, M.N. & GRIMES, R. 2019 A review of steady-state thermal and mechanical modelling on tubular solar receivers. *Renewable and Sustainable Energy Reviews* 119.
- CRESPI, F., TOSCANI, A., ZANI, P., SÁNCHEZ, D. & MANZOLINI, G. 2018 Effect of passing clouds on the dynamic performance of a CSP tower receiver with molten salt heat storage. *Applied Energy* 229 (January), 224–235.
- CUNAT, P.-J. 2004 Alloying elements in stainless steel and other chromium-containing alloys. EuroInox, pp. 1–24.

- DE BARBADILLO, J.J. 2017 INCONEL alloy 740H. In *Materials for Ultra-Supercritical and Advanced Ultra-Supercritical Power Plants*, 1st edn., chap. 14, pp. 469–510. Woodhead Publishing.
- DE BARBADILLO, J.J., BAKER, B.A., GOLLIHUE, R.D. & MCCOY, STEPHEN A. 2018 Properties of inconel alloy 740H for high pressure steam and supercritical CO₂ applications. In *ASME Symposium on Elevated Temperature Application of Materials for Fossil, Nuclear, and Petrochemical Industries (ETAM2018)*, Seattle, WA, United States, pp. 6741 1–11.
- DU, B.C., HE, Y.L., ZHENG, Z.J. & CHENG, Z.D. 2016 Analysis of thermal stress and fatigue fracture for the solar tower molten salt receiver. *Applied Thermal Engineering* 99, 741–750.
- ELLYIN, F. 1996 *Fatigue Damage, Crack Growth and Life Prediction*, 1st edn. Dordrecht: Springer Netherlands.
- ENO, D.R., YOUNG, G.A. & SHAM, T.-L. 2008 A Unified View of Engineering Creep Parameters. In *ASME Pressure Vessels and Piping Division Conference (PVP2008)*, Chicago, IL, United States, July 27–31, pp. 777–792. Chicago: ASME.
- ESLAMI, M.R., HETNARSKI, R.B., IGNACZAK, J., NODA, N., SUMI, N. & TANIGAWA, Y. 2013 *Theory of Elasticity and Thermal Stresses*, 1st edn., *Solid Mechanics and Its Applications*, vol. 197. Dordrecht: Springer.
- EUROPEAN COMMISION 2020 Photovoltaic geographical information system. https://re.jrc.ec.europa.eu/pvgf_tools/en/tools.html, accessed: 10/06/2020.
- FAHRMANN, M.G. & SRIVASTAVA, S.K. 2014 Low cycle fatigue behaviour of HAYNES 230 alloy. *Materials at High Temperatures* 31 (3), 221–225.
- FALCONE, P.K. 1986 A handbook for solar central receiver design. *Tech. Rep.* SAND-86-8009. Sandia National Laboratories, Livermore, CA, United States.
- FELDMAN, D.J., O'SHAUGHNESSY, E. & MARGOLIS, R.M. 2020 Q3/Q4 2019 Solar Industry Update. *Tech. Rep.* NREL/PR-6A20-76158. National Renewable Energy Laboratory (NREL), Golden, CO, United States.
- FELDMAN, D.J., ZWERLING, M. & MARGOLIS, R.M. 2019 Q2/Q3 2019 Solar Industry Update. *Tech. Rep.* NREL/PR-6A20-75484. National Renewable Energy Laboratory (NREL), Golden, CO, United States.

- FLESCH, J., MAROCCHI, L., FRITSCH, A., NIEDERMEIER, K. & WETZEL, T. 2020 Entropy Generation Minimization Analysis of Solar Salt, Sodium, and Lead-Bismuth Eutectic as High Temperature Heat Transfer Fluids. *Journal of Heat Transfer* 142 (4), 1–10.
- FORK, D.K., FITCH, J., ZIAEI, S. & JETTER, R.I. 2012 Life Estimation of Pressurized-Air Solar-Thermal Receiver Tubes. *Journal of Solar Energy Engineering* 134 (4), 041016–1–11.
- FRITSCH, A., UHLIG, R., MAROCCHI, L., FRANTZ, C., FLESCH, R. & HOFF-SCHMIDT, B. 2017 A comparison between transient CFD and FEM simulations of solar central receiver tubes using molten salt and liquid metals. *Solar Energy* 155, 259–266.
- GARBRECHT, O., AL-SIBAI, F., KNEER, R. & WIEGHARDT, K. 2013 CFD-simulation of a new receiver design for a molten salt solar power tower. *Solar Energy* 90, 94–106.
- GATEWOOD, B.E. 1941 XXIII. Thermal stresses in long cylindrical bodies. *The London, Edinburgh, and Dublin Philosophical Magazine and Journal of Science* 32 (213), 282–301.
- GLINKA, G. 1985 Calculation of inelastic notch-tip strain-stress histories under cyclic loading. *Engineering Fracture Mechanics* 22 (5), 839–854.
- GNIELINSKI, V.V. 1976 Neue Gleichungen für den Wärme- und Stoffaustausch in turbulent durchströmten Rohren und Kanälen, *Forsch. Ing. Wes.* 41 (1), 8–16 (1975). Englisch Translation: New equations for heat and mass transfer in turbulent pipe and channel flow. *Int. Chem. Eng* 16 (2), 359–368.
- GÓMEZ-HERNÁNDEZ, J., GONZÁLEZ-GÓMEZ, P.A., BRIONGOS, J.V. & SANTANA, D. 2018 Influence of the steam generator on the exergetic and exergoeconomic analysis of solar tower plants. *Energy* 145, 313–328.
- GONZÁLEZ-GÓMEZ, P.A., GÓMEZ-HERNÁNDEZ, J., BRIONGOS, J.V. & SANTANA, D. 2019 Lifetime analysis of the steam generator of a solar tower plant. *Applied Thermal Engineering* 159, 113805.
- GONZÁLEZ-GÓMEZ, P.A., RODRÍGUEZ-SÁNCHEZ, M.R., LAPORTE-AZCUÉ, M. & SANTANA, D. 2021 Calculating molten-salt central-receiver lifetime under creep-fatigue damage. *Solar Energy* 213, 180–197.

- GOODIER, J.N. 1957 Thermal Stress and Deformation. *Journal of Applied Mechanics* 24, 467–474.
- GROSSMAN, J.W. & JONES, W.B. 1990 Evaluation of thermal cycling creep-fatigue damage for a molten salt receiver. In *ASME international solar energy conference, Miami, FL, United States*.
- GUÉDEZ, R., SPELLING, J., LAUMERT, B. & FRANSSON, T. 2014 Optimization of thermal energy storage integration strategies for peak power production by concentrating solar power plants. *Energy Procedia* 49 (0), 1642–1651.
- HAYNES INTERNATIONAL 2020 Haynes ® 230 ® alloy. <http://haynesintl.com/docs/default-source/pdfs/new-alloy-brochures/high-temperature-alloys/brochures/230-brochure.pdf>, accessed: 12/03/2020.
- HERNÁNDEZ-JIMÉNEZ, F., SORIA-VERDUGO, A., ACOSTA-IBORRA, A. & SANTANA, D. 2019 Exergy recovery from solar heated particles to supercritical CO₂. *Applied Thermal Engineering* 146, 469–481.
- HILDEBRANDT, A.F., HAAS, G.M., JENKINS, W.R. & COLACO, J.P. 1972 Large-scale concentration and conversion of solar energy. *Eos, Transactions American Geophysical Union* 53 (7), 684–692.
- HO, C.K., MAHONEY, A.R., AMBROSINI, A., BENCOMO, M., HALL, A. & LAMBERT, T.N. 2012 Characterization of pyromark 2500 for high-temperature solar receivers. *ASME 2012 6th International Conference on Energy Sustainability, ES 2012, Collocated with the ASME 2012 10th International Conference on Fuel Cell Science, Engineering and Technology* 136 (PARTS A AND B), 509–518.
- HO, C.K. & PACHECO, J.E. 2014 Levelized Cost of Coating (LCOC) for selective absorber materials. *Solar Energy* 108, 315–321.
- IDEL'CHIK, I.E. 1960 *Handbook of hydraulic resistance*, 3rd edn. USA: Begell House.
- IPCC 2018 Global Warming of 1.5°C. An IPCC Special Report on the impacts of global warming of 1.5°C above pre-industrial levels and related global greenhouse gas emission pathways, in the context of strengthening the global response to the threat of climate change,. *Tech. Rep. 1. Intergovernmental Panel on Climate Change*, Geneva, Switzerland.

- IRENA 2012 Renewable Energy Cost Analysis: Concentrating Solar Power. *Tech. Rep.* June. International Renewable Energy Agency, Abu Dhabi.
- IRENA 2016 The Power to Change: Solar and Wind Cost Reduction Potential to 2025. *Tech. Rep.* June. Internation Renewable Energy Agency, Abu Dhabi.
- IRENA 2019 Global energy transformation: A roadmap to 2050 (2019 edition). *Tech. Rep.* April. International Renewable energy Agency, Abu Dhabi.
- IRENA 2020a Renewable Energy Statistics 2020. *Tech. Rep.* July. International Renewable Energy Agency, Abu Dhabi.
- IRENA 2020b Renewable Power Generation Costs in 2019. *Tech. Rep.* June. International Renewable Energy Agency, Abu Dhabi.
- JENA, P.S.M., SINGH, R.K., MAHANTA, L., PASWAN, S. & SAHU, J.K. 2018 Low cycle fatigue behaviour of nickel base superalloy IN 740H at 760°C: Influence of fireside corrosion atmosphere. *International Journal of Fatigue* 116, 623–633.
- JEONG, C.Y., NAM, S.W. & GINSZTLER, J. 1999 Activation processes of stress relaxation during hold time in 1Cr-Mo-V steel. *Materials Science and Engineering A* 264, 188–193.
- JIANFENG, L., JING, D. & JIANPING, Y. 2010 Heat transfer performance of an external receiver pipe under unilateral concentrated solar radiation. *Solar Energy* 84 (11), 1879–1887.
- JONES, D.R.H. & ASHBY, M.F. 2019a Creep and Creep Fracture. In *Engineering Materials 1*, chap. 21, pp. 351–366. Elsevier.
- JONES, D.R.H. & ASHBY, M.F. 2019b Mechanisms of Creep, and Creep-Resistant Materials. In *Engineering Materials 1*, chap. 23, pp. 381–394. Elsevier.
- KAAE, J.L. 2009 High-temperature low-cycle fatigue of Alloy 800H. *International Journal of Fatigue* 31, 332–340.
- KALNINS, A. 2006 Fatigue analysis in pressure vessel design by local strain approach: Methods and software requirements. *Journal of Pressure Vessel Technology, Transactions of the ASME* 128 (1), 2–7.

- KELLY, B., IZYGON, M. & VANT-HULL, L. 2010 Advanced Thermal Energy Storage for Central Receivers with supercritical coolants. *Tech. Rep.* DOE/GO18149. Abengoa Solar Inc., Lakewood, CO, United States.
- KHANNA, S., KEDARE, S.B. & SINGH, S. 2014 Deflection and stresses in absorber tube of solar parabolic trough due to circumferential and axial flux variations on absorber tube supported at multiple points. *Solar Energy* 99, 134–151.
- KHANNA, S. & SHARMA, V. 2015 Effect of number of supports on the bending of absorber tube of parabolic trough concentrator. *Energy* 93, 1788–1803.
- KHANNA, S., SHARMA, V., KEDARE, S.B. & SINGH, S. 2016 Experimental investigation of the bending of absorber tube of solar parabolic trough concentrator and comparison with analytical results. *Solar Energy* 125, 1–11.
- KISTLER, B.L. 1987 Fatigue analysis of a solar central receiver design using measured weather data. *Tech. Rep.* SAND86-8017. Sandia National Laboratories, Albuquerque, NM, United States.
- KOLB, G.J. 2011 An Evaluation of Possible Next-Generation High Temperature Molten-Salt Power Towers. *Tech. Rep.* SAND2011-9320. Sandia National Laboratories, Albuquerque, NM, United States.
- KOLB, G.J., HO, C.K., MANCINI, T.R. & GARY, J.A. 2011 Power tower technology roadmap and cost reduction plan. *Tech. Rep.* SAND2011-2419. Sandia National Laboratories, Albuquerque, NM, United States.
- KOUTA, A., AL-SULAIMAN, F., ATIF, M. & MARSHAD, S.B. 2016 Entropy, exergy, and cost analyses of solar driven cogeneration systems using supercritical CO₂ Brayton cycles and MEE-TVC desalination system. *Energy Conversion and Management* 115, 253–264.
- KUMAR, A., SHARMA, M., THAKUR, P., THAKUR, V.K., RAHATEKAR, S.S. & KUMAR, R. 2020 A review on exergy analysis of solar parabolic collectors. *Solar Energy* 197, 411–432.
- LARRAÑETA, M., FERNANDEZ-PERUCHENA, C., SILVA-PÉREZ, M.A. & LILLO-BRAVO, I. 2018 Methodology to synthetically downscale DNI time series from 1-h to 1-min temporal resolution with geographic flexibility. *Solar Energy* 162 (October), 573–584.

- LIAO, Z., LI, X., XU, C., CHANG, C. & WANG, Z. 2014 Allowable flux density on a solar central receiver. *Renewable Energy* 62, 747–753.
- LILLIESTAM, J., LABORDENA, M., PATT, A. & PFENNINGER, S. 2017 Empirically observed learning rates for concentrating solar power and their responses to regime change. *Nat. Energy* 2, 17094.
- LILLIESTAM, J. & PITZ-PAAL, R. 2018 Concentrating solar power for less than USD 0.07 per kWh: finally the breakthrough? *Renewable Energy Focus* 26, 17–21.
- LITWIN, R.Z. 2002 Receiver System: Lessons Learned From Solar Two. *Tech. Rep.* SAND2002-0084. Sandia National Laboratories, Albuquerque, NM, and Livermore, CA, United States.
- LIU, B.Y.H. & JORDAN, R.C. 1960 The interrelationship and characteristic distribution of direct, diffuse and total solar radiation. *Solar Energy* 4 (3), 1–19.
- LOGIE, W.R., PYE, J.D. & COVENTRY, J. 2018 Thermoelastic stress in concentrating solar receiver tubes: A retrospect on stress analysis methodology, and comparison of salt and sodium. *Solar Energy* 160, 368–379.
- LOPEZ, Z. & FATEMI, A. 2012 A method of predicting cyclic stress-strain curve from tensile properties for steels. *Materials Science & Engineering A* 556, 540–550.
- LOVEGROVE, K. & STEIN, W. 2012 *Concentrating solar power technology: principles, developments and applications*, 1st edn. Cambridge (U.K.): Woodhead publishing.
- LU, J.-T., LI, Y., YANG, Z., HUANG, J.-Y., ZHU, M. & GU, Y. 2017 Fireside Corrosion Behaviors of Inconel 740H Superalloy in Various SO₂ Contents. In *Energy Materials 2017. The Minerals, Metals & Materials Series*, 1st edn., pp. 193–201. Cham, Switzerland: Springer.
- LUO, K., LI, C., XUE, F., LIU, Y., ZHANG, L. & ZHANG, G. 2018 Oxidation and Hot Corrosion Behavior of Inconel 740H Alloy at High Temperature. In *High Performance Structural Materials. Proceedings of Chinese Materials Conference (CMC) 2017* (ed. Yafang Han), pp. 557–565. Singapore: Springer Singapore.

- MADAENI, S.H., SIOSHANSI, R. & DENHOLM, P. 2012 How thermal energy storage enhances the economic viability of concentrating solar power. *Proceedings of the IEEE* 100 (2), 335–347.
- MAIYA, P.S. 1980 Cyclic stress-strain curves and cyclic-hardening behavior for types 304 and 316 stainless steel and Incoloy alloy 800H. *Tech. Rep.* ANL-80-100. Argonne National Laboratory, Argonne, IL, United States.
- MAO, J., TANG, D., BAO, S., LUO, L. & GAO, Z. 2016 High temperature strength and multiaxial fatigue life assessment of a tubesheet structure. *Engineering Failure Analysis* 68, 10–21.
- MARUGÁN-CRUZ, C., FLORES, O., SANTANA, D. & GARCÍA-VILLALBA, M. 2016 Heat transfer and thermal stresses in a circular tube with a non-uniform heat flux. *International Journal of Heat and Mass Transfer* 96, 256–266.
- MATAVELI SUAVE, L., CORMIER, J., BERTHEAU, D., VILLECHASE, P., SOULA, A., HERVIER, Z. & HAMON, F. 2016 High temperature low cycle fatigue properties of alloy 625. *Materials Science and Engineering A* 650, 161–170.
- MATHWORKS 2017 Rainflow counting method. <https://mathworks.com/help/signal/ref/rainflow.html>, accessed: 21/03/2021.
- MAYTORENA, V.M. & HINOJOSA, J.F. 2019 Effect of non-uniform concentrated solar flux on direct steam generation in vertical pipes of solar tower receivers. *Solar Energy* 183 (December), 665–676.
- McCONOHY, G. & KUIZENGA, A. 2014 Molten nitrate salts at 600 and 680°C: Thermophysical property changes and corrosion of high-temperature nickel alloys. *Solar Energy* 103, 242–252.
- MCMURTREY, M.D. 2019 Creep-fatigue Behavior and Damage Accumulation of a Candidate Structural Material for Concentrating Solar Power Solar Thermal Receiver. *Tech. Rep.* INL/EXT-19-55551-Rev000. Idaho National Laboratory, Idaho Falls, ID, United States.
- MEHOS, M., PRICE, H., CABLE, R., KEARNEY, D., KELLY, B., KOLB, G. & MORSE, F. 2020 Concentrating Solar Power Best Practices Study. *Tech. Rep.* NREL/TP-5500-75763. National Renewable Energy Laboratory, Solar Dynamics LLC, Golden, CO, United States.

- MEHOS, M., TURCHI, C., VIDAL, J., WAGNER, M., MA, Z., HO, C., KOLB, W., ANDRAKA, C. & KRUIZENGA, A. 2017 Concentrating Solar Power Gen3 Demonstration Roadmap. *Tech. Rep.* NREL/TP-5500-67464. National Renewable Energy Laboratory, Sandia National Laboratories, Golden, CO, United States.
- MEYBODI, M. AGHAEI, RAMIREZ SANTIGOSA, L. & BEATH, A.C. 2017 A study on the impact of time resolution in solar data on the performance modelling of CSP plants. *Renewable Energy* 109, 551–563.
- MEYERS, M.A. & CHAWLA, K.K. 2008 *Mechanical behavior of materials*, 2nd edn. Cambridge university press.
- MILIOZZI, A., GIANNUZZI, G.M., TARQUINI, P. & LA BARBERA, A. 2001 Fluido termovettore: dati di base della miscela di nitrati di sodio e potassio. *Tech. Rep.* ENEA/SOL/RD/2001/07. ENEA, Rome, Italy.
- MINIS, N., ROSENBLUTH, E., HAYUT, R. & AM-SHALLEM, M. 2019 Spatial DNI measurement for accurate solar flux control in Megalim 121 MWe solar receiver power plant. *AIP Conference Proceedings* 2126 (July), 030037.
- MOFTAKHAR, A., BUCZYNSKI, A. & GLINKA, G. 1995 Calculation of elasto-plastic strains and stresses in notches under multiaxial loading. *International Journal of Fracture* 70 (4), 357–373.
- MONTOYA, A., RODRÍGUEZ-SÁNCHEZ, M.R., LÓPEZ-PUENTE, J. & SANTANA, D. 2018 Numerical model of solar external receiver tubes: Influence of mechanical boundary conditions and temperature variation in thermoelastic stresses. *Solar Energy* 174, 912–922.
- MORENO-TEJERA, S., SILVA-PÉREZ, M.A., RAMÍREZ-SANTIGOSA, L. & LILLO-BRAVO, I. 2017 Classification of days according to DNI profiles using clustering techniques. *Solar Energy* 146, 319–333.
- MORENO-TEJERA, S., SILVA-PÉREZ, M.A., RAMÍREZ-SANTIGOSA, L. & LILLO-BRAVO, I. 2018 Evaluation of classification methods according to solar radiation features from the viewpoint of the production of parabolic trough CSP plants. *Renewable Energy* 121, 429–440.
- MTSCO 2020 Mt stainless steel. <http://www.mtstainlesssteel.com>, accessed: 05/12/2020.

- MURPHY, C., SUN, Y., COLE, W., MACLAURIN, G., TURCHI, C. & MEHOS, M. 2019 The Potential Role of Concentrating Solar Power within the Context of DOE's 2030 Solar Cost Targets. *Tech. Rep.* NREL/TP-6A20-71912. National Renewable Energy Laboratory (NREL), Golden, CO, United States.
- NARAYANAN, T.V., RAO, M.S.M. & CARLI, G. 1985 Structural Design and Life Assessment of a Molten Salt Solar Receiver. *Journal of Solar Energy Engineering* 107 (3), 258–263.
- NATIONAL RENEWABLE ENERGY LABORATORY (NREL) 2020 Concentrating solar power projects: Power tower projects. <https://solarpaces.nrel.gov/by-technology/power-tower>, accessed: 07/06/2021.
- NECATI ÖZİSİK, M. 1993 *Heat Conduction*, 2nd edn. New York: Wiley-Interscience.
- NEISES, T.W., WAGNER, M.J. & GRAY, A.K. 2014 Structural Design Considerations for Tubular Power Tower. In *International Conference on Energy Sustainability (ES2014)*, Boston, MA, United States, pp. 6603 1–7. National Renewable Energy Laboratory.
- NICOL, K. 2013 Status of advanced ultra-supercritical pulverised coal technology. *Tech. Rep.* CCC/229. IEA Clean Coal Centre, London, UK.
- NITHYANANDAM, K. & PITCHUMANI, R. 2016 Thermal and structural investigation of tubular supercritical carbon dioxide power tower receivers. *Solar Energy* 135, 374–385.
- NODA, N., HETNARSKI, R.B. & TANIGAWA, Y. 2003 *Thermal Stresses*, 2nd edn. New York, London: Taylor & Francis.
- NOVALES, D., ERKOREKA, A., DE LA PEÑA, V. & HERRAZTI, B. 2019 Sensitivity analysis of supercritical CO₂ power cycle energy and exergy efficiencies regarding cycle component efficiencies for concentrating solar power. *Energy Conversion and Management* 182, 430–450.
- ORTEGA, J., KHIVSARA, S., CHRISTIAN, J., HO, C., YELLOWHAIR, J. & DUTTA, P. 2016 Coupled modeling of a directly heated tubular solar receiver for supercritical carbon dioxide Brayton cycle: Optical and thermal-fluid evaluation. *Applied Thermal Engineering* 109, 970–978.
- ÖZTÜRK, H.H. 2004 Experimental determination of energy and exergy efficiency of the solar parabolic-cooker. *Solar Energy* 77 (1), 67–71.

- PACHECO, J.E 2002 Final Test and Evaluation Results from the Solar Two Project. *Tech. Rep.* SAND2002-0120. Sandia International Laboratories, Albuquerque, NM, United States.
- PADILLA, R.V., FONTALVO, A., DEMIRKAYA, G., MARTINEZ, A. & QUIROGA, A.G. 2014 Exergy analysis of parabolic trough solar receiver. *Applied Thermal Engineering* 67 (1-2), 579–586.
- PATEL, N.S., PAVLÍK, V. & BOČA, M. 2017 High-Temperature Corrosion Behavior of Superalloys in Molten Salts-A Review. *Critical Reviews in Solid State and Materials Sciences* 42 (1), 83–97.
- PAYTEN, W.M., SNOWDEN, K.U. & DEAN, D.W. 2013 Effects of prior stress relaxation on the prediction of creep life using time and strain based methods. *Journal of Pressure Vessel Technology* 135, 041201–1–8.
- PCC ENERGY GROUP 2020 Inconel® Alloy 740H: A Superalloy Specifically Designed for Advanced Ultra Supercritical Power Generation. <http://www.specialmetals.com/files/PCCEG740HWhitePaper.pdf>, accessed: 07/04/2020.
- PERSKY, M.J. & SZCZESNIAK, M. 2008 Infrared, spectral, directional hemispherical reflectance of fused silica, Teflon polytetrafluoroethylene polymer, chrome oxide ceramic particle surface, Pyromark 2500 paint, Krylon 1602 paint, and Duraflect coating. *Applied Optics* 47 (10), 1389.
- PETELA, R. 1964 Exergy of Heat Radiation. *Journal of Heat Transfer* 86 (2), 187–192.
- PETELA, R. 2003 Exergy of undiluted thermal radiation. *Solar Energy* 74 (6), 469–488.
- PETELA, R. 2005 Exergy analysis of the solar cylindrical-parabolic cooker. *Solar Energy* 79 (3), 221–233.
- PYE, J., ZHENG, M., ASSELINEAU, C.-A. & COVENTRY, J. 2014 An exergy analysis of tubular solar-thermal receivers with different working fluids. *International Conference on Concentrating Solar Power and Chemical Energy Systems (SolarPACES 2014)*, Beijing pp. 1–10.
- QIU, Z. & LI, P. 2019 *Advanced Energy Efficiency Technologies for Solar Heating, Cooling and Power Generation*, 1st edn. Hull, UK: Springer International Publishing.

- RADKE, E.F., DEWEES, D.J., WASYLUK, D.T. & TANZOSH, J.M. 2017 Creep-fatigue design applied to molten salt solar receivers. In *ASME 2014 Symposium on Elevated Temperature Application of Materials for Fossil, Nuclear, and Petrochemical Industries (ETAM2014)*, Seattle, WA, United States, pp. 1032–232–247.
- RADOSEVICH, G. & SKINROOD, A.C. 1989 The Power Production Operation of Solar One, the 10 MWe Solar Thermal Central Receiver Pilot Plant 1. *Journal of solar Energy Engineering* 111, 144–151.
- RAO, K.B.S., SCHUSTER, H. & HALFORD, G.R. 1996 Mechanisms of high-temperature fatigue failure in alloy 800H. *Metallurgical and Materials Transactions A* 27 (4), 851–861.
- REN, W. & LIN, L. 2019 Consideration of Thermal Embrittlement in Alloy 316H for Advanced Non-Light Water Reactor Applications. *Pressure Vessels and Piping Conference (PVP2019)*, San Antonio, TX, United States, vol. 6B: Materials and Fabrication. V06BT06A016.
- RENO, M.J., HANSEN, C.W. & STEIN, J.S. 2012 Global horizontal irradiance clear sky models : implementation and analysis. *Tech. Rep.* SAND2012-2389. Sandia International Laboratories, Albuquerque, NM, United States.
- RICHTER, C., TESKE, S. & SHORT, R. 2009 Concentrating Solar Power Global Outlook 09- Why renewable energy is hot. *Tech. Rep.* June. Greenpeace international, SolarPACES, ESTELA.
- RODRÍGUEZ-SÁNCHEZ, M.R., MARUGÁN-CRUZ, C., ACOSTA-IBORRA, A. & SANTANA, D. 2014a Comparison of simplified heat transfer models and CFD simulations for molten salt external receiver. *Applied Thermal Engineering* 73 (1), 991–1003.
- RODRÍGUEZ-SÁNCHEZ, M.R., MARUGÁN-CRUZ, C., ACOSTA-IBORRA, A. & SANTANA, D. 2018 Thermo-mechanical modelling of solar central receivers: Effect of incident solar flux resolution. *Solar Energy* 165, 43–54.
- RODRÍGUEZ-SÁNCHEZ, M.R., SÁNCHEZ-GONZÁLEZ, A., MARUGÁN-CRUZ, C. & SANTANA, D. 2015 Flow patterns of external solar receivers. *Solar Energy* 122, 940–953.

- RODRÍGUEZ-SÁNCHEZ, M.R., SORIA-VERDUGO, A., ALMENDROS-IBÁÑEZ, J. A., ACOSTA-IBORRA, A. & SANTANA, D. 2014b Thermal design guidelines of solar power towers. *Applied Thermal Engineering* 63 (1), 428–438.
- ROHANI, S., FLURI, T.P., DINTER, F. & NITZ, P. 2017 Modelling and simulation of parabolic trough plants based on real operating data. *Solar Energy* 158, 845–860.
- ROMEO, E., ROYO, C. & MONZÓN, A. 2002 Improved explicit equations for estimation of the friction factor in rough and smooth pipes. *Chemical Engineering Journal* 86 (3), 369–374.
- SÁNCHEZ-GONZÁLEZ, A., RODRÍGUEZ-SÁNCHEZ, M.R. & SANTANA, D. 2018 Aiming factor to flatten the flux distribution on cylindrical receivers. *Energy* 153, 113–125.
- SÁNCHEZ-GONZÁLEZ, A. & SANTANA, D. 2015 Solar flux distribution on central receivers: A projection method from analytic function. *Renewable Energy* 74, 576–587.
- SCANNAPIECO, J.F. 1968 Irradiation of thermal control coatings, Final report. *Tech. Rep.* NASA-CR-94684, DOC.-68SD4224. General Electric Co.; Missile And Space Div., Philadelphia, PA, United States.
- SIEBERS, D. & KRAABEL, J. 1984 Estimating convective energy losses from solar central receivers. *Tech. Rep.* SAND-84-8717. Sandia National Laboratories, Albuquerque, NM, and Livermore, CA, United States.
- SINGER, C., BUCK, R., PITZ-PAAL, R. & MÜLLER-STEINHAGEN, H. 2010 Assessment of Solar Power Tower Driven Ultrasupercritical Steam Cycles Applying Tubular Central Receivers With Varied Heat Transfer Media. *Journal of Solar Energy Engineering* 132 (4), 041010.
- SINGER, C., GIULIANO, S. & BUCK, R. 2014 Assessment of improved molten salt solar tower plants. *Energy Procedia* 49, 1553–1562.
- SKARTVEIT, A. & OLSETH, J.A. 1992 The probability density and autocorrelation of short-term global and beam irradiance. *Solar Energy* 49 (6), 477–487.
- SOLAR CONCENTRA 2013 Plataforma Tecnológica de la Energía Solar Térmica de Concentración. <https://www.solarconcentra.org>.

- SPECIAL METALS CORP. 2004 INCOLOY alloy 800H & 800HT. <https://www.specialmetals.com/assets/smc/documents/alloys/incoloy/incoloy-alloys-800h-800ht.pdf>, accessed: 14/04/2020.
- SPECIAL METALS CORP. 2013 INCONEL alloy 625. <https://www.specialmetals.com/assets/smc/documents/alloys/inconel/inconel-alloy-625.pdf>, accessed: 12/04/2020.
- STEIN, J.S., HANSEN, C.W. & RENO, M.J. 2012 The variability index: A new and novel metric for quantifying irradiance and PV output variability. *World Renewable Energy Forum, WREF 2012, Including World Renewable Energy Congress XII and Colorado Renewable Energy Society (CRES) Annual Conference* 4 (May), 2764–2770.
- TALER, J., DZIERWA, P., JAREMKIEWICZ, M., TALER, D., KACZMARSKI, K., TROJAN, M. & SOBOTA, T. 2019 Thermal stress monitoring in thick walled pressure components of steam boilers. *Energy* 175, 645–666.
- TIAN, Y. & ZHAO, C.Y. 2013 A review of solar collectors and thermal energy storage in solar thermal applications. *Applied Energy* 104, 538–553.
- TIMOSHENKO, S. & GOODIER, J.N. 1951 *Theory of Elasticity*, 2nd edn. New York: McGraw-Hill Book Company.
- TORRESOL 2021 Torresol Energy: Gemasolar. <https://torresolenergy.com/en/gemasolar/>, accessed: 16/03/2021.
- UHLIG, R., FRANTZ, C., FLESCH, R. & FRITSCH, A. 2018 Stress analysis of external molten salt receiver. In *AIP Conference Proceedings of the SolarPACES 2017 conference on concentrating solar power and chemical energy systems, Santiago, Chile*, vol. 2033, pp. 040040 1–8. AIP Publishing.
- US DEPARTMENT OF ENERGY 2021 CSP Component Research and Development. <https://www.energy.gov/eere/solar/csp-component-research-and-development>, accessed: 17/03/2021.
- VANT-HULL, L.L. 2002 The role of "allowable flux density" in the design and operation of molten-salt solar central receivers. *Journal of Solar Energy Engineering, Transactions of the ASME* 124 (2), 165–169.
- WADE, W.R. & SLEMP, W.S. 1962 Measurements of total emittance of several refractory oxides, cermets, and ceramics for temperatures from 600 degrees

- F to 2,000 degrees F. *Tech. Rep.* NASA-TN-D-998; AD-272614. National Aeronautics and Space Administration (NASA), Langley Field, VA, United States.
- WAGNER, M.J. 2008 Simulation and Predictive Performance Modeling of Utility-Scale Central Receiver System Power Plants. PhD thesis, University of Wisconsin, Madison.
- WAGNER, M.J., HAMILTON, W.T., NEWMAN, A., DENT, J., DIEP, C. & BRAUN, R. 2018 Optimizing dispatch for a concentrated solar power tower. *Solar Energy* 174, 1198–1211.
- WANG, R.Z., ZHANG, X.C., GONG, J.G., ZHU, X.M., TU, S.T. & ZHANG, C.C. 2017 Creep-fatigue life prediction and interaction diagram in nickel-based GH4169 superalloy at 650 °C based on cycle-by-cycle concept. *International Journal of Fatigue* 97, 114–123.
- WHITTAKER, M.T., EVANS, M. & WILSHIRE, B. 2012 Long-term creep data prediction for type 316H stainless steel. *Materials Science and Engineering A* 552, 145–150.
- XU, C., WANG, Z., LI, X. & SUN, F. 2011 Energy and exergy analysis of solar power tower plants. *Applied Thermal Engineering* 31 (17-18), 3904–3913.
- YAN, X.L., ZHANG, X.C., TU, S.T., MANNAN, S.L., XUAN, F.Z. & LIN, Y.C. 2015 Review of creep-fatigue endurance and life prediction of 316 stainless steels. *International Journal of Pressure Vessels and Piping* 126, 17–28.
- YANG, X., YANG, X., DING, J., SHAO, Y. & FAN, H. 2012 Numerical simulation study on the heat transfer characteristics of the tube receiver of the solar thermal power tower. *Applied Energy* 90 (1), 142–147.
- ZAVOICO, A.B. 2001 Solar Power Tower - Design Basis Document. *Tech. Rep.* SAND2001-2100. Sandia National Laboratories, Albuquerque, NM and Livermore, CA, United States.
- ZHANG, S. & TAKAHASHI, Y. 2018 Creep and Creep-Fatigue Deformation and Life Assessment of Ni-Based Alloy 740H and Alloy 617. *Pressure Vessels and Piping Conference (PVP 2018)*, Prague, Czech Republic, vol. 6A: Materials and Fabrication. V06AT06A060.

- ZURITA, A., MATA-TORRES, C., CARDEMIL, J.M. & ESCOBAR, R.A. 2020
Assessment of time resolution impact on the modeling of a hybrid CSP-PV
plant: A case of study in Chile. *Solar Energy* 202, 553–570.
- ZURITA, A., MATA-TORRES, C., VALENZUELA, C., CARDEMIL, J.M. & Es-
COBAR, R. A. 2018 Techno-economic analysis of a hybrid CSP+PV plant
integrated with TES and BESS in Northern Chile. *AIP Conference Proceedings* (November), 180013.

